

Optical Tests of Complementarity and Nonlocality

by

David Andrew Branning

Submitted in Partial Fulfillment

of the

Requirements for the Degree

Doctor of Philosophy

Supervised by

Professor Leonard Mandel

Department of Physics and Astronomy

The College

Arts and Sciences

University of Rochester

Rochester, New York

1998

This page intentionally left blank.



In memory of my grandfather, Howell,
and to my parents, Charles and Frances

I am going to tell you what nature behaves like. If you will simply admit that maybe she does behave like this, you will find her a delightful, entrancing thing. Do not keep saying to yourself, if you can possibly avoid it, 'But how can it be like that?' because you will get 'down the drain,' into a blind alley from which nobody has yet escaped.

--Richard Feynman, in
The Character of Physical Law

Curriculum Vitae

The author was born in Menard, Texas on March 21, 1969. He entered Rice University in 1986 with a National Merit Scholarship and graduated with a Bachelor of Arts in Physics in 1990. After one year of graduate studies there, he left South Texas for a fifteen-month research appointment at the Los Alamos National Laboratory. In 1992 he began graduate studies at the University of Rochester as a G.A.A.N. Fellow of the United States Department of Education. In 1993 he received the Graduate Student Teaching Award from the Department of Physics and Astronomy, and began research under the supervision of Professor Leonard Mandel. In 1994 he received the degree Master of Arts in Physics. During the 1996-1997 academic year, he served as an adjunct lecturer in physics at the State University of New York at Geneseo and at the University of Rochester.

List of Publications

- “Engineering Indistinguishability”, D. Branning, W.P. Grice, R. Erdmann, and I.A. Walmsley, to be published.
- “Multiphoton Interference Effects at a Beam Splitter”, A. Kuzmich, D. Branning, L. Mandel, and I.A. Walmsley, to be published.
- “Spectral Distinguishability in Ultrafast Parametric Downconversion”, W.P. Grice, R. Erdmann, I.A. Walmsley, and D. Branning, *Phys. Rev. A* **57**, R2289 (1998).
- “Does Nature Violate Local Realism?”, D. Branning, *American Scientist* **85**, 160 (March-April 1997).
- “Reply to ‘EPR Skepticism’”, D. Branning and J.R. Torgerson, *Optics & Photonics News* **7**, No. 7 (July 1996).
- “Reply to Comment by Cabello and Santos on ‘Experimental Demonstration of the Violation of Local Realism without Bell Inequalities’”, J.R. Torgerson, D. Branning, C.H. Monken, and L. Mandel, *Phys. Lett. A* **214**, 319 (1996).
- “Experimental Test of Selleri’s Photodetection Model”, A. Garuccio, J. Torgerson, C. H. Monken, D. Branning, and L. Mandel, *Phys. Rev. A* **53**, 2944 (1996).
- “Generating Mutual Coherence from Incoherence with the Help of a Phase-Conjugate Mirror”, C.H. Monken, A. Garuccio, D. Branning, J.R. Torgerson, F. Narducci and L. Mandel, *Phys. Rev. A* **53**, 1782 (1996).
- “Violations of Local Realism in a Hardy-Jordan Type Experiment without use of Bell Inequalities”, D. Branning, J.R. Torgerson, C.H. Monken and L. Mandel, in **Coherence and Quantum Optics VII (Proceedings of the 7th Rochester Conference on Coherence and Quantum Optics**, eds. J.H. Eberly, L. Mandel and E. Wolf, Plenum Press, New York, NY, 1996) p. 661.
- “New Experimental Realization of a Quantum Eraser Based on Down-Conversion”, C.H. Monken, D. Branning and L. Mandel in **Coherence and Quantum Optics VII (Proceedings of the 7th Rochester Conference on Coherence and Quantum Optics**, eds. J.H. Eberly, L. Mandel and E. Wolf, Plenum Press, New York, NY, 1996) pg. 701.
- “Violations of Locality in Polarization-Correlation Measurements with Phase Shifters”, J.R. Torgerson, D. Branning, C.H. Monken, and L. Mandel, *Phys. Rev. A* **51**, 4400 (1995).
- “Experimental Demonstration of the Violation of Local Realism Without Bell Inequalities”, J.R. Torgerson, D. Branning, C.H. Monken and L. Mandel, *Phys. Lett. A* **204**, 323 (1995).

- “A Method of Demonstrating Violation of Local Realism with a Two-Photon Downconverter Without Use of Bell Inequalities”, J. Torgerson, D. Branning, and L. Mandel, *Applied Physics B*, **60** 267 (1994).
- “Time-Dependent Distinguishability: Choosing to be a Wave or a Particle”, T.P. Grayson, X.Y. Zou, D. Branning, J.R. Torgerson and L. Mandel, in **Conference Proceedings of 1993 UMBC Conference on Squeezed States and Uncertainty Relations**, eds. D. Han, Y. S. Kim, N. H. Rubin, Y. Shih and W. W. Zachary, (NASA Conference Publications, 1994) pg. 123.
- “Interference and Indistinguishability Governed by Time Delays in a Low-Q Cavity“, T.P. Grayson, X.Y. Zou, D. Branning, J.R. Torgerson and L. Mandel, *Phys. Rev. A* **48**, 4793 (1993).

Acknowledgments

The first thing I noticed when I entered Professor Mandel's office in the spring of 1992 was a bookshelf stacked to the ceiling with numbered reams of publication reprints. Upon closer inspection, I realized two things: that every article on the shelves bore his name in the list of authors, and that there were some 220 of them. Although I had never heard of Professor Mandel before that day, standing in front of that wall of paper stretching back to 1954, I began to feel somewhat awed. I was shown in to the second part of his office, where, in front of another wall of reprints, Professor Mandel kindly explained to me some of the recent work his research group had carried out. As our discussion continued, my intimidation gave way to excitement, and I realized that this was the kind of work I wanted to do. I owe Professor Mandel my sincerest gratitude for giving me his time that day, for accepting me into his group a year later, and for allowing me to pursue both the research and the teaching that has kept me excited about physics in the intervening years. I have benefited greatly from his wisdom and generosity during my tenure here, sometimes by his direct tutelage, sometimes just by reading one of the articles from the wall.

I am thankful to Justin Torgerson, who entered Professor Mandel's group at the same time I did, and with whom I shared many hundreds of hours in the laboratory and in the office. Justin was always the first person available to ask a question, and more often than not, we worked out the answers together. More than anyone else here, his experience in graduate school mirrors my own, and I wish him well.

Frank Narducci earned my admiration and respect from the first day I entered his lab. As a researcher, he showed me what true professionalism in graduate school was all about: he was always on top of the situation, in command of a dazzling array of

both technical and theoretical techniques, and dedicated to obtaining results under even the most difficult experimental circumstances. As a teacher and mentor, he was clear, direct, and unafraid to say the words “I don’t know.” I am privileged to count him as a friend and hope that we will meet again often.

André Fougères was also an excellent mentor during my early years in this group. Along with Tim Grayson, André and Frank put up with the constant barrage of questions from myself and Justin with good humor and a sincere desire to pass the torch on to us. Their integrity as scientists continues to be an inspiration to me.

Several of the experiments reported here were conducted with the help of Carlos Monken, a postdoctoral student whose considerable talents and practical lab experience allowed our work to progress much more swiftly. For two summers we also benefited from the presence of Professor Augusto Garuccio, whose primer lectures on Bell’s inequality have proved an invaluable resource to me over the years. Augusto’s unwavering interest in the foundations of quantum mechanics motivated many entertaining and enlightening discussions within our group, and I look forward to more of these discussions with him in the years to come.

On countless occasions, Jennifer Van Remmen, our group’s administrative assistant, ran the gauntlet of university red tape to ensure that things went smoothly for us. It has been a pleasure to know her and her husband, Bill: I will miss the science fiction movie outings. Thanks also to Barbara Warren for all her help and for notifying me of various impending deadlines throughout the years.

I am also hugely indebted to Professor Ian Walmsley, who once invited me to give a talk at one of his group meetings and hasn’t been able to get rid of me since. Ian and his senior student, Warren Grice, were kind enough to let me poke around in their lab and scribble on their papers. I learned much from Warren during his last year here.

In recent months, Reinhard Erdmann has been a stalwart companion during the long nights of data acquisition. From the beginning, all of the members of Ian's group -- Warren, Reinhard, Leon Waxer, Chris Iaconis, Tim Shumann, and Luis De Araujo -- treated me as one of their own without hesitation, and have helped me in one way or another. I am proud to have been associated with them and look forward to our future collaborations.

Thanks to Professor Nick Bigelow for occasional use of various critical pieces of lab equipment, and for lending a friendly ear from time to time. Thanks also to Professors Stan Dodds and Bill Wilson of Rice University for their friendship and words of wisdom during my time there. I am especially grateful to Bill for suggesting that I apply to the University of Rochester for graduate school.

Finally, I wish to thank my mother and father, who fostered my interest in science from a young age and never wavered in their support for the path I have chosen. I would not be who I am without the many opportunities they have provided me in life.

Abstract

Two of the most celebrated and counterintuitive aspects of quantum theory -- complementarity and nonlocality -- are investigated in a series of five experiments which use the entangled photon pairs generated via spontaneous parametric downconversion.

In the introduction, the complementary relationship between path distinguishability and interference of photons is presented, followed by an historical introduction to nonlocality, the EPR paradox, and Bell's inequality. The entangled quantum state for the signal and idler photons produced in the process of spontaneous parametric downconversion is derived heuristically.

An experimental realization of a "quantum eraser" is then presented. When the photon paths in a Mach-Zehnder interferometer are rendered distinguishable by coupling to an auxiliary observable, interference vanishes as demanded by complementarity. However, the experiment shows that if the auxiliary observable is measured in such a way as to permanently destroy this "which-path" information, interference reappears for two distinct subensembles of the photons. This shows that interference need not vanish as a result of "uncontrollable disturbances" linked to the uncertainty principle; it can be destroyed and revived solely on the basis of what information is available, in principle, to the observer.

Next, the effect of spectral distinguishability on two-photon interference is shown in a common-path fourth-order interferometer with type-II downconversion pumped by ultrafast pulses. The loss of interference visibility due to spectral distinguishability has important implications for future multi-particle interferometry experiments, including GHZ demonstrations of nonlocality and quantum teleportation schemes. The distinguishability is found to be related to the symmetry of the joint emission amplitude spectrum for the signal and idler photons. This suggests a

mechanism for full restoration of the interference which is successfully demonstrated in the next chapter.

In the next experiment, the Clauser-Horne-Shimony-Holt form of Bell's inequality is shown to be violated by 29 standard deviations by measurements of entangled photon pairs in the circular polarization basis. Possible reasons for the failure of earlier attempts to violate a Bell inequality with circularly polarized light are discussed.

Finally, the first experimental demonstration of the violation of local realism in nature without the use of Bell inequalities (but with supplementary assumptions) is presented.

Table of Contents

	Page
Curriculum Vitae	iv
List of Publications	v
Acknowledgments	vii
Abstract	x
Table of Contents	xii
List of Figures	xvii
Chapter 1: Introduction	1
1.1 Complementarity	1
1.1.1 The uncertainty principle and “which path” information	1
1.1.2 Indistinguishable in principle, or in practice?	2
1.1.3 Two-photon interference and spectral markers	6
1.2 Nonlocality	7
1.2.1 The limits of quantum information	7
1.2.2 The EPR Paradox	8
1.2.2.1 The EPR-Bohm thought experiment	8
1.2.2.2 Realism, locality, and the paradox	10
1.2.2.3 Bohr’s reply	13
1.2.3 Bell’s inequality	14
1.2.3.1 Bell’s theorem	14
1.2.3.2 Experimental violations of Bell’s inequality	16
1.2.3.3 Experimental non-violations of Bell’s inequality?	18
1.2.4 Beyond Bell’s inequality	18
1.3 Spontaneous parametric downconversion	20
1.3.1 Overview	20
1.3.2 The quantum state	24
1.3.3 Type-I and type-II phase-matching	25
1.3.4 Cw and pulsed pump sources	26
1.4 Methods, notation, and terminology	27
1.4.1 Using the interaction picture to describe monochromatic fields	27

1.4.2 Notation for the Hilbert-space norm	28
1.4.3 Photons	28
References for Chapter 1	30
 Chapter 2: The Quantum Eraser	 32
2.1 Introduction	32
2.1.1 Complementarity without the uncertainty principle?	32
2.1.2 “Which path” information in the Mach-Zehnder interferometer	35
2.1.3 Erasing “which path” information	38
2.2 Schematic and theory	42
2.2.1 Schematic of the experiment	42
2.2.2 Quantum state of the light	44
2.2.3 Predicted counting rates	45
2.3 Experimental procedure and results	47
2.3.1 Apparatus	47
2.3.2 Results	48
2.4 Discussion	49
2.4.1 Comparison with the “quantum preventer” of Zou et al.	49
2.4.2 “In principle” vs. “in practice” distinguishability revisited	53
References for Chapter 2	56
 Chapter 3: Spectral distinguishability and interference	 58
3.1 Introduction	58
3.1.1 Ultrafast pump pulses and type-II downconversion	58
3.1.2 Fourth-order interference in the Hong-Ou-Mandel interferometer	59
3.2 Schematic and theory	64
3.2.1 Schematic of the experiment	64
3.2.2 Quantum state of the light	66
3.2.3 Predicted counting rates	70
3.2.3.1 Two-photon coincidence probabilities from one pulse	70
3.2.3.2 Symmetry and indistinguishability	72
3.2.3.3 Coincidence counting rates	75
3.3 Experimental procedure and results	77
3.3.1 Apparatus	77

3.3.2 Results	82
3.3.2.1 Data taken with the broadband pump	82
3.3.2.2 Data taken with a narrowband pump	82
3.3.2.3 Data taken with the broadband pump and detector filters	84
3.4 Discussion	84
3.4.1 Comparison of spectral filtering in pulsed vs. cw experiments	84
3.4.2 Interpretation of the results	85
References for Chapter 3	87
 Chapter 4: Engineering spectral indistinguishability	 88
4.1 Introduction	88
4.2 Schematic and theory	91
4.2.1 Schematic of the experiment	91
4.2.2 Quantum state of the light	93
4.2.3 Predicted counting rates	94
4.2.3.1 Single-channel counts	94
4.2.3.2 Coincidence counts	97
4.2.4 Dispersion in the Michelson interferometer	101
4.2.4.1 Eliminating dispersion	101
4.2.4.2 The consequences of dispersion	105
4.3 Experimental procedure and results	111
4.3.1 Apparatus	111
4.3.2 Results	115
4.4 Discussion	120
4.4.1 Is the phase drift in the coincidence counts a systematic error?	120
4.4.2 Comparison with the experiments of Herzog, et al.	122
4.4.3 Interpretation of the interference terms	124
References for Chapter 4	126
 Chapter 5: Locality violations in the circular polarization basis	 127
5.1 Introduction	127
5.1.1 Non-violations of Bell's inequality	127
5.1.2 The Clauser-Horne-Shimony-Holt inequality	128
5.1.3 Entangled states in the circular basis	131

5.2 Schematic and theory	134
5.2.1 Schematic of the experiment	134
5.2.2 Quantum state of the light	134
5.2.3 Predicted counting rates	137
5.3 Experimental procedure and results	139
5.3.1 Apparatus	139
5.3.2 Results	142
5.4 Discussion	142
5.4.1 Comparison with the results of Clauser and Duncan, et al.	142
5.4.2 Supplementary assumptions	144
References for Chapter 5	147
Chapter 6: Violation of locality without Bell's inequality	149
6.1 Introduction	149
6.1.1 The Hardy-Jordan propositions	149
6.1.2 Dutch doors	153
6.1.3 Supplementary assumptions	156
6.2 Schematic and theory	159
6.2.1 Schematic of the experiment	159
6.2.2 Quantum state of the light	159
6.2.3 Predicted counting rates	161
6.3 Experimental procedure and results	163
6.3.1 Apparatus	163
6.3.2 Results	166
6.4 Discussion	168
6.4.1 Dutch doors with broken latches	168
6.4.2 Supplementary assumptions revisited	169
6.4.3 Comparison with the experiment of Boschi, et al.	171
References for Chapter 6	175
Chapter 7: Summary	176
Appendix A: Quantum state for type-I downconversion with a cw pump	179
A.1 The interaction picture and the weak-field approximation	179

A.2 Hamiltonian for the parametric downconversion interaction	180
A.3 Dynamics of the field operators	182
A.4 The multimode state	183
A.5 The two-mode state	190
Appendix B: Quantum state for type-II downconversion with a broadband pump	192
B.1 Derivation	192
B.2 Normalization	196
Appendix C: Quantum state for the “Engineering Indistinguishability” experiment	198
C.1 Derivation	198
C.2 Normalization	200
Appendix D: Locking system for an interferometer	202
D.1 Conceptual arrangement	202
D.2 Operational details	206

List of Figures

Figure 1.1	Young's double-slit experiment	3
Figure 1.2	Young's double-slit experiment with "markers"	5
Figure 1.3	The EPR-Bohm thought experiment	9
Figure 1.4	Parametric downconversion	21
Figure 1.5	Virtual levels for parametric downconversion	23
Figure 2.1	Variations on Young's double-slit experiment	33
Figure 2.2	A Mach-Zehnder interferometer	36
Figure 2.3	The quantum eraser	40
Figure 2.4	Experimental realization of a quantum eraser	43
Figure 2.5	Measured single-channel and coincidence counts without interference	50
Figure 2.6	Measured single-channel and coincidence counts with interference	51
Figure 2.7	The quantum preventer	52
Figure 2.8	The quantum eraser as a double-slit experiment	54
Figure 3.1	The Hong-Ou-Mandel interferometer	60
Figure 3.2	The collinear Hong-Ou-Mandel interferometer	65
Figure 3.3	The joint emission amplitude spectrum for type-II downconversion	68
Figure 3.4	Symmetry and indistinguishability of coincidence amplitudes	73
Figure 3.5	Predicted coincidence counting rates	78
Figure 3.6	Experimental realization of a collinear Hong-Ou-Mandel interferometer	79
Figure 3.7	Measured coincidence counts for three experimental configurations	83
Figure 4.1	Conceptual arrangement for symmetrization of the emission spectrum	90
Figure 4.2	Predicted coincidence counting rates	100
Figure 4.3	Dispersive elements in the Michelson interferometer	103
Figure 4.4	Predicted coincidence counting rates with dispersion	108
Figure 4.5	Predicted coincidence counting rates with dispersion and imbalance	110
Figure 4.6	The modified collinear Hong-Ou-Mandel interferometer	112
Figure 4.7	Measured single-channel and coincidence counts at three delay values	116
Figure 4.8	Measured coincidence counts for all delay values	117
Figure 4.9	Extracted minimum and maximum coincidence counts vs. delay	119
Figure 4.10	Relative phase of coincidence vs. single-channel fringes	121
Figure 4.11	The experiment of Herzog et al.	123

Figure 5.1	Testing the CHSH inequality	129
Figure 5.2	Testing the CHSH inequality in the circular polarization basis	132
Figure 5.3	Experimental test of the CHSH inequality in the circular basis	135
Figure 5.4	Diagram of the performed experiment	140
Figure 5.5	Experimental results for the quantity S	143
Figure 6.1	The Hardy-Jordan thought experiment	150
Figure 6.2	Dutch doors	154
Figure 6.3	Modified Dutch doors	158
Figure 6.4	Experimental test of the Hardy-Jordan propositions	160
Figure 6.5	Diagram of the performed experiment	164
Figure 6.6	Measured coincidence counts for the Hardy-Jordan polarizations	167
Figure A.1	Parametric downconversion with apertures	186
Figure A.2	The interaction volume for parametric downconversion	188
Figure B.1	Type-II collinear parametric downconversion	193
Figure D.1	Locking system for a Michelson interferometer	203
Figure D.2	Locking circuit schematic	205

This page intentionally left blank.

Chapter 1

Introduction

This thesis reports the results of five experiments which demonstrate complementarity and nonlocality in quantum mechanics with optical techniques. Each experiment made use of the correlated photon pairs produced in the process of spontaneous parametric downconversion. In the following sections we introduce the concepts of complementarity and nonlocality, and the process of parametric downconversion.

1.1 Complementarity

1.1.1 The uncertainty principle and “which path” information

For any system described by quantum mechanics, it is possible to find certain pairs of observables -- usually the quantum-mechanical counterparts of classical, canonically conjugate quantities like momentum and position -- which cannot be measured simultaneously to arbitrary precision. Such observables, denoted here as \hat{P} and \hat{Q} , are referred to as *complementary*, and they obey Heisenberg’s minimum uncertainty relation,

$$\delta\hat{P} \delta\hat{Q} \geq \frac{\hbar}{2}. \quad (1.1)$$

This tells us that there is a fundamental limit to how well the values of \hat{P} and \hat{Q} can be determined in the same measurement¹. The standard interpretation of this state of affairs, due to Bohr, is that the experimental arrangements required to measure complementary observables are always physically incompatible, so that making a precise measurement of one precludes making a precise measurement of the other [1].

The idea of complementarity may be extended to describe the wave/particle duality exhibited by all quantum mechanical objects. Although electrons, photons, and atoms all possess wave and particle properties, they never manifest both types of behavior together. And, just as is the case for complementary observables, any experimental arrangement designed to show one of these complementary attributes necessarily hides the other. For example, if we have an experimental arrangement designed to exhibit optical interference, such as Young's double-slit apparatus (see Figure 1.1), then the interference only appears in those cases in which it is impossible to determine which path the photons traversed to reach the screen where they were detected. The interference is taken to be a signature of wavelike behavior, while the "which-path" information is understood to be a "particle" property for the photons.

1.1.2 Indistinguishable in principle, or in practice?

"Indistinguishability leads to interference" is the mantra that will be encountered repeatedly throughout this work. It is a simple idea, but there are some situations in which it is quite a subtle matter to determine whether or not the paths leading to a given photodetection event really are indistinguishable or not.

¹ The standard deviations $\delta\hat{P} = \left\langle \left(\hat{P} - \langle \hat{P} \rangle \right)^2 \right\rangle^{1/2}$ and $\delta\hat{Q} = \left\langle \left(\hat{Q} - \langle \hat{Q} \rangle \right)^2 \right\rangle^{1/2}$ are statistical properties related to an ensemble of measurements, but may also be interpreted as widths of probability distributions for the outcome of any single measurements.

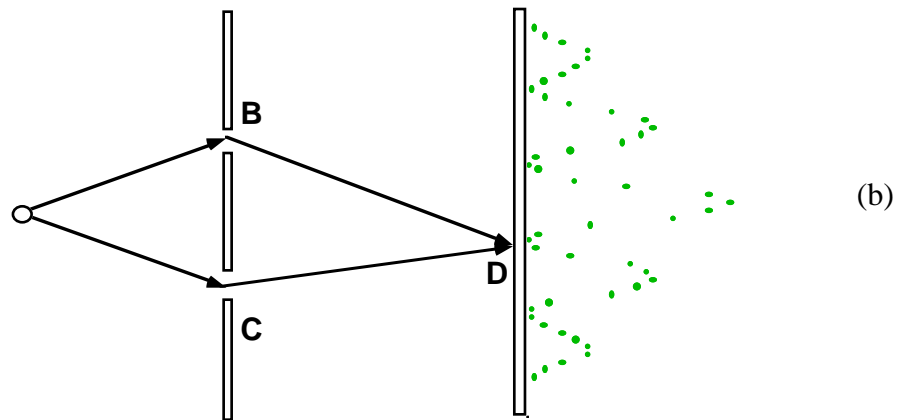
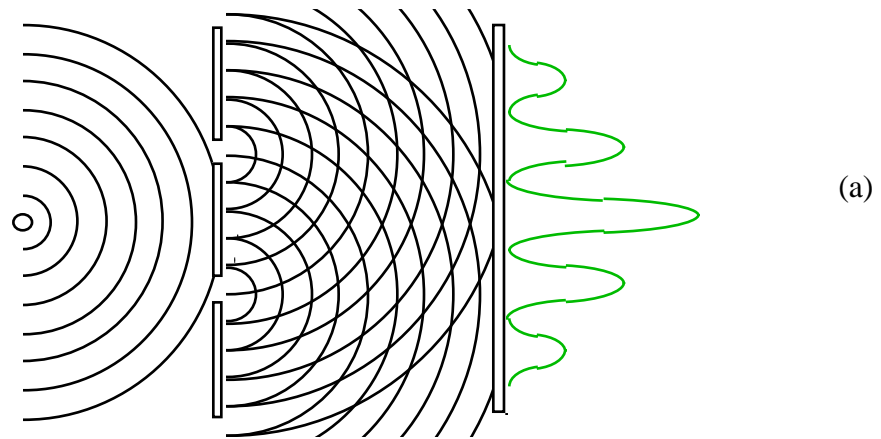


Figure 1.1 Young's double-slit experiment is the classic starting-point for discussions of wave/particle duality. To arrive at the detecting screen on the right, the light from the source at the left must pass through a pair of slits cut into an absorbing material. Classically, the light is described as an electromagnetic wave (a), so that secondary waves emerge from the slits and create an interference pattern on the screen. Quantum-mechanically, the light is described as a collection of photons, which cannot be split (b), but the interference pattern is still manifest in the ensemble of point-like detections of single photons at the screen so long as the paths ABD and ACD are indistinguishable.

For example, suppose we are able to modify the two-slit apparatus so that a marker of some kind is activated when the light passes through one or the other of the two slits, without disturbing the paths of the photons that reached the screen (see Figure 1.2). Now the question arises, will the photons reaching the screen now show interference or not? It is clear that if we choose to observe the markers in conjunction with the arrival of photons at the screen, there is no interference, because we know through which slit each photon passed on the way to the screen.

But what if we choose not to observe the markers? Is this enough to render the photons at the screen “indistinguishable” from the point of view of the measurements, so that the interference is displayed? The answer is no. As we will see from several experiments reported in this thesis, it is not enough for the measurement apparatus to simply ignore which-path information: whether interference occurs depends on whether this information exists, and not on whether some other part of the apparatus is accessing it. Paths for which no distinguishing information exists anywhere in the universe are said to be *indistinguishable in principle*, and it is only events of this type that ultimately exhibit interference.

Now suppose we that are to manipulate the markers in some way without observing them, so that afterwards they are incapable of revealing through which slit a given photon passed. Would the interference return at the screen in this case? It turns out that the answer to this question depends critically on the way in which the markers are manipulated. If they are manipulated so that they can never reveal which-path information no matter what is done with them later, then the photons at the screen become indistinguishable in principle, and interference returns.

If, on the other hand, the markers are manipulated so that the which-path information is hidden *only for a particular experimental arrangement*, then this might

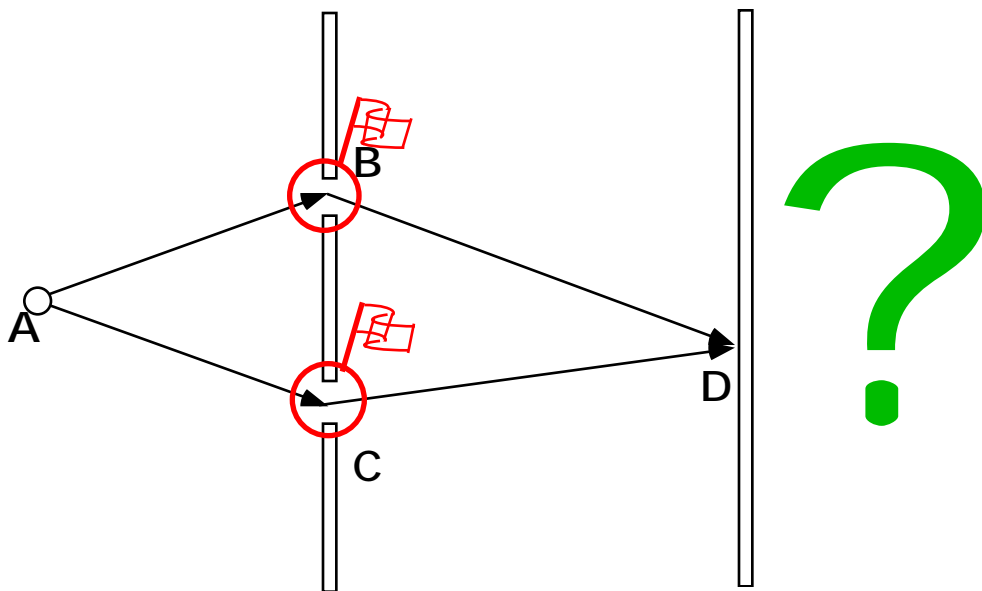


Figure 1.2 A thought-experiment in which the photons activate a “marker” as they pass through the slits, so that the which-path information is available in principle. Complementarity demands that the interference vanish in this case, but is there a way of “erasing” the information so that interference returns?

be said to make the paths for detection at the screen “indistinguishable in practice.” Does interference return for these events as well? We will see in Chapter 2 that it is indeed possible in this case to recover a limited kind of interference at the screen, contingent on our apparatus actually observing the markers in a way that erases the which-path information. In some sense, then, we will see that interference can occur between paths that have been rendered “indistinguishable in practice” by the action of the quantum eraser apparatus; not by ignoring the which-path information, but by destroying it. Ultimately, though, this interference will be seen to come from double-detection paths -- for the photons at the screen, and their corresponding markers -- that are *indistinguishable in principle*.

1.1.3 Two-photon interference and spectral markers

In Young’s double-slit experiment, interference occurs between different pathways leading to a final event that involves only a single photon: namely, the detection of light at the screen. However, in nature there exist events that involve emission or absorption of two photons, rather than one, such as atomic “cascade” transitions, or nonlinear “three-wave mixing” processes. These events may also be described by quantum mechanical probability amplitudes, and they are capable of exhibiting interference so long as the photon paths leading to them are indistinguishable. The “paths” under consideration may involve the multiple trajectories for each photon participating in the event. In Chapter 3, we will encounter an example of a two-photon interferometer, and observe the reduction in the two-photon interference visibility that occurs when the photon pairs are rendered distinguishable by their spectra. In Chapter 4, we will see that the interference returns when this “spectral

marker” is removed, so that the two-photon paths become indistinguishable in principle.

1.2 *Nonlocality*

1.2.1 The limits of quantum information

For any two operators \hat{A} and \hat{B} that do not commute, a more general form of the uncertainty relation holds [2]:

$$\Delta\hat{A} \Delta\hat{B} \geq \frac{1}{2} \left| \langle [\hat{A}, \hat{B}] \rangle \right|. \quad (1.2)$$

This equation implies that there is a fundamental limit on the accuracy with which the values of \hat{A} and \hat{B} can be determined at the same time -- in a sense, there is a limit on how much information may be specified by the quantum state.² If two observables do not commute, the quantum state cannot contain information which would specify the outcome of measurements of both of them. Quantum mechanics, then, is unable to make deterministic predictions of the outcomes of at least some measurements; it offers probabilities instead of certainty. But is this a limitation of the theory, or is it a necessary embodiment of limits in nature on what is knowable in principle? Could quantum mechanics conceivably be replaced by a more detailed theory, one capable of making deterministic predictions in all cases, or does it already reflect all there is to know?

² This limitation is built in to the formalism of quantum mechanics in the following way: 1.) the outcome of a measurement of \hat{A} or \hat{B} can only be predicted with certainty when the quantum state of the system is an eigenstate of \hat{A} or \hat{B} ; 2.) if \hat{A} and \hat{B} do not commute, there is no basis in which both operators are diagonal -- that is, there can be no states which are eigenstates of both \hat{A} and \hat{B} .

1.2.2 The EPR Paradox

1.2.2.1 The EPR-Bohm thought experiment

In 1935, Einstein, Podolsky, and Rosen posed the question, “Can Quantum-Mechanical Description of Physical Reality Be Considered Complete?” and concluded that the answer is “no.”[3]. They arrived at this conclusion after considering the results of a now-famous thought experiment that was later modified by Bohm [4]. As depicted in Figure 1.3, the *EPR-Bohm thought experiment* begins with a single spin-zero particle which is unstable and decays into two fermions. The new particles, A and B, fly away from each other in opposite directions, towards separate observers, each of whom is prepared to measure a component of the spin of the arriving particle with a suitably oriented Stern-Gerlach analyzer. In modern parlance, “Alice” measures the projection of particle A’s spin onto the unit vector \mathbf{a} -- represented by the operator $\hat{\sigma}_A \cdot \mathbf{a}$ -- while “Bob” measures a similar spin projection for particle B, $\hat{\sigma}_B \cdot \mathbf{b}$.³

It is assumed that the total spin is conserved in the decay process, so that the state of the system⁴ after the decay must be the spin-zero singlet state⁵

$$|\Psi\rangle = \frac{1}{\sqrt{2}} \left\{ |+\rangle_{A,\mathbf{n}} |-\rangle_{B,\mathbf{n}} - |-\rangle_{A,\mathbf{n}} |+\rangle_{B,\mathbf{n}} \right\}, \quad (1.3)$$

where \mathbf{n} is an arbitrary unit vector and we have introduced the notation

$$\hat{\sigma}_\mu \cdot \mathbf{n} |\pm\rangle_{\mu,\mathbf{n}} = \pm |\pm\rangle_{\mu,\mathbf{n}} \quad \mu = A, B \quad (1.4)$$

Eq. (1.4) implies that no matter how Alice and Bob choose to orient their analyzers, the results of their spin measurements can only be ± 1 . The state in (1.3) does not allow

³ Strictly speaking, the spin projection operators are $\hat{S} \cdot \mathbf{n} = (\hbar/2) \hat{\sigma} \cdot \mathbf{n}$; we will omit factors of $\hbar/2$.

⁴ The complete state of the system would be a direct product of the spinor presented here and a position/momentum state describing the spatial localization of the two particles. Because we are only concerned with spin measurements here, the spatial part of the state is ignored.

⁵ The eigentstate of the total spin $\hat{\mathbf{J}} = \hat{\mathbf{S}}_A + \hat{\mathbf{S}}_B$ with eigenvalue $\hat{\mathbf{J}}^2 = j(j+1)\hbar^2 = 0$ is the singlet state.

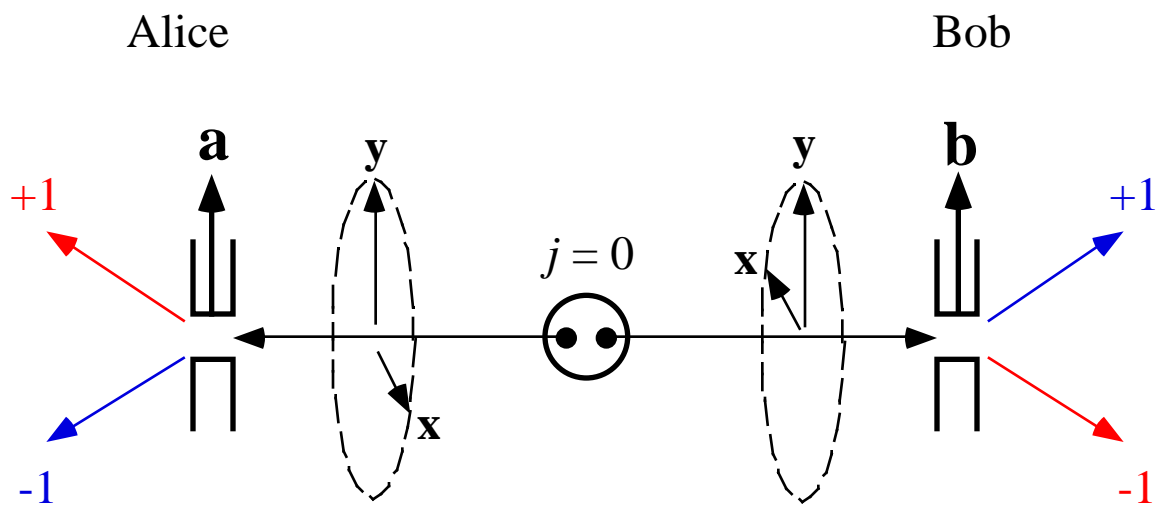


Figure 1.3 The EPR-Bohm thought experiment. A spin-zero particle decays into two fermions whose spin components are measured by Alice and Bob along directions \mathbf{a} and \mathbf{b} . The outcome of either measurement may be +1 or -1, but the two results must be opposite if Alice and Bob choose the same direction for their Stern-Gerlach orientations.

Alice or Bob to predict in advance which of these outcomes they will observe -- each result will occur with 50% probability -- but it does guarantee that if both Alice and Bob choose the same orientation for their analyzers, their results will be perfectly anticorrelated. That is, if Alice and Bob agree to make $\mathbf{a} = \mathbf{b} = \mathbf{n}$, then on those occasions when Alice happens to observe a spin value of $\hat{\sigma}_A \cdot \mathbf{n} = +1$, $|\psi\rangle$ is “collapsed” or projected and becomes

$$|\psi\rangle = |+\rangle_{A,\mathbf{n}} |-\rangle_{B,\mathbf{n}}, \quad (1.5)$$

which guarantees that Bob’s measurement will yield the opposite result, $\hat{\sigma}_B \cdot \mathbf{n} = -1$. On the remaining occasions when Alice’s measurement yields -1, Bob’s must yield +1. This anticorrelation holds no matter what direction Alice and Bob agree to choose for \mathbf{n} , because the state in (1.3) has the same form in any spin basis ($\mathbf{n} = \mathbf{x}, \mathbf{y}, \mathbf{z}$, etc.)⁶

This type of state, in which the spin components of each particle are undetermined yet correlated with each other, is referred to as an *entangled* state. The measured value of one particle’s spin is intimately tied to that of the other, even though neither one has a definite value before measurement. The entanglement is a consequence of the fact that the state for the two spins cannot be factored into a product of single-particle spin states, so that the collapse of $|\psi\rangle$ for one degree of freedom affects the other one as well.

1.2.2.2 *Realism, locality, and the paradox*

In their paper, Einstein, Podolsky and Rosen made the following assertion: “If, without in any way disturbing a system, we can predict with certainty the value of a physical quantity, then there exists an element of physical reality corresponding to this

⁶ The circular symmetry of the singlet state is no accident; it is the result of the rotational invariance required for any angular momentum eigenstate to have eigenvalue $j=0$.

physical quantity.” This statement defines a philosophical position known as objective realism, or just *realism*. In this example, realism implies that at the instant Alice measures, $\hat{\sigma}_A \mathbf{n}$, the quantity $\hat{\sigma}_B \mathbf{n}$ becomes an element of physical reality which has an objective, real existence in the natural world, whether or not Bob decides to measure it; $\hat{\sigma}_B \mathbf{n}$ acquires this “objectively real” status by virtue of the fact that Alice can now predict its value with certainty.

Now a paradox emerges when we consider two possible (but mutually exclusive) measurements that Alice might perform: she might decide to measure $\hat{\sigma}_A \mathbf{x}$, obtaining a definite value for this quantity and ensuring that the corresponding quantity for Bob’s particle, $\hat{\sigma}_B \mathbf{x}$, is an element of reality. On the other hand, Alice might decide to measure $\hat{\sigma}_A \mathbf{y}$ instead of $\hat{\sigma}_A \mathbf{x}$; in this case, she would make $\hat{\sigma}_B \mathbf{y}$ an element of reality instead.

But since the particles described by (1.3) can be arbitrarily far away from each other, Alice should not be able to influence any of the properties of Bob’s particle. For according to relativity, Alice’s analyzer cannot send an instantaneous signal to Bob’s particle to “tell” it which value of $\hat{\sigma}_B \mathbf{x}$ or $\hat{\sigma}_B \mathbf{y}$ to adopt, or indeed, which of these two quantities should become an element of reality. This means that if Bob and Alice make their measurements simultaneously⁷, there is no way the results of one can affect the other. The separate nature of the two measurements, insisted on by Einstein, is called *locality*.

The *EPR paradox*, then, is this: no signal can travel faster than light, and yet Alice is able to make either $\hat{\sigma}_B \mathbf{x}$ or $\hat{\sigma}_B \mathbf{y}$ into an element of reality for Bob’s particle at will, instantaneously and from a distance. Einstein, Podolsky, and Rosen argued that the only way to resolve this paradox is to accept that both the \mathbf{x} and \mathbf{y} spin components

⁷ The measurements must be made with spacelike separation, so that they cannot be connected by a light signal.

for each particle are actually elements of reality *from the moment the particles are created*. In that case, each of the particles must possess definite values for $\hat{\sigma}_\mu \mathbf{x}$ and $\hat{\sigma}_\mu \mathbf{y}$ all along, so that Alice and Bob merely uncover each of these predetermined spin values when they make their measurements.⁸

However, in the quantum mechanical description of nature, $\hat{\sigma}_\mu \mathbf{x}$ and $\hat{\sigma}_\mu \mathbf{y}$ are complementary to each other: the operators do not commute⁹. As mentioned earlier, this fact forbids any quantum state from specifying eigenvalues of both $\hat{\sigma}_\mu \mathbf{x}$ and $\hat{\sigma}_\mu \mathbf{y}$ for any particle. What this means, according to the EPR argument, is that quantum mechanics cannot be a complete theory: the above paradox implies that in at least one system, there exist elements of physical reality which quantum mechanics is unable to include by its very design.

The implication of this argument is that the statistical character of quantum mechanics arises from our ignorance of nature, and not from limitations of nature itself. Einstein wrote that it must remain for physicists to complete quantum mechanics with a deeper theory, in the same sense that thermodynamics is completed via classical mechanics. The more complete theory would rely on physical quantities which are currently unknown to us, analogous to the individual atomic positions and momenta whose average properties are described by statistical mechanics: the description of these “hidden variables” would then permit a return to a completely deterministic theory [5].

⁸ If this interpretation were correct, the situation would be no more “paradoxical” than the following: Alice and Bob decide to cut a coin in half along its thin edge, with the result that one of the pieces is “heads” and the other is “tails.” Without looking to see which is which, they each take a piece of the coin and walk away from each other. At some later time, Alice decides to look at her half of the coin, and discovers which piece she has been carrying all along. She now knows which piece Bob is carrying, as well, without the need for any “spooky action at a distance,” in the words of Einstein. They can carry out this procedure for two coins, corresponding to the two different anticorrelated elements of reality for each observer.

⁹ The pauli matrices satisfy $[\sigma \mathbf{x}, \sigma \mathbf{y}] = 2i\sigma \mathbf{z}$, so that the spins satisfy the angular momentum commutation relations $[\mathbf{S} \mathbf{x}, \mathbf{S} \mathbf{y}] = i\hbar \mathbf{S} \mathbf{z}$ and cyclic permutations thereof.

1.2.2.3 Bohr's reply

In essence, the EPR argument presents a contradiction between the following four statements: There exist in nature elements of physical reality as defined by *realism*; Nature is constrained by *locality*; Quantum mechanics is a *correct* description of nature¹⁰; Quantum mechanics is a *complete* description of nature. Unwilling to deny the first three statements, the authors concluded that the fourth one is false.

In his earliest reply to the EPR argument [7], Bohr defended the fourth statement and argued against the first. He wrote that the EPR definition of an “element of reality” is an ambiguous one, derived from “a priori philosophical considerations” rather than being “founded on a direct appeal to experiments and measurements.” According to Bohr, we should regard as real only those things which we are in a position to measure, and because certain types of measurements preclude us from making others, it is only right that quantum theory reflect the mutually exclusive nature of such complementary sets of measurements.

From Bohr's point of view, the flaw in the EPR argument is the use of *counterfactual reasoning*, in which the results of different possible, but mutually exclusive, measurements by Alice are used together as elements of a logical argument. A modern statement of this view is that “unperformed experiments have no results,” [8] and it is not necessary for a physical theory to explain them in order to be considered complete.

¹⁰ Strictly speaking, the EPR argument only requires that quantum mechanics give correct predictions for the thought-experiment under consideration [6].

1.2.3 Bell's inequality

1.2.3.1 Bell's theorem

Whatever the criticisms of Einstein's position, it remained a tenable one until 1964. In that year, J.S. Bell proved that it is impossible to reproduce all of the predictions of quantum mechanics using any "hidden variable" theory that incorporates locality and realism as axioms [9].

To prove this, Bell returned to the EPR-Bohm thought experiment and considered the correlations between Alice's and Bob's measurements not just for the particular analyzer orientations $\mathbf{n} = \mathbf{x}, \mathbf{y}$, but for the general case in which they are free to choose any orientations. Because the outcomes of their measurements can only be +1 or -1, with a 50% chance of finding each value¹¹, their mutual correlation function is equivalent to their joint expectation value:

$$Q = \frac{\langle AB \rangle}{\sqrt{\langle A^2 \rangle} \sqrt{\langle B^2 \rangle}} = \frac{\langle AB \rangle - \langle A \rangle \langle B \rangle}{\sqrt{\langle A^2 \rangle - \langle A \rangle^2} \sqrt{\langle B^2 \rangle - \langle B \rangle^2}} = \langle AB \rangle \quad (1.6)$$

when the variables are $A = \pm 1$ and $B = \pm 1$ and represent the outcome of any one of Alice and Bob's spin measurements, and the brackets denote ensemble averages. In the most general formulation of a "local hidden variable" (LHV) theory, the outcome of each measurement may depend on the particular values of some hidden variables, collectively denoted by λ , and on the orientation of the analyzer, \mathbf{a} or \mathbf{b} ; the expectation value on the far right in Eq. (1.6) is then given by

$$Q(\mathbf{a}, \mathbf{b}) = \langle A(\mathbf{a}, \lambda) B(\mathbf{b}, \lambda) \rangle = \int \rho(\lambda) A(\mathbf{a}, \lambda) B(\mathbf{b}, \lambda) d\lambda \quad (1.7)$$

where the distribution of values for the hidden variables among all the various decay events is governed by the probability density $\rho(\lambda)$. Note that the outcome of each

¹¹ These are empirical facts which are predicted by quantum theory, but do not rely upon it.

observer's measurement is not permitted to depend on the orientation of the other's analyzer; this is how locality is directly built in to the theory. On the other hand, A and B may both depend on the values of λ , which are determined at the source.

Bell considered measurements for two possible orientations of Alice's analyzer, (\mathbf{a}, \mathbf{a}) and of Bob's analyzer (\mathbf{b}, \mathbf{b}) , and showed that the following inequality must hold if the correlations between them are given by (1.7):

$$|Q(\mathbf{a}, \mathbf{b}) - Q(\mathbf{a}, \mathbf{b})| + |Q(\mathbf{a}, \mathbf{b}) + Q(\mathbf{a}, \mathbf{b})| \leq 2 \quad (1.8)$$

This is a form of *Bell's inequality*¹², and the statement that all correlations predicted by LHV theories must satisfy it is *Bell's theorem*. Note that Bell's inequality is not a statement about quantum mechanics: it is a statement about LHV theories intended to “complete” quantum mechanics.

Remarkably, the correlations predicted by quantum mechanics are able to violate this inequality¹³. The quantum mechanical expression for the mutual correlation between Alice's and Bob's measurements is

$$Q_{QM}(\mathbf{a}, \mathbf{b}) = \langle \psi | (\sigma_A \cdot \mathbf{a})(\sigma_B \cdot \mathbf{b}) | \psi \rangle \quad (1.9)$$

Evaluated with the singlet state¹⁴ in (1.3), this becomes

$$Q_{QM}(\mathbf{a}, \mathbf{b}) = -\mathbf{a} \cdot \mathbf{b}, \quad (1.10)$$

and the four unit vectors may be chosen¹⁵ so that

$$|Q_{QM}(\mathbf{a}, \mathbf{b}) - Q_{QM}(\mathbf{a}, \mathbf{b})| + |Q_{QM}(\mathbf{a}, \mathbf{b}) + Q_{QM}(\mathbf{a}, \mathbf{b})| = 2\sqrt{2}, \quad (1.11)$$

¹² This form of the inequality (not the original) is derived by Bell in reference [10]

¹³ This fact seems less remarkable if we notice that of the four quantities involved in (1.8), only one may be measured by Alice and Bob at a time; Bell's inequality therefore involves counterfactual reasoning, which is permitted for classical observables, for EPR “elements of reality,” and for the variables A and B , but not for quantum-mechanical observables.

¹⁴ It is not necessary that the spins be in the singlet state in order to violate Bell's inequality, but it is necessary that their state be an entangled one. See, for example, reference [11].

in clear violation of (1.8). According to Bell's theorem, no LHV theory can reproduce this prediction, which means that it is impossible to complete quantum mechanics in the manner envisioned by Einstein. The inconsistency of quantum mechanics with locality and realism is often referred to as the *nonlocality* of quantum mechanics. But is nature nonlocal as well?

1.2.3.2 *Experimental violations of Bell's inequality*

The fact that quantum mechanics violates Bell's inequality implies a contradiction between the following three statements, all of which were assumed true in the EPR argument: There exist in nature elements of physical reality as defined by *realism*; Nature is constrained by *locality*; Quantum mechanics is a *correct* description of nature.

Of course, it is possible that quantum mechanics is simply wrong in cases where it predicts nonlocal behavior by the failure to satisfy (1.8). Then quantum mechanics could be regarded as an (incorrect) approximation to some LHV theory which, in addition to being more complete, would also be more accurate than quantum mechanics. If, on the other hand, the quantum-mechanical prediction (1.11) could be verified -- that is, if nature could be seen to violate Bell's inequality -- then this would rule out any LHV theory as an accurate description of nature, however intuitively satisfying it might be.

The first proposal for an experimental test of Bell's inequality was made in 1969 by Clauser, Horne, Shimony, and Holt [12]. They derived a version of Bell's

¹⁵ One suitable choice is $\mathbf{a} = \mathbf{x}$, $\mathbf{a}' = \mathbf{y}$, $\mathbf{b} = (\mathbf{x} + \mathbf{y})/\sqrt{2}$, $\mathbf{b}' = (\mathbf{x} - \mathbf{y})/\sqrt{2}$

inequality that could be tested by making polarization measurements on pairs of photons¹⁶ emitted in atomic “cascade” decays. This inequality has the form

$$|R(\mathbf{a}, \mathbf{b}) - R(\mathbf{a}, \mathbf{b}') + R(\mathbf{a}, \mathbf{b}) + R(\mathbf{a}', \mathbf{b}) - R(\mathbf{a}, -) - R(-, \mathbf{b})| \leq 0 \quad (1.12)$$

where $R(\mathbf{a}, \mathbf{b})$ refers to a measured joint counting rate for two photodetectors positioned behind polarizers oriented along directions \mathbf{a} and \mathbf{b} , or with a polarizer removed as denoted by the dash (-). Unlike (1.8), the *CHSH inequality* can be tested with practical, inefficient photodetectors, but it requires that an additional “fair sampling” assumption be made, so that the subensemble of detected photons is representative of the whole ensemble of emitted photon pairs. To date, numerous experimental violations of the CHSH inequality have been observed. The most striking of these was an atomic cascade experiment conducted in 1982 by Aspect, Dalibard, and Roger [13], in which the orientations of Alice’s and Bob’s analyzers were changed in a pseudo-random fashion after the photons were emitted, but before they impinged onto the polarizers. This experimental arrangement was designed to guarantee the spacelike separation of the measurements and to ensure that Einstein’s locality condition applied to them¹⁷.

It would seem, then, that the predictions of quantum mechanics have been vindicated, so that we are forced to accept that nature behaves in direct contradiction to the EPR assumptions of locality and realism. However, staunch advocates of LHV theories¹⁸ continue to point out that, to date, there have been no experimental violations

¹⁶ The original EPR-Bohm thought experiment involved spin measurements of correlated fermions. Although photons are bosons, their polarization states may be described with a spin-1/2 algebra because only two orthogonal polarizations exist which are transverse to the direction of propagation.

¹⁷ Whether or not they completely succeeded seems open to debate, since the “random” setting of the analyzer encountered by each photon was determined by a periodic switching signal emanating from within the backward light cones of the two detection events [14,15].

¹⁸ See, for example, reference [16]

of Bell's inequality in its original form¹⁹: only the CHSH inequality, with its fair-sampling assumption, has been shown to be inconsistent with nature. Therefore, what these experiments actually tell us is that not all three of the following statements can be true: There exist in nature elements of physical reality as defined by *realism*; Nature is constrained by *locality*; The *fair sampling* assumption is valid. Because of this “loophole,” it is possible to construct alternative theories to quantum mechanics that are consistent with locality and realism and with all existing experimental data, so long as they violate the fair sampling assumption. Such theories must remain open as logical possibilities until a “loophole-free” experiment is able to demonstrate violations of the Bell inequality (1.8) without additional assumptions.

1.2.3.3 Experimental non-violations of Bell's inequality?

The CHSH inequality applies to rotationally invariant systems like the one presented in the EPR-Bohm thought experiment. This inequality, and the predictions of quantum mechanics, should have the same form even if circular, rather than linear, polarizations are measured by Alice and Bob. Despite this, there are two known cases in which attempts to show violations of the CHSH inequality by measurements in a circular polarization basis have failed. A modern version of these experiments which succeeded is presented in Chapter 5.

1.2.4 Beyond Bell's inequality

For twenty-five years, Bell's inequality reigned as the standard expression of the conflict between quantum mechanics and the EPR axioms of locality and realism.

¹⁹ The original form of Bell's inequality presented in (1.8) is sometimes referred to as the “strong” Bell inequality, while those forms that include additional assumptions, such as the CHSH inequality in (1.12), are called “weak” Bell inequalities.

But in 1989, an even more striking way of demonstrating this incompatibility was discovered by Greenberger, Horne, and Zeilinger²⁰. The *GHZ thought-experiment* involves spin measurements on three spin-correlated particles, instead of just two, and it shows that quantum mechanics is inconsistent with local-realism based on the results of a *single measurement*, without the use of inequalities. So far, there has been no experimental realization of this experiment for lack of a suitable three-particle source; the experiment may be feasible if the emissions from several parametric downconversion processes (see Section 1.3) could be synchronized, and this is part of the motivation for the experiments described in Chapters 3 and 4.

In 1993, Hardy devised another thought-experiment that demonstrates the nonlocality of quantum mechanics without the use of inequalities [18]. Hardy's approach, as adapted later by Jordan to spin- $\frac{1}{2}$ systems, was to return to the two-particle EPR-Bohm thought experiment and consider entangled states which do *not* possess the circular symmetry of the one given in Eq. (1.3). It turns out that for these asymmetric states it is possible to formulate a set of four logical statements about the outcomes of Alice and Bob's measurements, each of which may be independently verified by quantum mechanics and by direct measurement, but which create a logical contradiction when considered together. As with Bell's inequality, the GHZ experiment, and the EPR paradox, this conundrum arises from the use of counterfactual reasoning about the outcomes of mutually exclusive experimental arrangements -- reasoning which is valid from a local-realistic point of view, but which may not be valid for quantum mechanics. The *Hardy-Jordan propositions* are presented explicitly in Chapter 6, along with the results of the first experimental test of these propositions.

²⁰ A simplified form of the GHZ argument is presented in reference [17]

1.3 Spontaneous parametric downconversion

1.3.1 Overview

Parametric downconversion is a three-wave mixing process in which an incident electromagnetic field oscillating at the *pump* frequency drives the electrons in a dielectric medium to radiate energy at two lower frequencies: the so-called *signal* and *idler* frequencies (see Figure 1.4). The process can occur in materials whose induced polarization depends nonlinearly on the strength of the incident electric field; this nonlinear response is a consequence of the anharmonicity of the potential wells for the bound electrons in these media. In particular, certain noncentrosymmetric crystals may have a strong second-order nonlinear electric susceptibility $\chi^{(2)}$, which gives rise to an induced polarization of the form

$$\mathbf{P}^{(2)}(\mathbf{r}, t) = \chi^{(2)} \mathbf{E}(\mathbf{r}, t) \mathbf{E}(\mathbf{r}, t). \quad (1.13)$$

This is a tensor relation describing only the second-order nonlinear part of the induced polarization within the dielectric material. The nonlinear coupling is quite weak even for the most strongly nonlinear materials, but if a laser is used to supply a highly intense pump field, the effects can become significant.

The process is parametric in the sense that the atoms in the nonlinear medium play the role of spectators, and do not undergo state transitions during the mixing. As such, they do not exchange any energy or momentum with the fields, so that the fields themselves form a closed system in which energy and momentum must be conserved. For traveling planewave pump, signal, and idler fields, these energy and momentum constraints are expressed as the *phase-matching* conditions:

$$\omega_p = \omega_s + \omega_e \quad (1.14)$$

and

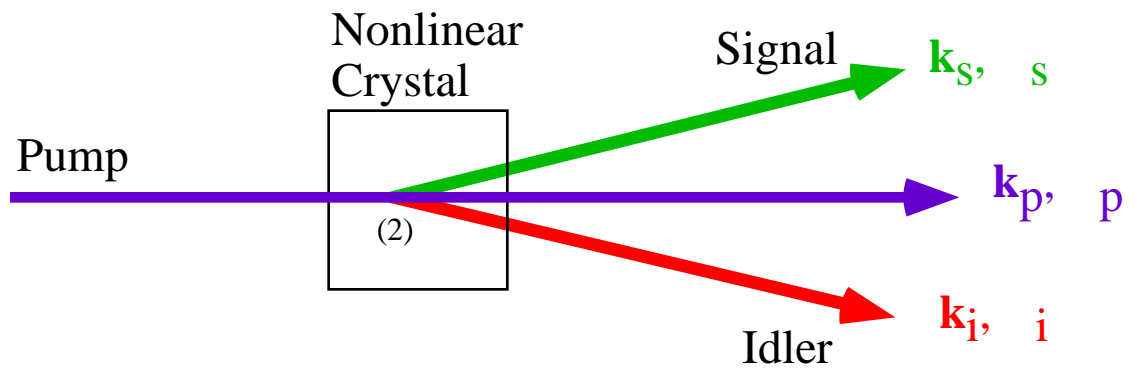


Figure 1.4 Parametric downconversion occurs in a nonlinear medium whose induced polarization is proportional to the square of the electric field. The pump field drives oscillations at two lower frequencies, creating signal and idler beams which emerge from the crystal in different directions.

$$\mathbf{k}_p = \mathbf{k}_s + \mathbf{k}_i. \quad (1.15)$$

Classically, the downconversion process can only occur when there is initially radiation in the signal or idler mode, along with the pump. In this case, the result is an amplification of the signal and a corresponding attenuation of the pump, with the excess energy radiated into the idler beam. This process is known as *parametric amplification*, and it can exhibit gain over a large range of signal and idler wavelengths. It forms the basis for highly tunable optical parametric amplifier (OPA) and oscillator (OPO) devices.

Quantum mechanically, the parametric amplification process may be viewed as stimulated parametric downconversion, in which a pump photon is absorbed and then excites an electron in the medium to a higher-energy “virtual” level (see Figure 1.5). The incident signal photon then stimulates a transition down to an intermediate virtual level, accompanied by the coherent emission of a second photon at the signal frequency. This emission is immediately followed by a decay back down to the ground state, accompanied by the emission of a photon at the idler frequency.

However, unlike the classical model, the quantum mechanical description of this process also allows for spontaneous emission to occur here, so that the pump photon may decay into a pair of signal and idler photons even in the absence of an incident signal field. This process of *spontaneous parametric downconversion* is often viewed as an amplification of the vacuum field, in the sense that spontaneous transitions from the excited virtual state are thought of as being stimulated by vacuum fluctuations in the signal mode, which are equally likely to occur at all frequencies. The phase-matching conditions ensure that the emerging photons are correlated in momentum and energy, even though these attributes are not defined for either photon until a measurement is performed on one of them. This entanglement, along with the fact that the photons are

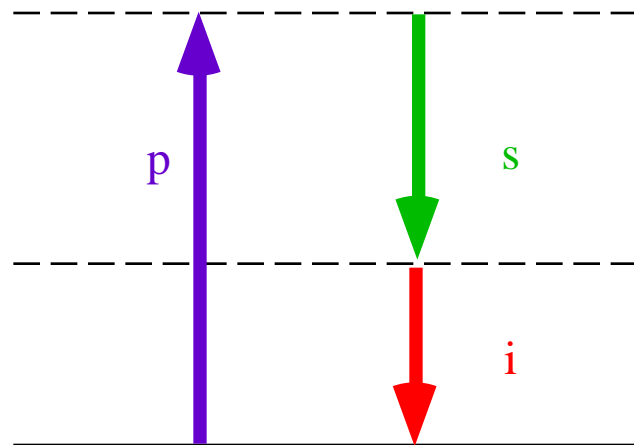


Figure 1.5 Parametric downconversion may be seen as the annihilation of a pump photon, with an accompanying transition within the material to an excited “virtual” level, followed by a decay back to the initial state and emission of the lower-frequency signal and idler photons.

emitted simultaneously within the coherence time, means that the photons produced in this process are capable of exhibiting nonclassical behavior in a variety of ways. The process of spontaneous parametric downconversion is the starting point of all the experiments described in this thesis.

1.3.2 The quantum state

A simplified description²¹ of spontaneous parametric downconversion begins with an interaction Hamiltonian that specifies the creation of a signal photon and an idler photon along with the simultaneous annihilation of a pump photon [19]:

$$\hat{H}_I = \hbar g \hat{a}_s^\dagger \hat{a}_i^\dagger \hat{a}_p + \text{h.c.} \quad (1.16)$$

Here \hat{a}_s^\dagger and \hat{a}_i^\dagger are the creation operators for the signal and idler field modes, while \hat{a}_p is the annihilation operator for the pump field mode, g is a coupling constant, and “h.c.” represents the Hermitian conjugate of the first term (see Appendix A). For this simple description, the pump, signal, and idler modes are assumed to be infinite planewaves satisfying the phase-matching conditions (1.14) and (1.15).

In the interaction picture, the state of the system evolves according to

$$|\psi(t)\rangle = \exp\left\{-\frac{i}{\hbar} \int_0^t \hat{H}_I(t') dt'\right\} |\psi(0)\rangle \quad (1.17)$$

where $|\psi(0)\rangle$ is the initial state of the system. When the pump field is supplied by a cw laser, this state is

$$|\psi(0)\rangle = |0\rangle_s |0\rangle_i |V_0\rangle_p \quad (1.18)$$

²¹ Detailed derivations of the quantum state for spontaneous parametric downconversion under various pumping conditions are presented in Appendices A and B.

where the signal and idler modes are initially empty, and the pump field is well-approximated by a coherent state with mean photon number $|V_0|^2$. With the help of (1.18) and (1.16), the unitary operation in (1.17) may be carried out and truncated to the lowest nonvanishing order in g . The result is

$$|\psi\rangle = |vac\rangle + \eta|1\rangle_s|1\rangle_i \quad (1.19)$$

where we have omitted the Hilbert space for the pump field, and included only the signal and idler modes, so that $|vac\rangle = |0\rangle_s|0\rangle_i$. Here η is a creation efficiency parameter proportional to g and V_0 that satisfies the weak interaction condition

$$|\eta|^2 \ll 1. \quad (1.20)$$

Hence, the probability for a pair of photons to be created in the signal and idler modes is small, but non-zero. More rigorously, the state in (1.19) is shown to be the single mode limit of a multimode superposition state in Appendix A.

1.3.3 Type-I and type-II phase matching

The phase-matching conditions (1.14) and (1.15) may be combined to give the following constraint for the refractive index of the medium:

$$n(\omega_p)\omega_s + n(\omega_p)\omega_i = n(\omega_s)\omega_s + n(\omega_i)\omega_i. \quad (1.21)$$

Because n is a monotonically increasing function over the optical range of frequencies, this equation cannot be satisfied if the same refractive index applies to the pump, signal and idler fields. However, if the nonlinear medium is birefringent, so that the index for the pump field is lower than the index for at least one of the downconverted fields, (1.21) may be satisfied. The two ways of achieving this in practice are labeled as “type-I” and “type-II” downconversions.

In type-I downconversion, the signal and idler fields have the same polarization, while the pump field is polarized orthogonally to them. For materials such as crystalline LiIO_3 and BBO which possess “negative uniaxial” symmetry, the index of refraction for the extraordinary (e) polarization is lower than that for the ordinary (o) polarization. The signal and idler beams are therefore o -polarized, while the pump is e -polarized. The phase-matching condition is satisfied when

$$n_e(\omega_p)\omega_s + n_e(\omega_p)\omega_i = n_o(\omega_s)\omega_s + n_o(\omega_i)\omega_i. \quad (1.22)$$

In type-II downconversion, the signal and idler fields possess orthogonal polarizations, and the pump is again polarized to experience the lower of the two refractive indices. For negative uniaxial crystals, the pump is again e -polarized, while the signal is o -polarized and the idler is e -polarized, so that

$$n_e(\omega_p)\omega_s + n_e(\omega_p)\omega_i = n_o(\omega_s)\omega_s + n_e(\omega_i)\omega_i. \quad (1.23)$$

Both types of downconversion are commonly used. For some interferometric experiments, however, type-II downconversion offers a practical advantage: because the signal and idler photons are orthogonally polarized, it is possible to construct interferometers in which the photons propagate collinearly and are separated by their polarizations before being detected (see Figure B.1 in Appendix B). Such “common-path” interferometers are much more stable than those with separate paths, since any drifts or vibrations of optical elements are experienced by both photons together.

1.3.4 Cw and pulsed pump sources

The pump field for the downconversion process is usually supplied by a narrow linewidth, cw laser, as treated in Section 1.3.2. However, the use of a broadband pulse as the pump source has become more common in recent years, because it offers the

possibility of synchronizing the emissions from multiple downconversion processes. This synchronization has proved useful in quantum teleportation experiments [20,21], and it is also a crucial step towards the realization of the GHZ nonlocality experiment mentioned in Section 1.2.4. The combination of a pulsed pump with a type-II downconversion source may seem optimal for the latter, as it would combine the advantages of synchronization and common-path interferometry. But, as shown in Chapter 3, this combination results in signal and idler photon pairs which are spectrally distinguishable from each other, a side-effect which threatens to destroy any quantum interference effects they might otherwise display. A solution to this problem is presented in Chapter 4.

1.4 Methods, notation and terminology

1.4.1 Using the interaction picture to describe monochromatic fields

Throughout this thesis, we will use the interaction picture for the theoretical treatment of the experiments. In addition, we will often find it convenient to disregard the broad spectrum of the signal and idler fields and to represent each of them by a monochromatic plane wave as in Section 1.3.2. In this “two-mode” limit, the signal and idler modes have infinite length, and even extend to regions of space behind the downconversion crystals. Since the signal and idler photons are excitations of these infinitely long modes, it is possible to obtain some unphysical results in this limit for certain experimental configurations. In particular, if the modes from two downconverters are combined at a beamsplitter without careful attention to the input-output relations, the two-mode theory in the interaction picture can produce nonzero probabilities for the photons to be localized *behind* the downconverters [22]. These unphysical results vanish when the multimode treatment of the process presented in

Appendix A is used, because timing constraints for the creation of the photon wavepackets are then automatically imposed.

When applied to the detection of photons *after* the downconverters, however, the two-mode interaction picture agrees with the monochromatic limits of the multimode theory, and offers the simplest analysis possible. In this thesis, care has been taken not to push the two-mode theory beyond this domain of validity.

1.4.2 Notation for the Hilbert space norm

In the ensuing chapters, we will frequently encounter expectations of the form

$$\langle \psi | \hat{O}^\dagger \hat{O} | \psi \rangle = |\hat{O} | \psi \rangle|^2, \quad (1.24)$$

where $\hat{O}^\dagger \hat{O}$ represents a normally-ordered collection of number operators for the various fields being detected. The notation on the right-hand side of this equation is meant to imply multiplication of $\hat{O} | \psi \rangle$ by its Hermitian conjugate $\langle \psi | \hat{O}^\dagger$.

1.4.3 Photons

Like most researchers, this author does not have a license to use the word “photon” as apparently issued by one W.E. Lamb, Jr. at the 1960 Rochester Conference on Coherence and Quantum Optics [23], having been born too late to qualify. Nevertheless, the term will be used freely -- though not ambiguously -- throughout this work to refer to a single quantum excitation of some normal mode of the electromagnetic field. The modes need not be monochromatic; in fact, the broad spectral widths of some of these modes are central to Chapters 3 and 4. The photons in those modes are represented by pure superposition states of single excitations over the range of possible frequencies, and, as such, each of them can be said to possess the

entire spectrum of the mode [24]. Likewise, the word “photon” does not automatically imply spatially or temporally localized particles, though it will be used most often in conjunction with photodetection events that occur within very short times.

References for Chapter 1

- [1] N. H. Bohr, *The Philosophical Writings of Neils Bohr* (Ox Bow Press, Woodbridge, CN, 1958).
- [2] C. Cohen-Tannoudji, B. Diu, and F. Laloe, *Quantum Mechanics* (Wiley, New York, 1977).
- [3] A. Einstein, B. Podolsky, and N. Rosen, *Phys. Rev.* **47**, 777 (1935).
- [4] D. Bohm, *Quantum Theory* (Prentice-Hall, Englewood Cliffs, NJ, 1951).
- [5] A. Einstein, in *Albert Einstein: Philosopher-Scientist*, The Library of Living Philosophers, Vol. 7, ed. by P. A. Schlipp (Open Court, Peru, IL, 1970).
- [6] J. F. Clauser and A. Shimony, *Rep. Prog. Phys.* **41**, 1881 (1978).
- [7] N. H. Bohr, *Phys. Rev.* **48**, 696 (1935).
- [8] A. Peres, *Quantum Theory: Concepts and Methods* (Kluwer, Norwell, MA, 1995).
- [9] J. S. Bell, *Physics* **1**, 195 (1964).
- [10] J. S. Bell, in *Speakable and Unsayable in Quantum Mechanics* (Cambridge University Press, New York, 1987), p. 14.
- [11] C. H. Bennett, D. P. Di Vincenzo, J. A. Smolin, and W. K. Wothers, *Phys. Rev. A* **54**, 3824 (1996).
- [12] J. F. Clauser, M. A. Horne, A. Shimony, and R. A. Holt, *Phys. Rev. Lett.* **23**, 880 (1969).
- [13] A. Aspect, J. Dalibard, and G. Roger, *Phys. Rev. Lett.* **49**, 1804 (1982).
- [14] A. Zeilinger, *Phys. Lett. A* **118**, 1 (1986).
- [15] P. G. Kwiat, P. A. Eberhard, A. M. Steinberg, and R. Y. Chiao, *Phys. Rev. A* **49**, 3209 (1994).
- [16] F. Selleri, in *Fundamental Problems in Quantum Theory: A Conference Held in Honor of Professor John A. Wheeler*, edited by D. M. Greenberger and A. Zeilinger, *Annals of the New York Academy of Sciences* Vol. 755 (New York Academy of Sciences, New York, 1995), p. 798.
- [17] N. D. Mermin, *Phys. Today* **43**, 9 (1990).
- [18] L. Hardy, *Phys. Rev. Lett.* **71**, 1665 (1993).

- [19] L. Mandel and E. Wolf, *Optical Coherence and Quantum Optics* (Cambridge University Press, Cambridge, 1995).
- [20] D. Bouwmeester *et al.*, *Nature* (London) **390**, 575 (1997).
- [21] J. W. Pan, D. Bouwmeester, H. Weinfurter, and A. Zeilinger, *Phys. Rev. Lett.* **80**, 3891 (1998).
- [22] D. Branning, A. Kuzmich, and L. Mandel, 1998 (unpublished).
- [23] W. E. Lamb, Jr., *App. Phys. B* **60**, 77 (1995).
- [24] T. P. Grayson, Ph.D. thesis, University of Rochester, 1994 (unpublished).

This page intentionally left blank.

Chapter 2

The Quantum Eraser

2.1 Introduction

2.1.1 Complementarity without the uncertainty principle?

For any events in nature which could have occurred via many distinct pathways, complementarity demands that if “which-path” information is made available, then it must always be at the cost of interference. But what is the mechanism that makes this interference disappear? From the earliest days of quantum theory, the uncertainty principle has appeared at the heart of discussions about complementarity. The more famous among these discussions are based on ingenious thought experiments which illustrate the consequences of trying to observe wave and particle behavior in a system at the same time, and show how the uncertainty principle ultimately provides a “measurement back-action” of some sort which has the effect of blurring the interference fringes. The two most well-known examples are Einstein’s recoiling double-slit apparatus and Feynman’s light microscope, depicted in Figure 2.1; both are variations of Young’s double-slit apparatus. In Einstein’s version (a), the slits are mounted on springs which allow them to recoil from the impact of photons colliding with them en route to the screen. The momentum of this recoil can be measured and used to determine which of the two slits a given photon passed through, without blocking either path to the detection screen. In Feynman’s version (b), the interfering particles are electrons which are illuminated by a very weak light source just after passing through the slits. The scattered light may be observed independently and used

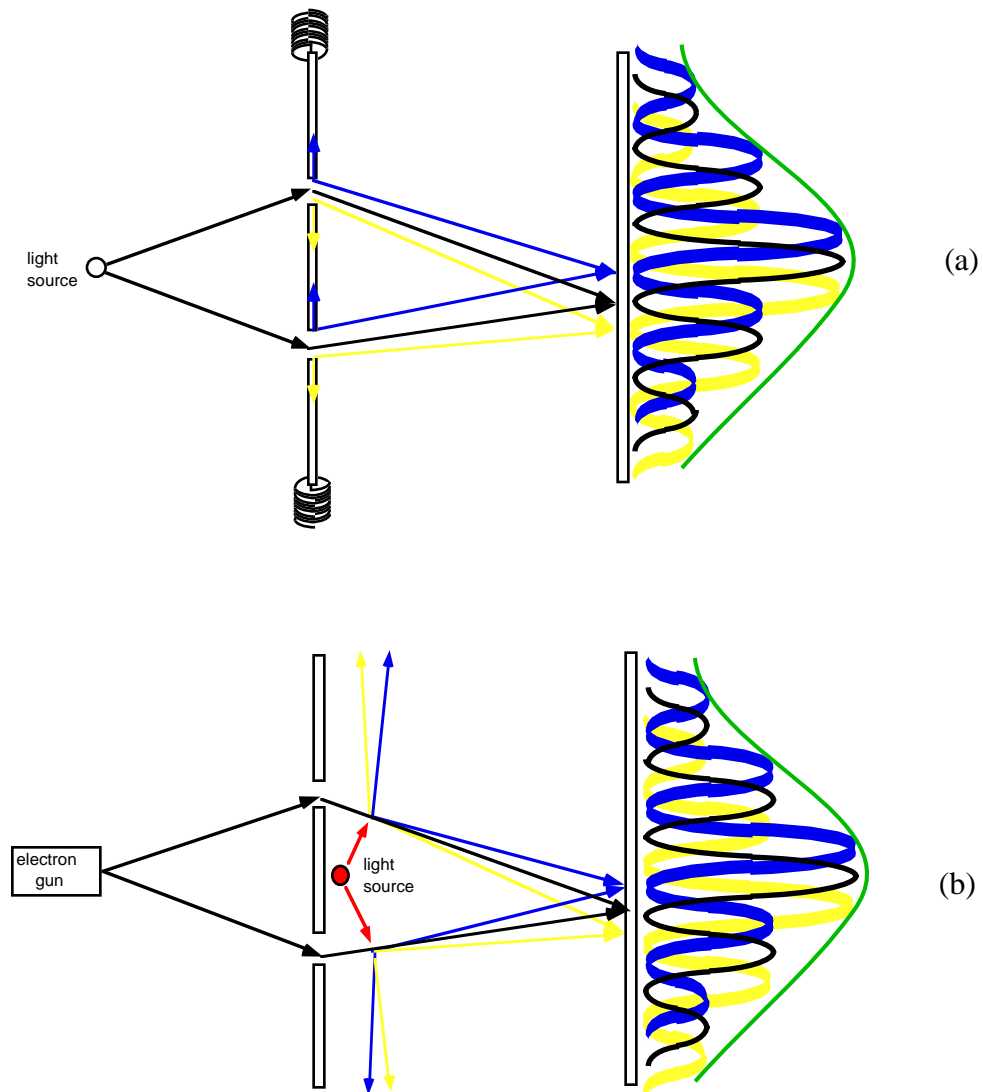


Figure 2.1 (a) Einstein's recoiling slit variation on Young's double-slit experiment. A photon en route to the screen collides with either the upper or the lower slit, imparting a momentum kick which can identify the photon's path. (b) Feynman's light microscope variation, in which a weak light source illuminates the electrons just after they emerge from the slits. By detecting the photons in conjunction with the electrons, we can determine which slit each electron traversed. In both experiments, however, the uncertainty principle guarantees that if the measurements are sensitive enough to determine "which-path" information, they will also result in an unavoidable "back-action" on the interfering particles that is large enough to blur the interference pattern, thereby eliminating wave-like behavior.

to determine which of the two slits a given electron passed through, again without blocking either path to the screen.

In both scenarios it can be shown that the act of obtaining this “which path” information disturbs the interfering photons or electrons to such a degree that the interference fringes are lost. This occurs because both Einstein’s recoiling slits and Feynman’s illuminating photons must be treated quantum mechanically. In the case of the recoiling slits, one must determine their initial momentum precisely enough that a change in momentum due to the collision with a photon may be detected. Heisenberg’s uncertainty relation for momentum and position then imposes a lower bound on how well-defined the position of the slits may be, which is equal to the spacing of the fringes themselves [1]. Similar arguments reveal that the photons Feynman might have used to identify the electron paths must exchange an uncertain amount of momentum with the electrons, thereby deflecting them on their way to the screen and smearing out the interference pattern [2,3]. Thus, in the foregoing cases, the uncertainty principle acts to enforce complementarity by ensuring that if “which path” information is obtained, the wave behavior will be destroyed.

These examples illustrate the traditional way in which complementarity has been understood to apply to wave-particle duality -- always, it seems, this kind of complementarity is “protected” by the uncertainty principle, in the same way that attempts to simultaneously measure complementary observables must always fail due to the inevitable back-action onto the system from the measuring device [4]. But must complementarity always follow from the uncertainty principle? Remarkably, the answer is “no.” We will see, in this chapter, an experiment which demonstrates wave/particle complementarity as a fundamental phenomenon, without using the uncertainty principle in any way.

2.1.2 “Which path” information in the Mach-Zehnder interferometer

It has been shown quite generally that in any optical interference experiment, the visibility of the interference fringes is equal to the degree of intrinsic indistinguishability of the photon paths [5]. If the paths can be made distinguishable in principle somehow, then interference must vanish as a result, even if the distinguishing information is never recorded. To demonstrate this type of complementarity without invoking the uncertainty principle requires some means of identifying the paths of the interfering particles that does not disturb their motion.

Let us consider a photon which is allowed to take two different paths on its way to a detector¹, as in the Mach-Zehnder interferometer shown in Figure 2.2 (a). Just before the light is recombined at the final beamsplitter, its state is the superposition of two Fock states

$$|\psi\rangle_\ell = \frac{1}{\sqrt{2}} \{ e^{i\phi_1} |1\rangle_1 + e^{i\phi_2} |1\rangle_2 \} \quad (2.1)$$

where the subscript 1 is a label for the mode of the upper path, and 2 denotes the mode for the lower path. The phases ϕ_1 and ϕ_2 are equal to $\omega\tau_1$ and $\omega\tau_2$, respectively, where $c\tau_1$ and $c\tau_2$ are the optical lengths of the upper and lower paths from the initial beamsplitter to the final beamsplitter. The light which emerges and is subsequently detected is described by the annihilation operator

$$\hat{a} = \frac{1}{\sqrt{2}} (i\hat{a}_1 + \hat{a}_2). \quad (2.2)$$

Over many trials, the average number of detected photons at the output will be given by the expectation

¹ The following discussion is adapted from reference [6], in which the interfering particles were atoms.

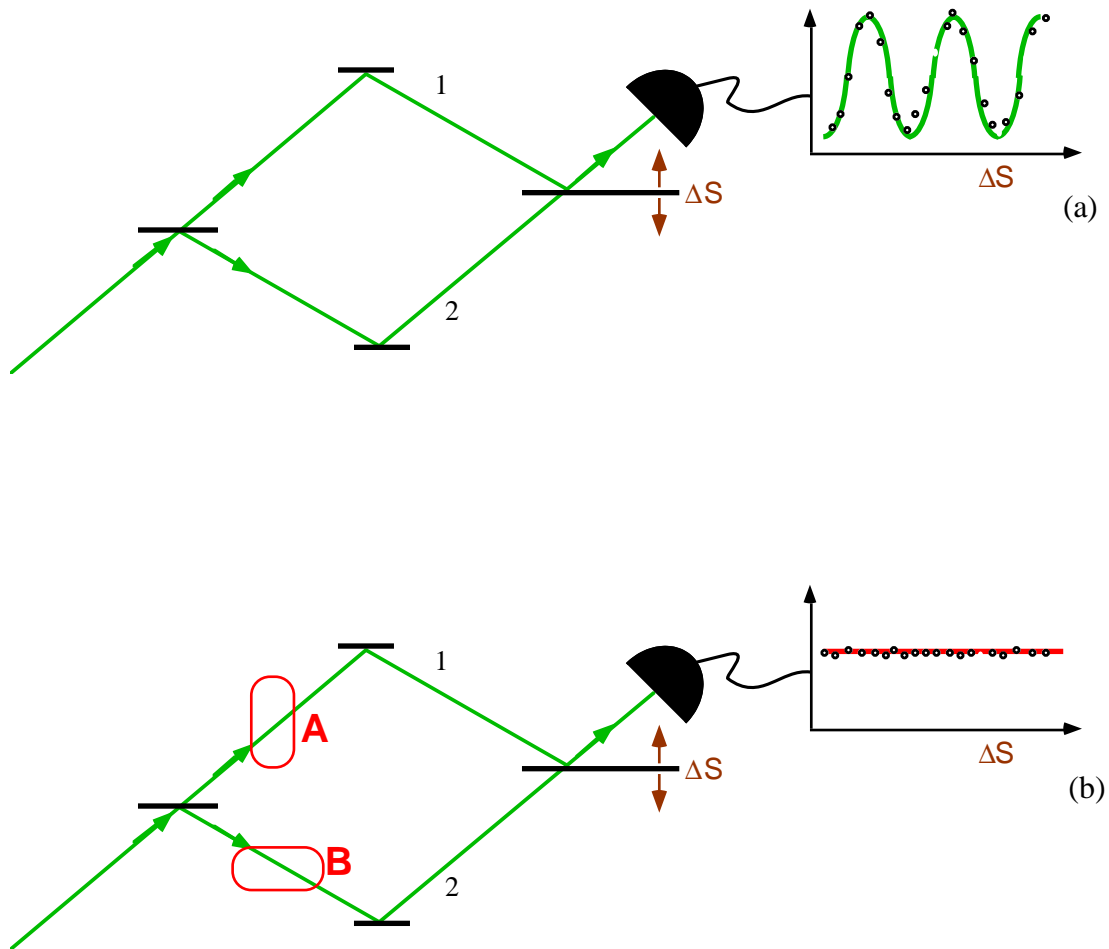


Figure 2.2 (a) A Mach-Zehnder interferometer. Light is incident on the beamsplitter from the left, and may take path 1 or path 2 to the output beamsplitter, where it is recombined. A photodetector monitors one of the output ports of the beamsplitter. As the phase difference between path 1 and path 2 is altered via small displacements of the final beamsplitter (ΔS), the photon counting rate exhibits interference modulation. This modulation occurs even if the incident light beam is weak enough that only one photon is in the interferometer at a time. (b) The same interferometer, but with the light in each path coupled to an external observable with distinguishable eigenstates $|A\rangle_M$ and $|B\rangle_M$. Interference vanishes as a result of the distinguishability of the interfering paths.

$$\langle \hat{n} \rangle = |\hat{a}|\psi\rangle_d|^2 = \left| \frac{1}{2} \{ ie^{i\phi_1} |vac\rangle + e^{i\phi_2} |vac\rangle \} \right|^2 = \frac{1}{2} (1 + \sin(\phi_2 - \phi_1)) \quad (2.3)$$

which exhibits interference.

Now suppose that before the light is recombined at the output beamsplitter, it is coupled to another system that can be found in one of two orthogonal states, $|A\rangle_M$ and $|B\rangle_M$, which are nondegenerate eigenstates of some observable \hat{O} , as in Figure 2.2 (b). The precise nature of the coupling is unimportant so long as it has the form

$$\begin{array}{l} |1\rangle_1 \xrightarrow{\text{interaction}} |1\rangle_1 |A\rangle_M \\ |1\rangle_2 \xrightarrow{\text{interaction}} |1\rangle_2 |B\rangle_M. \end{array} \quad (2.4)$$

We note two important features here: first, these relations indicate that the final state of the auxiliary system is completely determined by which path the photon takes through the interferometer; second, because the auxiliary states $|A\rangle_M$ and $|B\rangle_M$ are orthogonal, they may in principle be distinguished from one another in a single measurement of \hat{O} by their eigenvalues. Therefore, a single measurement of observable \hat{O} would constitute a determination of “which path” information for each photon in the interferometer..

Because of the interaction specified in (2.4), the initial state of the system must now be amended to include states for the measuring apparatus as well as for the light. The new state may be written in the larger Hilbert space as

$$|\chi\rangle_{LM} = \frac{1}{\sqrt{2}} \{ e^{i\phi_1} |1\rangle_1 |A\rangle_M + e^{i\phi_2} |1\rangle_2 |B\rangle_M \}. \quad (2.5)$$

This state is entangled, since it cannot be written as a product of two states in distinct Hilbert spaces for the light and the measuring apparatus. If we now calculate the number of photons arriving at the detector, averaged over many trials, we obtain

$$\langle \hat{n} \rangle = |\hat{a}|\chi\rangle_M|^2 = \left| \frac{1}{2} \{ ie^{i\phi_1} |vac\rangle |A\rangle_M + e^{i\phi_2} |vac\rangle |B\rangle_M \} \right|^2 = \frac{1}{2}. \quad (2.6)$$

There is no interference here; the terms which would have displayed a dependence on the phase difference $(\phi_2 - \phi_1)$ have vanished due to the orthogonality of the states $|A\rangle_M$ and $|B\rangle_M$. As noted earlier, this orthogonality is the very property which allows the path of the photon to be unambiguously identified in a single measurement of \hat{O} . This means that the wave behavior is destroyed here not as a result of the uncertainty principle, but due to the presence of “which path” information within the measuring apparatus. Note that the interference disappears even if no measurements are actually made on the auxiliary system: the mere fact that the “which path” information exists is enough to eliminate the interference.

2.1.3 Erasing “which-path” information

In view of the more traditional approaches to complementarity, one might suspect that somewhere in the physical details of the coupling between the interferometer and the measuring apparatus, an uncontrollable disturbance is acting to destroy the interference. But this is not the case, for it is possible to regain interference while leaving the coupling between the two systems intact. All that is required, according to complementarity, is that the photon paths be made indistinguishable again. This implies that the “which path” information stored in the measuring system must be “erased” somehow, so that even in principle it can never be accessed. As Scully and Druhl first pointed out, all of this can be done without invoking the uncertainty principle, and without altering the paths of the interfering particles [7].

Suppose that instead of measuring \hat{O} on the remote apparatus, we choose to measure another observable, \hat{O}' , with eigenstates $|A'\rangle_M$ and $|B'\rangle_M$ which are given by the linear combinations

$$\begin{aligned}
|A\rangle_M &= \frac{1}{\sqrt{2}} \{|A\rangle_M + |B\rangle_M\} \\
|B\rangle_M &= \frac{1}{\sqrt{2}} \{|A\rangle_M - |B\rangle_M\}.
\end{aligned}
\tag{2.7}$$

No matter what state the measuring device was in initially, if the observable \hat{O} is measured, the system must be found in one of the two states above. Note that these states do not give “which path” information for the photons. In fact, once the system is in either of the \hat{O} eigenstates, it is equally likely that a subsequent measurement of \hat{O} will put the system into state $|A\rangle_M$ or $|B\rangle_M$, regardless of what the photons are doing. Thus, by measuring \hat{O} before a measurement of \hat{O} can be made, the “which path” information can be destroyed forever (see Figure 2.3).

To show this more clearly, we first rewrite the quantum state of the system in the form

$$|\chi\rangle_{\ell M} = \frac{1}{\sqrt{2}} \frac{1}{\sqrt{2}} (e^{i\phi_1} |1\rangle_1 + e^{i\phi_2} |1\rangle_2) |A\rangle_M + \frac{1}{\sqrt{2}} (e^{i\phi_1} |1\rangle_1 - e^{i\phi_2} |1\rangle_2) |B\rangle_M. \tag{2.8}$$

This state is identical to the one given in (2.5), but we can see more clearly from this expression for it that if the measuring apparatus is found in state $|A\rangle_M$, the light will be found in the superposition state

$$|\psi\rangle_\ell^S = \frac{1}{\sqrt{2}} \{e^{i\phi_1} |1\rangle_1 + e^{i\phi_2} |1\rangle_2\}. \tag{2.9}$$

This is the state originally presented in Eq. (2.1), before the light was entangled with the measuring apparatus. This state is capable of exhibiting interference, as is seen by computing the expected number of photons at the output beamsplitter:

$$\langle \hat{n} \rangle = \frac{1}{2} |\hat{a} |\psi\rangle_\ell^S|^2 = \frac{1}{2} \left| \frac{1}{\sqrt{2}} \{ie^{i\phi_1} |vac\rangle + e^{i\phi_2} |vac\rangle\} \right|^2 = \frac{1}{4} (1 + \sin(\phi_2 - \phi_1)). \tag{2.10}$$

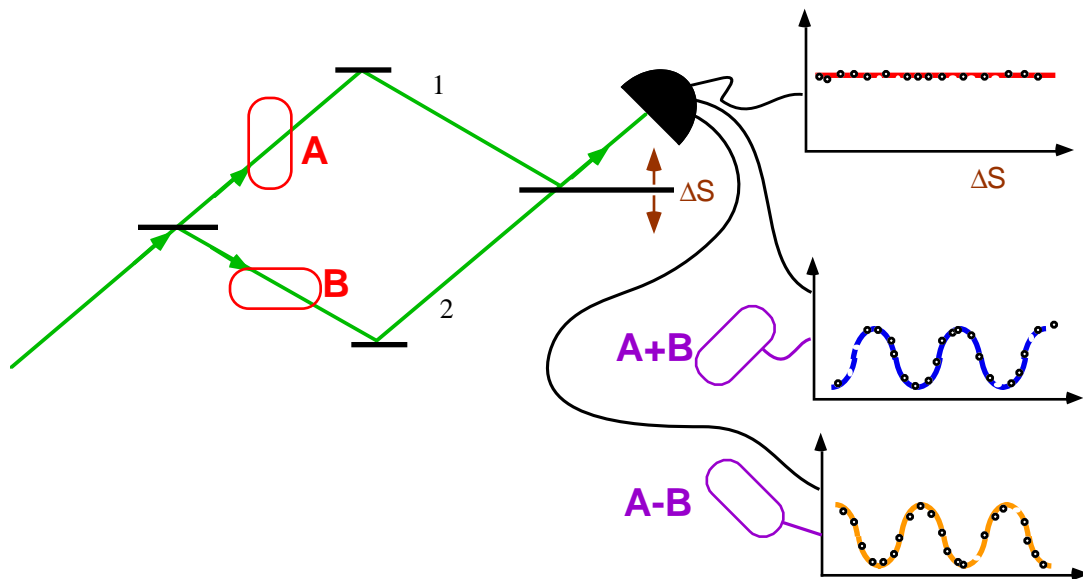


Figure 2.3 The quantum eraser. If the external observable is detected in the basis $\{|A\rangle_M + |B\rangle_M; |A\rangle_M - |B\rangle_M\}$, the “which-path” information is irrevocably destroyed, and interference returns for each subensemble of the photocounts that is correlated with such measurements.

The projection of the initial state onto $|\psi\rangle_\ell^S$ is contingent upon a measurement of \hat{O} being performed and yielding the eigenvalue for the state $|A\rangle_M$. Thus, in order to see the fringes, we must make repeated joint measurements of both the light and the measuring apparatus, selecting only those events for which the measuring apparatus is in state $|A\rangle_M$. The subensemble selected in this manner will contain half of the total events; this is the origin of the extra factor of $1/2$ in the preceding equation.

Similarly, whenever the measuring apparatus is found to be in the state $|B\rangle_M$, the light will be in the antisymmetric superposition state

$$|\psi\rangle_\ell^A = \frac{1}{\sqrt{2}} \{ e^{i\phi_1} |1\rangle_1 - e^{i\phi_2} |1\rangle_2 \}, \quad (2.11)$$

Here again we have interference, according to

$$\langle \hat{n} \rangle = \frac{1}{2} |\hat{a}|\psi\rangle_\ell^A|^2 = \frac{1}{2} \left| \frac{1}{\sqrt{2}} \{ ie^{i\phi_1} |vac\rangle - e^{i\phi_2} |vac\rangle \} \right|^2 = \frac{1}{4} (1 - \sin(\phi_2 - \phi_1)). \quad (2.12)$$

This interference will only be observed when the measuring apparatus is in state $|B\rangle_M$ rather than $|A\rangle_M$. This second subensemble therefore contains all of the photodetections that were missing from the first.

The interference fringes described by (2.12) are exactly 180 degrees out of phase with those described by (2.10), and are therefore referred to as “antifringes.”² If we do not select a subensemble of the photodetections by correlating them with one or the other of the apparatus states, then the result for the light will be given by adding the fringes and antifringes, which yields $\langle \hat{n} \rangle = 1/2$ once again. Thus, the interference which was lost as a result of the distinguishability of the photon paths cannot be regained if we

² The term “complementary fringes” is often used, but may be confusing because the fringes and antifringes are not complementary in the same sense as are noncommuting observables.

continue to measure only the light -- we must correlate the light measurements with the results of the \hat{O} measurements in order to see the interference.

Any apparatus in which “which path” information can be obtained and then destroyed by correlation with an auxiliary measurement may be called a “quantum eraser.” Various proposals for accomplishing this have been presented and analyzed in the last decade [7-19], though few have been carried out, and only two [14,16] have qualified as true quantum erasers.³

2.2 Schematic and theory

2.2.1 Schematic of the experiment

Our scheme for creating a quantum eraser [16] is depicted in Figure 2.4. The pump beam is incident from the left, and is split at the input to a Mach-Zehnder interferometer. Each arm of the interferometer contains a type-I parametric downconverter (NL1, NL2), which converts a small fraction of the x -polarized pump photons in modes $p1$ and $p2$ into pairs of y -polarized signal and idler photons. The signal beams are allowed to continue through the interferometer in modes $s1$ and $s2$, and are ultimately recombined at beamsplitter BSs and sent to detector A. Meanwhile, the idler beam from NL1 passes through a half-wave plate (R1) that rotates its polarization from y to x ; accordingly, we label the idler modes from NL1 and NL2 as ix and iy , respectively.

³ Reference [13] contains an illuminating discussion about what features distinguish true quantum erasers from other demonstrations of complementarity. Three “true quantum erasers” are proposed there, one of which is very similar to our experiment. An earlier experiment [12] by the same authors is then regarded as not being an optimal demonstration of a true quantum eraser.

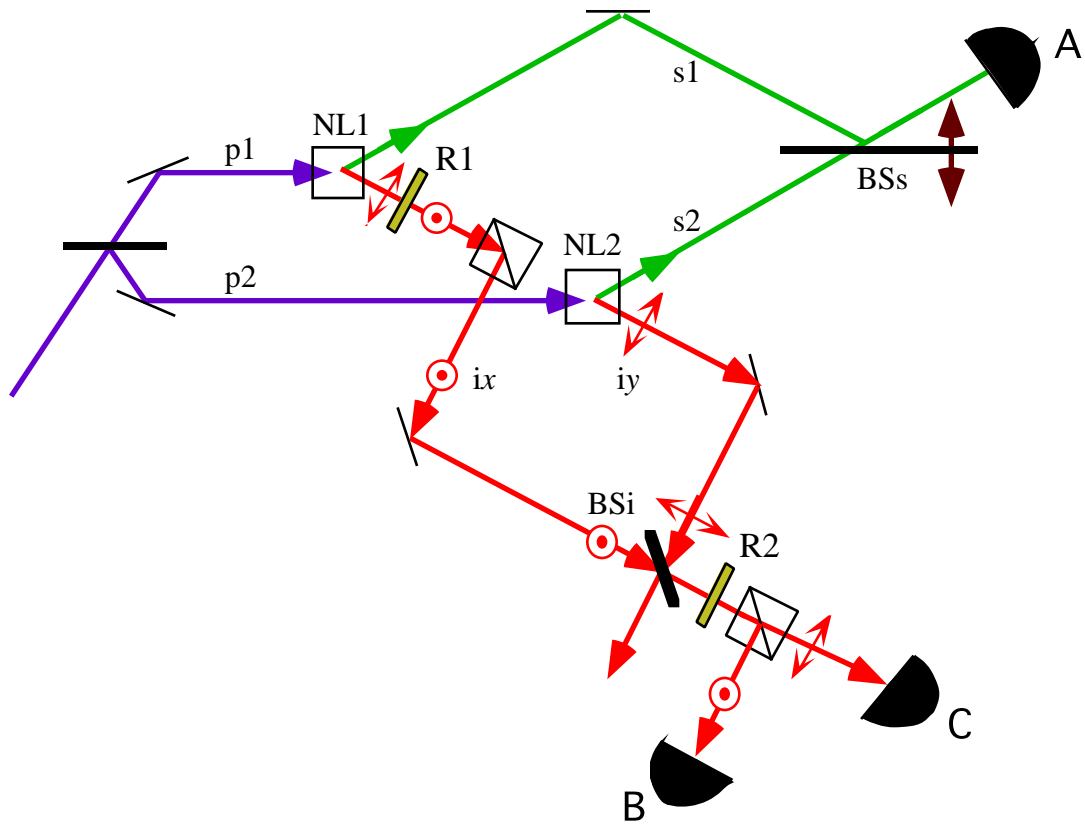


Figure 2.4 Experimental realization of a quantum eraser. The pump beam is split at the input and is downconverted in either NL1 or NL2. The signals are allowed to interfere, while the idlers carry the "which path" information which may be erased.

2.2.2 Quantum state of the light

The interaction Hamiltonian for this system is the sum of the Hamiltonians for each downconverter:

$$\begin{aligned}\hat{H}_I &= \hat{H}_{I1} + \hat{H}_{I2} \\ &= \left[g\hat{a}_{p1}\hat{a}_{s1}^\dagger\hat{a}_{ix}^\dagger + g\hat{a}_{p2}\hat{a}_{s2}^\dagger\hat{a}_{iy}^\dagger \right] + \text{h.c}\end{aligned}\quad (2.13)$$

Each interaction in the brackets specifies the annihilation of a pump photon and simultaneous creation of a signal and idler pair in the modes specified above. This provides a coupling of exactly the form required by Eqs. (2.4), as shown explicitly by

$$\begin{aligned}\hat{H}_I|1\rangle_{p1} &= g|1\rangle_{s1}|1\rangle_{ix} \\ \hat{H}_I|1\rangle_{p2} &= g|1\rangle_{s2}|1\rangle_{iy}\end{aligned}\quad (2.14)$$

Here the idler polarization plays the role of the external observable \hat{O} and takes on one of two distinct values depending on the path of the signal photon.

Because the pump field is generated by a laser, it is more accurately represented by the coherent state $|V_0\rangle$ than by a one-photon fock state. After the first beamsplitter, the initial state of the system is the direct product of two coherent states for the pump beams in modes p1 and p2 [20] with the signal and idler modes in the vacuum state:

$$|\psi(0)\rangle = \left| i\frac{V_0}{\sqrt{2}} \right\rangle_{p1} \left| \frac{V_0}{\sqrt{2}} \right\rangle_{p2} |vac\rangle_{s1,s2,ix,iy} \quad (2.15)$$

If the interaction is weak, the state of the light after the downconverters may be found by the perturbative method in Chapter 1. The result is

$$\begin{aligned}|\psi\rangle &= |vac\rangle + \eta \frac{1}{\sqrt{2}} \left\{ |1\rangle_{s1}|1\rangle_{ix} + |1\rangle_{s2}|1\rangle_{iy} \right\} \\ &= |vac\rangle + \eta |\psi^{(1)}\rangle,\end{aligned}\quad (2.16)$$

where η is a creation efficiency parameter satisfying

$$|\eta|^2 \ll 1. \quad (2.17)$$

Since the vacuum will not contribute any photodetections, we may use the state

$$|\Psi^{(1)}\rangle = \frac{1}{\sqrt{2}} \{ |1\rangle_{s1} |1\rangle_{ix} + |1\rangle_{s2} |1\rangle_{iy} \} \quad (2.18)$$

to compute the expectation values of any measured quantities. Note that this state has the same entangled form as the one in Eq. (2.5).

2.2.3 Predicted counting rates

The single-mode field operator for the light at detector A is given by

$$\hat{E}_A^{(+)} = \frac{\ell}{\sqrt{2}} (ie^{i\phi_1} \hat{a}_{s1} + e^{i\phi_2} \hat{a}_{s2}) \quad (2.19)$$

where ℓ is a unit constant with dimensions such that the intensity $|\hat{E}_A|^2$ is in units of photons per second. If the photodetector A is perfectly efficient, it will detect photons at the rate

$$R_A = \langle \Psi^{(1)} | \hat{E}_A^{(-)} \hat{E}_A^{(+)} | \Psi^{(1)} \rangle = |\langle \hat{E}_A^{(+)} | \Psi^{(1)} \rangle|^2 = \frac{1}{2} \quad (2.20)$$

which does not exhibit interference, in analogy with (2.6). This is to be expected, because in principle a measurement of the idler polarization could reveal which crystal produced each signal photon. In the scheme of Figure 2.4, this information is accessed by combining the ix and iy idler modes at BSi and sending them through a polarizing beamsplitter, whose outputs are monitored by detectors B and C. The field operators at these detectors are

$$\begin{aligned} \hat{E}_B^{(+)} &= \frac{\ell}{\sqrt{2}} \hat{a}_{iy} e^{i\phi_y} \\ \hat{E}_C^{(+)} &= \frac{\ell}{\sqrt{2}} \hat{a}_{ix} e^{i\phi_x}. \end{aligned} \quad (2.21)$$

It is not surprising to find that in this configuration, the joint detection rates

$$R_{AB,AC} = \langle \Psi^{(1)} | \hat{E}_A^{(-)} \hat{E}_B^{(-)} \hat{E}_A^{(+)} \hat{E}_B^{(+)} | \Psi^{(1)} \rangle = \left| \hat{E}_A^{(+)} \hat{E}_B^{(+)} | \Psi^{(1)} \rangle \right|^2 = \frac{1}{4} \quad (2.22)$$

do not display interference⁴.

The quantum eraser is formed by insertion of a half-wave plate (R2) into the mixed idler beam with its optical axis oriented at 22.5° to either the x or y polarization. This has the effect of rotating both polarizations by 45°, so that the fields at detectors B and C become

$$\begin{aligned} \hat{E}_B^{(+)} &= \frac{\ell}{2} (\hat{a}_{iy} e^{i\phi_y} + \hat{a}_{ix} e^{i\phi_x}) \\ \hat{E}_C^{(+)} &= \frac{\ell}{2} (\hat{a}_{iy} e^{i\phi_y} - \hat{a}_{ix} e^{i\phi_x}). \end{aligned} \quad (2.23)$$

Measurement of the idler polarization in this rotated basis ($x + y$, $x - y$), by detecting the idler at B or C, is equivalent to measuring the observable \hat{O} in the previous section, so that the “which-path” information is permanently erased. Accordingly, the interference must return for each subensemble of signal photons detected in coincidence with the idlers at B or C: the interference fringes are displayed by

$$\begin{aligned} R_{AB} &= \langle \Psi^{(1)} | \hat{E}_A^{(-)} \hat{E}_B^{(-)} \hat{E}_A^{(+)} \hat{E}_B^{(+)} | \Psi^{(1)} \rangle = \left| \hat{E}_A^{(+)} \hat{E}_B^{(+)} | \Psi^{(1)} \rangle \right|^2 \\ &= \frac{1}{4} (1 + \cos(\phi_1 - \phi_2 + \quad)) \end{aligned} \quad (2.24)$$

while the antifrings are seen in

$$\begin{aligned} R_{AC} &= \langle \Psi^{(1)} | \hat{E}_A^{(-)} \hat{E}_C^{(-)} \hat{E}_A^{(+)} \hat{E}_C^{(+)} | \Psi^{(1)} \rangle = \left| \hat{E}_A^{(+)} \hat{E}_C^{(+)} | \Psi^{(1)} \rangle \right|^2 \\ &= \frac{1}{4} (1 - \cos(\phi_1 - \phi_2 + \quad)). \end{aligned} \quad (2.25)$$

⁴ These probabilities sum to 1/2, rather than 1, because only half of the idler photons are collected from BSi in this arrangement. If a polarizing beamsplitter were used for BSi, this would be avoided.

Here $\phi_x - \phi_y$ is an overall phase shift acquired by the idlers during propagation to BSi.

2.3 Experimental procedure and results

2.3.1 Apparatus

For the experiment, the pump was a 250 mW ultraviolet laser beam generated by a cw Argon-ion laser operating at a wavelength of 351 nm. The downconverters NL1 and NL2 were 2.5 cm long LiIO₃ crystals cut for type-I phase-matching. The mean signal and idler wavelengths were chosen to be 789 nm and 633 nm, respectively, so that the idler paths could be more easily aligned with the help of a HeNe laser beam. To observe interference fringes, BSs was mounted on a piezoelectric ceramic transducer (PZT). The PZT expanded linearly in response to an applied voltage, at the rate of about 2 nm per volt: this allowed the relative lengths of the two paths to be varied on a scale comparable to the wavelength of the light.

The photodetectors were EG&G model SPCM-200 avalanche photodiodes with dead time of about 150 ns and quantum efficiency of about 50%⁵. The 150 ns TTL pulses generated by the detectors were used to trigger discriminators; these, in turn, emitted 4.5 ns NIM pulses that were fed to single-channel counters and to a coincidence counter. The detector jitter time of about 4.5 ns implied that any signals reaching the coincidence counter within a resolving time of 9ns could have been due to the simultaneous arrival of photons at the pair of detectors. The number of “accidental” coincidences due to uncorrelated photons that could occur in this time was computed

⁵ The imperfect photodetection efficiencies have the effect of scaling all of the predicted counting rates by linear factors; these factors do not affect the ability of the apparatus to display the fringes and antifrings, and were omitted from the preceding discussions for the sake of clarity.

from the measured single-channel counting rates and the coincidence resolving time, and subtracted out.

1 nm-bandwidth filters were placed in front of the detectors to eliminate background noise. For the signal beams, the range of frequencies selected by these filters corresponded to a coherence time of roughly 2 ps for the photon wavepackets, so that the optical path lengths of the two possible photon paths in the interferometer were required to be equal to within 600 μm for interference to occur. Lenses were also placed in front of each detector to focus the light onto their 100 μm -diameter active areas.

The pump laser delivered an average of 4×10^{17} photons to the initial beamsplitter per second. However, the downconversion efficiency was very low -- the probability of a given pump photon producing a signal/idler pair was only

$$|\eta|^2 = 10^{-11}, \quad (2.26)$$

in keeping with (2.17). It was therefore extremely unlikely that each crystal independently generated a photon pair within the 2 ps coherence time required for the signals to overlap at the final beamsplitter, so that only one signal photon at a time was in the interferometer.

2.3.2 Results

Starting with the input of a pump photon at the initial beamsplitter, we see that there were two distinct ways for a signal photon to reach the final photodetector within the coherence time: either the pump photon traversed the upper arm and was downconverted at NL1, or it traversed the lower arm and was downconverted at NL2. These two paths were distinguishable, because in principle, any signal measurement at A might have been correlated with an idler polarization measurement, which would have

revealed the origin of the pair. Accordingly, the signals did not display interference, as seen in Figure 2.5.

However, when we erased the “which path” information by detecting the idlers in the 45° rotated basis, the interference fringes returned in each subensemble. The coincidence counts from detectors A and B displayed fringes, while the coincidences between A and C revealed antifrings. The recorded fringes and antifrings are shown in Figure 2.6.

2.4 Discussion

2.4.1 Comparison with the “quantum preventer” of Zou et al.

It has been shown that a more direct means of destroying the information about the origin of the signal photons is simply to align the path of idler 1 so that it overlaps completely with that of idler 2 everywhere [21,22]. This makes the idlers forever indistinguishable, owing to the fact that they belong to the same mode, so that the “which path” information for the signals cannot be obtained, even in principle. In this elegant demonstration of complementarity, which has been called “Induced coherence without induced emission,” the signal interference returns without the need to observe the idlers at all, as shown in Figure 2.7 (a).

In this case, it is tempting to speak of the overlap of the idler beams as “erasing” the which-path information for the signals [23]. But it is more accurate to say that when the idler paths overlap, the which-path information is not so much erased as it is *prevented from ever existing*. It is this fact which accounts for the return of the interference of the single-channel counts without the need to divide them into “fringe” and “antifringe” subensembles -- see Figure 2.7 (b). This lack of post-selection through coupling to an external observable is what ultimately prevents this apparatus

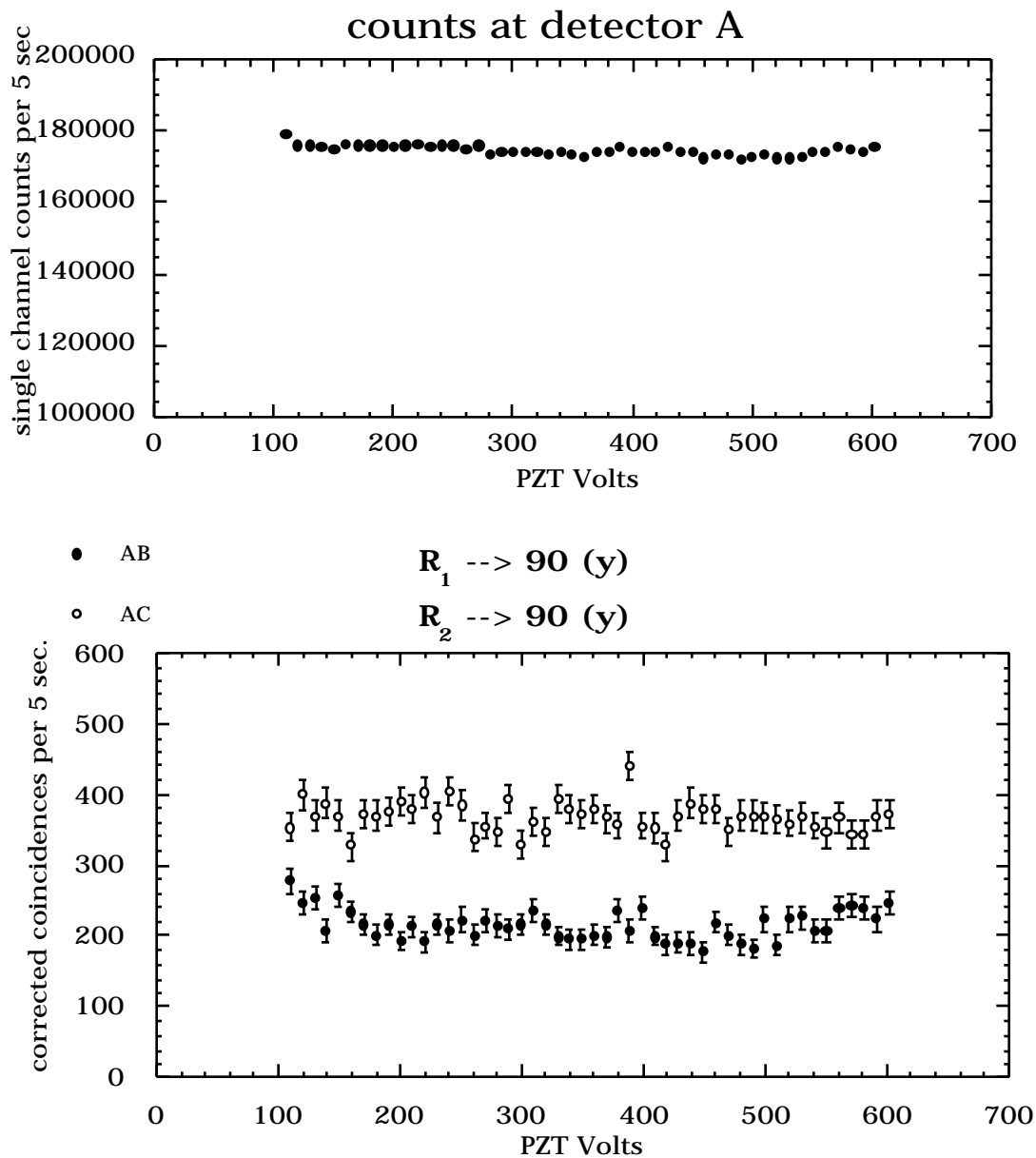


Figure 2.5 Measured single-channel and coincidence counts when the paths of the photons were distinguishable. The coincidence counts have been corrected for accidentals.

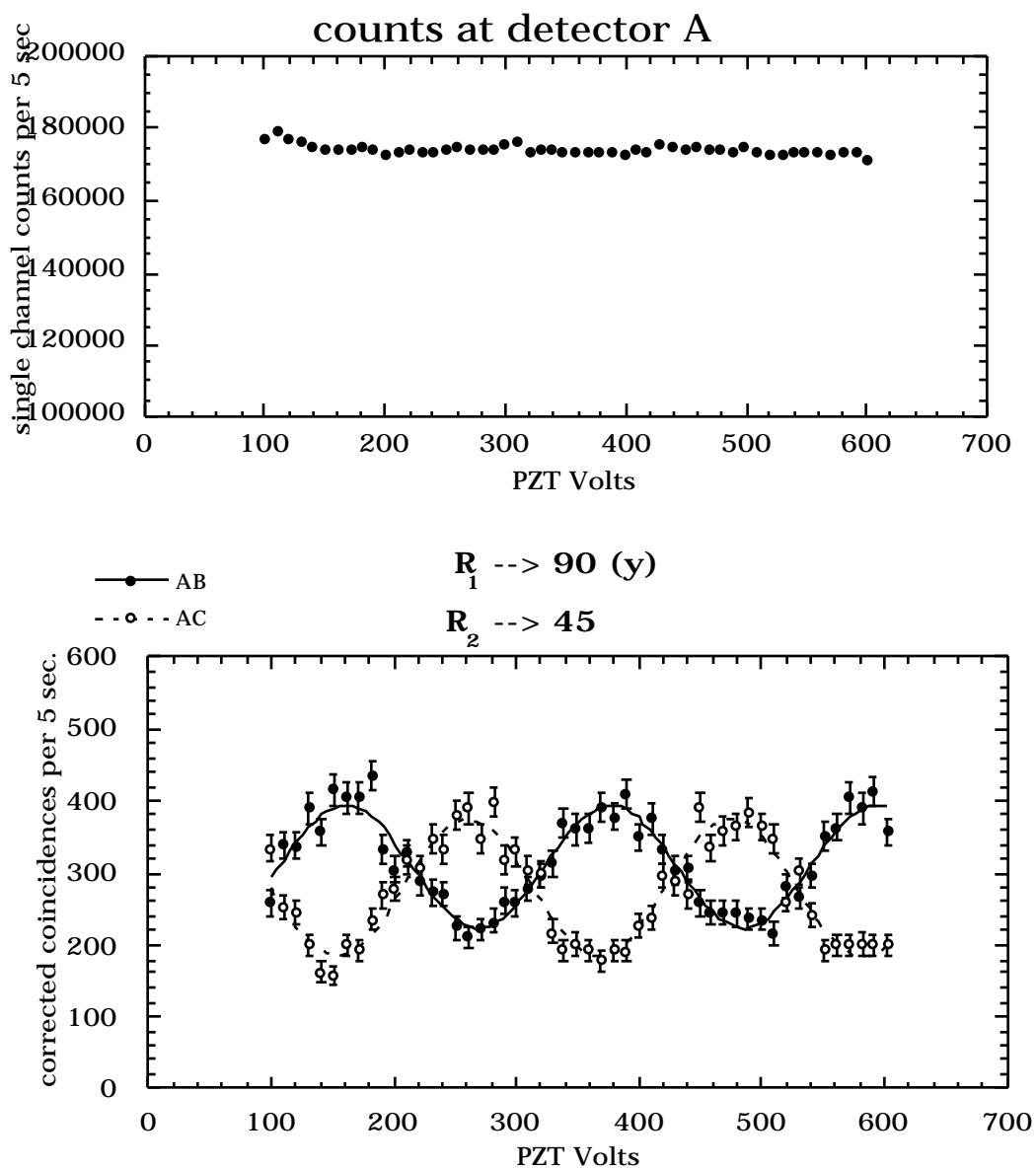


Figure 2.6 Measured single-channel and coincidence counts when the paths of the signals were distinguishable, but the paths for coincidence detection were indistinguishable. The coincidence counts have been corrected for accidentals.

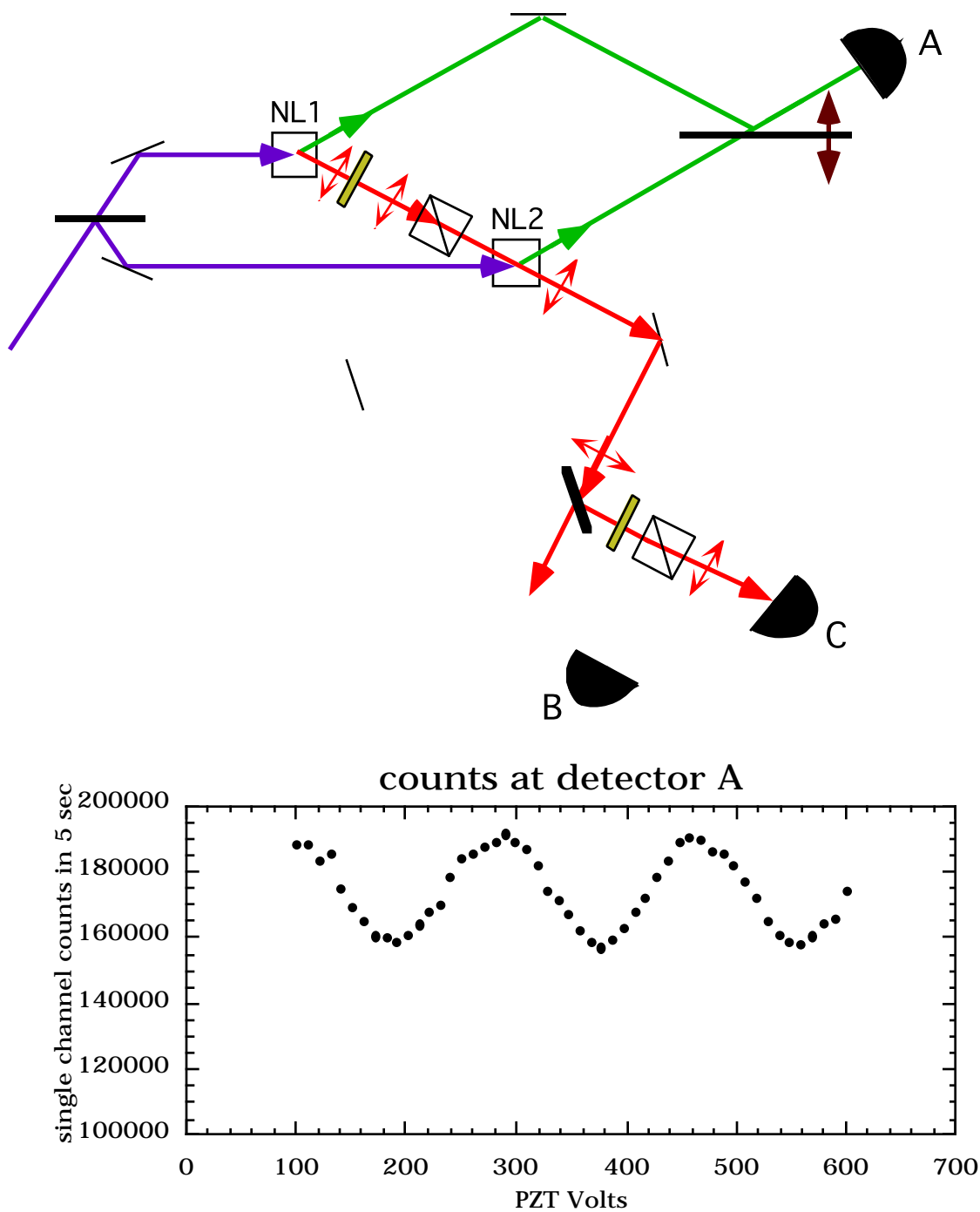


Figure 2.7 (a) Experimental arrangement which makes the signal paths indistinguishable in principle. Here R1 does not alter the idler polarization, so that the idler paths overlap completely. (b) Measured single-channel photodetections for the above apparatus. Interference returns for the signals without the need to select a subensemble via an auxiliary measurement. This is not a quantum eraser.

from being a true quantum eraser.⁶ Similar arguments also prevent at least two other interference experiments [12,25] from qualifying as quantum erasers in the strict sense [13].

2.4.2 “In principle” vs. “in practice” distinguishability revisited

In the introductory chapter, we asked what the implications would be for interference in a 2-slit interferometer if we were to allow each slit to create a “marker” as the photon passed through it, without disturbing the path of the photons themselves. The experiment described in this chapter corresponds to exactly this situation: the idlers play the role of the markers, while the signal photons complete the paths begun by the pump photons (see Figure 2.8). The “final screen” where the interfering photons are registered is analogous to detector A, and we explore different parts of the interference pattern by actively changing the relative phase between the two arms and counting photons according to

$$R \quad \langle \psi | \hat{E}^{(-)} \hat{E}^{(+)} | \psi \rangle. \quad (2.27)$$

This expectation value, which is of the second-order in the field operator, exhibits interference modulation whenever it is impossible in principle to identify which path a photon may have taken to arrive at the detector. As shown in Eq. (2.20) and Figures 2.5 (a) and 2.6 (a), this kind of interference never occurs in the quantum eraser experiment, because the marker photons always have the potential to identify the signal paths.

However, if the markers are manipulated properly and subsequently measured along with the signals in a way that prevents them from identifying the signal paths, interference returns. The events of this type are coincidence counts of the form

⁶It may not be a quantum eraser, but this experiment has been called a “remarkable” [13] and “mind-boggling” [24] demonstration of complementarity by other researchers.

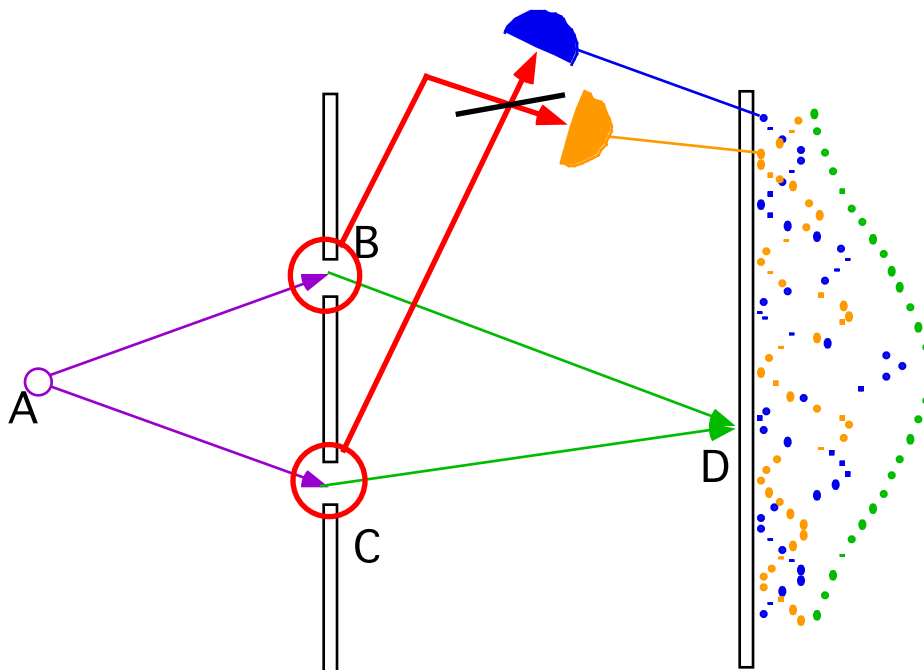


Figure 2.8 The quantum eraser presented as a variant of Young’s double-slit experiment. The marker (idler) photons are generated at points B and C, while the signal photons continue undeflected towards the screen. If the markers are measured in the “eraser” basis, the fringes and antifringes may be seen at the screen in conjunction with these measurements. Viewed without these correlations, the complete ensemble of events at the screen does not display interference, because the paths ABD and ACD remain distinguishable in principle.

$$R_{cc} = \langle \psi | \hat{E}_1^{(-)} \hat{E}_2^{(-)} \hat{E}_2^{(+)} \hat{E}_1^{(+)} | \psi \rangle. \quad (2.28)$$

In the quantum eraser, it is only these fourth-order measurements which display interference.

The standard interpretation, presented in this chapter, views this coincidence modulation as a kind of “gated second-order” interference, in which paths for the single-channel events within the fringe and antifringe subensembles have been rendered “indistinguishable in practice” by the appropriate detection of the marker photons in the rotated basis -- so long as the markers are actually detected in this basis, the signal paths are indistinguishable. But strictly speaking, the quantum eraser does not actually recover the second-order interference of the signal photons, because the signal photon paths remain *distinguishable in principle* via an auxiliary measurement, whether or not they are actually distinguished in practice. Instead, the quantum eraser displays fourth-order interference on those occasions when the sets of signal and idler paths leading to coincidence detection are *indistinguishable in principle*.⁷

In the quantum eraser, then, we see a clear demonstration of the principle of complementarity for wave and particle behavior: interference occurs between indistinguishable pathways that lead to the final event. One must keep in mind, though, that “events” may involve several particles, that “pathways” may include the multiple paths traveled by these particles, and that the pathways must be indistinguishable in principle, and not just in practice.

⁷ The “quantum preventer” discussed in the previous section does not make this distinction, because it shows a return of second-order interference whenever those paths are made indistinguishable in principle by overlapping the idlers.

References for Chapter 2

- [1] C. Cohen-Tannoudji, B. Diu, and F. Laloe, *Quantum Mechanics* (Wiley, New York, 1977).
- [2] R. P. Feynman, R. B. Leighton, and M. Sands, *The Feynman Lectures on Physics* (Addison-Wesley, Reading, 1965).
- [3] P. A. Tipler, *Modern Physics* (Worth, New York, 1978).
- [4] L. J. Wang, Ph.D. thesis, University of Rochester, 1992 (unpublished).
- [5] L. Mandel, *Opt. Lett.* **16**, 1882 (1991).
- [6] M. O. Scully, B.-G. Englert, and H. Walther, *Nature (London)* **351**, 111 (1991).
- [7] M. O. Scully and K. Druhl, *Phys. Rev. A* **25**, 2208 (1982).
- [8] M. O. Scully, R. Shea, and J. D. McCullen, *Phys. Rep.* **43**, 485 (1978).
- [9] A. G. Zajonc, *Phys. Lett.* **96A**, 61 (1983).
- [10] M. O. Scully and H. Walther, *Phys. Rev. A* **39**, 5229 (1989).
- [11] B.-G. Englert, H. Walther, and M. O. Scully, *App. Phys. B* **54**, 366 (1992).
- [12] P. G. Kwiat, A. M. Steinberg, and R. Y. Chiao, *Phys. Rev. A* **45**, 7729 (1992).
- [13] P. G. Kwiat, A. M. Steinberg, and R. Y. Chiao, *Phys. Rev. A* **49**, 61 (1994).
- [14] T. J. Herzog, P. G. Kwiat, H. Weinfurter, and A. Zeilinger, *Phys. Rev. Lett.* **75**, 3034 (1995).
- [15] H. Weinfurter *et al.*, in *Fundamental Problems in Quantum Theory: A Conference Held in Honor of Professor John A. Wheeler*, edited by D. M. Greenberger and A. Zeilinger, *Annals of the New York Academy of Sciences Vol. 755* (New York Academy of Sciences, New York, 1995), p. 61.
- [16] C. H. Monken, D. Branning, and L. Mandel, in *Coherence and Quantum Optics VII*, Proceedings of the 7th Rochester Conference on Coherence and Quantum Optics, edited by J. H. Eberly, L. Mandel and E. Wolf Vol. (Plenum Press, New York, 1995), p. 701.
- [17] P. Bogar and J. A. Bergou, *Phys. Rev. A* **53**, 49 (1996).
- [18] C. Gerry, *Phys. Rev. A* **53**, 1179 (1996).
- [19] Z. Y. Ou, *Phys. Lett. A* **226**, 323 (1997).
- [20] Z. Y. Ou, C. K. Hong, and L. Mandel, *Opt. Commun.* **63**, 118 (1987).

- [21] X. Y. Zou, L. J. Wang, and L. Mandel, *Phys. Rev. Lett.* **67**, 318 (1991).
- [22] L. J. Wang, X. Y. Zou, and L. Mandel, *Phys. Rev. A* **44**, 4614 (1991).
- [23] A. G. Zajonc, L. J. Wang, X. Y. Zou, and L. Mandel, *Nature (London)* **353**, 507 (1991).
- [24] D. M. Greenberger, M. A. Horne, and A. Zeilinger, *Physics Today*, 22 (1993).
- [25] Z. Y. Ou, L. J. Wang, X. Y. Zou, and L. Mandel, *Phys. Rev. A* **41**, 566 (1990).

Chapter 3

Spectral distinguishability and interference

3.1 Introduction

3.1.1 Ultrafast pump pulses and type-II downconversion

Up to this point we have been discussing experiments involving type-I parametric downconverters pumped by a cw laser source. But as we noted in the first chapter, there are situations in which it might be advantageous to use type-II phase-matching instead; in particular, this allows the possibility of constructing common-path interferometers, in which the signal and idler beams are emitted collinearly and separated later via their orthogonal polarizations.

Moreover, there are also advantages in using a pulsed, rather than cw, pump source. When the pump is cw, the photon pairs are produced at random times so long as the pump is turned on. Although we have not made explicit use of the multimode state for the photon pairs generated with cw pumping, it is shown in Appendix A that the signal and idler photon wavepackets may actually be quite short, only a few ps, in duration. So long as we are only interested in interference experiments involving one set of downconverted photon pairs at a time, this is not a problem, since the two members of the pair are emitted simultaneously. But if we are interested in performing multi-particle interference experiments, like the GHZ nonlocality experiment mentioned in Chapter 1, for example, the random photon emission time and the short photon wavepackets make it very unlikely that the photons from one downconverter are generated at the right time to interfere with those emitted from another. A pulsed pump has the potential to solve this problem, because if a photon pair is produced, it must be

created while the pump pulse is inside the downconversion crystal. In the domain of so-called “ultrafast” lasers, pulse durations on the order of 100 fs are now routine. It might seem a trivial matter, then, to pump several thin crystals simultaneously and to synchronize their emissions to within the few ps needed for the various signal and idler wavepackets to overlap within the apparatus.

It may seem straightforward, but as we will see below, if we wish to use type-II phase matching along with an ultrafast pump pulse, we must tread carefully into the domain of quantum interference. We have already encountered several examples of the intimate relationship between interference and indistinguishability. In this chapter, we will see that the broad bandwidth of an ultrafast pump pulse, in conjunction with the birefringence of the type II downconversion crystal, produces distinguishing “which-path” information in the spectral domain that effectively destroys the potential for interference of these photon pairs in at least one apparatus—the Hong-Ou-Mandel interferometer.

3.1.2 Fourth-order interference in the Hong-Ou-Mandel interferometer

In the quantum eraser experiment, we have an example of fourth-order interference, in which interference fringes can be seen in the coincidence counts generated by the simultaneous detection of signal and idler photons at two detectors. The Hong-Ou-Mandel interferometer (HOMI) [1] is another type of fourth-order interference apparatus, displayed in Figure 3.1. The signal and idler photons from a parametric downconverter are incident on a “symmetric” beamsplitter having reflectivities and transmissivities

$$R = R = iT = iT = \frac{1}{\sqrt{2}}. \quad (3.1)$$

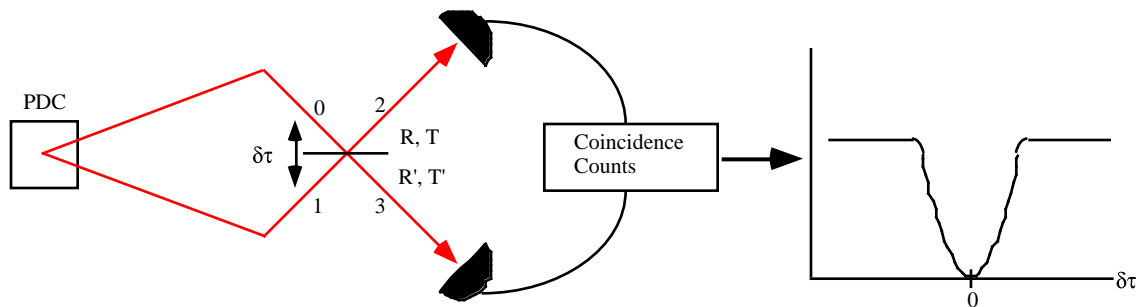


Figure 3.1 The Hong-Ou-Mandel interferometer, in which two photons produced in the process of parametric downconversion are brought together at a beamsplitter. The output ports of the beamsplitter are monitored by a pair of photodetectors which register coincidence counts. When the beamsplitter is positioned correctly, so that it is impossible in principle to determine whether a coincidence count occurred via double-transmission or double-reflection, these two coincidence paths interfere destructively and result in a coincidence counting rate of zero. If the beamsplitter is moved away from this position, the destructive interference is degraded because it is now possible to use the relative timing of the two detections to determine whether a double-reflection or double-transmission actually took place. As the two paths become more and more distinguishable, the coincidence counts rise from zero to the nominal “background” rate of half the total pair production rate. The “dip” in the plot of coincidence counts vs. beamsplitter position is a signature of quantum interference for the photon pairs.

A pair of photodetectors monitors the output modes of the beamsplitter, which are related to the input modes by the usual transformations:

$$\begin{aligned}\hat{a}_2 &= R\hat{a}_0 + T\hat{a}_1 \\ \hat{a}_3 &= T\hat{a}_0 + R\hat{a}_1.\end{aligned}\quad (3.2)$$

In the simple monochromatic mode treatment, the state of the light produced by the downconverter is

$$|\psi\rangle = |vac\rangle + \eta|1\rangle_0|1\rangle_1. \quad (3.3)$$

The predicted coincidence counting rate is then given by

$$\begin{aligned}R_{cc} \quad \langle\psi| : \hat{n}_2 \hat{n}_3 : |\psi\rangle &= |\hat{a}_2 \hat{a}_3 |\psi\rangle|^2 \\ &= |(R\hat{a}_0 + T\hat{a}_1)(T\hat{a}_0 + R\hat{a}_1)\{|vac\rangle + \eta|1\rangle_0|1\rangle_1\}|^2. \\ &= |\eta|^2 |RR|vac\rangle + TT|vac\rangle|^2\end{aligned}\quad (3.4)$$

The last line shows that the coincidence counting rate is the squared modulus of the sum of two quantum-mechanical amplitudes for the processes that lead to coincidence counts: double-reflection and double-transmission. Using the relations in (3.1) leads us to

$$\begin{aligned}R_{cc} \quad &|\eta|^2 \left| \frac{1}{2}|vac\rangle - \frac{1}{2}|vac\rangle \right|^2 \\ &= 0\end{aligned}\quad (3.5)$$

That is, because of the net phase-shift of 180° between the double-reflection and double-transmission amplitudes, the two processes destructively interfere and result in no coincidence counts. What is inferred from this is that when the two photons meet from

different sides of a symmetric beamsplitter, they must both emerge in the same direction, that is, into mode 2 or mode 3.¹

If, instead of the monochromatic two-mode state in (3.3), we analyze the HOMI when the light is in the cw-pumped multimode state derived in Appendix A,

$$|\psi\rangle = |vac\rangle + \eta \int_0 d\omega_s (\omega_s, \omega_p - \omega_s) |1\rangle_{\omega_s, o} |1\rangle_{\omega_p - \omega_s, o}, \quad (3.6)$$

we find that the coincidence counting rate is

$$R_{cc} = |\eta|^2 [1 - e^{-\delta\tau/\tau_c}], \quad (3.7)$$

where $c\delta\tau$ is the displacement of the beamsplitter from the central position in which the signal and idler photon path lengths to the beamsplitter are identical. Here $\tau_c = 1/\omega$ is the coherence length of the signal and idler wavepackets, where ω denotes the bandwidth of the phase-matching function for each downconverted field. Equation (3.7) predicts a coincidence counting rate of zero for the symmetric beamsplitter position $\delta\tau = 0$, and a rising rate as the beamsplitter moves away from this position. This is an indication that, for positions other than $\delta\tau = 0$, the destructive interference of the double-reflection and double-transmission paths is no longer complete; in fact it vanishes entirely when the signal and idler path lengths to the beamsplitter differ by more than $c\tau_c$. In that case, the two coincidence paths are completely distinguishable in principle from the relative arrival time of each photon at its detector. When the time delay is longer than the coherence time of the wavepackets, the order in which the detectors fire is enough to reveal which of the two coincidence paths actually generated the event.

¹ Of course, the choice of exit mode (2 or 3) is not actually made by the photons until a measurement forces the issue. Until then, the photon pairs are in a superposition state of having chosen mode 2 together or mode 3 together.

Interestingly, it does not matter whether we have photodetectors with sufficient time-resolution to actually make the necessary distinction as to which photon arrived first. The fact that our (slow) photodetectors are often unable to reveal which of the two processes generated the coincidence event might seem to make the processes “indistinguishable in practice”, but as we have already seen, this kind of indistinguishability — which comes from ignoring information that is really present in the system — is not good enough to generate interference. It remains possible, in principle, to use faster photodetectors and discover which process led to the event, provided that $|\delta\tau| \ll \tau_c$, and this is what prevents the two-photon detection amplitudes from interfering with each other.

On the other hand, if the light itself is modified before it reaches the photodetectors, this can have an impact on the interference. For example, if the signal and idlers are sent through a narrowband filter which increases their coherence times, then the “dip” becomes wider as the new coherence time plays the role of τ_c in (3.7). This is in keeping with our maxim that “indistinguishability in principle” is what matters, because for the light that survives the filtering process, no photodetector timing resolution can be high enough to provide complete “which-process” information for delays inside this (widened) dip structure. The information does not exist, because the photons may be found anywhere inside their wavepackets.

Several variations of the HOMI experiment have been carried out in recent years,[2-11] usually with the aim of demonstrating the effects produced by various kinds of distinguishing information for the coincidence processes. Most of these experiments have been conducted with cw-pumped type-I downconverters. A few have used cw-pumped type-II downconversion, with signal and idler photons sometimes incident on a polarizing beamsplitter (PBS), rather than a conventional beamsplitter.

The experiment reported in this chapter is yet another variation[12], in which an ultrafast pump is used for the type-II downconversion. As with other variations, this experiment was undertaken with the idea of exploring the effects of distinguishing information on the “dip” visibility. We chose to look at this information as “spectral” in nature[13], but it is also worth noting that a similar set of experiments was recently conducted and fully analyzed in the time domain [14,15]. The two ways of expressing the distinguishing information are of course equivalent, and this has been shown recently by Grice[16]. In the interests of simplicity, we will focus only on the spectral interpretation.

3.2 Schematic and theory

3.2.1 Schematic of the experiment

We will investigate the effects of ultrafast pumping on the interference visibility for photon pairs in the collinear HOMI. A schematic of this system is shown in Figure 3.2. An ultrafast pump pulse is incident from the left on a nonlinear crystal (PDC) cut for type-II phase-matching. Inside the crystal, the pump pulse has a small chance to produce a pair of signal and idler photons, polarized along the o and e axes of the crystal, respectively. The signal and idler beams exit the crystal collinearly. Because the crystal is birefringent and imposes different degrees of dispersion on the o and e polarizations, the group velocity inside it is higher for the idler, which emerges ahead of the signal. This is referred to as “temporal walk-off.”

The signal and idler are next transmitted through a series of birefringent quartz plates. These plates can be inserted separately in various combinations to create a variable delay $\delta\tau$ between the signal and idler wavepackets. The signal and idler then have their polarizations rotated through 45° by the $\lambda/2$ plate, and enter the polarizing

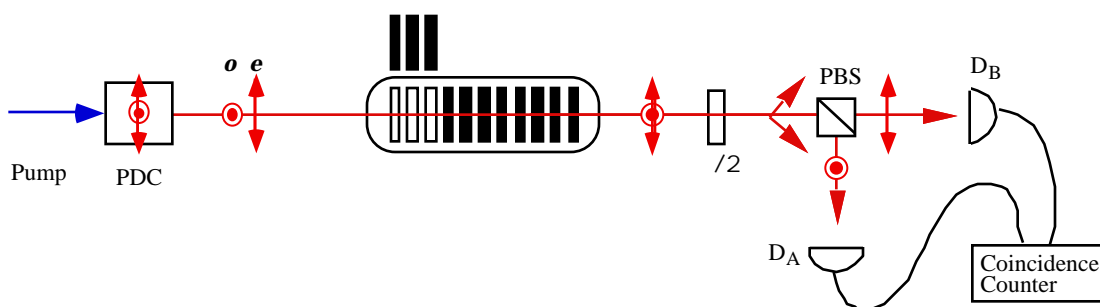


Figure 3.2 The collinear Hong-Ou-Mandel interferometer. The photon pairs are produced by type-II parametric downconversion from an ultrafast pump pulse, and emerge with orthogonal o and e polarizations. Because the downconverter is birefringent, the o -polarized signal lags behind the e -polarized idler. The photons travel through several birefringent quartz plates, imparting a net relative delay of $\delta\tau$ between the signal and idler wavepackets. The $\lambda/2$ plate then rotates both polarizations by 45° , and the photons enter the PBS, which transmits the horizontal polarization while reflecting the vertical. Since the rotated signal and idler polarizations are equally weighted superpositions of these two, each has a 50% probability of being projected into the vertical or horizontal output mode. This leads to two distinct two-photon paths for coincidence counts, whose amplitudes are expected to interfere destructively when $\delta\tau = 0$.

beamsplitter (PBS), which has its selection basis matched to the initial o and e polarizations. Because each photon has a 50% chance of being reflected or transmitted by the PBS, there are two equally probable ways for a pair of photodetectors monitoring the output ports to register coincidence counts. As in the type-I HOMI, the amplitudes for these processes are 180° out of phase with each other, so as to cancel all coincidences in the cases where they are indistinguishable.

In the experiment we record the coincidence counting rate as a function of the delay $\delta\tau$. The extent to which the rate dips down to zero at its minimum is then a measure of the indistinguishability of the coincidence paths.

3.2.2 Quantum state of the light

The quantum state for the downconversion produced by a single pump pulse can be obtained from the appropriate interaction Hamiltonian, by letting the resulting time evolution operator act on the input vacuum state, and truncating the resulting state to the lowest nonvanishing order in the perturbation². The state of the downconverted light in the interaction picture is then

$$\begin{aligned} |\psi\rangle &= |vac\rangle + \eta \delta\omega \int_{\omega_o} \int_{\omega_e} \alpha(\omega_o + \omega_e) (\omega_o, \omega_e) |\omega_o\rangle_o |\omega_e\rangle_e \\ &= |vac\rangle + \eta |\psi^{(1)}\rangle, \end{aligned} \quad (3.8)$$

where the labels o and e denote the polarizations and frequencies of the signal and idler, respectively, T is the interaction time equal to the pump pulse duration, and $\delta\omega$ is the mode spacing. This state is a continuous superposition of two-photon states, in which the probability amplitude for each pair of frequencies to be emitted is the product of the spectral pump envelope, $\alpha(\omega_o + \omega_e)$, and the phase-matching function (ω_o, ω_e) .

² See reference [16]. For an explicit derivation of this state, see Appendix B.

The creation efficiency parameter η is defined as

$$\eta = \frac{g \ell_x \ell_y \ell_z V_0}{i\hbar} \quad (3.9)$$

where the ℓ_m are the dimensions of the interaction region, $|V_0|^2$ is the peak intensity of the pump pulse, and g is a coupling constant between the pump and downconversion modes that contains whatever units are necessary to ensure that η is dimensionless. This state is valid in when the “nondepleted pump” approximation holds, for which we require

$$|\eta|^2 \langle \psi^{(1)} | \psi^{(1)} \rangle < 1. \quad (3.10)$$

The spectral pump envelope is the Fourier transform of the time-dependent part of the classical pump field. The amplitude spectrum of a single pump pulse is assumed to have a normalized gaussian form with bandwidth σ , centered at twice the mean downconversion frequency $2\bar{\omega}$,

$$\alpha(\omega_o + \omega_e) = \frac{2}{\sigma\sqrt{\pi}} e^{-\frac{(\omega_o + \omega_e - 2\bar{\omega})^2}{\sigma^2}}. \quad (3.11)$$

α is real and has units that ensure $|\psi^{(1)}\rangle$ is dimensionless. It is written as $\alpha(\omega_o + \omega_e)$ to remind us that in the long interaction time-limit, only those photons are emitted whose signal and idler frequencies sum to the pump frequency³. Plots of this function for several different bandwidths are displayed in Figure 3.3 (a).

Of course, for a given pump frequency, there are an infinite number of values for ω_o and ω_e that satisfy $\omega_p = \omega_o + \omega_e$. The relative amplitudes for emission of all these possible combinations are determined by the phase-matching function,

$$(\omega_o, \omega_e) = \text{sinc}\left(\frac{1}{2} [k_o(\omega_o) + k_e(\omega_e) - k_p(\omega_o + \omega_e)]L\right). \quad (3.12)$$

³ This satisfies the energy-conserving phase-matching condition. See Appendix B for details.

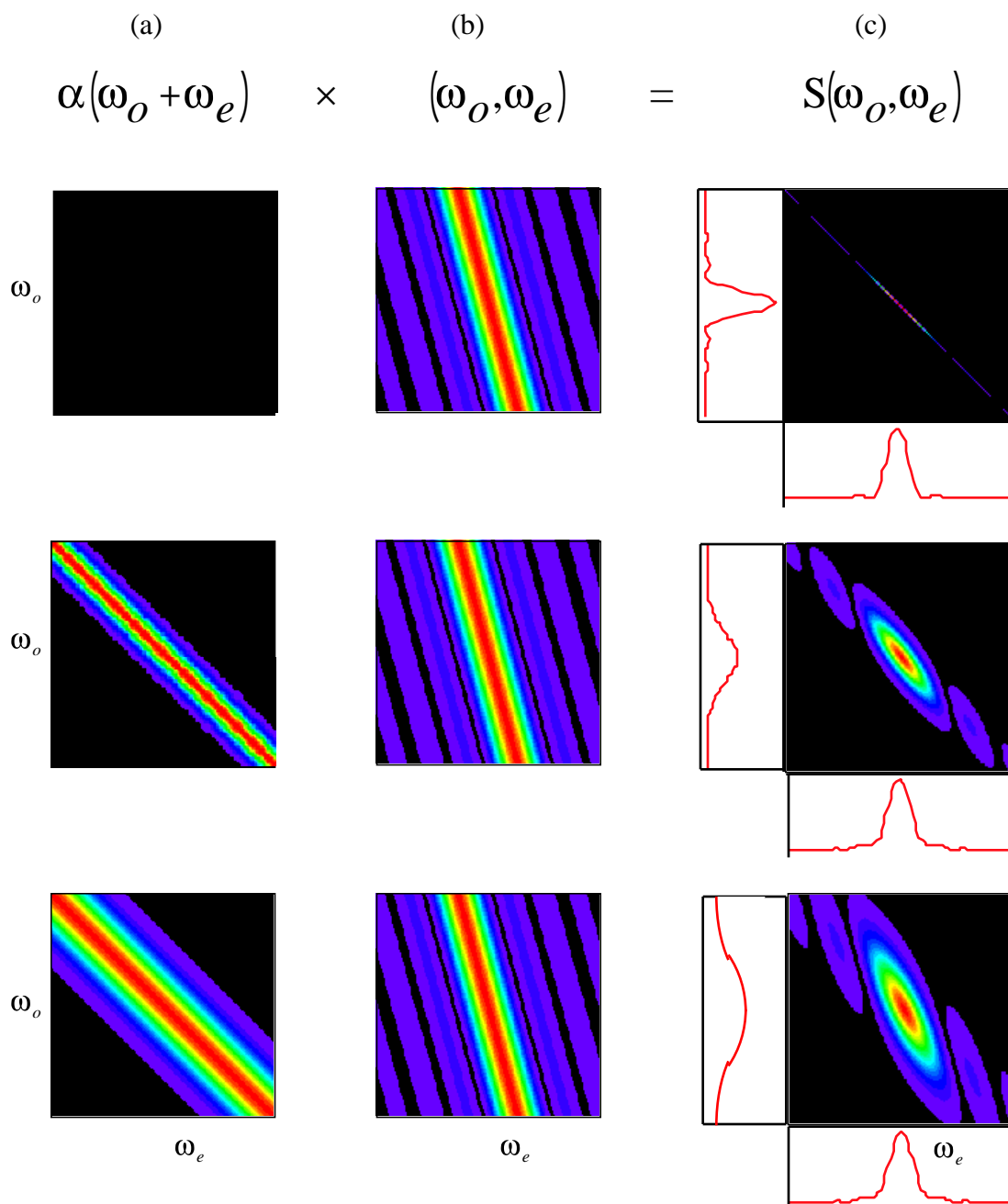


Figure 3.3 Pump envelope function $\alpha(\omega_o + \omega_e)$ for three different values of the pump bandwidth (a) and the phase-matching function (ω_o, ω_e) for BBO (b). As the pump bandwidth gets larger, more of the asymmetric character of (ω_o, ω_e) is revealed in the joint emission amplitude spectrum $S(\omega_o, \omega_e)$ (c). Consequently, the marginal signal and idler spectra are more dissimilar.

where $L = \ell_z$ is the length of the crystal along the direction of propagation. If the PDC is oriented for optimal downconversion at the mean pump, signal, and idler frequencies so that $k_o(\bar{\omega}) + k_e(\bar{\omega}) - k_p(2\bar{\omega}) = 0$, this function may be approximated by

$$\begin{aligned} (\omega_o, \omega_e) \quad & \text{sinc}\left(\frac{1}{2}\left[(\omega_o - \bar{\omega})k_o + (\omega_e - \bar{\omega})k_e - (\omega_o + \omega_e - 2\bar{\omega})k_p\right]L\right) \\ & = \text{sinc}\left(\frac{1}{2}\left[(\omega_o - \bar{\omega})(k_o - k_p) + (\omega_e - \bar{\omega})(k_e - k_p)\right]L\right). \end{aligned} \quad (3.13)$$

The parameters $k_{o,e} \left. \frac{\partial k_{o,e}}{\partial \omega} \right|_{\bar{\omega}}$ and $k_p \left. \frac{\partial k_p}{\partial \omega} \right|_{2\bar{\omega}}$ are the inverse group velocities within the PDC⁴. This function is depicted in Figure 3.3 (b).

Figure 3.3 (c) shows what happens when these two functions are multiplied together to produce the joint two-photon emission amplitude spectrum,

$$S(\omega_o, \omega_e) \propto (\omega_o + \omega_e) (\omega_o, \omega_e). \quad (3.14)$$

The magnitude of this function determines the relative likelihood of emission for the various possible signal and idler frequencies ω_o and ω_e . By integrating over one or the other of these frequencies, we can obtain emission spectra for just the signal or idler wavepackets. We see from these marginal distributions that for a narrowband cw pump, the signal and idler spectra are identical, but for a broadband pump they are not. This asymmetry occurs because the phase-matching function in (3.13) depends on the inverse group velocities k_o and k_e , which are not identical for the two different polarizations within the birefringent type-II crystal. Therefore, the ranges of frequencies determined by $\left. \frac{\partial k_{o,e}}{\partial \omega} \right|_{\bar{\omega}}$ for the signal and idler are not the same. This carries implications for interference, because, in principle, measurement of the frequencies of these photons could sometimes reveal whether it was the signal or the idler that was detected. In other words, the emitted signal and idler photons have become at least partially “spectrally distinguishable” from each other, which reduces the visibility of interference effects.

⁴ For type II downconversion in BBO, the pump must be e -polarized (see Section 1.3.3).

3.2.3 Predicted counting rates

3.2.3.1 Two-photon coincidence probabilities from one pulse

How does this “spectral distinguishability” impact the two-photon interference in our interferometer? Let us calculate the expected rate of coincidence counting for the apparatus described above. For a single pump pulse, the probability that D_A registers a photon within a time interval dt_A centered at time t_A and that D_B registers a photon within dt_B centered at t_B is $p_{AB}(t_A, t_B)dt_A dt_B$. The instantaneous probability density p_{AB} is given by the normally ordered expectation value

$$\begin{aligned} p_{AB}(t_A, t_B; \delta\tau, \theta) &= \langle \Psi | : \hat{E}_A^{(-)}(t_A) \hat{E}_A^{(+)}(t_A) \hat{E}_B^{(-)}(t_B) \hat{E}_B^{(+)}(t_B) : | \Psi \rangle \\ &= \left| \hat{E}_A^{(+)}(t_A) \hat{E}_B^{(+)}(t_B) | \Psi \right|^2, \end{aligned} \quad (3.15)$$

where the dimensions of $\left| \hat{E}_{A,B} \right|^2$ are photons per second. For the moment we are assuming perfect detection efficiency for D_A and D_B . Because of the PBS, the electric field which impinges onto D_A is the sum of the vertical projections of the e and o downconversion fields after they have been time-delayed by the quartz and rotated through 45 degrees by the $\lambda/2$ plate:

$$\hat{E}_A^{(+)}(t; \delta\tau) = \frac{1}{\sqrt{2}} \left[\hat{E}_e^{(+)}(t - \delta\tau) + \hat{E}_o^{(+)}(t) \right]. \quad (3.16)$$

Likewise, the field at D_B is the horizontal projection

$$\hat{E}_B^{(+)}(t; \delta\tau) = \frac{1}{\sqrt{2}} \left[\hat{E}_e^{(+)}(t - \delta\tau) - \hat{E}_o^{(+)}(t) \right] \quad (3.17)$$

The electric field operators for the e and o modes each have Fourier decompositions in terms of their own frequency-specific annihilation operators, given by

$$\hat{E}_{o,e}^{(+)}(t) = \sqrt{\frac{\delta\omega}{2\pi}} \int_{\omega} \hat{a}_{o,e}(\omega) e^{-i\omega t}, \quad (3.18)$$

so that we may rewrite the time-dependent field operators at the detectors as

$$\begin{aligned}\hat{E}_A^{(+)}(t; \delta\tau) &= \sqrt{\frac{\delta\omega}{2\pi}} \frac{1}{\sqrt{2}} \left[\hat{a}_e(\omega) e^{i\omega\delta\tau} + \hat{a}_o(\omega) \right] e^{-i\omega t} \\ \hat{E}_B^{(+)}(t; \delta\tau) &= \sqrt{\frac{\delta\omega}{2\pi}} \frac{1}{\sqrt{2}} \left[\hat{a}_e(\omega) e^{i\omega\delta\tau} - \hat{a}_o(\omega) \right] e^{-i\omega t}.\end{aligned}\quad (3.19)$$

Substituting (3.19) and the state (3.8) into (3.15) and taking the limit $\delta\omega \rightarrow 0$ yields

$$\begin{aligned}P_{AB}(t_A, t_B; \delta\tau) &= \frac{|\eta|^2}{(4\pi)^2} \int_0^\infty d\omega_o d\omega_e \alpha(\omega_o + \omega_e) \left| \langle \omega_o, \omega_e \right. \\ &\quad \left. \times \left\{ e^{-i[\omega_e(t_A - \delta\tau) + \omega_o t_B]} - e^{-i[\omega_e(t_B - \delta\tau) + \omega_o t_A]} \right\} |vac\rangle \right|^2\end{aligned}\quad (3.20)$$

for the instantaneous coincidence probability density. The probability of obtaining a coincidence count regardless of the exact time of arrival for each photon is found by integrating this probability density over all possible t_A and t_B values within the coincidence time. Because this coincidence time (usually tens of ns) is much longer than the duration of the pump pulse (a few hundred fs), we are justified in extending the time limits of integration to $\pm \infty$ and writing

$$P_{AB}(\delta\tau) = \int_{-\infty}^{\infty} dt_A dt_B P_{AB}(t_A, t_B; \delta\tau). \quad (3.21)$$

After substituting (3.20) into this and carrying out the time integration, we obtain the result

$$\begin{aligned}P_{AB}(\delta\tau) &= \frac{|\eta|^2}{2} \int_0^\infty d\omega_o d\omega_e \left| \alpha(\omega_o + \omega_e) \right|^2 \left\{ \left| \langle \omega_o, \omega_e \right. \right. \\ &\quad \left. \left. - \langle \omega_e, \omega_o \rangle \langle \omega_o, \omega_e \rangle e^{i(\omega_o - \omega_e)\delta\tau} \right\}.\end{aligned}\quad (3.22)$$

Because η is small, this probability never approaches 1: we must keep in mind that in the weak-interaction approximation, the most likely outcome is that no downconversion is produced at all.

The first term in (3.22) is an integration of the total two-photon probability density distribution over all frequencies, and represents the total “background” rate of coincidence detection independent of $\delta\tau$. The second term, which contributes only for small values of $\delta\tau$, is the source of the coincidence “dip” observed in the traditional HOMI experiments.⁵ For $\delta\tau = 0$ the coincidence rate reaches zero if

$$\left| \langle \omega_o, \omega_e \rangle \right|^2 = \langle \omega_e, \omega_o \rangle \langle \omega_o, \omega_e \rangle \quad (3.23)$$

over the entire range of frequencies that contribute to the integral in (3.22). As discussed above, this range is set by the bandwidth of the pump spectrum specified by $\alpha(\omega_o + \omega_e)$. Equation (3.23) would be satisfied if the phase-matching function were symmetric under exchange of the signal and idler frequencies; however, we have already noted that the phase-matching function for type-II downconversion does not possess this symmetry. Furthermore, because the range of sum-frequencies allowed by an ultrafast pump is quite broad, the value of $P_{AB}(\delta\tau)$ can be appreciable even at $\delta\tau = 0$, which degrades the interference visibility of the dip.

3.2.3.2 Symmetry and indistinguishability

Why should the two-photon interference visibility be sensitive to the symmetry of $\langle \omega_o, \omega_e \rangle$? We will pause here to examine this question in more detail. Consider the two coincidence processes depicted in Figure 3.4, and suppose for the moment that we

⁵ The complex conjugation of $\langle \omega_o, \omega_e \rangle$ is included for the cases in which the origin is chosen at a point other than the center of the interaction region, leading to a complex-valued phase-matching function. See Appendix B.

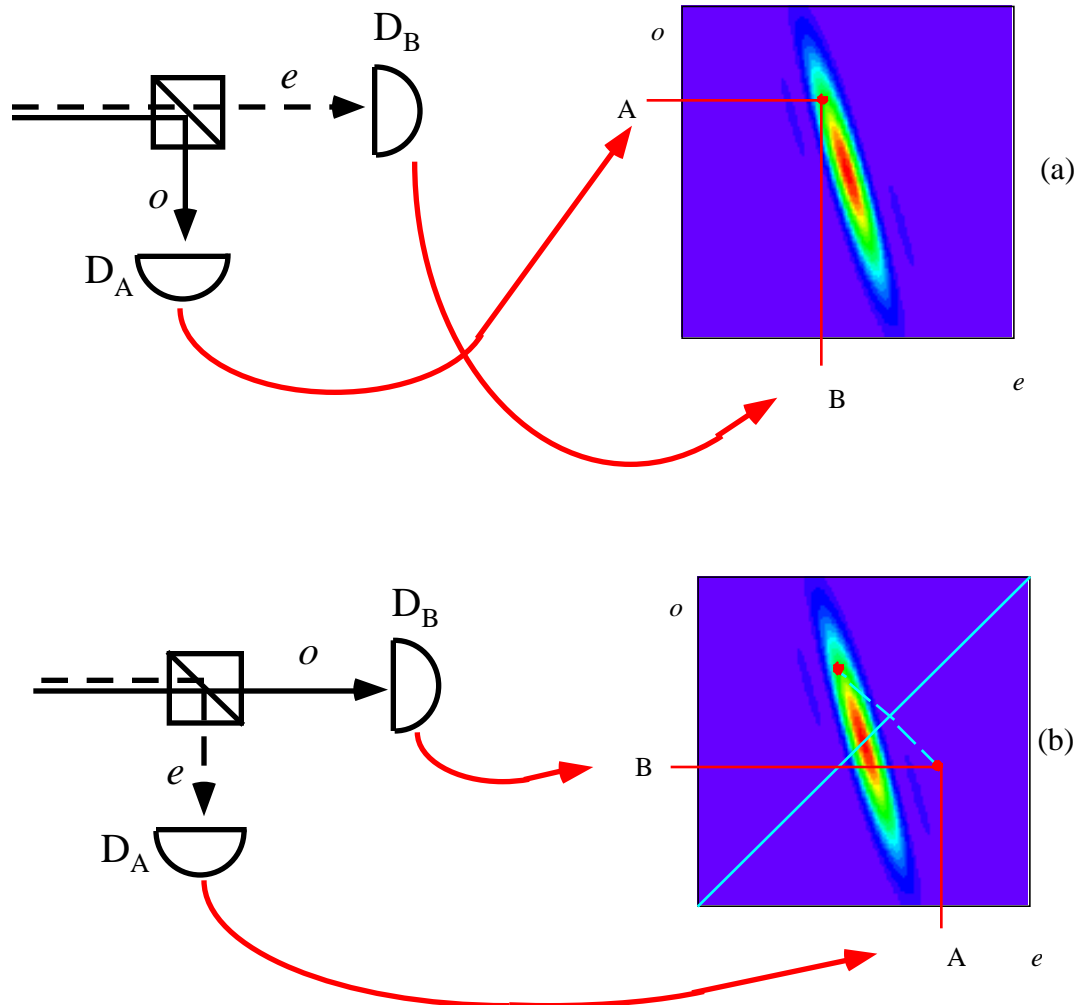


Figure 3.4 Two distinct processes may lead to the detection of a particular pair of frequencies ω_A and ω_B at detectors D_A and D_B : reflection of the idler and transmission of the signal (a) or transmission of the idler and reflection of the signal (b). The amplitudes for the emission of photon pairs with the correct frequencies for these two cases (shown to the right) lie across the line of symmetry $\omega_o = \omega_e$ from each other.

are employing photodetectors D_A and D_B with very high frequency resolution, so that they identify the frequencies of their detected photons as ω_A and ω_B , respectively. This coincidence event could have come from either of two distinct processes. Figure 3.4 (a) shows reflection of the signal (so that $\omega_o = \omega_A$) and transmission of the idler ($\omega_e = \omega_B$): the amplitude for the signal and idlers being emitted with this combination of frequencies is

$$S(\omega_o = \omega_A, \omega_e = \omega_B) = \alpha(\omega_A + \omega_B) (\omega_A, \omega_B). \quad (3.24)$$

Figure 3.4 (b) shows the second process, reflection of the idler ($\omega_e = \omega_A$) and transmission of the signal ($\omega_o = \omega_B$): the two-photon emission amplitude for this combination of frequencies is

$$S(\omega_o = \omega_B, \omega_e = \omega_A) = \alpha(\omega_B + \omega_A) (\omega_B, \omega_A). \quad (3.25)$$

If the amplitudes for these competing two-photon processes are not equal, it is more likely that one or the other of them actually generates the coincidence event. In fact, one might be able to identify the actual signal and idler paths with certainty, if the amplitude for the other set of paths were zero. The degree of exchange symmetry in (ω_o, ω_e) is therefore an indicator of how “spectrally indistinguishable” the possible photon pairs will be from one another, and this is why it controls the degree of “dip” visibility.

Of course, for the experiment we did not use detectors with the high frequency resolution required to make these distinctions. Once again, though, this “indistinguishability in practice”, which comes about from ignoring the spectral “which-path” information after the light has been detected, is not enough to restore the dip visibility. The fact that the two-photon paths are distinguishable, in principle, is all that is required to degrade the interference.

This discussion suggests another approach for improving the interference visibility, namely, modification of the spectral characteristics of the light itself, so that the distinguishing information is lost before the light reaches the detectors. The idea is to use spectral filters to restrict the range of detection frequencies to just those regions where the signal and idler frequencies are most similar -- that is, to the regions where (ω_o, ω_e) is nearly symmetric. The two-photon events that are the most distinguishable would then be the ones that were discarded by the filters before reaching the detector. This method of discarding quantum information to regain interference is very much in the spirit of the quantum eraser, and has even been performed before in the context of polarization measurements in a type I HOMI [2]. However, it is not a true “quantum eraser” in the strict sense, because it does not involve recovery of fringes and antifringes as subensembles of a larger data set via correlation with an auxiliary measurement [17]. In this scenario, it is the interfering particles themselves, the “two-photon entities,” that are being selected or discarded to improve interference.

3.2.3.3 *Coincidence counting rates*

We will now complete our calculations for the expected coincidence counting rates. The photodetectors in our laboratory are not perfectly efficient. We will assign each detector, D_μ , a quantum efficiency $0 < \alpha_\mu < 1$ that reflects the fraction of impinging photons which actually cause a photoelectric pulse to be emitted. In our real apparatus, there will also inevitably be losses due to absorption or unwanted reflections at all of the various optical interfaces. The percentage of emitted photons that arrive in each single-channel of detection will be denoted by a collection efficiency $0 < \beta_\mu < 1$. After multiplying the single-pulse coincidence probability (3.22) by all of these factors,

and by the pulse repetition rate R_p , we have an expression for the expected coincidence counting rate in the experiment:

$$R_{AB}(\delta\tau) = \frac{|\eta|^2}{2} \alpha_A \alpha_B \beta_A \beta_B R_p [B - D(\delta\tau)]. \quad (3.26)$$

Here

$$B = \int_0^{\infty} \int_0^{\infty} d\omega_o d\omega_e |\alpha(\omega_o + \omega_e)|^2 |\alpha(\omega_o, \omega_e)|^2 = \frac{4\sqrt{2\pi}}{\sigma\tau_-} \quad (3.27)$$

is the degree of spectral overlap for the photons created in the two downconversion processes, while

$$\begin{aligned} D(\delta\tau) &= \int_0^{\infty} \int_0^{\infty} d\omega_o d\omega_e |\alpha(\omega_o + \omega_e)|^2 |\alpha(\omega_e, \omega_o)|^2 e^{-i(\omega_e - \omega_o)\delta\tau} \\ &= 2B \frac{\sqrt{2\pi}}{\sigma(\tau_o + \tau_e)} \operatorname{erf} \left[\frac{\sigma(\tau_o + \tau_e)}{2\sqrt{2}} \left(\frac{1}{2} - \frac{|\delta\tau|}{\tau_-} \right) \right] \operatorname{rect} \left[\delta\tau; \frac{-\tau_-}{2}, \frac{\tau_-}{2} \right] \end{aligned} \quad (3.28)$$

is the ‘‘dip’’ generating term that depends critically on the symmetry of α . In these expressions,

$$\tau_{o,e} = L \left. \frac{\partial k_p}{\partial \omega} \right|_{\omega} - \left. \frac{\partial k_{o,e}}{\partial \omega} \right|_{\omega} \quad (3.29)$$

is the maximum difference between the group delays experienced by the pump pulse and the o -wave or e -wave, after traveling the entire length of the PDC, and

$$\tau_- = \tau_e - \tau_o = L \left. \frac{\partial k_o}{\partial \omega} \right|_{\omega} - \left. \frac{\partial k_e}{\partial \omega} \right|_{\omega} \quad (3.30)$$

is the maximum temporal walk-off between the signal and idler photons. It is convenient to re-express (3.26) in the form

$$R_{AB}(\delta\tau) = R_{AB0} \frac{1}{2} - \frac{\sqrt{2\pi}}{\sigma(\tau_o + \tau_e)} \operatorname{erf} \frac{\sigma(\tau_o + \tau_e)}{2\sqrt{2}} \frac{1}{2} - \frac{|\delta\tau|}{\tau_-} \operatorname{rect} \delta\tau; \frac{-\tau_-}{2}, \frac{\tau_-}{2} \quad (3.31)$$

where

$$R_{AB0} = |\eta|^2 \alpha_A \alpha_B \beta_A \beta_B R_p B \quad (3.32)$$

is the number of pairs per second that would be counted by the detectors without the PBS in place. The nominal coincidence counting for $|\delta\tau| > \tau_-/2$ (outside the dip) is half this value, which reflects the fact that in the absence of quantum interference effects, only two of the four possibilities at the PBS lead to coincidence counts (double transmission and double reflection).

From (3.31), we see that the pump bandwidth plays a significant role in the shape of the coincidence dip. The crystal length L also affects this shape, since it determines the values of τ_o, τ_e , and τ_- . To illustrate the effects of varying these two parameters, $R_{AB}(\delta\tau)$ is plotted for several different values of the dimensionless product $\sigma\tau_-$ in Figure 3.5. For the cw case, the coincidence probability falls all the way to zero in the familiar triangle shape reported for earlier type-II HOMI experiments [10]. As $\sigma\tau_-$ increases, more and more of the asymmetric character of (ω_o, ω_e) is “revealed” by multiplication with larger pump bandwidths, and the minimum value is increased from zero.

3.3 Experimental procedure and results

3.3.1 Apparatus

The experiment is depicted in Figure 3.6. The output of a modelocked Ti:sapphire laser was frequency-doubled by focusing onto a .7 mm BBO crystal, cut and aligned for type-I phase-matching. In the type-I upconversion process, two

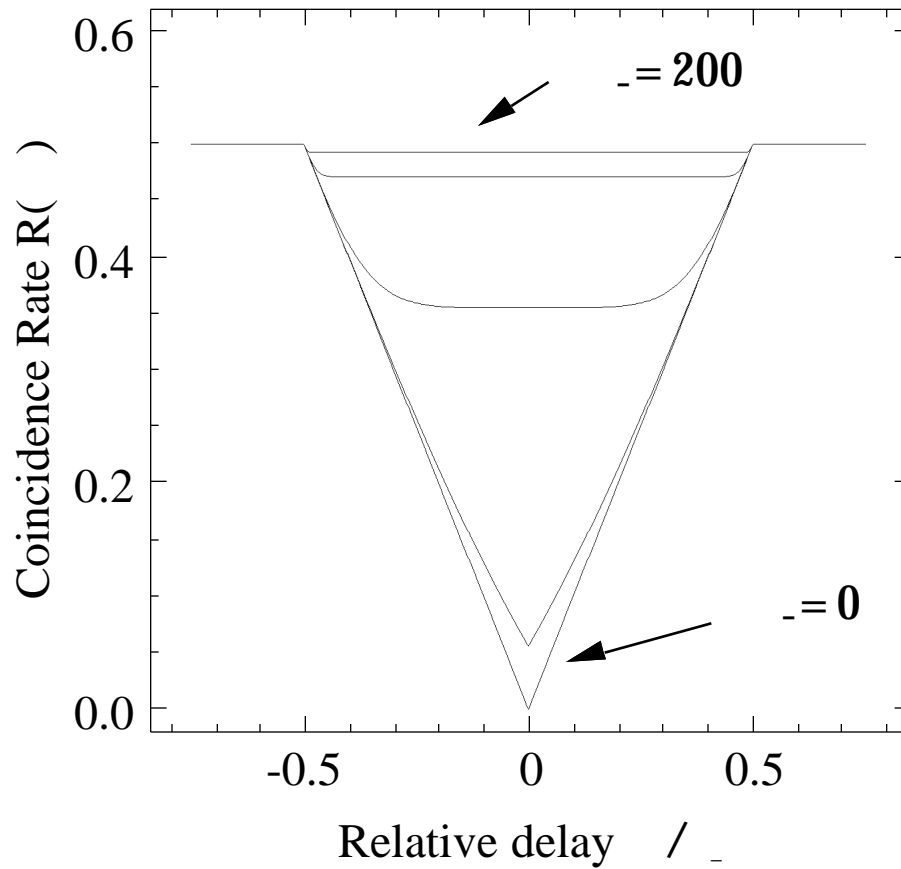


Figure 3.5 Predicted coincidence counting rate for several different values of the pump bandwidth / temporal walkoff product $\sigma\tau$. The two-photon interference dip is degraded as this product increases. Plots are shown for $R_{AB0} = 1$ (Adapted from [16]).

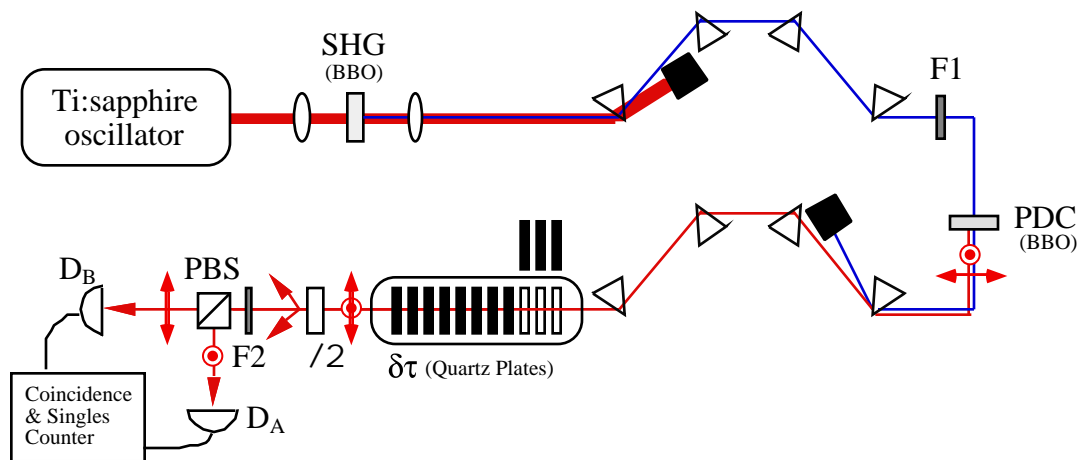


Figure 3.6 Experimental realization of the ultrafast pulse-pumped type-II collinear Hong-Ou-Mandel interferometer. The second-harmonic was separated from the fundamental beam by a sequence of prisms before impinging onto the .8 mm long BBO downconverter. Another prism sequence separated the downconversion from the residual pump. The quartz plates imposed a variable delay between the signal and idler photons. Their polarizations were rotated through 45° by a suitably oriented half-wave plate before they encountered the polarizing beamsplitter (PBS). Avalanche photodiodes D_A and D_B monitored the horizontally and vertically polarized output ports of the PBS, and the electronic pulses from these detectors are fed to a coincidence counter with a 9 ns coincidence window.

vertically-polarized o-wave photons at the fundamental frequency are annihilated to create one horizontally-polarized e-wave photon at twice this frequency. The Ti:sapphire radiation had a mean wavelength of 810 nm, with a bandwidth of 10 nm, and a repetition rate of 80 MHz. The frequency-doubled pulses had a mean wavelength of 405 nm, and measured bandwidth of $\lambda_p = 3 \text{ nm}$, corresponding to a frequency amplitude bandwidth of $\sigma = 34.5 \text{ ps}^{-1}$. The FWHM duration of a transform-limited gaussian pulse with these characteristics is 97 fs. To test the dip visibility as a function of $\sigma\tau$, an optional bandpass filter (F1) was placed in the pump beam to restrict this bandwidth to $\lambda_p = .8 \text{ nm}$, or $\sigma = 9.2 \text{ ps}^{-1}$.

The upconverted pump pulses were collimated by a second lens and separated from the fundamental Ti:sapphire beam with a sequence of four prisms, each of which was cut so that light incident at Brewster's angle also experienced minimum deviation at the output. The first prism introduced a frequency-dependent angular spread, so that the 810 nm beam could be blocked while the 405 nm beam continued on. The second prism halted the angular spread, so that the 810 nm beam emerged with all of its frequency components traveling parallel to each other, but separated in space. This "spatial chirp" was undone by the last two prisms, which resulted in a collimated pump beam with no transverse separation of the frequency components.

The pump beam was then directed onto the downconversion medium, a BBO crystal 1 mm in length, cut and aligned for type-II phase-matching with its extraordinary axis parallel to the horizontal pump polarization. The collinear downconversion was selected with apertures and separated from the residual pump radiation with another dispersion-compensated series of prisms.

The delay line for the collinear Hong-Ou-Mandel interferometer consisted of a series of antireflection-coated quartz plates, oriented so that their fast and slow axes

were aligned with the signal and idler polarizations. By inserting different numbers of plates with different orientations, we were able to vary the delay between the signal and idler wavepackets ($\delta\tau$) in discrete steps. The plates imposed a relative delay of 32 fs per mm of quartz inserted.

The downconverted photons then passed through a zero-order half-wave plate ($\lambda/2$) oriented with its optical axis at an angle of 22.5° to the o polarization. This had the effect of rotating the o and e polarizations of the signal and idler by 45° . As a result, both photons had a 50% chance to be reflected or transmitted by the subsequent polarizing beamsplitter (PBS). The output ports of the PBS were monitored by two EG&G SPCM 200-PQ avalanche photodiodes (D_A and D_B). The light was focused onto the small active areas of these detectors with the help of long focal-length (~ 10 cm) lenses. Broadband interference filters ($\Delta\lambda \sim 20$ nm) were placed in front of each detector to reduce spurious background counts. An optional filter (F2) could be placed in the path of the downconversion to reduce the bandwidth of the downconverted light to 10 nm; this was done in the hopes of improving the visibility with the “quantum-eraser” type scheme discussed in Section 4.2.3.2.

The pulses from the detectors were fed into discriminators which emitted 4.5 ns-long NIM pulses that were triggered on the leading edge of each input pulse. These pulses were then fed to a coincidence “AND” gate, which sent out a NIM pulse whenever both of its inputs registered a “logical 1.” The 4.5 ns duration of the input pulses implied that the AND gate would put out a signal whenever both pulses arrived within 9 ns of each other, a coincidence time much longer than the coherence time of the downconverted light (less than 100 fs), which justifies the steps taken before Eq. (3.21) above. Coincidence counts were recorded by computer for various lengths of quartz inserted into the beam. The maximum length of quartz available was 12 mm,

corresponding to a relative delay of $\delta\tau = .384$ ps . This was more than enough to cover the dip width of $\tau_- = .152$ ps expected for our BBO crystal.

3.3.2 Results

3.3.2.1 Data taken with the broadband pump

The coincidence counts registered as a function of $\delta\tau$ are shown in Figure 3.7 (a), along with the theoretical curve corresponding to $\sigma = 34.5$ ps⁻¹, $\tau_o = .061$ ps, and $\tau_e = .213$ ps (corresponding to the range of pump wavelengths $\lambda_p = 3$ nm and BBO crystal length $L = .8$ mm), so that $\sigma\tau_- = 5.25$. The theoretical curve has been normalized to match the nominal counting rates for the data outside the dip. As predicted, the two-photon interference visibility is not very good, with the minimum counting rate equal to about half the rate outside the dip. The dip is not centered at $\delta\tau = 0$ because it requires about 2.5 mm of quartz to correct for the temporal walk-off separation between the signal and idler after traveling half the length of the BBO crystal, $\tau_-/2 = .076$ ps.

3.3.2.2 Data taken with a narrowband pump

In keeping with our earlier discussions of the role of pump bandwidth, Figure 3.5 indicates that if the product $\sigma\tau_-$ is reduced, the visibility of the dip is improved as a consequence of the smaller range of frequencies contributing to the integral in (3.22). To check this, we inserted the filter F1 into the pump. The .8 nm range of wavelengths transmitted by F1 corresponds to a pump bandwidth of $\sigma = 9.2$ ps⁻¹, so that the bandwidth / temporal walk-off product is $\sigma\tau_- = 1.40$. The data are presented in Figure 3.7 (b), together with the theoretical counting rate for these parameters. The predicted

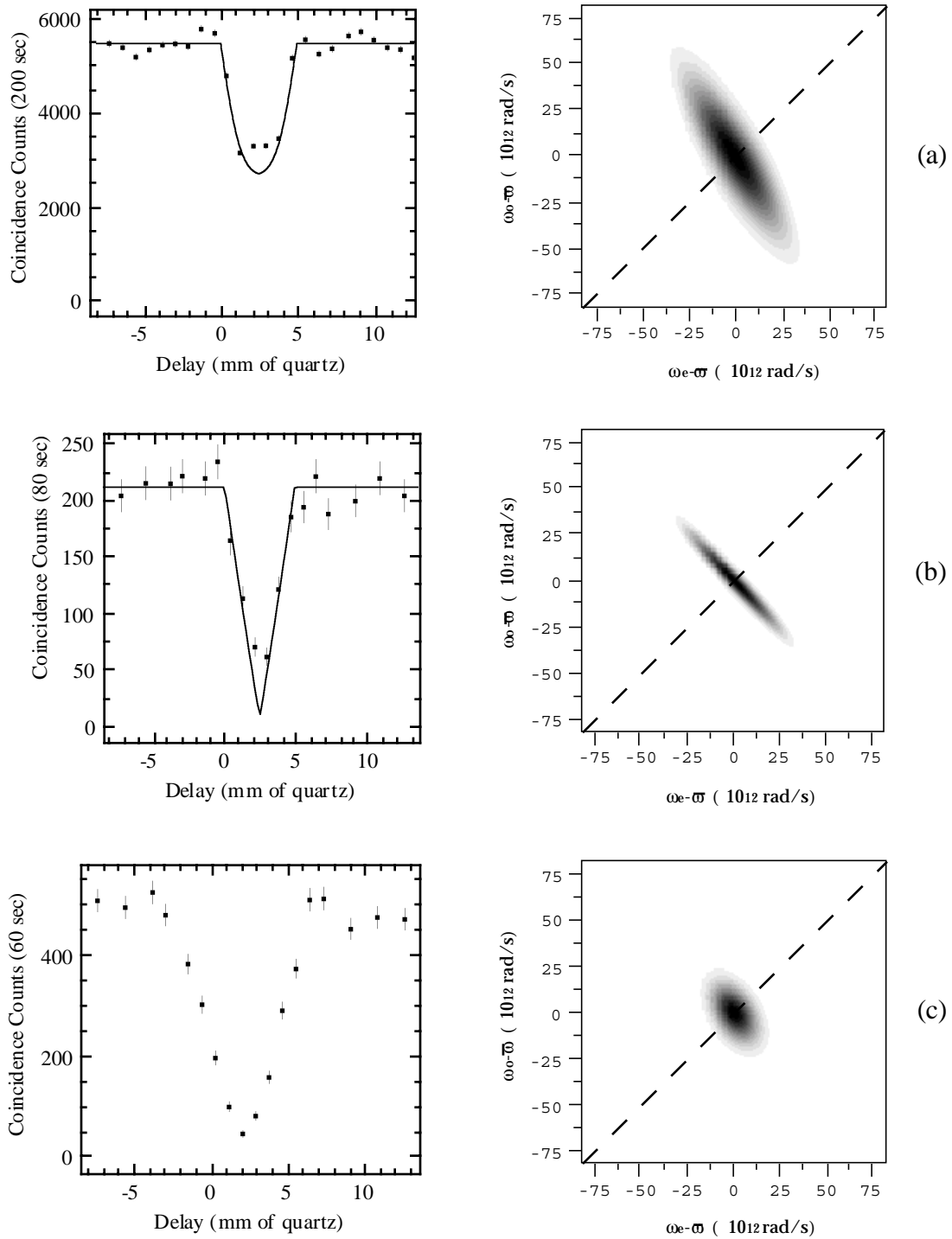


Figure 3.7 Experimental data and joint emission amplitude spectrum seen by the detectors for pump bandwidths of 3 nm (a) 0.8 nm (b), and 3 nm with 10 nm bandpass filters in front of the detectors (c). Data reproduced from [12], spectra from [16].

improvement in the fourth-order visibility is borne out by the data, although in both cases the measured minimum counting rates are higher than expected from the theory.

3.3.2.3 Data taken with the broadband pump and detector filters

Finally, we recorded coincidence counts with the broad pump bandwidth restored, but with the spectral filter F2 inserted to restrict the range of signal and idler wavelengths that reached the detector. These counts are shown in Figure 3.7 (c). The photon pairs that emerged from this filter were much less spectrally distinguishable from each other in principle (see Section 4.2.3.2), and the result was a much improved interference dip, although the counting rates were significantly reduced.

3.4 Discussion

3.4.1 Comparison of spectral filtering in pulsed vs. cw experiments

The use of spectral filters is not uncommon in this type of experiment, in which a coincidence rate is measured for different values of the relative delay between the signal and idler [1,10]. However, the earlier experiments differed from the present one by their use of cw pumping; in that case, the filters are not needed for high visibility in principle (see Section 4.1.2.), either in the type-I or type-II case. For those experiments, the filters were helpful in a practical sense, in that they increased the coherence times of the photons, which relaxed the stability requirements, but the minimum coincidence rate is predicted to reach zero for those cases even without spectral filtering. As seen in Figure 3.3, this is a consequence of the fact that the cw-pump “window” does not reveal the asymmetric character (if any) of the phase-matching function, so that the spectral two-photon emission amplitudes $S(\omega_{\text{signal}}, \omega_{\text{idler}})$ are always symmetric under

exchange of their arguments; this renders the photon pairs spectrally indistinguishable even without filters.

In contrast, the downconversion filter was required for good visibility in our experiment with the broadband pump source. In this case, the spectral filtering constituted a kind of “quantum erasing” of the distinguishing spectral information after it had been created, in that the most distinguishable pairs were discarded before they reached the detectors. The part of the two-photon spectrum which survives this filtering is the part that appears the most symmetric under exchange of ω_o and ω_e , as shown in Figure 3.7 (c).

3.4.2 Interpretation of the results

From the evidence presented above it is clear that one must proceed with caution when performing quantum interference experiments with ultrafast-pumped type-II downconversion. As in any fourth-order interference experiment, the visibility is directly dependent on the indistinguishability in principle of the interfering two-photon detection processes. For the HOMI, this indistinguishability is expressed by the symmetry of the two-photon emission amplitude, $S(\omega_o, \omega_e)$, under exchange of its arguments. The consequence of pumping a birefringent type-II medium with a broadband pump pulse is to create an emission source which does not obey this symmetry very well. The effects of this asymmetry on the interference “dip” visibility are evident in our data.

We also showed that the interference may be restored by spectrally filtering the pump pulses, which is tantamount to moving towards cw-pumping: the smaller the bandwidth allowed for the pump, the better will be the dip visibility. But the consequence of this is that the pump pulses are extended in time, so that the benefits of synchronization for multiple sources may be lost.

Finally, we showed that interference visibility may be recovered if the downconverted light is filtered before it reaches the detectors. Here again, the narrower the passband of the spectral filters, the longer the temporal extent of the signal and idler wavepackets. While this might be helpful when one wishes to synchronize the emission from multiple sources, the coincidence count rates are then considerably reduced.

In the next chapter we will take up another solution to the problem of reduced visibility in the type-II HOMI, in which the emission spectrum is symmetrized at the source. This method allows us to recover the dip interference visibility without loss of timing resolution or reduced counting rates.

References for Chapter 3

- [1] C. K. Hong, Z. Y. Ou, and L. Mandel, Phys. Rev. Lett. **59**, 2044 (1987).
- [2] P. G. Kwiat, A. M. Steinberg, and R. Y. Chiao, Phys. Rev. A **45**, 7729 (1992).
- [3] Z. Y. Ou and L. Mandel, Phys. Rev. Lett. **61**, 54 (1988).
- [4] Z. Y. Ou, X. Y. Zou, and L. J. Wang, Phys. Rev. A **42**, 2957 (1990).
- [5] A. M. Steinberg, P. G. Kwiat, and R. Y. Chiao, Phys. Rev. Lett. **71**, 708 (1993).
- [6] R. Y. Chiao, P. G. Kwiat, and A. M. Steinberg, Scientific American (8), 52 (1993).
- [7] Y. H. Shih and A. V. Sergienko, Phys. Lett. A **186**, 29 (1994).
- [8] Y. H. Shih and A. V. Sergienko, Phys. Lett. A **191**, 201 (1994).
- [9] T. B. Pittman, Y. H. Shih, A. V. Sergienko, and M. H. Rubin, Phys. Rev. A **51**, 3495 (1995).
- [10] A. V. Sergienko, Y. H. Shih, and M. H. Rubin, J. Opt. Soc. Am. B **12**, 859 (1995).
- [11] T. B. Pittman *et al.*, Phys. Rev. Lett. **77**, 1917 (1996).
- [12] W. P. Grice, R. Erdmann, I. A. Walmsley, and D. Branning, Phys. Rev. A **57**, R2289 (1998).
- [13] W. P. Grice and I. A. Walmsley, Phys. Rev. A **56**, 1627 (1997).
- [14] G. Di Giuseppe, L. Haiberger, and F. De Martini, Phys. Rev. A **56**, R21 (1997).
- [15] T. E. Keller and M. H. Rubin, Phys. Rev. A **56**, 1534 (1997).
- [16] W. P. Grice, Ph.D. thesis, University of Rochester, 1998 (unpublished).
- [17] P. G. Kwiat, A. M. Steinberg, and R. Y. Chiao, Phys. Rev. A **49**, 61 (1994).

Chapter 4

Engineering spectral indistinguishability

4.1 Introduction

In the previous chapter, we saw that the visibility of two-photon interference in a Hong-Ou-Mandel interferometer was reduced when the interferometer was based on type II downconversion pumped by a train of ultrafast pulses. This reduction in visibility was attributed to the presence of spectral information in the two-photon wavepackets, which served as a “which-path” identifier for the double-detection process. The two double-paths which could lead to a coincidence count (double reflection or double transmission) were rendered almost completely distinguishable, and hence, incapable of effectively interfering with each other. In those cases, what allowed us to identify “which path” was actually the asymmetric character of the joint emission amplitude spectrum for the downconversion, $S(\omega_o, \omega_e)$. We saw that if this function was made more symmetric, by narrowing the pump bandwidth or by restricting the photodetectors to look only at the most symmetric region of the spectrum, the interference “dip” visibility could be restored.

However, because both of these methods use narrow bandwidth filters, which have the effect of lengthening the pulses, they eliminate most of the precise timing information that is the main reason for using ultrafast pulses in the first place. Additionally, the counting rates suffer substantial losses after the light has been attenuated by these filters. This makes filtering an even more unattractive solution to the problem.

The new approach, then, is this: rather than throw away the parts of the emission which are not symmetric, we could attempt to symmetrize the entire joint emission amplitude spectrum for all the pairs at the source. The asymmetry arises from the different dispersion characteristics for the *e*-ray and the *o*-ray within the downconversion medium: these are crystal properties which we are not at liberty to alter. But we can make use of the fact that for any function of two variables $g(x, y)$, it is always possible to construct the function

$$g(x, y) = g(x, y) + g(y, x), \quad (4.1)$$

which is symmetric under exchange of the arguments x and y by definition, regardless of the symmetry properties of $g(x, y)$. Symmetrizing the joint amplitude emission spectrum in this manner implies adding a second downconversion process to the first one, with the signal and idler polarizations exchanged, so that the total amplitude for emission from the system is governed by the new, symmetric joint amplitude emission spectrum

$$S(\omega_s, \omega_i) = S(\omega_s, \omega_i) + S(\omega_i, \omega_s). \quad (4.2)$$

Note that if we want the emission amplitudes to add like this, we must add the second process to the first in such a way that it is ultimately impossible to distinguish which of the two downconversion processes generates each photon pair (see Figure 4.1). This coherent addition was carried out in the laboratory, and new interference data were collected for the downconverted pairs having the new emission spectrum. The result was that the interference “dip” visibility for these new photon pairs was significantly improved, without any reduction in counting rates or bandwidth.

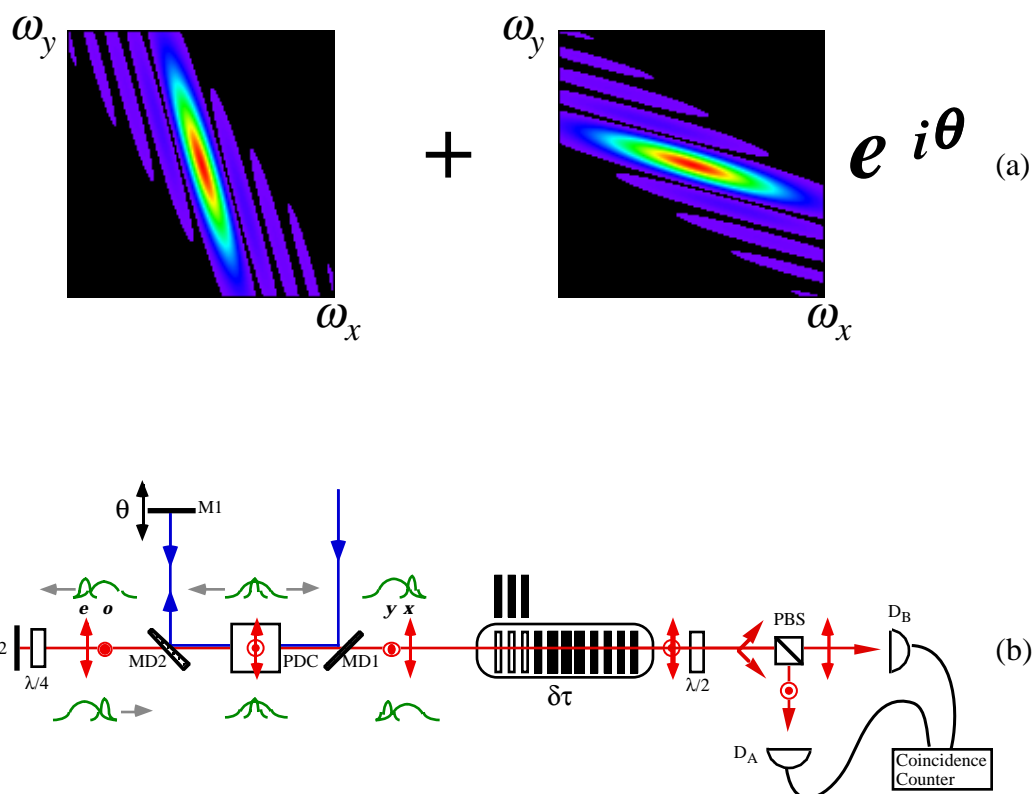


Figure 4.1 Conceptual arrangement for the addition of two fields produced by downconversion processes, in which the resulting photon pairs could have come from either process with equal probability. The addition is coherent if the “which-process” origin of the pairs cannot be determined even in principle; in this case, the photon pairs carry a joint emission amplitude spectrum that is the superposition of the spectra for each process (a). A scheme for producing this addition is shown in (b). A pump pulse passes through the parametric downconverter (PDC) and is separated from the downconverted light by means of a dichroic mirror MD2. The pump pulse is reflected back into the PDC by mirror M1. The signal and idler beams are also reflected back via M2, with their polarizations exchanged by the $\lambda/4$ plate. The photon pairs which ultimately emerge from the downconverter could have been generated on either the first or second pass of the pump through the crystal. The downconversion from this modified source is separated from the outgoing pump beam by MD1 and sent through a collinear Hong-Ou-Mandel interferometer to a pair of photodetectors, which produce coincidence counts.

4.2 Schematic and theory

4.2.1 Schematic of the experiment

The coherent addition depicted in Figure 4.1 (a) can be accomplished experimentally by using the scheme shown in Figure 4.1 (b). The pump pulse enters the parametric downconverter (PDC) from the right, possibly creating an orthogonally polarized, frequency degenerate pair of photons somewhere inside. After exiting the PDC, the pump is reflected by a dichroic mirror (MD2), while the lower-wavelength downconverted light is transmitted through it. The pump is normally incident on a mirror (M1) that reflects it back into the PDC. The signal and idler, meanwhile, are sent through a $\lambda/4$ plate and then onto a mirror (M2) at normal incidence. They are then reflected back through the $\lambda/4$ plate and into the PDC, overlapping with the pump pulse in the center of the crystal.

The $\lambda/4$ plate is oriented with its optical axis at 45 degrees to the “ o ” and “ e ” axes of the PDC. After their first pass through this plate, the polarizations of the signal and idler photons are converted from linear o and e to circular LHC and RHC states, respectively. After reflection from M2, these circular signal and idler polarizations are then converted to e and o linear polarizations, respectively, by passing the light through the $\lambda/4$ plate a second time. The net result is a 90 degree rotation of both the signal and idler polarizations, effectively exchanging their roles as the e and o polarized photons. As a result, the e -polarized light that is sent back into the downconverter actually carries the spectrum belonging to the original o polarization, and vice versa; more generally, the joint emission amplitude spectrum for these pairs is switched from $S(\omega_o, \omega_e)$ to $S(\omega_e, \omega_o)$. Interestingly, this switch also has the effect of canceling the temporal walk-off for photon pairs emitted near the center of the crystal: the photon with the fast o polarization on the way out will have the slow e polarization on the way back in.

This system functions as a Michelson interferometer, with the dichroic mirror MD2 playing the role of the central beamsplitter, separating and recombining the “red arm” and “blue arm.” Here, though, the interfering pathways begin and end at the center of the PDC, not at the beamsplitter. With the arms properly aligned, and with their optical path lengths balanced to within the coherence time of the pump, it becomes impossible in principle to discern whether the downconverted light that ultimately emerges from the PDC is generated from the first or the second pass of the pump pulse through the crystal. The resulting o and e -polarized photon pairs therefore carry a superposition of the joint emission amplitude spectra for each process, given by

$$S(\omega_o, \omega_e) = S(\omega_o, \omega_e) + e^{i\theta} S(\omega_e, \omega_o), \quad (4.3)$$

where $S(\omega_o, \omega_e)$ refers to the fields generated on the first pass, $S(\omega_e, \omega_o)$ to those generated on the second, and

$$\theta = k_s(\omega_s)\ell_{signal} + k_i(\omega_i)\ell_{idler} - k_p(\omega_p)\ell_{pump} \quad (4.4)$$

is the total phase difference between the pairs generated on the first or second pass.

This phase difference can be varied by changing ℓ_{pump} , the length of the blue arm. For suitable values of θ ($0, \pm 2\pi, \dots$) the joint emission amplitude spectrum can be made symmetric in accordance with (4.2).

After emerging from the PDC, the downconverted photons are separated from the pump with another dichroic mirror and sent into the common-path Hong-Ou-Mandel interferometer. This consists of a controllable birefringent delay line ($\delta\tau$), a $\lambda/2$ plate, a polarizing beamsplitter (PBS), and a pair of photodetectors (D_A, D_B). The x-polarized photon is delayed by an amount $\delta\tau$ relative to the y-polarized photon before entering the PBS. The $\lambda/2$ plate rotates both the x and y polarizations by 45 degrees: each photon may then be either reflected or transmitted at the PBS, with equal

probability. A coincidence count at the detectors could have come from transmission of the x and reflection of the y, or reflection of the x and transmission of the y-polarized photons. As in the previous chapter, these two coincidence processes can interfere with each other, producing a “dip” in the coincidence counting rate as $\delta\tau \rightarrow 0$.

4.2.2 Quantum state of the light

The quantum state describing the photon pairs created by a single pump pulse can be obtained in the same fashion as in the previous chapter, but using a two-stage evolution in the interaction picture to describe the first and second downconversion processes¹. The state of the downconverted light emerging from the PDC is then

$$\begin{aligned} |\psi\rangle &= |vac\rangle + \eta \delta\omega_{\omega_o, \omega_e} \alpha(\omega_o + \omega_e) \left[|\omega_o\rangle_x |\omega_e\rangle_y - e^{i\theta} |\omega_o\rangle_y |\omega_e\rangle_x \right] \\ &= |vac\rangle + \eta |\psi^{(1)}\rangle, \end{aligned} \quad (4.5)$$

where we now use the labels x and y to denote the two orthogonally polarized output modes, but retain the e and o labels for the frequencies. θ is as defined in (4.4); for the moment, we will treat θ as being frequency-independent over the bandwidth of the signal, idler, and pump photons. As always, the dimensionless creation efficiency parameter η is defined by

$$\eta = \frac{gV_0 l_x l_y l_z}{i\hbar} \quad (4.6)$$

where l_x, l_y, l_z are the dimensions of the interaction region, $|V_0|^2$ is the peak intensity of the pump pulse, and g is a coupling constant between the pump and downconversion modes. Once again, we are restricting our calculations to the “nondepleted pump” regime, in which we assume

¹ See reference [1]. For an explicit derivation of this state and its normalization, see Appendix C.

$$|\eta|^2 \langle \psi^{(1)} | \psi^{(1)} \rangle \ll 1 . \quad (4.7)$$

As in the previous chapter, the spectrum of a single pump pulse is assumed to have a normalized gaussian form with bandwidth σ , centered on the frequency $2\bar{\omega}$,

$$\alpha(\omega_o + \omega_e) = \frac{2}{\sigma\sqrt{\pi}} e^{-\frac{\omega_o + \omega_e - 2\bar{\omega}}{\sigma}} , \quad (4.8)$$

while the phase-matching function is given by

$$(\omega_o, \omega_e) = \text{sinc} \left[k_o(\omega_o) + k_e(\omega_e) - k_p(\omega_o + \omega_e) \right] \frac{L}{2} . \quad (4.9)$$

4.2.3 Predicted counting rates

4.2.3.1 Single-channel counts

Our experiment measured both single-channel and coincidence counts as the quartz delay $\delta\tau$ and phase θ were varied; we will begin here by calculating the single-channel counting rate at detector D_A as a function of these two parameters. For a single pump pulse, the probability that detector D_A registers a photon within a time interval dt around the time t is $p_A(t)dt$, with the instantaneous probability density given by

$$p_A(t; \delta\tau, \theta) = \langle \psi | \hat{E}_A^{(-)}(t) \hat{E}_A^{(+)}(t) | \psi \rangle = \left| \hat{E}_A^{(+)}(t) | \psi \rangle \right|^2 . \quad (4.10)$$

Here $|\hat{E}_A|^2$ is in photons per second, and we are assuming perfect detection efficiency for D_A .

As in Chapter 4, we may rewrite the instantaneous field operator at the detector as a Fourier decomposition of the polarization components of the signal and idler modes projected onto D_A by the $\lambda/4$ plate and PBS:

$$\hat{E}_A^{(+)}(t; \delta\tau) = \sqrt{\frac{\delta\omega}{2\pi}} \int_{\omega} \frac{1}{\sqrt{2}} \left[\hat{a}_x(\omega) e^{i\omega\delta\tau} + \hat{a}_y(\omega) \right] e^{-i\omega t} . \quad (4.11)$$

Substituting (4.11) and the state (4.5) into (4.10) and carrying out the action of each annihilation operator onto the state yields

$$p_A(t; \delta\tau, \theta) = \frac{|\eta|^2 (\delta\omega)^3}{4\pi} \Big|_{\omega_o, \omega_e} \alpha(\omega_o + \omega_e) (\omega_o, \omega_e) \times \left\{ e^{-i\omega_o(t-\delta\tau)} |\omega_e\rangle_y + e^{-i\omega_e t} |\omega_o\rangle_x - e^{i\theta} e^{-i\omega_e(t-\delta\tau)} |\omega_o\rangle_y - e^{i\theta} e^{-i\omega_o t} |\omega_e\rangle_x \right\}^2 \quad (4.12)$$

for the instantaneous probability density. The total photodetection probability accumulated over all times is

$$P_A(\delta\tau, \theta) = \int dt p_A(t; \delta\tau, \theta). \quad (4.13)$$

Substituting (4.12) into (4.13) and carrying out the required Hermitian conjugation and integration gives the result

$$P_A(\theta) = |\eta|^2 2 \{ B - K \cos(\theta) \} \quad (4.14)$$

where, in the limit $\delta\omega \rightarrow 0$,

$$B = \int_0^{\infty} \int_0^{\infty} d\omega_o d\omega_e |\alpha(\omega_o + \omega_e)|^2 (\omega_o, \omega_e)^2 = \frac{4\sqrt{2\pi}}{\sigma\tau} \quad (4.15)$$

and

$$K = \int_0^{\infty} \int_0^{\infty} d\omega_o d\omega_e |\alpha(\omega_o + \omega_e)|^2 (\omega_e, \omega_o) (\omega_o, \omega_e) = 2B \frac{\sqrt{2\pi}}{\sigma(\tau_o + \tau_e)} \operatorname{erf} \frac{\sigma(\tau_o + \tau_e)}{4\sqrt{2}} \quad (4.16)$$

is the degree of spectral overlap for the photons created in the two downconversion processes. Once again, $\tau_o = L \left. \frac{\partial k_p}{\partial \omega} \right|_{2\omega} - \left. \frac{\partial k_o}{\partial \omega} \right|_{\omega}$ is the maximum difference between the group delays experienced by the pump pulse and the o -wave (after traveling the entire

length of the PDC), τ_e is the analogous quantity for the e -wave, and $\tau_- = \tau_e - \tau_o$ is the maximum group delay between o -wave and the e -wave.

Note that if (ω_o, ω_e) were completely symmetric, then K would equal B by definition, and the visibility of the single-channel interference governed by (4.14) would be 100%. Once again, we see a case in which interference visibility is reduced as a consequence of the asymmetry of (ω_o, ω_e) . This will be discussed in more detail in section 5.4.3, after the experimental results are presented.

From (4.14) we can see that the measured rate of single-channel counts at our imperfect detector D_A in the laboratory will be

$$R_A(\theta) = \alpha_A \beta_A R_p |\eta|^2 2 \{ B - K \cos(\theta) \} \quad (4.17)$$

where α_A is the quantum efficiency of D_A , β_A is the fraction of emitted photons which is transmitted through the optics to D_A , and R_p is the repetition rate of the pump pulses. The above expression can be rewritten as

$$\begin{aligned} R_A(\theta) &= R_{A0} \left[\frac{1}{2} - \frac{K}{2B} \cos(\theta) \right] \\ &= R_{A0} \left[\frac{1}{2} - \frac{\sqrt{2\pi}}{\sigma(\tau_o + \tau_e)} \operatorname{erf} \frac{\sigma(\tau_o + \tau_e)}{4\sqrt{2}} \cos(\theta) \right] \end{aligned} \quad (4.18)$$

where

$$R_{A0} = 4\alpha_A \beta_A R_p |\eta|^2 B \quad (4.19)$$

is twice the mean counting rate at D

The single-channel counting rate at D_B is computed in exactly the same fashion, starting with a field operator representing the horizontally polarized output of the PBS:

$$\hat{E}_B^{(+)}(t; \delta\tau) = \sqrt{\frac{\delta\omega}{2\pi}} \int_{\omega} \frac{1}{\sqrt{2}} [\hat{a}_x(\omega) e^{i\omega\delta\tau} - \hat{a}_y(\omega)] e^{-i\omega t} \quad (4.20)$$

The result is

$$\begin{aligned}
 R_B(\theta) &= R_{B0} \frac{1}{2} - \frac{K}{2B} \cos(\theta) \\
 &= R_{B0} \frac{1}{2} - \frac{\sqrt{2\pi}}{\sigma(\tau_o + \tau_e)} \operatorname{erf} \frac{\sigma(\tau_o + \tau_e)}{4\sqrt{2}} \cos(\theta)
 \end{aligned} \tag{4.21}$$

where

$$R_{B0} = 4\alpha_B \beta_B R_p |\eta|^2 B \tag{4.22}$$

is twice the mean counting rate at D_B .

4.2.3.2 Coincidence counts

Finally, we will calculate the rate of coincidence counts. For a single pump pulse, the probability that D_A registers a photon within a time interval dt_A centered at time t_A and that D_B registers a photon within dt_B centered at t_B is $p_{AB}(t_A, t_B) dt_A dt_B$. The instantaneous probability density p_{AB} is given by the normally ordered expectation value

$$\begin{aligned}
 p_{AB}(t_A, t_B; \delta\tau, \theta) &= \langle \Psi | : \hat{E}_A^{(-)}(t_A) \hat{E}_A^{(+)}(t_A) \hat{E}_B^{(-)}(t_B) \hat{E}_B^{(+)}(t_B) : | \Psi \rangle \\
 &= | \hat{E}_A^{(+)}(t_A) \hat{E}_B^{(+)}(t_B) | \Psi \rangle^2.
 \end{aligned} \tag{4.23}$$

Substituting (4.11) and (4.20) into this, and carrying out the annihilation operations onto the state in (4.5) gives

$$\begin{aligned}
 p_{AB}(t_A, t_B; \delta\tau, \theta) &= \frac{|\eta|^2 (\delta\omega)^4}{(4\pi)^2} \Big|_{\omega_o, \omega_e} \alpha(\omega_o + \omega_e) (\omega_o, \omega_e) \\
 &\times \left\{ \left(e^{-i[\omega_o(t_B - \delta\tau) + \omega_e t_A]} - e^{-i[\omega_o(t_A - \delta\tau) + \omega_e t_B]} \right) \right. \\
 &\left. + e^{i\theta} \left(e^{-i[\omega_e(t_A - \delta\tau) + \omega_o t_B]} - e^{-i[\omega_e(t_B - \delta\tau) + \omega_o t_A]} \right) \right\} |vac\rangle^2
 \end{aligned} \tag{4.24}$$

As in the previous chapter, we obtain the total probability for a coincidence count by integrating p_{AB} over all possible photon arrival times within the coincidence resolving time, and extending the limits of these integrations to $\pm \infty$:

$$P_{AB}(\delta\tau, \theta) = \int_{-\infty}^{\infty} dt_A \int_{-\infty}^{\infty} dt_B p_{AB}(t_A, t_B; \delta\tau, \theta) \quad (4.25)$$

After performing these integrations and taking the limit $\delta\omega \rightarrow 0$, we arrive at the result

$$P_{AB}(\delta\tau, \theta) = |\eta|^2 \{ B - K \cos(\theta) + C(\delta\tau) \cos(\theta) - D(\delta\tau) \} \quad (4.26)$$

where B is given by (4.15), K by (4.16),

$$\begin{aligned} C(\delta\tau) &= \int_0^{\infty} d\omega_o d\omega_e |\alpha(\omega_o + \omega_e)|^2 |\alpha(\omega_o, \omega_e)|^2 e^{-i(\omega_o - \omega_e)\delta\tau} \\ &= 2B \frac{1}{2} - \frac{|\delta\tau|}{\tau_-} e^{-\frac{\sigma(\tau_o + \tau_e)}{\sqrt{2}\tau_-} \delta\tau} \text{rect} \left[\delta\tau; \frac{-\tau_-}{2}, \frac{\tau_-}{2} \right] \end{aligned} \quad (4.27)$$

and

$$\begin{aligned} D(\delta\tau) &= \int_0^{\infty} d\omega_o d\omega_e |\alpha(\omega_o + \omega_e)|^2 |\alpha(\omega_e, \omega_o)|^2 |\alpha(\omega_o, \omega_e)|^2 e^{-i(\omega_e - \omega_o)\delta\tau} \\ &= 2B \frac{\sqrt{2\pi}}{\sigma(\tau_o + \tau_e)} \text{erf} \left[\frac{\sigma(\tau_o + \tau_e)}{2\sqrt{2}} \left(\frac{1}{2} - \frac{|\delta\tau|}{\tau_-} \right) \right] \text{rect} \left[\delta\tau; \frac{-\tau_-}{2}, \frac{\tau_-}{2} \right] \end{aligned} \quad (4.28)$$

Using the relations above and multiplying by the appropriate detector and collection efficiencies along with the pulse repetition rate gives

$$\begin{aligned}
R_{AB}(\delta\tau, \theta) = & R_{AB0} \frac{1}{2} - \cos(\theta) \frac{\sqrt{2\pi}}{\sigma(\tau_o + \tau_e)} \operatorname{erf} \frac{\sigma(\tau_o + \tau_e)}{4\sqrt{2}} \\
& + \cos(\theta) \frac{1}{2} - \frac{|\delta\tau|}{\tau_-} e^{-\frac{\sigma(\tau_o + \tau_e)}{\sqrt{2}\tau_-} \delta\tau^2} \operatorname{rect} \delta\tau; \frac{-\tau_-}{2}, \frac{\tau_-}{2} \\
& - \frac{\sqrt{2\pi}}{\sigma(\tau_o + \tau_e)} \operatorname{erf} \frac{\sigma(\tau_o + \tau_e)}{2\sqrt{2}} \frac{1}{2} - \frac{|\delta\tau|}{\tau_-} \operatorname{rect} \delta\tau; \frac{-\tau_-}{2}, \frac{\tau_-}{2}
\end{aligned} \tag{4.29}$$

where

$$R_{AB0} = 2\alpha_A \alpha_B \beta_A \beta_B R_p |\eta|^2 B \tag{4.30}$$

is the mean coincidence counting rate for $|\delta\tau| > \tau_-/2$ (outside the shallow “trough” structure). A plot of $R_{AB}(\delta\tau, \theta)$ is shown in Figure 4.2 (a), with $R_{AB0} = 1$. For the fixed value $\theta = \pi$, we expect to see the modified “dip” structure shown in Figure 4.2 (b) (solid line); theoretically, the coincidence rate can fall to zero as $\delta\tau \rightarrow 0$, indicating full recovery of the quantum interference of the photon pairs. For the fixed value $\theta = 0$, we expect to observe a “peak” structure as $\delta\tau \rightarrow 0$ (Figure 4.2 (b), dashed line). As θ is varied while $\delta\tau$ is kept fixed, sinusoidal interference fringes between the “peak” and “dip” values are expected. For $\delta\tau = 0$, these fringes should have 100% visibility, and should be 180 degrees out of phase with the single-channel fringes predicted by (4.14). These out of phase “peak” to “dip” fringes are generated by the third term in (4.29), given by (4.27). As $\delta\tau$ is shifted away from zero, the magnitude of this term rapidly diminishes due to its narrow gaussian character, and the visibility of the fringes is reduced; they remain out of phase with the single-channel fringes until the crossing point where $\delta\tau = \tau_-/2$ satisfies

$$\frac{1}{2} - \frac{|\delta\tau|}{\tau_-} e^{-\frac{\sigma(\tau_o + \tau_e)}{\sqrt{2}\tau_-} \delta\tau^2} = \frac{\sqrt{2\pi}}{\sigma(\tau_o + \tau_e)} \operatorname{erf} \frac{\sigma(\tau_o + \tau_e)}{4\sqrt{2}}. \tag{4.31}$$

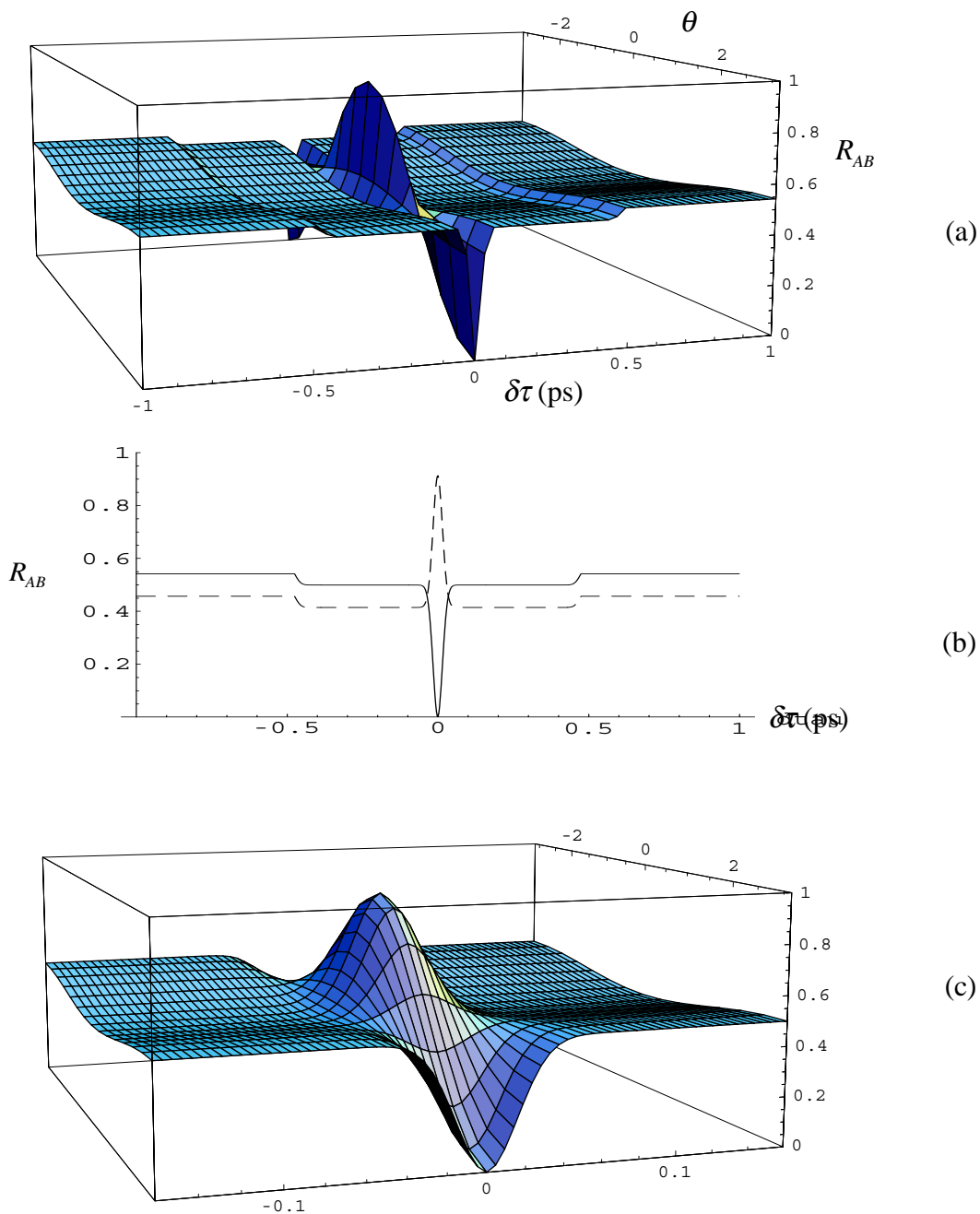


Figure 4.2 (a) The coincidence counting rate $R_{AB}(\delta\tau, \theta)$ shows sinusoidal modulation as θ is varied, with a visibility that depends on the value of $\delta\tau$. For fixed values of θ , the variation with $\delta\tau$ is a modified version of the familiar type II Hong-Ou-Mandel “dip” structure. In particular, the value $\theta = \pi$ leads to coincidence counts that dip all the way to zero (b, solid line). Figure (c) is a close-up of the dip region. Plots were made for $R_{AB0} = 1$ using the parameters of the actual experiment: $\sigma = 34.5\text{ps}^{-1}$, $\tau_o = .38\text{ps}$, and $\tau_e = 1.33\text{ps}$

At this point, the third term in (4.29) has diminished to the same magnitude as the second term, which has a small value independent of $\delta\tau$ and gives rise to fringes which are in phase with the single-channel counts. At the crossing point, these two terms cancel each other and there is no net fringe visibility whatsoever. For even larger $\delta\tau$ values, the second term dominates to produce low-visibility fringes in phase with the single-channel counts; for $\theta = \pi$ this region corresponds to the familiar “trough” in the fourth-order interference, presented in the last chapter.

4.2.4 Dispersion in the Michelson interferometer

4.2.4.1 Eliminating dispersion

Underlying all of the calculations above is the assumption that θ , the relative phase between process 1 and process 2, is a frequency-independent quantity. This approximation allowed the factor $e^{i\theta}$ to be treated as a constant multiplier for the integrals in (4.16) and (4.27), which simplifies the calculations. However, this assumption is not strictly correct, as we can see by expanding (4.4) in a Taylor series about the mean signal, idler, and pump frequencies:

$$\begin{aligned}
\theta(\omega_s, \omega_i) &= k_s(\omega_s)\ell_s + k_i(\omega_i)\ell_i - k_p(\omega_s + \omega_i)\ell_p \\
&= [k_s(\bar{\omega})\ell_s + k_i(\bar{\omega})\ell_i - k_p(2\bar{\omega})\ell_p] \\
&\quad + [(\omega_s - \bar{\omega})k_s\ell_s + (\omega_i - \bar{\omega})k_i\ell_i - (\omega_s + \omega_i - 2\bar{\omega})k_p\ell_p] \\
&\quad + \frac{1}{2}(\omega_s - \bar{\omega})^2 k_s\ell_s + \frac{1}{2}(\omega_i - \bar{\omega})^2 k_i\ell_i - \frac{1}{2}(\omega_s + \omega_i - 2\bar{\omega})^2 k_p\ell_p
\end{aligned} \tag{4.32}$$

where $k_{s,i} = \left. \frac{\partial k_{s,i}}{\partial \omega} \right|_{\bar{\omega}}$, $k_p = \left. \frac{\partial k_p}{\partial \omega} \right|_{2\bar{\omega}}$, $k_{s,i} = \left. \frac{\partial^2 k_{s,i}}{\partial \omega^2} \right|_{\bar{\omega}}$, and $k_p = \left. \frac{\partial^2 k_p}{\partial \omega^2} \right|_{2\bar{\omega}}$. The first bracketed term depends only on the mean frequency of the downconversion, and not on the

particular signal and idler frequencies which are ultimately detected. The second and third terms, however, exhibit linear and quadratic frequency dependence. Labeling these terms as $\theta^{(0)}$, $\theta^{(1)}$, and $\theta^{(2)}$, respectively, we may write

$$\theta(\omega_s, \omega_i) = \theta^{(0)} + \theta^{(1)}(\omega_s, \omega_i) + \theta^{(2)}(\omega_s, \omega_i). \quad (4.33)$$

To determine whether the frequency-independent phase approximation $\theta = \theta^{(0)}$ is valid, we must investigate the relative magnitudes of these terms.

Starting from the center of the crystal, the light accumulates the total phase difference as the signal, idler, and pump beams traverse their respective paths in the two arms of the interferometer, including propagation through dispersive media (see Figure 4.3). Due to the polarization rotation induced by the $\lambda/4$ plate, the signal and idler beams each spend half their time in the interferometer with o polarization, and half their time with e polarization. The zero-order phase difference for the beams returning to the center of the crystal is therefore

$$\theta^{(0)} = k_o(\bar{\omega})\ell_o + k_e(\bar{\omega})\ell_e - k_p(2\bar{\omega})\ell_p + \frac{\bar{\omega}}{c} (L_o + L_e - 2L_p) \quad (4.34)$$

The first three terms in (4.34) represent the accumulated phase difference within the various dispersive elements: the BBO downconversion crystal, the fused silica dichroic mirror, and the BK-7 glass slide.² The free-space propagation lengths for the o and e downconversion beams are labeled L_e and L_o , and are identical and fixed; the free-space length for the pump L_p depends on the position of the pump mirror M1. We see that if L_p is changed by a length ΔL , the resulting change in $\theta^{(0)}$ will be

$$\theta^{(0)} = L \frac{2\bar{\omega}}{c} = 2\pi \frac{L}{\lambda_p}. \quad (4.35)$$

² The $\lambda/4$ plate, consisting of a thin piece of quartz (<1mm), is expected to contribute a negligible amount of dispersion and is omitted from these calculations.

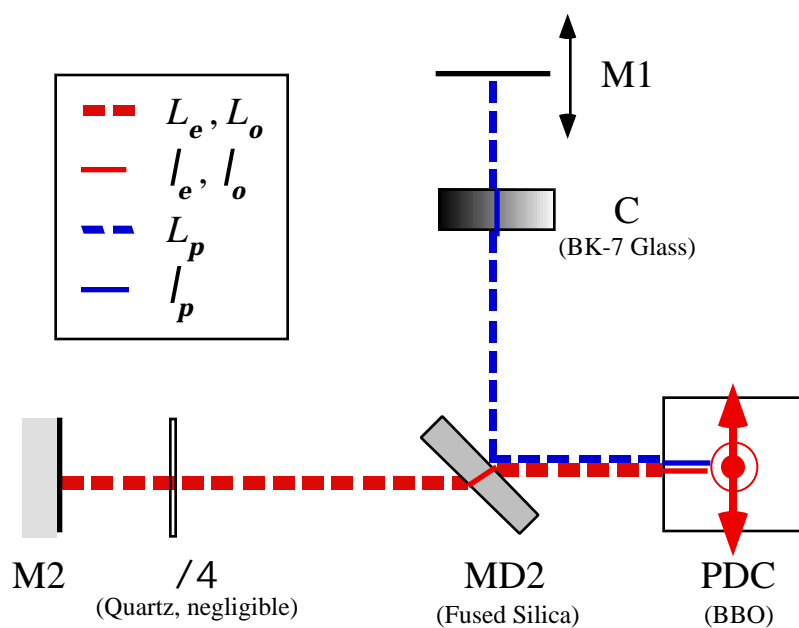


Figure 4.3 The signal and idler photon pairs accumulate a frequency-dependent phase-shift relative to the pump pulse as each color travels differently through dispersive elements in the Michelson interferometer.

We therefore expect the interference fringes in the coincidence and single-channel counting rates to be governed by the mean pump wavelength $\bar{\lambda}_p = 405$ nm.

The first-order phase difference is

$$\begin{aligned} \theta^{(1)}(\omega_o, \omega_e) &= (\omega_o - \bar{\omega})k_o\ell_o + (\omega_e - \bar{\omega})k_e\ell_e - (\omega_o + \omega_e - 2\bar{\omega})k_p\ell_p \\ &\quad + (\omega_o - \bar{\omega})\frac{L_o}{c} + (\omega_e - \bar{\omega})\frac{L_e}{c} - (\omega_o + \omega_e - 2\bar{\omega})\frac{L_p}{c} \end{aligned} \quad (4.36)$$

where $k_{o,e,p}$ now refer to the inverse group velocities within all the various dispersive media in the interferometer. This can be written more simply as

$$\begin{aligned} \theta^{(1)}(\omega_o, \omega_e) &= (\omega_o + \omega_e - 2\bar{\omega}) \frac{1}{2} (k_o\ell_o + k_e\ell_e - 2k_p\ell_p) + \frac{1}{2c} (L_o + L_e - 2L_p) \\ &= (\omega_o + \omega_e - 2\bar{\omega})\theta \end{aligned} \quad (4.37)$$

where θ is not a phase, but is a frequency-independent coefficient which depends on the dispersive elements and path lengths in the interferometer. For an appropriate choice of L_p , θ can become zero, eliminating all of the first-order frequency dependence in θ . This is equivalent to balancing the path lengths in the interferometer to within the coherence length of the pump. Averaged over the range of pump frequencies $\omega_o + \omega_e$, the change in $\theta^{(1)}$ due to a change in L_p by a length ΔL is

$$\left\langle \theta^{(1)} \right\rangle_{\omega_o + \omega_e} = \frac{\langle \omega_o + \omega_e - 2\bar{\omega} \rangle_{\omega_o + \omega_e}}{2c} \Delta L = 2\pi \frac{\Delta L}{L_p}, \quad (4.38)$$

where $L_p = 2\pi \frac{c}{\sigma} \approx 50$ μm is the coherence length of the pump pulse.

After similar simplifications, the second-order phase difference may be written

$$\begin{aligned} \theta^{(2)}(\omega_o, \omega_e) &= \left((\omega_o - \bar{\omega})^2 + (\omega_e - \bar{\omega})^2 \right) \frac{1}{4} (k_o\ell_o + k_e\ell_e) - (\omega_o + \omega_e - 2\bar{\omega})^2 \frac{k_p\ell_p}{2} \\ &= \left((\omega_o - \bar{\omega})^2 + (\omega_e - \bar{\omega})^2 \right) \theta_{oe} - (\omega_o + \omega_e - 2\bar{\omega})^2 \theta_p \end{aligned} \quad (4.39)$$

with $k_{\alpha,e} = \left. \frac{\partial^2 k_{\alpha,e}}{\partial \omega^2} \right|_{\omega}$ and $k_p = \left. \frac{\partial^2 k_e}{\partial \omega^2} \right|_{2\bar{\omega}}$ representing the group velocity dispersions for each of the various media; the products $k \ell$ are understood to be summed over the path lengths traveled within these media. Again, the parameters θ_{oe} and θ_p are not phases, but are coefficients which reflect the total group velocity dispersion for the downconversion and pump pulses, respectively. Unfortunately, no values of θ_{oe} and θ_p can be chosen that will entirely eliminate $\theta^{(2)}$ for all frequencies; however, we can choose values that minimize (4.39) for the most likely downconversion frequencies in our experiment [1]. To do this, we note that the most likely pairs of frequencies are those which maximize (ω_o, ω_e) , by zeroing the argument of the sinc function in Eq. (4.9):

$$(k_o - k_p)(\omega_o - \bar{\omega}) + (k_e - k_p)(\omega_e - \bar{\omega}) = 0 \quad (4.40)$$

This expression can be used to eliminate ω_o or ω_e in (4.39): it is then possible to choose θ_{oe} and θ_p such that the remaining frequency dependence is zero. For our interferometer³, this calculation revealed that $\theta^{(2)}$ could be minimized by placing 2.04 mm of BK-7 glass into the pump arm. The plate C had an actual thickness of 1.58 mm, which left some residual quadratic dispersion uncompensated in the experiment.

4.2.4.2 *The consequences of dispersion*

In practice, it is possible that some first order dispersion remains uncanceled if the interferometer is not exactly balanced. In addition, as noted above, the quadratic dispersion was not entirely canceled with the compensator plate C. To see the effects of any residual first and second order dispersion, we need only replace our original

³ 5 mm BBO crystal, .25" fused silica dichroic (oriented at 45° for an effective length 7.27 mm)

parameter θ by its expansion (4.33) in the quantum state (4.5), and recompute the quantities of interest. The new single pulse coincidence probability is given by

$$P_{AB}(\delta\tau, \theta^{(0)}, \theta, \theta_{oe}, \theta_p) = |\eta|^2 \left\{ B - |K_D(\theta, \theta_{oe}, \theta_p)| \cos\left(\theta^{(0)} + \arg\left(K_D(\theta, \theta_{oe}, \theta_p)\right)\right) + |C_D(\delta\tau, \theta, \theta_{oe}, \theta_p)| \cos\left(\theta^{(0)} + \arg\left(C_D(\delta\tau, \theta, \theta_{oe}, \theta_p)\right)\right) - D(\delta\tau) \right\} \quad (4.41)$$

where B and D remain as defined in (4.15) and (4.28). The new dispersion-dependent quantities are

$$K_D(\theta, \theta_{oe}, \theta_p) = \int_0^{\omega_o} \int_0^{\omega_e} d\omega_o d\omega_e |\alpha(\omega_o + \omega_e)|^2 (\omega_e, \omega_o) (\omega_o, \omega_e) \times e^{i\left\{(\omega_o + \omega_e - 2\bar{\omega})\theta + ((\omega_o - \bar{\omega})^2 + (\omega_e - \bar{\omega})^2)\theta_{oe} - (\omega_o + \omega_e - 2\bar{\omega})^2\theta_p\right\}} \quad (4.42)$$

and

$$C_D(\delta\tau, \theta, \theta_{oe}, \theta_p) = \int_0^{\omega_o} \int_0^{\omega_e} d\omega_o d\omega_e |\alpha(\omega_o + \omega_e)|^2 (\omega_o, \omega_e)^2 e^{-i(\omega_o - \omega_e)\delta\tau} \times e^{i\left\{(\omega_o + \omega_e - 2\bar{\omega})\theta + ((\omega_o - \bar{\omega})^2 + (\omega_e - \bar{\omega})^2)\theta_{oe} - (\omega_o + \omega_e - 2\bar{\omega})^2\theta_p\right\}} \quad (4.43)$$

After some manipulation, the first of these quantities may be rewritten as

$$K_D(\theta, \theta_{oe}, \theta_p) = 2B \frac{\tau_-}{\sigma|\tau_o + \tau_e|} \sqrt{\frac{i}{4\theta_{oe}}} \times \{I_0^+ + I_1^+ + I_0^- + I_1^-\} \quad (4.44)$$

where

$$I_{0,1}^\pm = \int_0^{1 \pm \frac{2\theta}{\tau_o + \tau_e}} dz e^{-i\frac{(\tau_- z)^2}{8\theta_{oe}}} \operatorname{erf} \frac{|(\tau_o + \tau_e)(1 - z) \pm 2\theta|}{2\sqrt{\frac{8}{\sigma^2} + 2i(2\theta_p - \theta_{oe})}} \quad (4.45)$$

The remaining quantity can be expressed as

$$C_D(\delta\tau, \theta, \theta_{oe}, \theta_p) = 2B \frac{\tau_-}{2\sqrt{2\pi}} \frac{1}{\sqrt{\theta_{oe} [\sigma^2 (2\theta_p - \theta_{oe}) - 4i]}} \times I_2 \quad (4.46)$$

where

$$I_2 = \int_{-1}^1 dz (1 - |z|) e^{-i \frac{\tau_- z - \delta\tau}{2\theta_{oe}} - \frac{\sigma \frac{\tau_o + \tau_e}{2} z - \theta}{8 + 2i\sigma^2 (2\theta_p - \theta_{oe})}}. \quad (4.47)$$

The resulting expression for the coincidence counting rate with dispersion is

$$\begin{aligned} R_{AB}(\delta\tau, \theta^{(0)}, \theta, \theta_{oe}, \theta_p) = R_{AB0} & \frac{1}{2} - \frac{\tau_-}{\sigma|\tau_o + \tau_e|} \left| \sqrt{\frac{i}{4\theta_{oe}}} \times \{I_0^+ + I_1^+ + I_0^- + I_1^-\} \right| \\ & \times \cos\left(\theta^{(0)} + \arg\left(K_D(\theta, \theta_{oe}, \theta_p)\right)\right) \\ & + \frac{\tau_-}{2\sqrt{2\pi}} \left| \frac{1}{\sqrt{\theta_{oe} [\sigma^2 (2\theta_p - \theta_{oe}) - 4i]}} \times I_2 \right| \\ & \times \cos\left(\theta^{(0)} + \arg\left(C_D(\delta\tau, \theta, \theta_{oe}, \theta_p)\right)\right) \\ & - \frac{\sqrt{2\pi}}{\sigma(\tau_o + \tau_e)} \operatorname{erf} \frac{\sigma(\tau_o + \tau_e)}{2\sqrt{2}} \frac{1}{2} - \frac{|\delta\tau|}{\tau_-} \operatorname{rect} \delta\tau; \frac{-\tau_-}{2}, \frac{\tau_-}{2} \end{aligned} \quad (4.48)$$

A comparison with (4.29) reveals many similarities for the cases with and without dispersion: the first and last terms in the expression are unchanged, and, as before, the second and third terms are the only ones which depend on θ . Recalling (4.35) and (4.38), and assuming

$$L_p \gg \bar{\lambda}_p, \quad (4.49)$$

we can regard small changes in L_p (on the order of $\bar{\lambda}_p$) as affecting $\theta^{(0)}$, but not θ .

The factors $\arg\left(K_D(\theta, \theta_{oe}, \theta_p)\right)$ and $\arg\left(C_D(\delta\tau, \theta, \theta_{oe}, \theta_p)\right)$ then appear as fixed phase offsets for the new interference fringes. The new expected coincidence rate is plotted in Figure 4.4, as $\delta\tau$ and $\theta^{(0)}$ are varied. The integrals (4.45) and (4.47) were computed

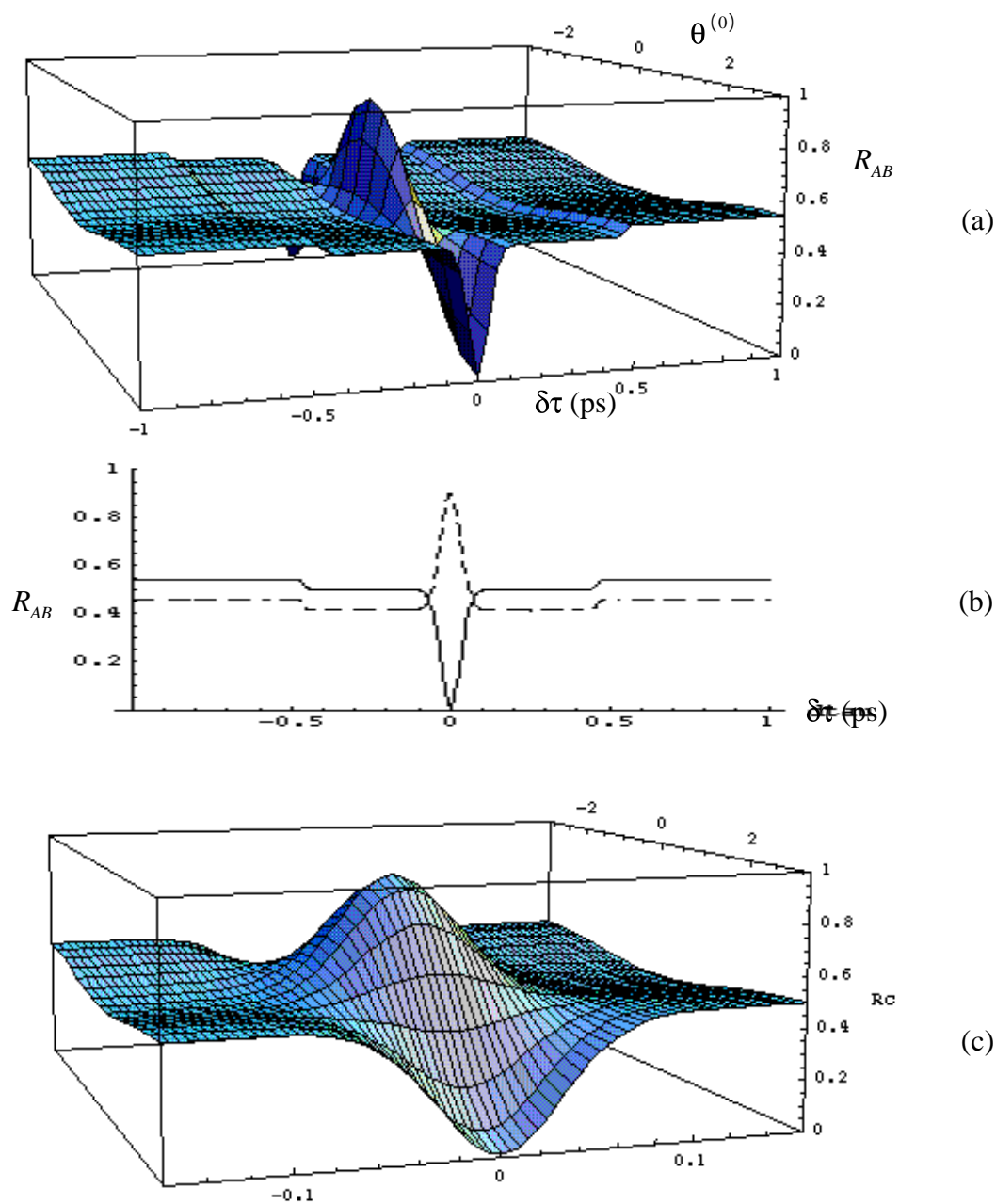


Figure 4.4 (a) With dispersion in θ included, the coincidence rate $R_{AB}(\delta\tau, \theta, \theta_{oe}, \theta_p)$ still displays sinusoidal variation with the zero order, frequency-independent phase $\theta^{(0)}$. For $\theta^{(0)} = \pi$ (b, solid line) the dip is wider than before, and does not fall to zero. Plots were made using our best estimates for the parameters of the actual experiment: $\sigma = 34.5\text{ps}^{-1}$, $\tau_o = .38\text{ps}$, $\tau_e = 1.33\text{ps}$, $\theta = 0$, $\theta_{oe} = 2.95 \times 10^{-4}\text{ps}^2$, $\theta_p = 7.42 \times 10^{-4}\text{ps}^2$

numerically, with the assumption that the interferometer was perfectly balanced so that $\theta = 0$, with values for θ_{oe} and θ_p representing the dispersion of the actual optical elements in the experiment.

It is interesting to note what happens to this structure if the path lengths in the interferometer are out of balance by an amount comparable to the coherence length of the pump. In this situation, the first-order dispersion coefficient θ is no longer zero. In fact, the alignment procedure in the actual experiment may have allowed the pump mirror M1 to be offset from the optimal path length balancing condition by as much as 10 μm . The effect of such an error is shown in Figure 4.5: the net result is a translation of the central dip and peak structures away from $\delta\tau = 0$, and a slight reduction in the dip visibility.

The shift in the dip indicates that in the collinear HOMI, some extra dispersive material is needed to make the two coincidence processes indistinguishable -- i.e., to make the signal and idler photons overlap perfectly before the $\lambda/4$ plate and PBS⁴. This occurs because the total blue and red path lengths in the Michelson interferometer are no longer balanced for pulses emitted from and returning to the center of the PDC; instead, they are balanced for pulses emitted and returning to some other point within the crystal. This implies a different amount of temporal walk-off, which is corrected by the additional dispersive material in the HOMI. For these photons, the new dip position is actually the one for which the net delay between signal and idler is zero.

⁴ In this experiment, the overlap of the signal and idler wavepackets at the beamsplitter implies the indistinguishability of the resulting coincidence processes. This is not always the case, however. For elucidation of this point, see reference [2]

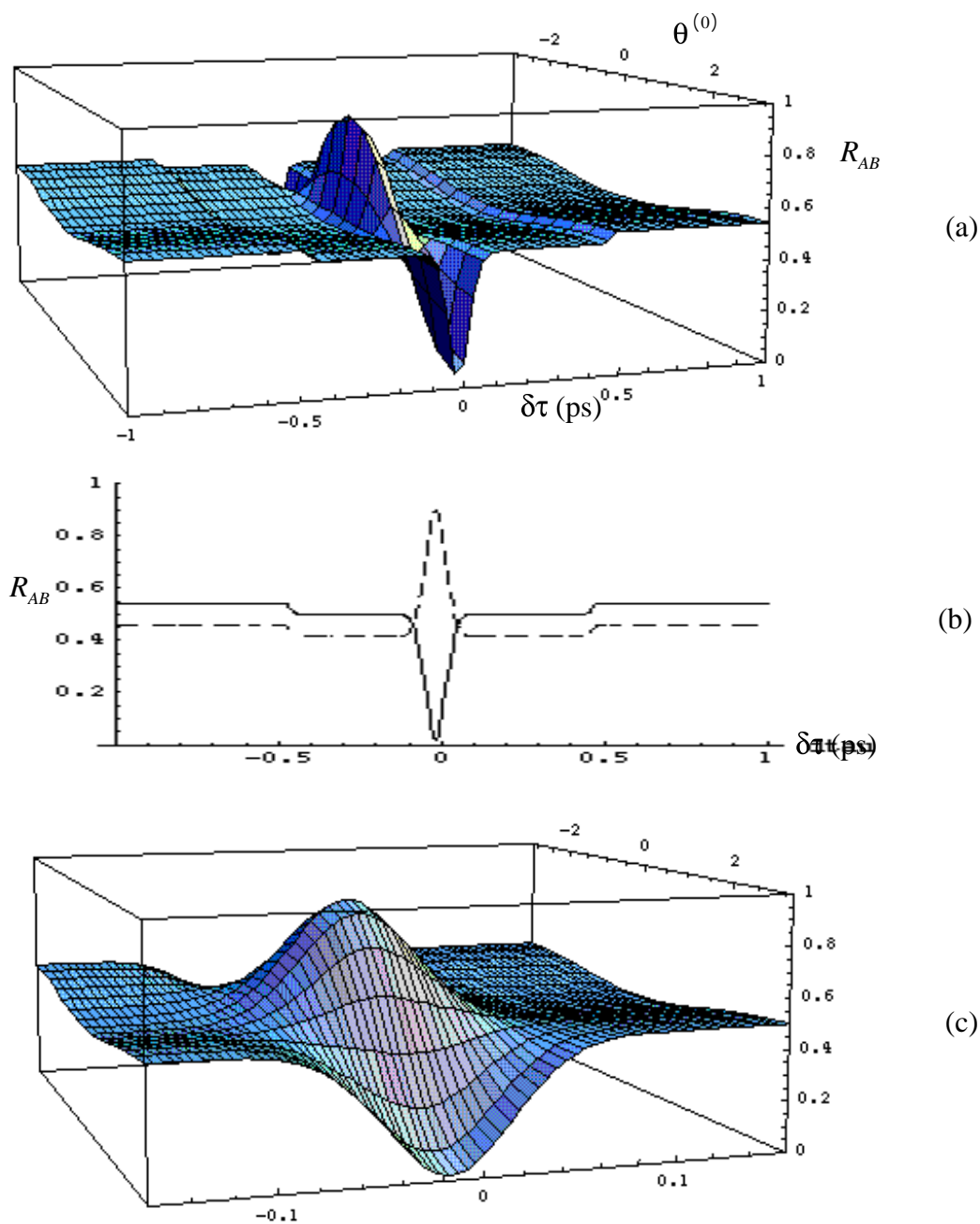


Figure 4.5 The effects of a $-10 \mu\text{m}$ shift in L_p . In this case, the Michelson interferometer is not balanced, and the first order dispersion term (nominally zero) has a value of $\theta = -0.033\text{ps}$. There is a shift in the position of the dip away from $\delta\tau = 0$, and a slight reduction in visibility.

4.3 Experimental procedure and results

4.3.1 Apparatus

The experimental apparatus is depicted in Figure 4.6; it makes use of many of the same optical elements as the experiments of the preceding chapter. Once again, an ultrafast pump source for the spontaneous downconversion process was created by frequency doubling the 810 nm output of a mode-locked Ti:sapphire oscillator with a .7 mm BBO crystal cut and aligned for type-I phase matching. And, as before, the resulting 405 nm pulses were separated from the residual, undoubled 810 nm pulses by means of a dispersion compensated prism sequence, before impinging onto the downconversion crystal (PDC). This method delivered an average pump power of 330 mW, with a pulse repetition rate of 80 MHz. The measured bandwidth of the pump was $\lambda_p = 3\text{nm}$, implying $\sigma = 34.5\text{ps}^{-1}$ and a coherence length $L_p = 50\mu\text{m}$, satisfying our earlier assumption (4.49).

For this experiment, the downconversion crystal was a 5 mm piece of BBO, cut and aligned for type-II phase matching. This represents a sixfold increase in the crystal length from the one used in the preceding experiment, and from Figure 4.5 we can see that this would ordinarily result in a poorer visibility for two-photon interference in the HOMI. We chose this “shallower” trough to make the improvement in visibility for the new symmetrized source more dramatic, as seen in Figure 4.2, so that it could be easily spotted in the laboratory data.

The pump pulses were guided onto the PDC by means of a dichroic mirror (MD1) that is reflective at 405 nm, but transmissive at 810 nm. After passing through the crystal, the pump pulses were separated from the downconverted fields by reflection at a second dichroic mirror (MD2), and sent to another mirror (M1) mounted on a piezoelectric transducer (PZT) and a motorized translation stage. M1 was aligned for

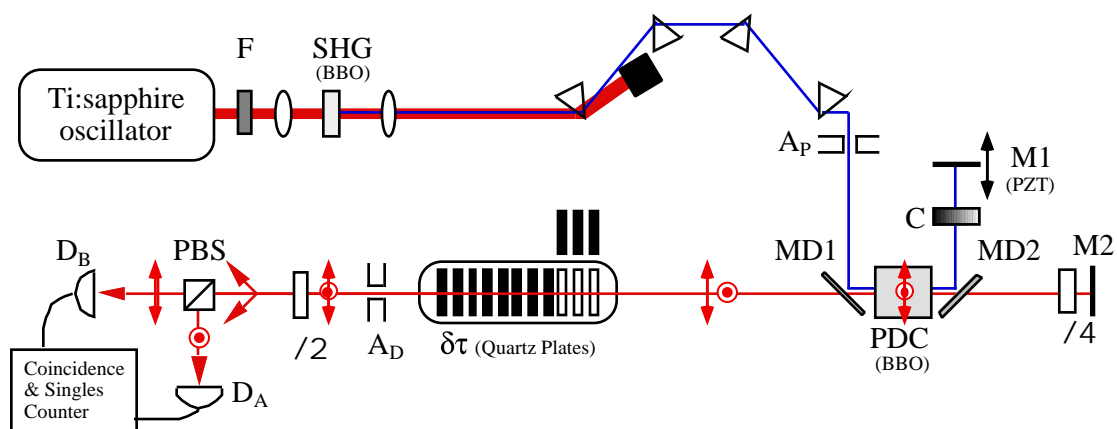


Figure 4.6 Schematic of the new collinear Hong-Ou-Mandel interferometer. This arrangement is almost identical to the one shown in the previous chapter, but contains two important modifications: the downconversion crystal is 6 times longer, and a two-color Michelson interferometer has been added to the downconversion region to symmetrize the joint emission spectrum of the signal and idler pairs.

normal incidence, to reflect the pump pulses back to MD2, and back into the downconversion crystal for a second pass. Meanwhile, the first downconversion beams passed through MD1, then through a quarter-wave plate ($\lambda/4$), and impinged onto another mirror (M2) aligned for normal incidence. They were reflected back along their paths through $\lambda/4$, MD2, and into the crystal. We attempted to balance the losses and dispersion for the red arm by placing a compensator (C) in the pump arm. This was a BK-7 glass slide with a neutral-density gradient along its length. The slide was mounted on a translation stage, so that more or less transmissive parts of the slide could be inserted into the pump beam until the intensities coming from the two arms were equalized. As already mentioned, the 1.58 mm thickness also served to cancel most of the second-order dispersion experienced by the signal and idler photons.

The phase difference θ was varied by changing L_p with the PZT. A locking system⁵ ensured the stability of the Michelson interferometer by sending negative feedback to the PZT, so that θ could be held constant while the photons were counted. The locking system was able to keep L_p constant to within $L_p \pm 20\text{nm}$; from (4.35) this implies a stability in θ of $\delta\theta \approx 2\pi/20$.

After its second pass through the PDC, the pump beam was again reflected at the dichroic mirror MD1 and was sent back along its input path, ultimately to be absorbed by a broadband red-pass filter (F). Meanwhile, the signal and idler photons passed through MD1 and into the quartz delay line. To vary $\delta\tau$, we used a set of 6 crystal quartz plates, 4 of thickness 1mm and 2 of thickness .5 mm. The plates remained in the beam at all times, and were oriented with their fast axes aligned either to the e or o polarization of the BBO crystal. Different combinations of orientations for the plates resulted in different net delays between the signal and idler photons. A fixed

⁵ The locking circuit and feedback technique were adapted from a design by Mike Noel [3]. For a schematic of the circuit and notes on its operation, see Appendix D.

compensator plate was also inserted to cancel the temporal walk-off in the BBO crystal, so that pairs created in the center of the downconverter (in either process) would experience only the net delay specified by $\delta\tau$. For a 5 mm piece of BBO, the appropriate compensator was a 16.2 mm quartz plate with its fast axis oriented to the e axis of the BBO.

After the quartz delay line, the photons passed through a zero-order half wave plate ($\lambda/2$), a polarizing beamsplitter (PBS), and onto a pair of EG&G SPCM-200 avalanche photodiodes (D_A and D_B). The TTL electronic pulses from D_A and D_B were inverted and sent to discriminators which generated uniform NIM pulses triggered on the leading edge of each APD pulse. These pulses were then fed to a coincidence counter which produced an output NIM pulse whenever the two inputs arrived within 200 ns of each other⁶. The single-channel and coincidence NIM pulses were counted by an EG&G Ortec model 974 counter, under computer control via GPIB.

After aligning the system, we typically saw coincidence count rates of around 4000/sec with all apertures wide open. To improve the interference visibility, we closed aperture A_p to 2 mm and A_d to 1mm diameter. The mean single channel rates R_{A0} and R_{B0} were then around 3000/sec, while the mean coincidence rate R_{AB0} was roughly 15/sec. From these numbers and the relations (4.19), (4.22), and (4.30) we find

$$\alpha_A \beta_A = \alpha_B \beta_B \quad .01 \quad (4.50)$$

and, with $R_p = 8 \times 10^7$,

$$|\eta|^2 B = 10^{-3} \quad (4.51)$$

⁶ The coincidence counter was an “AND” gate that produced an output NIM pulse whenever both inputs registered a “logical 1” (-1.5V to -0.6V for the NIM standard.) The 200 ns coincidence window is a result of convolving the two rectangular input pulses with each other; the first was of duration 150 ns, while the second was of duration 50 ns.

which ensures that the nondepleted pump approximation (4.7) is well satisfied.⁷

4.3.2 Results

We collected photocounts for 11 different values of $\delta\tau$, covering the range $-0.16 \text{ ps} < \delta\tau < 0.16 \text{ ps}$. For each value of $\delta\tau$, we recorded counts at 11 different θ values, producing interference fringes in both the single-channel and coincidence counts. Counts were collected for 200 seconds at each θ value. The total time for all these scans was 9 hours. During that time, the laser power dropped steadily from its initial value, and re-alignment was forbidden once the data collection began. Therefore, the average pump power was measured during the course of each data taking interval, so the drop in power could be divided out.⁸ The data presented and analyzed here have all been re-normalized in this way.

Data for three values of $\delta\tau$ are shown in Figure 4.7. The dashed lines represent the best fits of the data to sinusoidal curves. As predicted, the low-visibility coincidence fringes for large $\delta\tau$ are in-phase with the single-channel fringes, while the high-visibility coincidence fringe near the center is out of phase with the single-channel fringes recorded there.

All of the coincidence data are plotted in Figure 4.8 as a function of $\delta\tau$ and θ . The data with positive $\delta\tau$ values were renormalized to account for a systematic error related to the orientation of a particular quartz plate.⁹ The resulting picture is qualitatively similar to the theory curves given in Figure 4.5, showing a gradual improvement in interference visibility as $\delta\tau$ nears zero.

⁷ See Eq. (C.18) in Appendix C.

⁸ This solution to the problem is valid because R_{A0} , R_{B0} , and R_{AB0} all depend linearly on the pump intensity, owing to the spontaneous nature of the downconversion.

⁹ The data for $\delta\tau > 0$ were all recorded with a particular .5 mm quartz plate oriented with its slow axis aligned to the o polarization; the orientation was flipped for the $\delta\tau < 0$ scans, and the mean counting rate for these data dropped by roughly 10%. The $\delta\tau > 0$ data were therefore renormalized by this 10% factor.

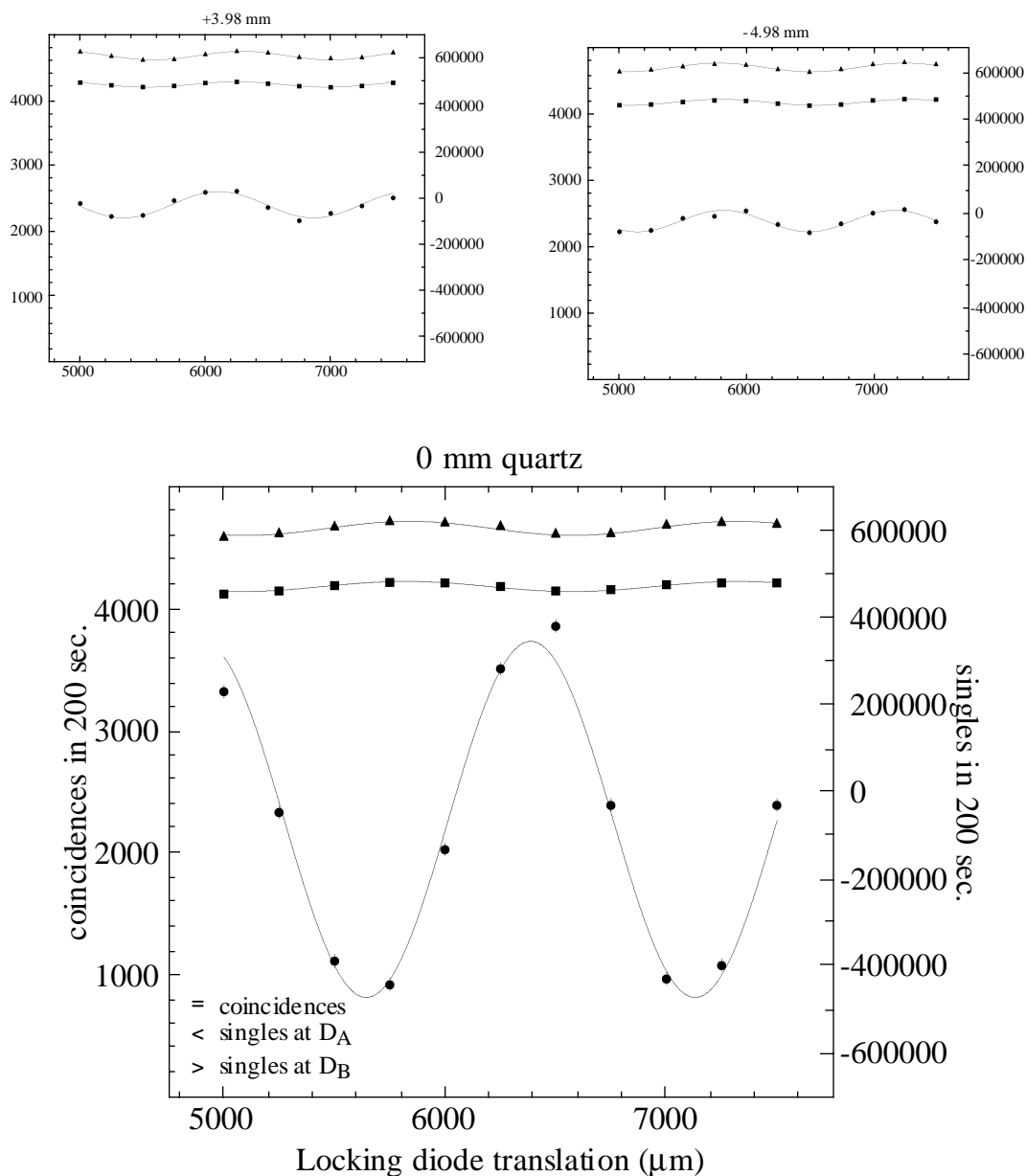


Figure 4.7 Recorded coincidence and single-channel counts as a function of the pump mirror displacement, for fixed values of $\delta\tau$. The counts have been renormalized to eliminate the effects of laser power drifts. The pump mirror was displaced by translating the pair of locking photodiodes through the fringe pattern generated by the HeNe (see Appendix D). The interference visibility reached 64% for the case $\delta\tau = 0$.

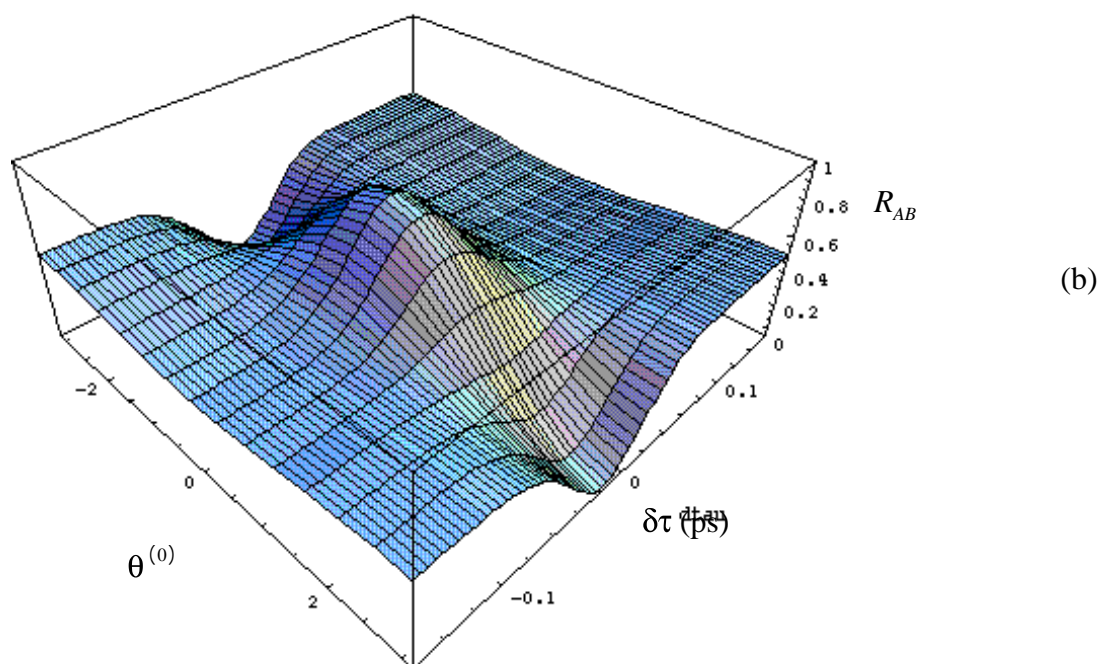
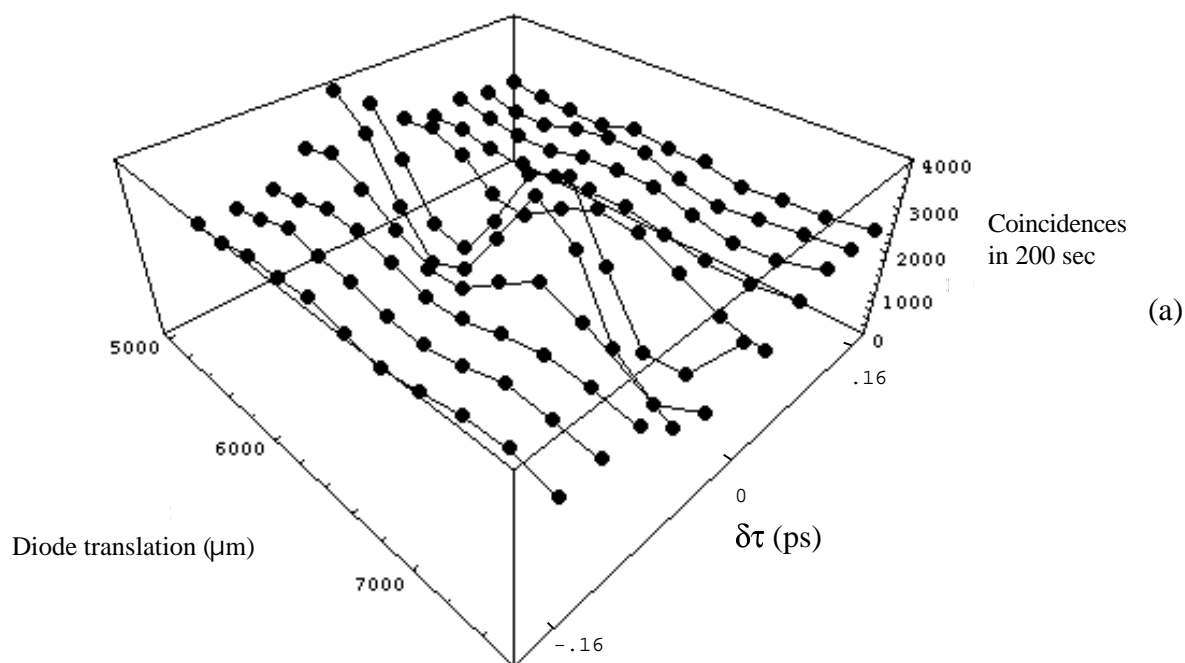


Figure 4.8 (a) Compilation of all eleven renormalized coincidence fringes, recorded over the range $-0.16 \text{ ps} < \delta\tau < 0.16 \text{ ps}$. Note the gradual transition of the fringe phases. The theoretical prediction in (b) includes a $-10 \mu\text{m}$ shift in the position of M1.

A maximum visibility of 64% was observed for the scan at $\delta\tau = 0$. The main reason why this visibility was not 100% is that the losses in the Michelson interferometer were not equal for the two arms, despite our efforts to balance them with the pump attenuator C. Scans taken with each arm of the interferometer blocked revealed that the red arm contributed a mean intensity of 959 ± 52 counts per 200 seconds, while the pump arm contributed 1348 ± 30 counts per 200 sec. The maximum possible interference visibility allowed under these conditions is 71%. As we have seen, our best estimates for the dispersion parameters in the interferometer also result in a slight degradation of the interference visibility. The maxima and minima implied by the sinusoidal fits for all 11 values of $\delta\tau$ are shown in Figure 4.9. The improvement in the fourth-order interference with our symmetrized source is evident here, as the counting rate in the center of the dip falls well below the dashed line representing the unsymmetrized case. The solid line is the result of a theoretical calculation, including dispersion and a $-10 \mu\text{m}$ error in the position of M1, scaled to the mean counting rate given by the sum of the red-arm and pump-arm contributions. The data appear to be in good agreement with this calculation.

The minimum and maximum count values on these curves represent the conditions $\theta^{(0)} = \pi$ and $\theta^{(0)} = 0$, respectively, for values of $\delta\tau$ that lie between the crossing points satisfying (4.31). Outside this range, the minimum count values must correspond to $\theta^{(0)} = 0$, while the minima represent $\theta^{(0)} = \pi$. The theory predicts a sharp transition between these two regions, marked by an interference visibility of zero at the crossing point. However, this sharp transition was not observed. Instead, our coincidence data displayed a smooth phase drift as $\delta\tau$ increased -- evident in Figure 4.8 (a) -- while the phase of the single-channel fringes remained constant. The relative

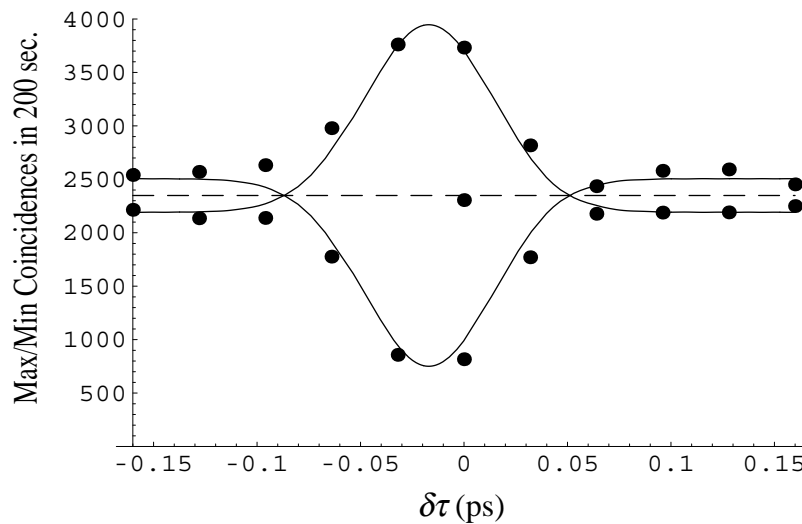


Figure 4.9 Extracted minimum and maximum coincidence counts as a function of $\delta\tau$. The solid line is a curve calculated for a pump mirror placement error of $-10\ \mu\text{m}$, with our best estimates of the dispersion and pump bandwidth parameters, and adjusted for the measured unequal contributions from the two arms of the interferometer. The dashed line represents the expected counting rate for the unsymmetrized source: the data point on this line is the sum of the “red arm” and “pump” arm contributions taken separately, without interference effects.



phase of the coincidence and single channel sinusoidal fits is plotted in Figure 4.10 (a): the relative coincidence phase appears to vary linearly with $\delta\tau$.

This phase drift is not predicted by our theory. A close inspection of (4.48) does reveal that, in principle, the fringe attributed to the third term of the counting rate will have an additional phase given by $\arg\left(C_D(\delta\tau, \theta, \theta_{oe}, \theta_p)\right)$, allowing the possibility of a $\delta\tau$ -dependent phase shift. However, calculations showed that this shift is not appreciable even with 100 times the amount of dispersion in our interferometer. Furthermore, the magnitude of this term, which is generating the enhanced dip structure, falls to zero fairly quickly, while the phase shift persists over the entire region of our data. These points are illustrated in Figure 4.10 (b) - (d).

4.4 Discussion

4.4.1 Is the phase drift in the coincidence counts a systematic error?

It appears that our second-order dispersion theory is unable to account for the smooth phase drift of the coincidence fringes. On the other hand, it is hard to imagine a systematic error which could produce this trend. The interferometer remained locked at all times in each of these regions, and the single channel fringes reflect this in the sense that their phases did not drift from scan to scan; therefore, the systematic error would have to produce the drift only in the phase of the coincidence counts. Additionally, the phase drift never changed direction with regard to $\delta\tau$, despite the fact that the time order of the scans for $\delta\tau < 0$ was opposite that of the scans for $\delta\tau > 0$; therefore, it seems more likely that the systematic effects are tied to the quartz plates themselves. But since different sets of plates were changed each time to produce the various delays, one would expect a quartz-related effect to produce essentially random phase changes with respect to $\delta\tau$. Instead, the phase drift appears insensitive to how specific plates were oriented,

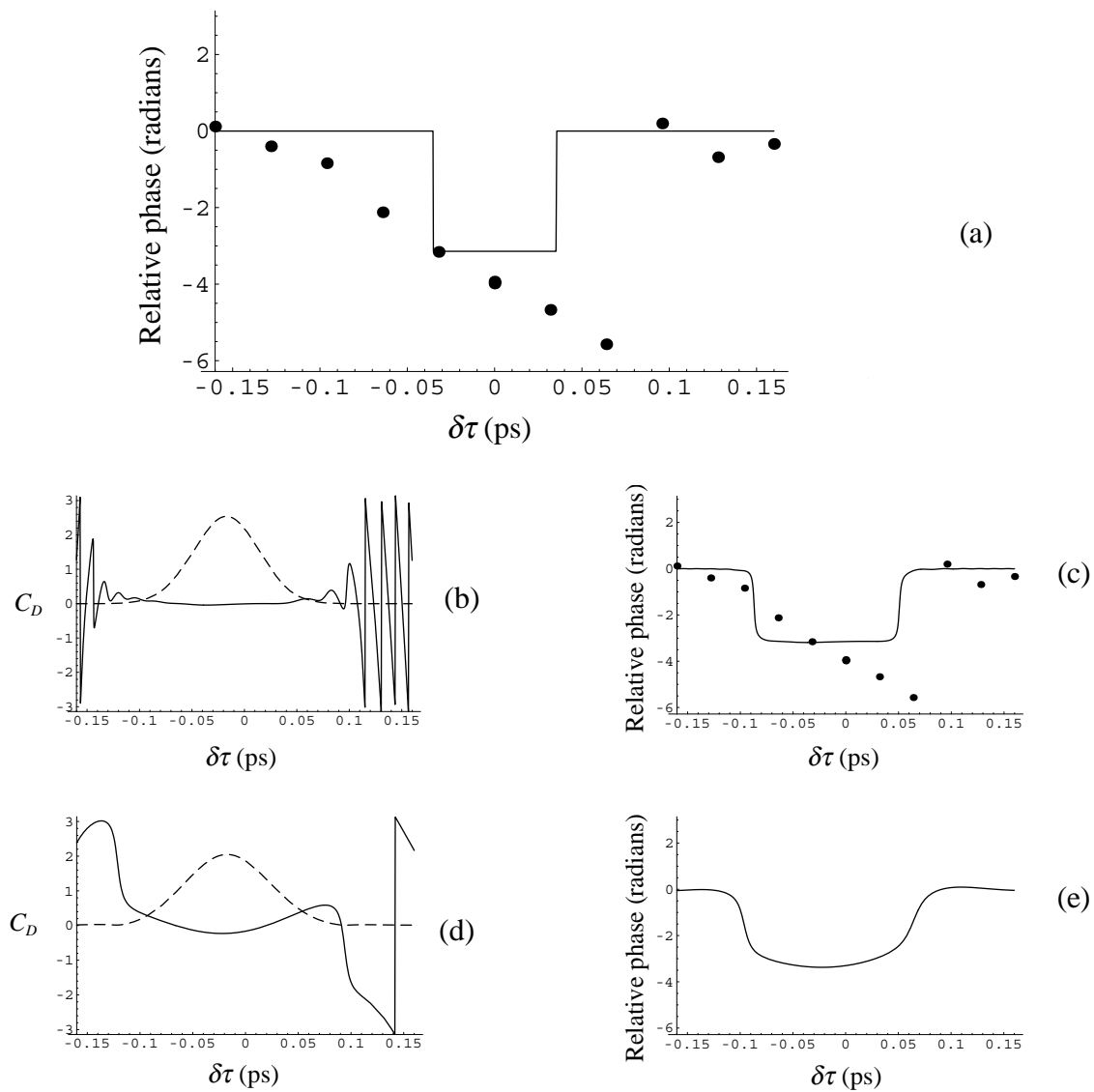


Figure 4.10 (a) The phase of the coincidence fringes relative to the single-channel fringes does not undergo a sharp transition as predicted by the dispersionless theory (solid line), but instead varies smoothly with $\delta\tau$ over the range of our data. The only term capable of generating such shifts in the theory with dispersion included is $C_D(\delta\tau, \theta', \theta''_{oe}, \theta''_p)$. The magnitude and phase of this term are plotted in (b), and the effect Figure on the relative phase between coincidences and singles is shown in (c). Figures (d) and (e) repeat these plots with the dispersion increased by a factor of ten.

depending only on the total amount of quartz involved. Indeed, the two scans at $\delta\tau = 0$ yielded identical relative phases despite their different specific quartz plate orientations. All of this leads us to doubt that the effect is a systematic one.

It is possible that a more detailed calculation, performed without the assumption (4.49), might account for this effect. Alternatively, we note that a slow drift between the “dip” and “peak values as the delay is varied was observed in another type-II experiment with polarizers in front of each detector [4]; perhaps an analysis that allows for some imperfections in the PBS, so that different polarizations may appear at the detectors, would reveal the source of this phase drift.

4.4.2 Comparison with the experiments of Herzog, et al.

In many ways, the Michelson interferometer in this experiment is reminiscent of several earlier experiments [5-7] conducted with a cw-pumped, type-I parametric downconverter, in which the signal, idler, and pump beams were all reflected back into the crystal for a second pass to produce interference in the signal and idler modes as the pump phase was varied (see Figure 4.11). However, our experiment is distinguished from these by the use of an ultrafast pump source and type-II downconversion, by the addition of the HOMI, and most importantly by the exchanging of the signal and idler beams before they are reflected back into the crystal. Furthermore, in the earlier experiments the modulation in the coincidence rate was a direct consequence of the modulation in the pair-creation rate, so that the coincidence and single-channel counts were always in phase with each other as θ was varied. A striking departure from this situation occurs for our coincidence counting rate, which is *out of phase* with the single channel counting rate in the dip region near $\delta\tau = 0$, and which exhibits a 64%

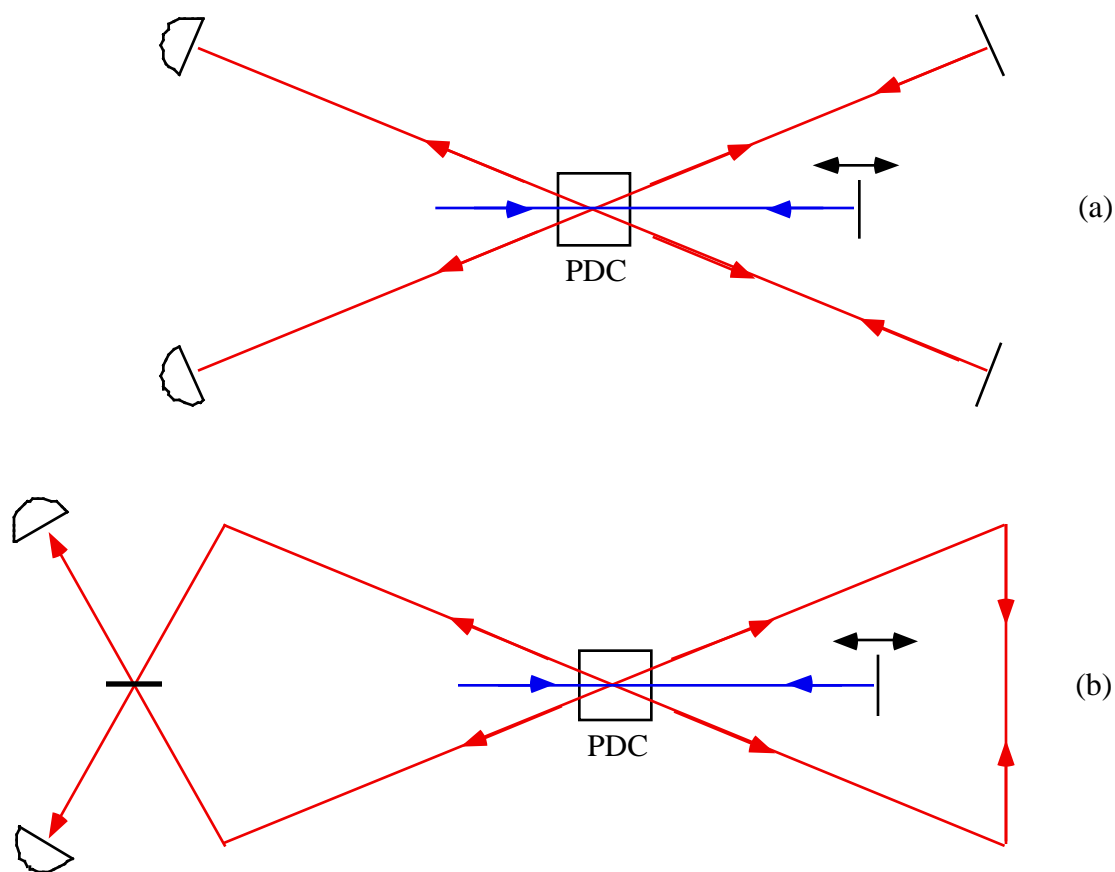


Figure 4.11 (a) Earlier experiments have demonstrated nonclassical interference effects by reflecting signal, idler, and pump beams back into a type I cw-pumped downconverter so that a second downconversion process could interfere with the first. This leads to second-order interference at both the signal and idler photodetectors as is varied, and (trivially) to fourth-order interference as the coincidences are monitored. Unfolded in this way, our experiment (b) shares many of the same features, but displays coincidence interference which is out of phase with the (reduced visibility) single-channel interference.

modulation, while the single-channel (or pair-creation) interference visibility is less than 3%.

4.4.3 Interpretation of the interference terms

It is interesting to note that the single-channel detection probability in (4.14) depends on θ , but not on $\delta\tau$. This is an indication that for the single-channel counts, some degree of interference is taking place between the two different downconversion processes, but not between the delayed (initially x -polarized) and undelayed (initially y -polarized) photons. As such, we can label the interfering photons as being “polarization distinct” but “process indistinct”. For example, it would be possible to tell that one of these photons emerged from the PDC with, say, x polarization, but it would be impossible to discern whether this photon was created as an e -photon in the first process, or an o -photon in the second. The interference between the two creation processes for these photons is manifested by a modulation as θ is varied.

In this light, it is easy to see why the second-order interference visibility depends on the extent to which the spectra of the e and o polarized photons are similar. The more symmetric $S(\omega_o, \omega_e)$ is, the more overlap there will be between the marginal single-photon spectra $\phi(\omega_o) = \int d\omega_e S(\omega_o, \omega_e)$ and $\phi(\omega_e) = \int d\omega_o S(\omega_o, \omega_e)$; that is, the less often it will be possible to use the frequency of the detected light to discover whether a definite x (y) polarized photon really started off as an e (o)-photon in process 1 or an o (e)-photon in process 2. As the e and o spectra become more similar, these two processes become more and more indistinguishable, leading to a higher interference visibility as more and more of the single photons become “process indistinct.”

It is possible to interpret the coincidence count probability, (4.26), in a similar fashion, keeping in mind that all the terms represent contributions arising from different types of coincidence detection, or two-photon, amplitudes. Once again, the term $K \cos(\theta)$ is the modulation term for events which are “process indistinct” but “polarization distinct”. This term arises from the sets of two-photon amplitudes for which both polarizations are knowable in principle, but the creation process is not. The next term, $C(\delta\tau) \cos(\theta)$, is the interference modulation for photon pairs which are both “process indistinct” and “polarization indistinct”. This term arises from amplitudes for the cases where no definite creation process could be assigned to the photon pairs, and for which no definite polarization before the PBS could be assigned to either photon arriving at the detectors. The final term, $D(\delta\tau)$, is the modulation term for photon pairs which are “process distinct” but “polarization indistinct”. This term arises from amplitudes for the cases in which the creation process was identifiable in principle, but the polarization of each detected photon before the PBS was not.

The last term represents the standard pulsed type II HOM interference seen in the previous chapter, and produces a trough structure whose depth depends on the symmetry of the joint spectral emission amplitude for each process taken separately. The much lower counting rate in the central dip produced by $C(\delta\tau) \cos(\theta)$ is the signature of improved interference visibility for the photon pairs with symmetrized joint emission spectra. The degree to which our experimental data show this improved visibility is a measure of the success of our “engineering indistinguishability” method.

References for Chapter 4

- [1] W. P. Grice, Ph.D. thesis, University of Rochester, 1998 (unpublished).
- [2] T. B. Pittman *et al.*, Phys. Rev. Lett. **77**, 1917 (1996).
- [3] M. W. Noel, Ph.D. thesis, University of Rochester, 1996 (unpublished).
- [4] Y. H. Shih and A. V. Sergienko, Phys. Lett. A **191**, 201 (1994).
- [5] T. J. Herzog, J. G. Rarity, H. Weinfurter, and A. Zeilinger, Phys. Rev. Lett. **72**, 629 (1994).
- [6] H. Weinfurter *et al.*, in *Fundamental Problems in Quantum Theory: A Conference Held in Honor of Professor John A. Wheeler*, edited by D. M. Greenberger and A. Zeilinger, Annals of the New York Academy of Sciences Vol. 755 (New York Academy of Sciences, New York, 1995), p. 61.
- [7] T. J. Herzog, P. G. Kwiat, H. Weinfurter, and A. Zeilinger, Phys. Rev. Lett. **75**, 3034 (1995).

This page intentionally left blank.

Chapter 5

Locality violations in the circular polarization basis

5.1 Introduction

5.1.1 Non-violations of Bell's inequality

We now turn our attention away from complementarity, and investigate another celebrated feature of quantum mechanics: nonlocality. As explained in Chapter 1, nonlocality refers to the incompatibility of quantum mechanics with the Einstein-Podolsky-Rosen axioms known as *realism* and *locality* [1]. This incompatibility is apparent from the fact that quantum mechanics predicts a violation of Bell's inequality [2], which must hold true for any local-realistic hidden-variable (LHV) theories. In the years since Bell's discovery, numerous experiments have been undertaken to determine whether nature, too, exhibits this nonlocal behavior. If violations of Bell's inequality could be demonstrated experimentally, it would end the search for a local-realistic theory capable of completing quantum mechanics in the manner envisioned by Einstein [3].

To date, no such violations have been established in a loophole-free experiment: the difficulty is that currently available detectors do not have high enough efficiencies for conclusive experiments. However, the Clauser-Horne-Shimony-Holt (CHSH) form of Bell's inequality [4], which requires a supplementary "fair sampling" assumption, has been shown to be violated in experiments with correlated pairs of photons from atomic cascade sources [5-8] and from parametric downconverters [9-12]. Because the supplementary assumption is a seemingly reasonable one, the results of these experiments are taken by most researchers as strong evidence that the nonlocality inherent to quantum mechanics is a fundamental property of nature, and, indeed, is a signature of the nonclassical character of entangled systems.

There are, however, at least two published examples of experiments whose results appear to contradict the others, in the sense that they do not violate the CHSH inequality [13,14]. In both of these experiments, the polarization correlations of photons generated by an atomic cascade source were measured in the circular, rather than the linear, polarization basis. The change of basis does not affect the predictions of quantum mechanics (as we shall see), and should not prevent violations of the CHSH inequality. In the interest of clarifying this situation, we performed a new measurement of these correlations with the aim of either confirming or refuting the anomalous results.

5.1.2 The Clauser-Horne-Shimony-Holt inequality

The general arrangement required for an optical test of the CHSH inequality is shown in Figure 5.1; the source in the center emits a pair of photons traveling in opposite directions, whose polarizations are described by the rotationally-invariant entangled state

$$|\psi\rangle = \frac{1}{\sqrt{2}} \left\{ |1\rangle_{Ax} |1\rangle_{By} - |1\rangle_{Bx} |1\rangle_{Ay} \right\}. \quad (5.1)$$

The polarizations of the two photons are measured by spacelike separated observers Alice and Bob, who pass the light through polarizers (P) and onto photodetectors (D); the detection of a photon with the linear polarizer P oriented at an angle θ relative to some fixed x -axis is taken to be a measurement of that photon's polarization. Assuming perfectly efficient detectors, the quantum mechanical prediction for the probability of measuring polarizations θ_A at D_A and θ_B at D_B when the photons are in the state given by Eq. (5.1) is

$$P(\theta_A, \theta_B) = \frac{1}{2} \sin^2(\theta_B - \theta_A). \quad (5.2)$$

The Clauser-Horne-Shimony-Holt inequality for the measured coincidence counting rates $R(\theta_A, \theta_B)$ is

$$|R(\theta_A, \theta_B) - R(\theta_A, \theta_B)| + R(\theta_A, \theta_B) + R(\theta_A, \theta_B) - R(\theta_A, -) - R(-, \theta_B) \leq 0, \quad (5.3)$$

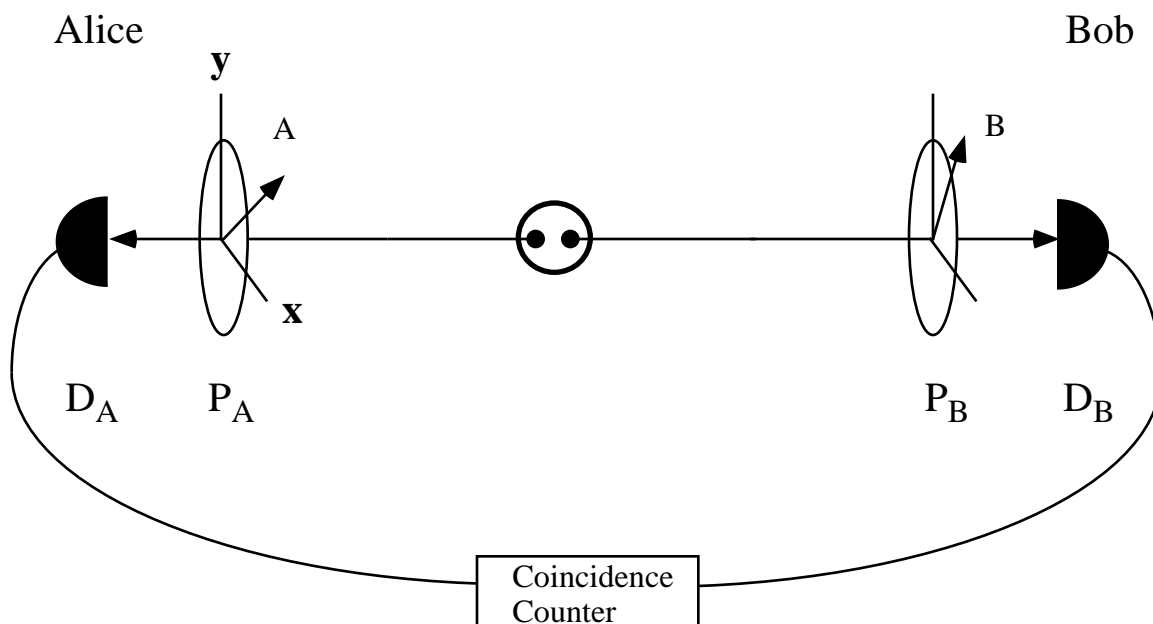


Figure 5.1. Experimental arrangement for measuring two-photon polarization correlations, $P(\theta_A, \theta_B)$. A central source emits pairs of polarization-entangled photons, which are passed through polarizers P_A, P_B , and detected at photodetectors D_A, D_B . Provided the subensemble of detected counts is unbiased (the fair-sampling assumption), the measured coincidence counting rate is indicative of the correlation function. Many experiments of this type have demonstrated violations of the CHSH inequality.

where $\theta_A, \bar{\theta}_A, \theta_B$ and $\bar{\theta}_B$ are any four polarization angles, and the dash $(-)$ indicates a joint counting rate with a polarizer removed. This inequality can be derived from the axioms of locality and realism if a supplementary assumption, the so-called “fair sampling assumption,” is introduced. The assumption is that if a pair of photons emerges from Alice and Bob’s polarizers, the probability of their subsequent joint detection is independent of the orientations of the polarizers. This assumption allows us to identify the joint probability in (5.2) for the ensemble of all *emitted* pairs with the measured relative frequency of joint detections within the subensemble of all *detected* coincidence counts, so that

$$P(\theta_A, \theta_B) = \frac{R(\theta_A, \theta_B)}{R(-, -)}, \quad (5.4)$$

where

$$R(-, -) = \alpha_A \alpha_B R_0 \quad (5.5)$$

is the rate of coincidence detections when both polarizers are removed and the source emits pairs at the rate R_0 . Note that within this subensemble,

$$P(-, -) = 1. \quad (5.6)$$

Furthermore, because the space of transverse polarizations is a two-dimensional vector space, we have the identities

$$\begin{aligned} P(-, -) &= P(\theta_A, -) + P(\bar{\theta}_A, -) = P(-, \theta_B) + P(-, \bar{\theta}_B) \\ P(\theta_A, -) &= P(\theta_A, \theta_B) + P(\theta_A, \bar{\theta}_B) \\ P(-, \theta_B) &= P(\theta_A, \theta_B) + P(\bar{\theta}_A, \theta_B). \end{aligned} \quad (5.7)$$

Here we introduce the notation $\bar{\theta} = \theta \pm \pi/2$ to denote the linear polarization orthogonal to θ .

With the help of (5.4) - (5.7), the CHSH inequality may be rewritten as

$$S = |P(\theta_A, \theta_B) - P(\theta_A, \bar{\theta}_B)| + |P(\bar{\theta}_A, \theta_B) - P(\bar{\theta}_A, \bar{\theta}_B)| \leq 0. \quad (5.8)$$

For the particular choices

$$\begin{aligned}
 \theta_A &= \theta_0 \\
 \theta_B &= \theta_0 + 3\pi/8 \\
 \theta_A &= \theta_0 + 3\pi/4 \\
 \theta_B &= \theta_0 + \pi/8
 \end{aligned}
 \tag{5.9}$$

the form of $P(\theta_A, \theta_B)$ given by quantum mechanics in (5.2) yields the result

$$S = \frac{1}{\sqrt{2}} - \frac{1}{2} \quad 0.207,
 \tag{5.10}$$

in violation of (5.8).

5.1.3 Entangled states in the circular basis

Figure 5.2 shows the insertion of a pair of quarter-wave plates into the two photon paths with their ordinary axes oriented at an angle $\chi = \pi/4$ to the x axis. These quarter-wave plates connect the linear x and y -polarization modes at the polarizers (a_x, a_y) to right-handed and left-handed circular polarization modes at the source:

$$\begin{aligned}
 \hat{a}_x &= \frac{1}{2}(\hat{a}_x + \hat{a}_y) - \frac{i}{2}(\hat{a}_x - \hat{a}_y) = \hat{a}_R \\
 \hat{a}_y &= \frac{1}{2}(\hat{a}_x + \hat{a}_y) + \frac{i}{2}(\hat{a}_x - \hat{a}_y) = \hat{a}_L
 \end{aligned}
 \tag{5.11}$$

where the RHC and LHC modes may be written more simply as properly phased superpositions of the linearly polarized modes X and Y :

$$\begin{aligned}
 \hat{a}_R &= \frac{1}{\sqrt{2}}(\hat{a}_x - i\hat{a}_y) \\
 \hat{a}_L &= \frac{1}{\sqrt{2}}(\hat{a}_x + i\hat{a}_y)
 \end{aligned}
 \tag{5.12}$$

with inverse transformations

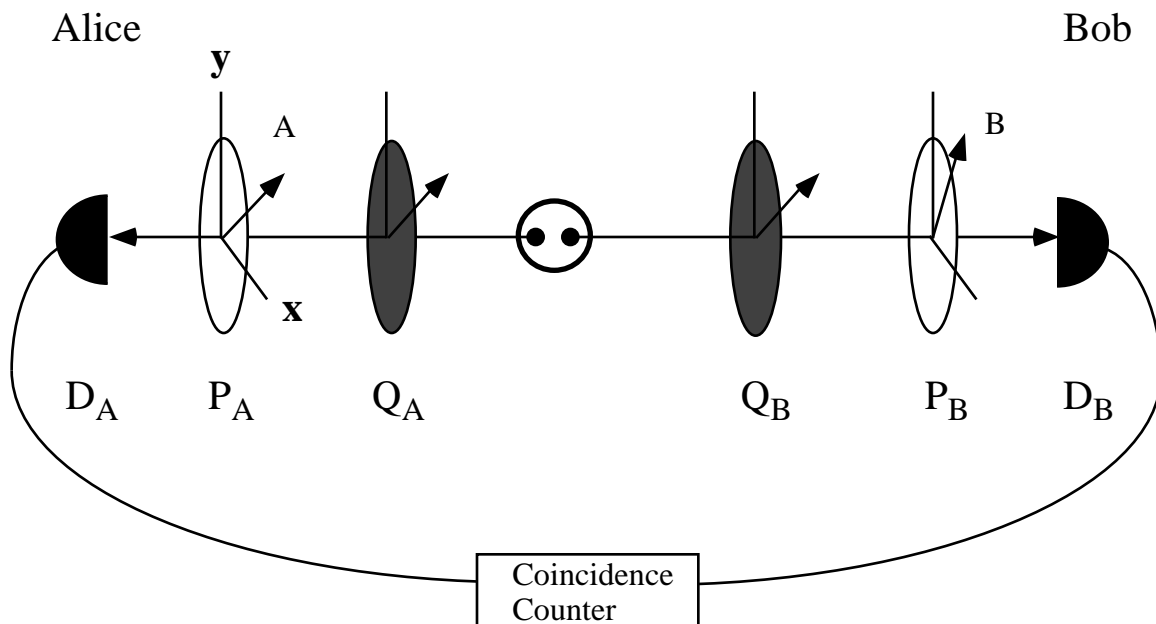


Figure 5.2 Experimental arrangement for measuring two-photon correlations in the circular basis. The quarter-wave plates Q_A , Q_B are inserted at an orientation $\chi = \pi/4$, transforming linear polarizations into circular ones and vice versa. The entanglement is preserved in this basis, and the same violations of Bell's inequality are predicted by quantum mechanics. However, two early experiments performed with the plates inserted failed to demonstrate violations of the CHSH inequality.

$$\begin{aligned}\hat{a}_x &= \frac{1}{\sqrt{2}}(\hat{a}_L + \hat{a}_R) \\ \hat{a}_y &= \frac{-i}{\sqrt{2}}(\hat{a}_R - i\hat{a}_L)\end{aligned}\tag{5.13}$$

For the right-hand side of Eqs. (5.11), the modes $\hat{a}_x = (\hat{a}_x + \hat{a}_y)/\sqrt{2}$, $\hat{a}_y = (\hat{a}_x - \hat{a}_y)/\sqrt{2}$ were chosen, but because of rotational invariance, X and Y can be any two orthogonal linear polarizations in the definitions (5.12) and (5.13). In particular, we may choose $X = x$ and $Y = y$ so that the Hermitian conjugate of Eqs. (5.13) implies that the states before the quarter-wave plates may be expressed in the circular basis as

$$\begin{aligned}|1\rangle_x &= \frac{1}{\sqrt{2}}(|1\rangle_R + |1\rangle_L) \\ |1\rangle_y &= \frac{i}{\sqrt{2}}(|1\rangle_R - |1\rangle_L)\end{aligned}\tag{5.14}$$

With these substitutions, the entangled state in (5.1) becomes

$$|\psi\rangle = \frac{i}{\sqrt{2}}(|1\rangle_{AR}|1\rangle_{BL} - |1\rangle_{AL}|1\rangle_{BR})\tag{5.15}$$

This expression for $|\psi\rangle$ has the same symmetric and entangled form as the one in the linear polarization basis, and differs from it only by an inconsequential phase factor. Since measurements of the linear polarizations x and y after the quarter-wave plates are actually measurements of the L and R modes according to (5.11), the same violations of the CHSH inequality should result when the plates are inserted [15]. It is this conclusion which makes the earlier failures to observe violation the CHSH inequality under these circumstances [13,14] so curious.

5.2 Schematic and theory

5.2.1 Schematic of the experiment

A schematic of our experiment [16] is shown in Figure 5.3. Two photons are emitted simultaneously with similar frequencies and polarizations¹ from a type-I spontaneous parametric downconversion source (PDC). The polarization of the signal photon is labeled as x . The polarization of the idler photon is rotated to be orthogonal to x by a suitably oriented half-wave plate (R_0). The x and y -polarized photons are then incident from opposite sides on beamsplitter (BS) at near-normal incidence.

The mixed beams emerge from BS traveling in almost opposite directions and enter analyzer arms A and B . Each analyzer consists of a quarter-wave plate (Q_A, Q_B), a linear polarizer (P_A, P_B), and a photodetector (D_A, D_B). Depending on the orientation (θ_A, θ_B) of each quarter-wave plate relative to x , it may produce polarizations ranging from linear (unchanged) to circular when the input light is linearly polarized; alternatively, if the input light is circularly polarized, the output polarization may range from circular (unchanged) to linear. Thus, a measurement of linear polarization after a suitably oriented quarter-wave plate is actually a measurement of the input light in the circular polarization basis. The polarizers are oriented at angles θ_A and θ_B with respect to x , and pass the linear polarizations θ_A and θ_B to the detectors. The coincidence counting rates $R(\theta_A, \theta_B)$ are measured for various settings ($\theta_A, \theta_A, \theta_B, \theta_B$) of the polarizers.

5.2.2 Quantum state of the light

Before the beamsplitter, the state of the light may be approximated with the perturbative method of Chapter 1:

¹ Though the signal and idler photons must propagate as ordinary waves inside the crystal, as demanded by type-I phase-matching, they may emerge with different polarizations if the optic axis of the crystal is tilted [17]. In this experiment, they are nevertheless made orthogonal by the half-wave plate (R).

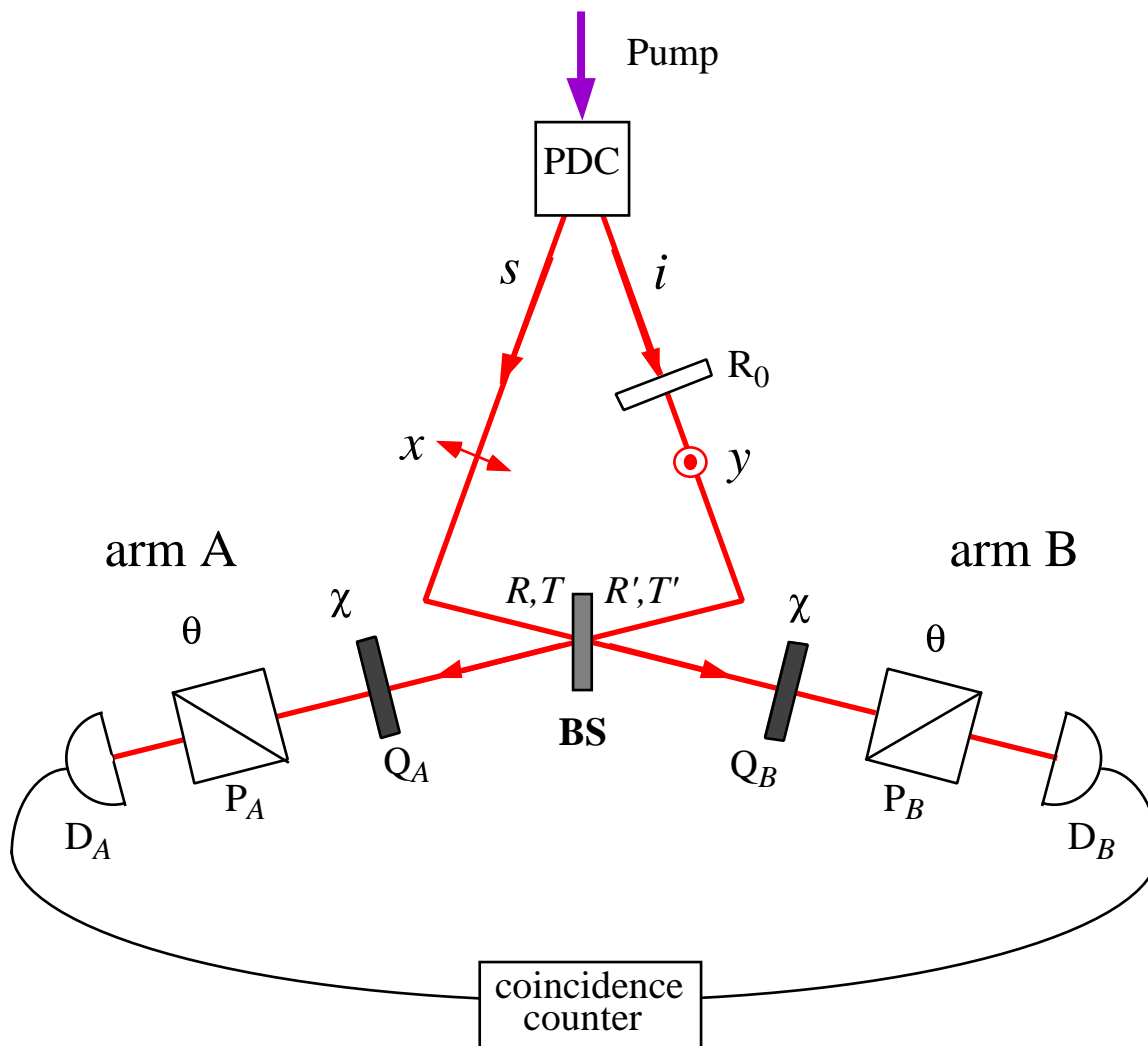


Figure 5.3 Schematic of the experiment for testing local realism in various polarization bases. The idler polarization is made orthogonal to that of the signal with the help of the rotator R_0 . The photons then impinge onto a beamsplitter with reflectivities and transmissivities that are ideally equal in magnitude. The photons which emerge in arms A and B each pass through a quarter-wave plate Q and a polarizer P before falling onto a detector D.

$$\begin{aligned}
|\psi\rangle &= |vac\rangle + \eta |1\rangle_{s,x} |1\rangle_{i,y} \\
&= |vac\rangle + \eta |\psi^{(1)}\rangle.
\end{aligned}
\tag{5.16}$$

Here we have suppressed the frequency labels and treated the downconversion process in the single-mode approximation (see Appendix A). The signal and idler are assumed to be degenerate in frequency. Only the second part, $|\psi^{(1)}\rangle$, of the state $|\psi\rangle$ will contribute photon counts.

At the beamsplitter, each photon may be transmitted or reflected independently of the other, so that we may write [18]

$$|\psi^{(1)}\rangle = (R|1\rangle_{Ax} + T|1\rangle_{Bx}) (R|1\rangle_{By} + T|1\rangle_{Ay}).
\tag{5.17}$$

The labels A and B refer to the modes for arms A and B , and the complex transmissivities T , T and reflectivities R , R characterize the beamsplitter BS². Note that this state is not an entangled one, because it is a direct product of single-photon states. The product may be expanded to yield

$$|\psi^{(1)}\rangle = RR |1\rangle_{Ax} |1\rangle_{By} + TT |1\rangle_{Bx} |1\rangle_{Ay} + RT |1\rangle_{Ax} |1\rangle_{Ay} + TR |1\rangle_{Bx} |1\rangle_{By}
\tag{5.18}$$

This is a pure state, representing four possible outcomes at the beamsplitter which must be indistinguishable in principle from each other via auxiliary measurements. If it were possible to distinguish which of these outcomes actually occurred for a given pair of photons, say by measuring their relative arrival times at the detectors, or their frequencies, the pure state $|\psi^{(1)}\rangle$ would have to be replaced by a density matrix representing the (classical) probabilities of these outcomes, and no quantum interference effects would be possible -- a fact which has been amply demonstrated by the preceding three chapters. For this reason, frequency-degenerate downconversion must be used, and the optical paths of the photon wavepackets to the beamsplitter BS must be equal to within the coherence time of the detected light, as described in Chapter 2.

² Because of the near-normal incidence of the photons onto the beamsplitter, we may assume that variations of T and R with polarization are negligible. Hence, we will not bother to distinguish between T_x , T_y , etc.

All four of the amplitudes in (5.18) may contribute to the single-channel counting rates at the detectors; however, the last two terms represent the cases in which both photons end up in the same arm, and do not contribute to the coincidence counting rates. Thus, coincidence counting has the effect of projecting the state onto the subspace in which one photon is present in each arm. The (renormalized) projection of $|\psi^{(1)}\rangle$ onto this subspace is

$$|\psi_S^{(1)}\rangle = \frac{1}{\sqrt{|RR|^2 + |TT|^2}} \{RR |1\rangle_{Ax} |1\rangle_{By} + TT |1\rangle_{Bx} |1\rangle_{Ay}\}, \quad (5.19)$$

which is an entangled state. It is this entanglement which allows the counting rates to violate a Bell inequality,³ as we will now show.

5.2.3 Predicted counting rates

According to quantum mechanics, the probability of detecting a pair of photons after the polarizers within the subspace just described -- that is, given that there is a photon in each arm -- is

$$\begin{aligned} P_{AB}(\theta_A, \theta_B) &= \langle \psi_S^{(1)} | \hat{a}_A^\dagger(\theta_A) \hat{a}_B^\dagger(\theta_B) \hat{a}_B(\theta_B) \hat{a}_A(\theta_A) | \psi_S^{(1)} \rangle \\ &= \left| \hat{a}_B(\theta_B) \hat{a}_A(\theta_A) | \psi_S^{(1)} \rangle \right|^2 \end{aligned} \quad (5.20)$$

where, for the moment, we assume the photodetectors are perfectly efficient. Here $\hat{a}_A(\theta_A)$ and $\hat{a}_B(\theta_B)$ are the annihilation operators for the modes reaching the detectors; due to the action of the polarizers and quarter-wave plates, these operators may be written in terms of the modes just after the beamsplitter as

$$\begin{aligned} \hat{a}_\mu(\theta_\mu) &= \left[\cos(\theta_\mu - \chi_\mu) \cos(\chi_\mu) - e^{i\phi_\mu} \sin(\theta_\mu - \chi_\mu) \sin(\chi_\mu) \right] \hat{a}_{\mu x} \\ &\quad + \left[\cos(\theta_\mu - \chi_\mu) \sin(\chi_\mu) - e^{i\phi_\mu} \sin(\theta_\mu - \chi_\mu) \cos(\chi_\mu) \right] \hat{a}_{\mu y}, \end{aligned} \quad (5.21)$$

³This approach is valid provided that the beamsplitter does not transmit or reflect individual photons according to their particular values of those “hidden variables” which control their subsequent photodetection; we are making a tacit “random beamsplitter” assumption here [19].

where $\mu = A, B$, the polarizers are taken to be ideal, and the ϕ_μ are the relative phase delays between the ordinary and extraordinary waves imposed by the quarter-wave plates⁴. The parameters ϕ and χ together determine the basis (linear, circular, or elliptical) for the polarization measurements. The operators $\hat{a}_{\mu x}, \hat{a}_{\mu y}$ are the annihilation operators for the modes just after the beamsplitter. We then have

$$\begin{aligned}
P_{AB}(\theta_A, \theta_B) = & \left[RR \left[\cos(\theta_A - \chi_A) \cos(\chi_A) - e^{i\phi_A} \sin(\theta_A - \chi_A) \sin(\chi_A) \right] \right. \\
& \left[\cos(\theta_B - \chi_B) \sin(\chi_B) - e^{i\phi_B} \sin(\theta_B - \chi_B) \cos(\chi_B) \right] \\
& + TT \left[\cos(\theta_B - \chi_B) \cos(\chi_B) - e^{i\phi_B} \sin(\theta_B - \chi_B) \sin(\chi_B) \right] \\
& \left. \left[\cos(\theta_A - \chi_A) \sin(\chi_A) - e^{i\phi_A} \sin(\theta_A - \chi_A) \cos(\chi_A) \right] \right]^2 \\
& \left(|RR|^2 + |TT|^2 \right)^{-1}.
\end{aligned} \tag{5.22}$$

This may be simplified further if the beamsplitter is symmetric and characterized by the values

$$R = R = iT = iT = \frac{1}{\sqrt{2}}. \tag{5.23}$$

Moreover, if the quarter-wave plates have the same orientation, $\chi_A = \chi_B = \chi$, then the coincidence probability reduces to

$$P_{AB}(\theta_A, \theta_B) = \frac{1}{2} \left| \cos(\theta_A - \chi) \sin(\theta_B - \chi) e^{i\phi_B} - \sin(\theta_A - \chi) \cos(\theta_B - \chi) e^{i\phi_A} \right|^2. \tag{5.24}$$

Finally, if the waveplates produce identical phase delays so that $\phi_A = \phi_B = \phi$, this simplifies to become

$$P_{AB}(\theta_A, \theta_B) = \frac{1}{2} \sin^2(\theta_B - \theta_A), \tag{5.25}$$

which is of the usual form for systems exhibiting violations of Bell-type inequalities, as presented in (5.2). This result is independent of ϕ and χ , implying the same coincidence

⁴ For an ideal quarter-wave plate, the relative phase delay has the fixed value $\phi = k\lambda/4$; ϕ is introduced here as a free parameter to allow for the possibility of retardation errors in the waveplates used in the experiment.

probability no matter what basis (circular, linear, or elliptical) is chosen for the measurements, as expected from the symmetry considerations in Section 5.1. The expected coincidence counting rate is given by

$$R_{AB} = \alpha_A \alpha_B R_0 P_{AB}(\theta_A, \theta_B), \quad (5.26)$$

where, as before, α_A and α_B represent the detector quantum efficiencies and R_0 is the rate of photon pair emission into the detected signal and idler modes.

5.3 Experimental procedure and results

5.3.1 Apparatus

The pump source was a 70 mW ultraviolet laser beam generated by a cw Ar⁺ laser operating at a wavelength of 351.1 nm. The downconversion medium was a 2.5 cm long LiIO₃ crystal cut and oriented for frequency-degenerate type-I phase-matching. The signal and idler beams had a mean wavelength of $\lambda = 702.2$ nm and were selected by a combination of 1 mm apertures near the PDC and in front of the detectors. The beamsplitter BS had nominal values of $|R|^2 = |T|^2 = .500 \pm .005$. The rotator R_0 was a multi-order half-wave plate, while Q_A and Q_B were multi-order quarter-wave plates; all three plates were antireflection coated and produced retardation errors of $\phi < k\lambda/200$.

The polarizers P_A and P_B were Wollaston polarizing beam splitters which transmitted the polarization θ and rejected $\bar{\theta}$ with an extinction ratio of $1:10^5$ for the intensities. Because these polarizers deviated the beam significantly when rotated, they were mounted with a fixed orientation and the polarization angles θ_A and θ_B were adjusted by rotating a pair of additional half-wave plates, R_A and R_B , through angles $\theta_A/2$ and $\theta_B/2$ (see Figure 5.4). In this manner, the light was rotated before impinging onto the fixed polarizers, which was operationally equivalent to rotating the polarizers themselves. An additional benefit from this scheme was that the light falling on the photodetectors always had the same

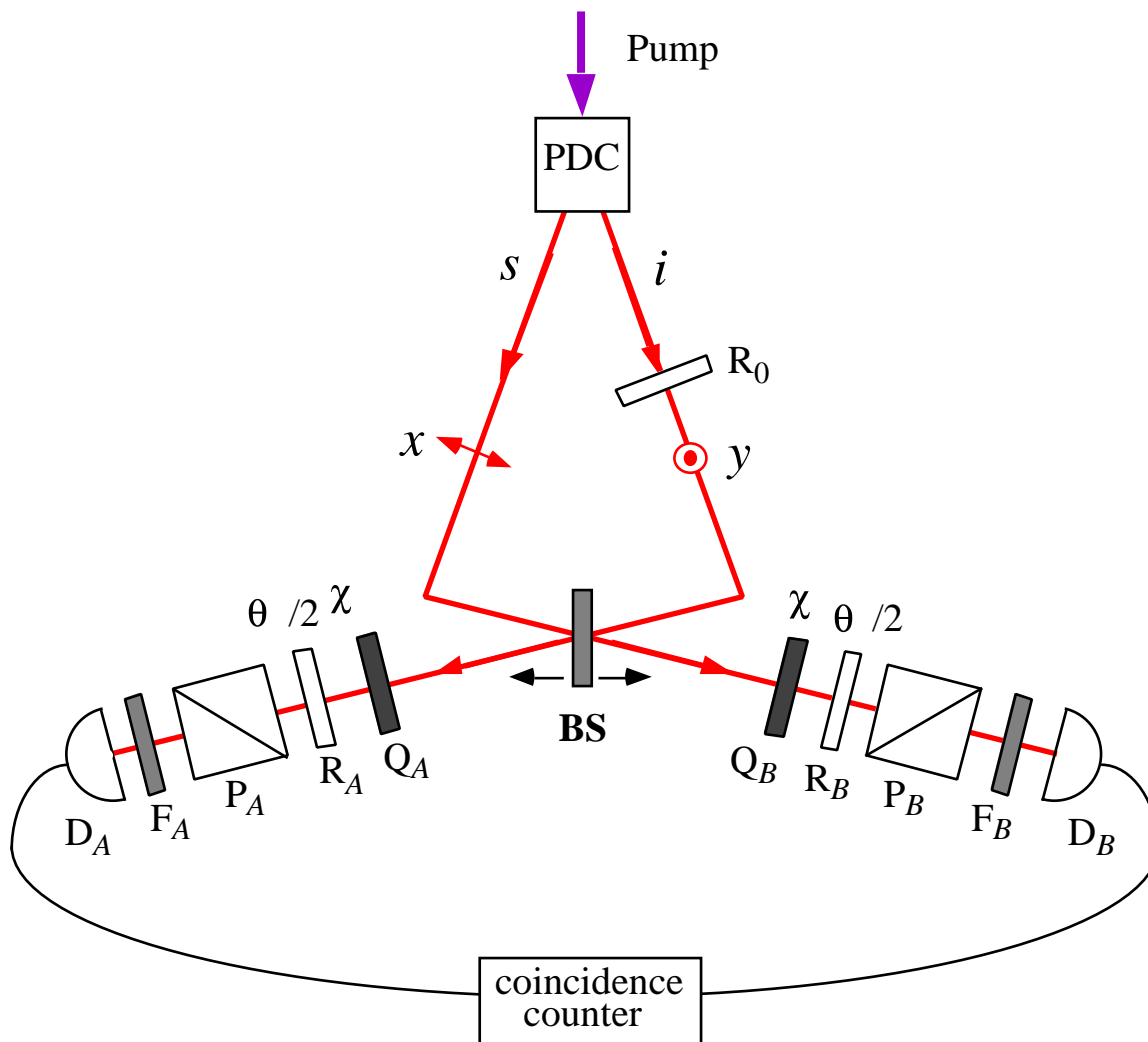


Figure 5.4 Diagram of the performed experiment, which differed slightly from the schematic presented in Figure 5.3. The beam splitter was mounted on a motorized translation stage for the purpose of equalizing the signal and idler path lengths to BS. The rotators R_A and R_B were used to select the polarizations transmitted to the detectors by P_A and P_B . Interference filters F_A and F_B were used in conjunction with apertures (not shown) to select the frequency-degenerate downconversion.

polarization as θ_A and θ_B were varied, so that any possible systematic effects arising from polarization-dependent detector efficiencies were eliminated⁵.

The photodetectors were EG&G model SPCM-200 avalanche photodiodes with 4.5 ns jitter time, 150 ns dead time, and roughly 50% quantum efficiency. Lenses were used to focus the light onto the active areas of these detectors, 100 μm in diameter. The 150 ns TTL pulses generated by the detectors were used to trigger discriminators, which emitted 4.5 ns NIM pulses that were fed to single-channel counters and to a coincidence counter. Signals arriving together at the coincidence counter within a 9 ns resolving time were considered to be simultaneous. The coincidence counts were corrected for a background level of “accidental” coincidences due to the arrival of signals from uncorrelated photons within the coincidence window; the rate of accidental coincidence was computed from the measured single-channel counting rates and the coincidence resolving time. Interference filters F_A and F_B were placed in front of the detectors; these filters had a bandwidth of 1 nm, centered on 702 nm, and a maximum transmission of 60%.

For the counting rates calculated with the pure state in Eq. (5.19) to be valid, the optical paths to the beamsplitter had to be balanced to within the 500 μm coherence length determined by the filter bandwidths. To accomplish this, the beamsplitter was mounted on a motorized translation stage capable of making reproducible displacements in increments of 10 μm over a range of several mm. The beamsplitter position was scanned to produce Hong-Ou-Mandel type interference “dips” in the coincidence counts [20]; the counts for the experiment were recorded at the lowest point in the dip, where the quantum interference was at a maximum⁶.

⁵ This does not eliminate the need to make a “fair sampling” assumption, since the efficiencies could theoretically depend on the values of “hidden variables” whose measured distributions might be post-selected on the basis of the settings θ_A and θ_B .

⁶ Ordinarily, this interference should not occur when the photons incident on the beamsplitter have orthogonal polarizations: the reason is that they are distinguishable in principle via an auxiliary polarization measurement. However, once the photons have passed through the polarizers P_A and P_B , this information is “erased” in the spirit (though not the letter) of the quantum eraser experiment [21], and interference returns.

5.3.2 Results

We collected coincidence and single-channel counts for the settings of θ_A and θ_B specified in Eqs. (5.9), which gave the maximum violation of the CHSH inequality, for the particular case $\theta_0 = 0$. We also recorded the counts for the remaining polarization angles needed to obtain $R(-, -)$ via the polarization completeness relation similar to the first of Eqs. (5.7):

$$R(-, -) = R(\theta_A, \theta_B) + R(\bar{\theta}_A, \theta_B) + R(\theta_A, \bar{\theta}_B) + R(\bar{\theta}_A, \bar{\theta}_B). \quad (5.27)$$

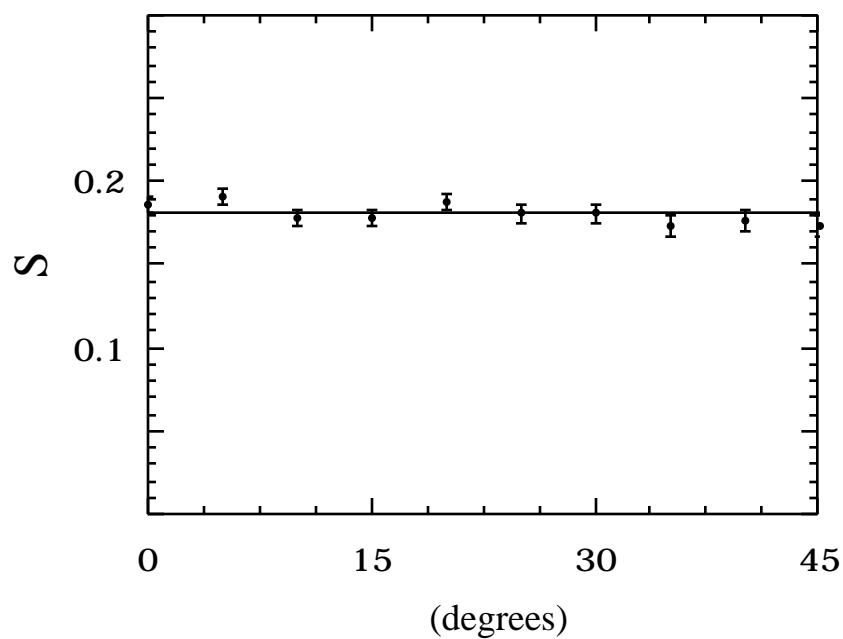
Typical counting rates were on the order of 50,000 per second in the singles, and from 200 to 1200 per second in the coincidences. The counts were collected for intervals of 10 seconds, and coincidence counts were corrected for accidentals. The joint probabilities $P(\theta_A, \theta_B)$ were computed according to (5.4), and the CHSH parameter S appearing in (5.8) was computed from these. We repeated this procedure for seven settings of the quarter wave plate orientations $\chi_A = \chi_B = \chi$ ranging from 0 to $\pi/4$; this implies measurements in bases ranging from linear to circular, with five elliptical bases in between. We set the angles θ_A , θ_B , χ_A , and χ_B to an accuracy of about 0.1° .

The resulting values of S are displayed in Figure 5.5. Although none of the values equal the theoretical maximum of $S = 0.207$, they are all greater than 0.170, and clearly violate (5.8). The largest value, $S(\chi = 5^\circ) = 0.192 \pm .005$, violates the CHSH inequality by 38 standard deviations. The value found for the circular basis, $S(\chi = 45^\circ) = 0.174 \pm .006$, is in violation by 29 standard deviations.

5.4 Discussion

5.4.1 Comparison with the results of Clauser and Duncan, et al.

These results are in conflict with the two earlier reported experiments with quarter-wave plates [13,14] that exhibited no violation of the CHSH inequality in the basis of



χ	0°	5°	10°	15°	20	25	30	35	40	45
$S(\chi)$	0.187	0.192	0.179	0.179	0.188	0.181	0.181	0.174	0.177	0.174
σ_s	0.005	0.005	0.005	0.005	0.005	0.005	0.006	0.006	0.006	0.006

Figure 5.5 Experimental results for the quantity S and its standard deviation for various settings χ of the quarter-wave plates. The largest value violates the CHSH inequality $S \leq 0$ by 38 standard deviations.

circular polarizations. We can only speculate here as to why the earlier attempts failed, but one clue did present itself during the course of our experiment: a dependence of S on the parameter θ was observed whenever the photons did not pass through the centers of the quarter-wave plates. This dependence could have been caused by surface imperfections in the wave plates, so that when they were turned in the path of a non-centered beam, the photons encountered slightly different phase-shifts from one another for different settings. This effect would invalidate the assumption $\phi_A = \phi_B = \phi$ required for the final, independent form of the joint detection probability (5.25). In effect, these imperfections may have resulted in the measurements of Alice and Bob not being performed in quite the same basis, which would lead to a reduction of the strong correlations necessary for the violation of the CHSH inequality. This is in agreement with Clauser's speculation that "retardation errors" were too large in his experiment [13] to show the violation.

5.4.2 Supplementary assumptions

That quantum mechanics violates Bell's inequality, and hence, local realism, is an undisputed fact. What is disputed is whether nature can be shown to exhibit such violations. To cast the theoretical arguments into a form testable by our apparatus, we made use of several auxiliary assumptions that lie outside the axioms of locality and realism required for Bell's inequality. Because of this, our experimental results can only be said to contradict locality and realism if these additional assumptions are valid.

The first assumption is that two orthogonal polarizations form a complete polarization basis. This allows the use of the identities (5.7) in the derivation of the final form of the CHSH inequality in (5.8). The assumption is common to both classical and quantum optics, and it seems to be natural in treating optical polarization phenomena by electromagnetic theory. It is not often contradicted even by LHV theory advocates, but objections have been raised against an experiment similar to this one [22] on the grounds that LHV theories are not required to describe polarization in this fashion. Presumably,

though, they are required to duplicate all of the well-known physical observations attributed to the vector nature of polarization, such as Malus' Law⁷.

The second assumption is that the beamsplitter transmittances and reflectances are constant, in that they do not make selections as to which photons will end up in opposite or similar arms of the apparatus based on the distribution of whatever hidden variables might ultimately determine their detection. This assumption validates the projection procedure that produces the renormalized, entangled state in (5.19) from the factorizable one in (5.18). An objection [25] has been raised against this renormalization procedure, and it has been noted that without it, violations of Bell-type inequalities are impossible to realize in type-I downconversion schemes with beam splitters like the one presented here. The issue is not only one of normalization, but also of the replacement of certain single-channel detection rates $R(\theta_A), R(\theta_B)$ by the joint detection rates $R(\theta_A, -), R(-, \theta_B)$ that appear in (5.3).

The third assumption is the fair-sampling assumption used in the original derivation of the CHSH inequality, and in the steps leading to (5.8). Two points should be made with regard to this assumption. First, the inequality (5.8) may be derived with the help of a “no-enhancement” assumption instead of the fair sampling assumption; this was first done by Clauser and Horne in 1974 [26]. The no-enhancement assumption is “weaker” than the fair-sampling assumption, in the sense that it rules out an even broader class of local-realistic theories [27]. Second, it has been shown that the fair-sampling assumption is not equivalent to the assumption common to quantum mechanics that photodetection is a “random” process; the latter is actually a more stringent requirement than is needed for the derivation of the CHSH inequality [28].

Finally, this experiment rests on the assumption common to all other reported “violations of locality” except one [8]: that the properties of the photons at the source and at distant analyzers are not affected by the settings of local analyzers *even when they can be connected by a light signal*. In other words, despite the fact that spacelike separation is not

⁷ See, as examples, the LHV theories presented in references [23,24].

enforced in this experiment, the two analyzer systems and the source are still maintained as being independent from one another in the spirit of Einstein's locality condition. This mutual independence is crucial to the derivation of Bell's inequality and the CHSH inequality, and when it is assumed to hold even for non-spacelike separated systems, it is given the name *Bell locality*; the relativistic demand that only spacelike separated systems be mutually independent is then referred to as *Einstein locality* or *Einstein separability* [29,30].

What this experiment shows, then, is that not all of the following five statements can be true: There exist in nature elements of physical reality as defined by *realism*; The settings of one analyzer do not affect measurements at the other, or the source, as demanded by *Bell locality*; The *fair sampling* assumption is valid; Polarization is a two-dimensional linear vector; The beamsplitter is unbiased. The last three statements on this list may be regarded as "loopholes" in the experiment, in the sense that negation of any one of them allows the experimental results to be predicted by a LHV theory. The second statement is also a loophole, as it is an easily-negated substitute for Einstein locality⁸. As of this writing, no "loophole-free" violation of a Bell inequality has been observed, but recent progress toward that goal has been reported in the literature [32-34].

⁸ See, for example, the class of LHV theories proposed in [31]

References for Chapter 5

- [1] A. Einstein, B. Podolsky, and N. Rosen, *Phys. Rev.* **47**, 777 (1935).
- [2] J. S. Bell, *Physics* **1**, 195 (1964).
- [3] F. Selleri, in *Fundamental Problems in Quantum Theory: A Conference Held in Honor of Professor John A. Wheeler*, edited by D. M. Greenberger and A. Zeilinger, *Annals of the New York Academy of Sciences* Vol. 755 (New York Academy of Sciences, New York, 1995), p. 798.
- [4] J. F. Clauser, M. A. Horne, A. Shimony, and R. A. Holt, *Phys. Rev. Lett.* **23**, 880 (1969).
- [5] S. J. Freedman and J. F. Clauser, *Phys. Rev. Lett.* **28**, 938 (1972).
- [6] A. Aspect, P. Grangier, and G. Roger, *Phys. Rev. Lett.* **47**, 460 (1981).
- [7] A. Aspect, P. Grangier, and G. Roger, *Phys. Rev. Lett.* **49**, 91 (1982).
- [8] A. Aspect, J. Dalibard, and G. Roger, *Phys. Rev. Lett.* **49**, 1804 (1982).
- [9] Z. Y. Ou and L. Mandel, *Phys. Rev. Lett.* **61**, 50 (1988).
- [10] Y. H. Shih and C. O. Alley, *Phys. Rev. Lett.* **61**, 2921 (1988).
- [11] T. E. Kiess, Y. H. Shih, A. V. Sergienko, and C. O. Alley, *Phys. Rev. Lett.* **71**, 3893 (1993).
- [12] P. G. Kwiat *et al.*, *Phys. Rev. Lett.* **75**, 4337 (1995).
- [13] J. F. Clauser, *Nuovo Cimento* **338**, 740 (1976).
- [14] A. J. Duncan, H. Kleinpoppen, and Z. A. Sheikh, in *Bell's Theorem and the Foundations of Modern Physics*, edited by A. van der Merwe, F. Selleri and G. Tarozzi (World Scientific, Singapore, 1991), p. 161.
- [15] L. De Caro, *Found. Phys. Lett.* **2**, 151 (1989).
- [16] J. R. Torgerson, D. Branning, C. H. Monken, and L. Mandel, *Phys. Rev. A* **51**, 4400 (1995).
- [17] A. Migdall, *J. Opt. Soc. Am. B* **14**, 1093 (1997).
- [18] Z. Y. Ou, C. K. Hong, and L. Mandel, *Opt. Commun.* **63**, 118 (1987).
- [19] J. R. Torgerson, Ph.D. thesis, University of Rochester, 1997 (unpublished).
- [20] C. K. Hong, Z. Y. Ou, and L. Mandel, *Phys. Rev. Lett.* **59**, 2044 (1987).
- [21] P. G. Kwiat, A. M. Steinberg, and R. Y. Chiao, *Phys. Rev. A* **45**, 7729 (1992).

- [22] J. R. Torgerson, D. Branning, C. H. Monken, and L. Mandel, *Phys. Lett. A* **204**, 323 (1995).
- [23] K. Schatten, *Phys. Rev. A* **48**, 103 (1993).
- [24] S. Mirell, *Phys. Rev. A* **50**, 839 (1994).
- [25] A. Garuccio, in *Fundamental Problems in Quantum Theory: A Conference Held in Honor of Professor John A. Wheeler*, edited by D. M. Greenberger and A. Zeilinger, *Annals of the New York Academy of Sciences* Vol. 755 (New York Academy of Sciences, New York, 1995), p. 632.
- [26] J. F. Clauser and M. A. Horne, *Phys. Rev. D* **10**, 526 (1974).
- [27] J. F. Clauser and A. Shimony, *Rep. Prog. Phys.* **41**, 1881 (1978).
- [28] A. Garuccio, *Phys. Rev. A* **52**, 2535 (1995).
- [29] B. d'Espagnat, *Phys. Rev. D* **11**, 1424 (1975).
- [30] A. Aspect, *Phys. Rev. D* **14**, 1944 (1976).
- [31] J. D. Franson, *Phys. Rev. D* **31**, 2529 (1985).
- [32] P. A. Eberhard, *Phys. Rev. A* **47**, R747 (1993).
- [33] P. G. Kwiat, P. A. Eberhard, A. M. Steinberg, and R. Y. Chiao, *Phys. Rev. A* **49**, 3209 (1994).
- [34] E. S. Fry, T. Walther, and S. Li, *Phys. Rev. A* **52**, 4381 (1995).

Chapter 6

Violation of locality without Bell's inequality

6.1 Introduction

6.1.1 The Hardy-Jordan propositions

As mentioned in Chapter 1, two new proposals for demonstrating the incompatibility of quantum mechanics with the Einstein-Podolsky-Rosen (EPR) axioms of locality and realism [1] have been presented within the last decade. These proposals are novel in that they allow quantum mechanics to predict outcomes that directly contradict the expectations of local realism without use of Bell's inequality. While the experiment proposed by Greenberger, Horne, and Zeilinger [2] has remained unperformed, the Hardy-Jordan proposal [3,4] was first implemented in 1994. The results of that experiment are presented in this chapter.

The Hardy-Jordan thought experiment begins in much the same way as the EPR-Bohm thought experiment: a source emits a pair of photons whose anticorrelated polarizations are then measured by spacelike-separated observers Alice and Bob (see Figure 6.1). However, in this version of the experiment, the polarizations are described by the asymmetric, non-maximally entangled state

$$|\psi\rangle = a|1\rangle_{Ax}|1\rangle_{By} + b|1\rangle_{Bx}|1\rangle_{Ay} \quad (6.1)$$

where, unlike the previous situations, $a \neq b$. Normalization demands that

$$|a|^2 + |b|^2 = 1. \quad (6.2)$$

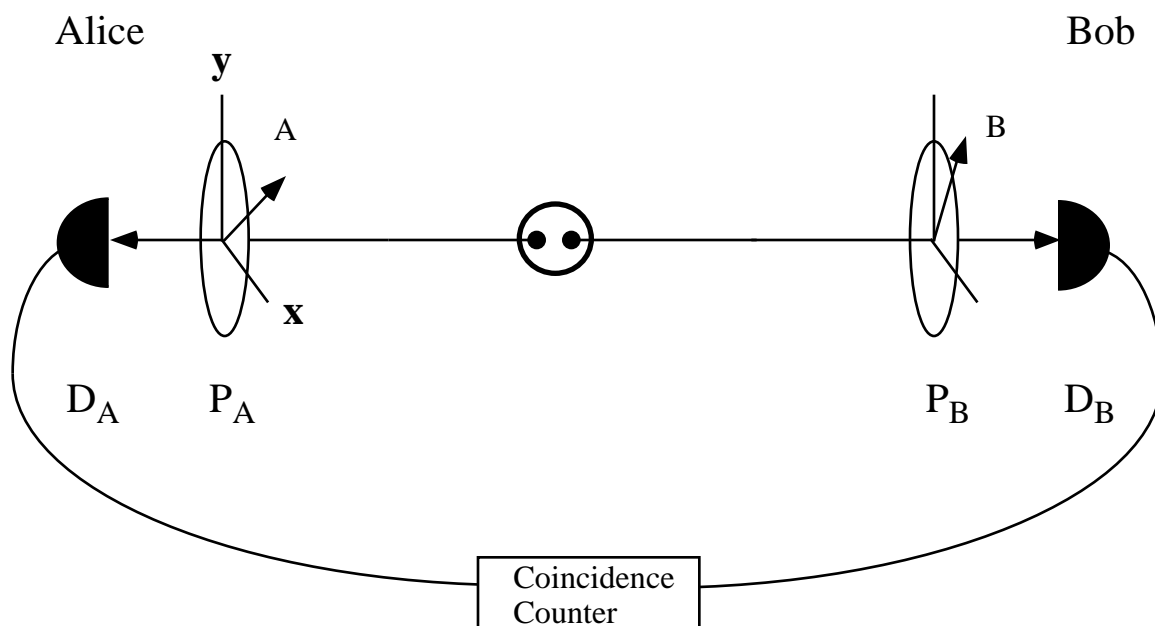


Figure 6.1 The Hardy-Jordan thought experiment, which is identical to those presented in Chapters 1 and 5 with one exception: the photon pairs share a non-maximally entangled polarization state that does not possess circular symmetry.

Now for states of the form (6.1), it is possible to find two polarization directions for Alice's measurement, θ_A, θ_A , and for Bob's measurement θ_B, θ_B , which satisfy the following four propositions

$$P(\theta_B | \theta_A) = 1 \quad (6.3)$$

$$P(\theta_A | \theta_B) = 1 \quad (6.4)$$

$$P(\theta_A, \theta_B) > 0 \quad (6.5)$$

$$P(\theta_A, \theta_B) = 0 \quad (6.6)$$

where $P(\theta_A, \theta_B)$ is the joint probability that Alice finds her photon to have polarization θ_A while Bob finds his to have polarization θ_B , and $P(\theta_A | \theta_B)$ is the conditional probability to find polarization θ_A given that θ_B has already been found.

Hardy and Jordan showed that the polarization angles $\theta_A, \theta_A, \theta_B, \theta_B$ whose quantum-mechanical expectation values satisfy (6.3) - (6.6) *must* exist for all states of the form (6.1), provided $a \neq b$. And yet, these four propositions create a logical contradiction when analyzed with the EPR axioms of locality and realism (see Chapter 1).

The contradiction emerges as follows: the first proposition (6.3) says that on the occasions when Alice finds her photon to have polarization θ_A , Bob will find his photon to have polarization θ_B with probability one if he chooses to measure along that direction. Now according to the EPR definition of an element of reality, [1] "If, without in any way disturbing a system, we can predict with certainty the value of a physical quantity, then there exists an element of physical reality corresponding to this physical quantity." Thus, in this case the fact that the polarization of Bob's photon can be predicted with certainty means that the photon's polarization along θ_B is an objective

element of reality, which exists whether or not Bob decides to measure it. Furthermore, locality demands that the existence of this element of reality for Bob's photon be independent of anything Alice does at her remote location. In other words, Alice cannot create this element of reality for Bob's photon by her measurements; rather, on those occasions when Alice finds her photon to have polarization θ_A , it must be the case that Bob's photon possessed the polarization θ_B as an element of reality from the moment it was created.

In a similar fashion, the second proposition (6.4) guarantees that if Bob measures polarization θ_B , then Alice will find her photon to have polarization θ_A if she orients her polarizer in that direction. In these cases, the polarization θ_A of Alice's photon is an element of reality which need not be measured by Alice in order to be considered real, because Bob can predict the outcome of such a measurement with certainty. And again, because of locality, Alice's particle must have possessed this element of reality from the moment it was created.

The third proposition (6.5) says that on at least some occasions, Alice's photon may be found with polarization θ_A while Bob's is found to have polarization θ_B . According to the first two propositions, this means that the photons must have left the source with elements of reality for their polarizations along θ_B and θ_A as well, even though those polarizations were never measured. In other words, if Alice and Bob had chosen to do so, they could have observed the polarizations θ_A and θ_B together instead of θ_A and θ_B . Furthermore, because they can choose the orientations of their polarizers while the photons are in flight towards them, locality demands that the polarizer settings cannot alter the properties of the particles as they were emitted from the source, so that if the elements of reality θ_A and θ_B existed from the moment the photons were created,

Alice and Bob should be able to observe them at least as often as they observe θ_A and θ_B together.

But according to the fourth proposition (6.6), whenever Alice and Bob actually choose those directions, they can never observe the θ_A and θ_B polarizations together. This, then, is the Hardy-Jordan paradox: the first two statements imply the existence of elements of reality θ_A and θ_B ; the third implies that they should be observed together some of the time, while the fourth guarantees that they will not be observed together at all.

From a quantum mechanical point of view, there is no reason why this cannot happen. The paradox arises when considering the Hardy-Jordan propositions in conjunction with locality and realism, but as we have seen, quantum mechanics is not bound by these principles. Unlike the EPR elements of reality, which have objectively real existence if their values can be determined in principle, a quantum mechanical observable takes on a value only when it is measured. Thus it is meaningless to argue about what Alice or Bob would have observed had they changed their analyzer settings at the last minute, however well this counterfactual reasoning may serve us in the classical world.

6.1.2 Dutch doors

The counterfactual reasoning involved in the Hardy-Jordan paradox may be simply illustrated by the system depicted in Figure 6.2, in which two doors are portrayed [5,6]. Each door has an upper and lower half, which may be opened or closed independently. Let us say that measuring a particular polarization is like opening one of the halves of the doors, which are labeled in the figure as $\theta_A, \theta_A, \theta_B, \theta_B$. Now in this particular style of door, called a “Dutch Door,” the top half is latched onto the bottom

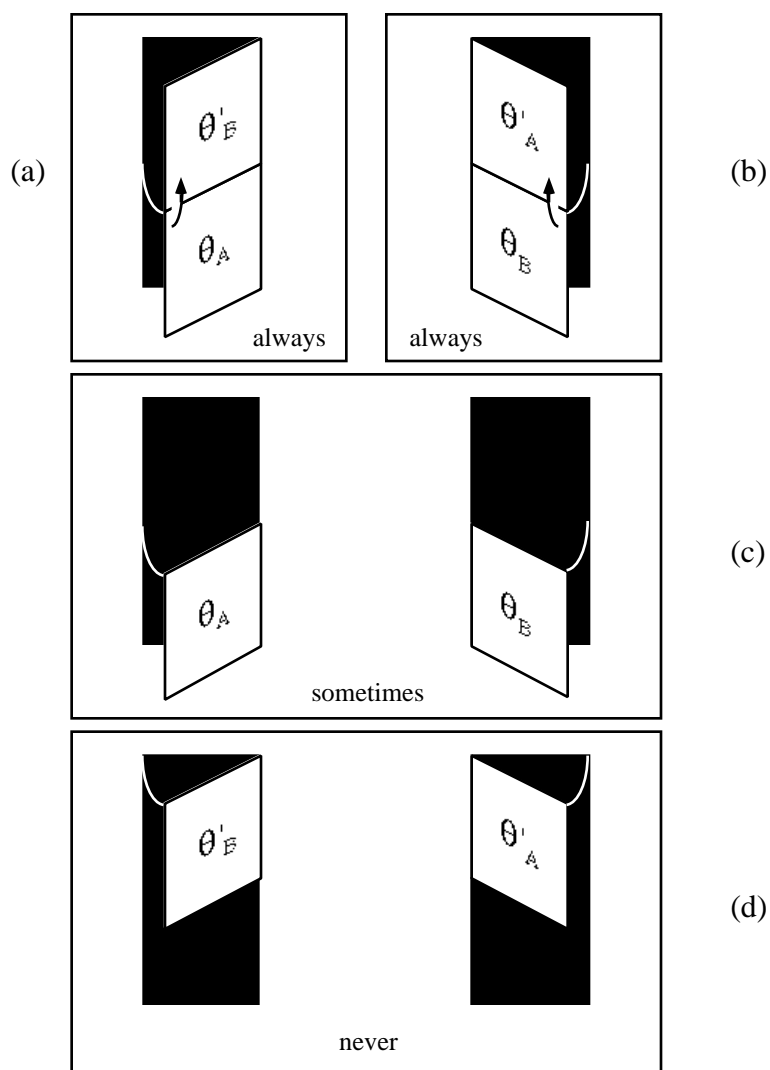


Figure 6.2 Dutch doors show how the Hardy-Jordan propositions lead to a paradox from a local-realistic viewpoint. Open doors represent polarization measurements by Alice and Bob. Figure (a) illustrates $P(\theta_A, \theta_B) = 1$; Figure (b) illustrates $P(\theta'_A, \theta'_B) = 1$. These two propositions indicate that the tops are “latched” to open with the bottoms. Figure (c) shows that the bottom two doors are sometimes open together, $P(\theta_A, \theta_B) > 0$. Figure (d) shows that the top two doors may never be open together, $P(\theta'_A, \theta'_B) = 0$. No objectively real, locally independent set of Dutch doors could behave this way, but Hardy proved that quantum mechanical observables corresponding to $\theta_A, \theta'_A, \theta_B$, and θ'_B must exist for all non-maximally entangled systems.

half, so that it is always constrained to open whenever the bottom half is opened. Therefore, if the bottom-left door labeled θ_A is opened, we are certain that the top-left door labeled θ_B must also be opened along with it, in analogy with the first Hardy-Jordan proposition (6.3). Similarly, the bottom-right door is labeled θ_B , and must force open the top-right door θ_A whenever it is opened, in accord with the second proposition (6.4). The third proposition (6.5) can now be interpreted as follows: if we examine only the bottom two doors, we will find that, on occasion, they are both open together. Because the doors are latched together, this implies that if we were to look at the top two doors instead on those occasions, we would certainly find them both to be open. However, proposition four (6.6) insists that when we actually look at the top doors, they are never found to be open together.

This seems to create an inescapable paradox: no everyday system of “Dutch doors” could ever behave in such a fashion. And yet, quantum mechanics demands that some systems exhibit just this peculiar behavior. Once again, we have a situation in which counterfactual reasoning, as permitted by realism and locality, can be applied to quantum mechanical predictions to generate a logical paradox. The fact is, only two of the four doors in Figure 6.2 may be observed in any given trial, so that according to quantum mechanics, it is both impossible and meaningless to make statements about the behavior of the other two doors. From this point of view, as espoused by Bohr [7], the only two doors which really exist at any moment are the two which are actually looked at and found to be open or closed. The paradox arises only when we insist that all four of them must exist no matter which two we observe.

In the words of N. David Mermin [8], the Hardy propositions “reign supreme in the *gedanken* realm. There they achieve their effectiveness by leading you down the garden path every bit as enticingly as the full EPR argument does and then turning

around and kicking out you of the garden with unprecedented efficiency and force.” But we are still left with the question, “is it really possible for nature to behave this way?”

6.1.3 Supplementary assumptions

For an experimental test of the Hardy-Jordan propositions with inefficient photodetectors, it is necessary to employ the same pair of supplementary assumptions that are used in the derivation of the Clauser-Horne-Shimony-Holt inequality in Chapter 5. The first of these is the “fair sampling” assumption, which allows us to identify the joint emission probability with the relative frequency of joint photodetections:

$$P(\theta_A, \theta_B) = \frac{R(\theta_A, \theta_B)}{R(-, -)}, \quad (6.7)$$

where $R(\theta_A, \theta_B)$ is a measured coincidence counting rate with the two polarizers oriented at angles θ_A and θ_B , and $R(-, -)$ is the coincidence rate with both polarizers removed as denoted by the dashes. The joint probabilities are therefore renormalized within the space of detected coincidence counts, as is evident from

$$P(-, -) = 1 \quad (6.8)$$

which is a special case of (6.7).

The second assumption required for the experiment is that the space of polarizations is a two-dimensional linear vector space, so that the completeness relations

$$\begin{aligned} P(-, -) &= P(\theta_A, -) + P(\bar{\theta}_A, -) = P(-, \theta_B) + P(-, \bar{\theta}_B) \\ P(\theta_A, -) &= P(\theta_A, \theta_B) + P(\theta_A, \bar{\theta}_B) \\ P(-, \theta_B) &= P(\theta_A, \theta_B) + P(\bar{\theta}_A, \theta_B). \end{aligned} \quad (6.9)$$

hold. Here again we are using the notation $\bar{\theta} = \theta \pm \pi/2$ to denote the linear polarization orthogonal to θ .

Within the subspace of coincidence counts, the conditional probability for a measurement of θ_B given a measurement of θ_A is defined as

$$P(\theta_B | \theta_A) = \frac{P(\theta_A, \theta_B)}{P(\theta_A, -)}. \quad (6.10)$$

The first Hardy-Jordan proposition (6.3) may then be rewritten as

$$P(\theta_A, \theta_B) = P(\theta_A, -) \quad (6.11)$$

or, with the help of (6.8) and (6.9),

$$P(\theta_A, \theta_B) = P(\theta_A, \theta_B) + P(\theta_A, \bar{\theta}_B), \quad (6.12)$$

which can only be true if

$$P(\theta_A, \bar{\theta}_B) = 0. \quad (6.13)$$

Similarly, the second Hardy-Jordan proposition (6.4) may be written as

$$P(\bar{\theta}_A, \theta_B) = 0 \quad (6.14)$$

while the third and fourth remain:

$$P(\theta_A, \theta_B) > 0 \quad (6.15)$$

$$P(\theta_A, \theta_B) = 0 \quad (6.16)$$

With the first two Hardy-Jordan conditions recast as (6.13) and (6.14), the analogy with the Dutch doors remains intact: the functioning of the latches is now determined by the fact that a top door can never remain closed when its bottom counterpart is opened (see Figure 6.3.) If the doors can only be “open” or “closed,” -- i.e., if failure to observe a

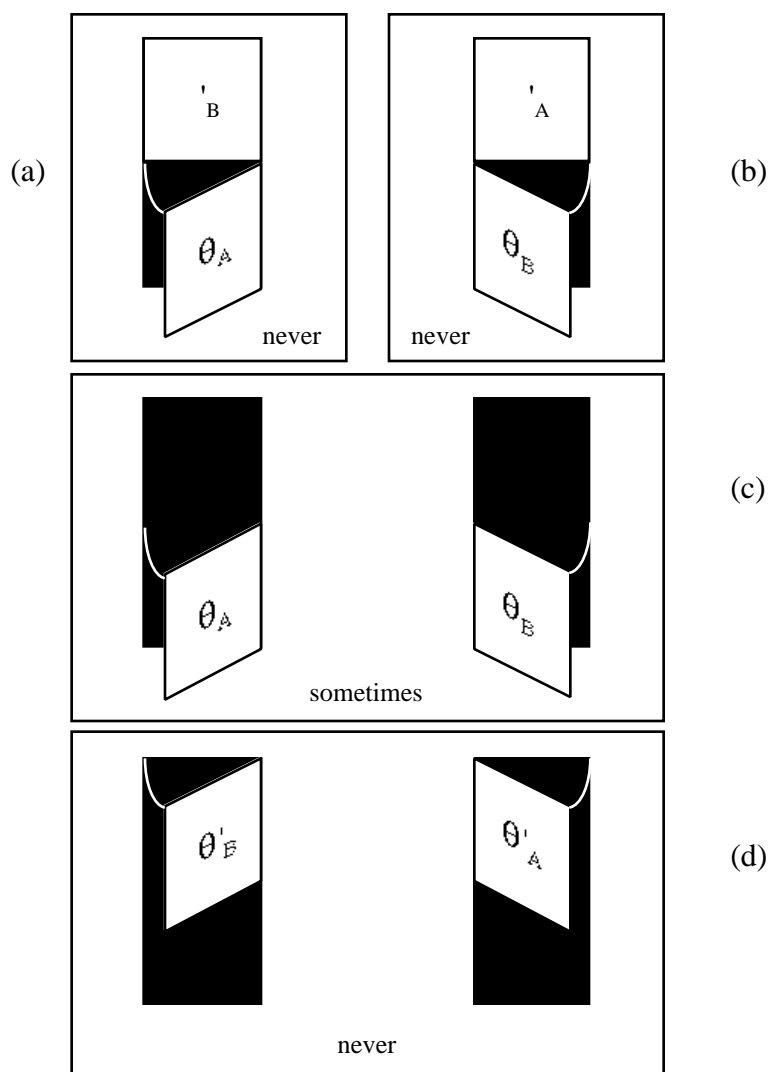


Figure 6.3 A slightly modified version of the Hardy-Jordan “Dutch doors.” Figures (a) and (b) now illustrate the fact that top doors can never be closed while bottom ones are open. These conditions are equivalent to the first two Hardy-Jordan propositions if the doors only have the states “open” or “closed,” corresponding to the two possible orthogonal polarizations θ and $\bar{\theta}$. The last two propositions, illustrated by (c) and (d), are unchanged.

particular polarization with perfect detectors is equivalent to observing the orthogonal polarization -- then this implies that the tops must open whenever the bottoms are opened.

6.2 Schematic and theory

6.2.1 Schematic of the experiment

Our goal was to carry out the Hardy-Jordan experiment by making joint polarization measurements on correlated photon pairs in a system capable of verifying the Hardy-Jordan propositions. A schematic of such a system is shown in Figure 6.4. As in Chapter 5, a type-I downconverter (PDC) emits a frequency-degenerate pair of signal and idler photons, whose polarizations are made orthogonal with the help of a half-wave plate (R_0) before they impinge onto beamsplitter BS from opposite sides at near-normal incidence. The emerging photons pass through linear polarizers (P_A, P_B) oriented at angles θ_A and θ_B before falling onto photodetectors (D_A, D_B) in each analyzer arm. The coincidence counting rates $R(\theta_A, \theta_B)$ are measured for various settings $(\theta_A, \bar{\theta}_A, \theta_A, \bar{\theta}_A, \theta_B, \bar{\theta}_B, \theta_B, \bar{\theta}_B)$ of the polarizers, to establish the probabilities (6.13) - (6.16).

6.2.2 Quantum state of the light

It was shown in Section 5.2.1 that, provided the optical path lengths from PDC to BS are equal for the signal and idler, the light after the beamsplitter may be approximated by the two-mode pure state

$$|\Psi^{(1)}\rangle = RR |1\rangle_{Ax} |1\rangle_{By} + TT |1\rangle_{Bx} |1\rangle_{Ay} + RT |1\rangle_{Ax} |1\rangle_{Ay} + TR |1\rangle_{Bx} |1\rangle_{By} \quad (6.17)$$

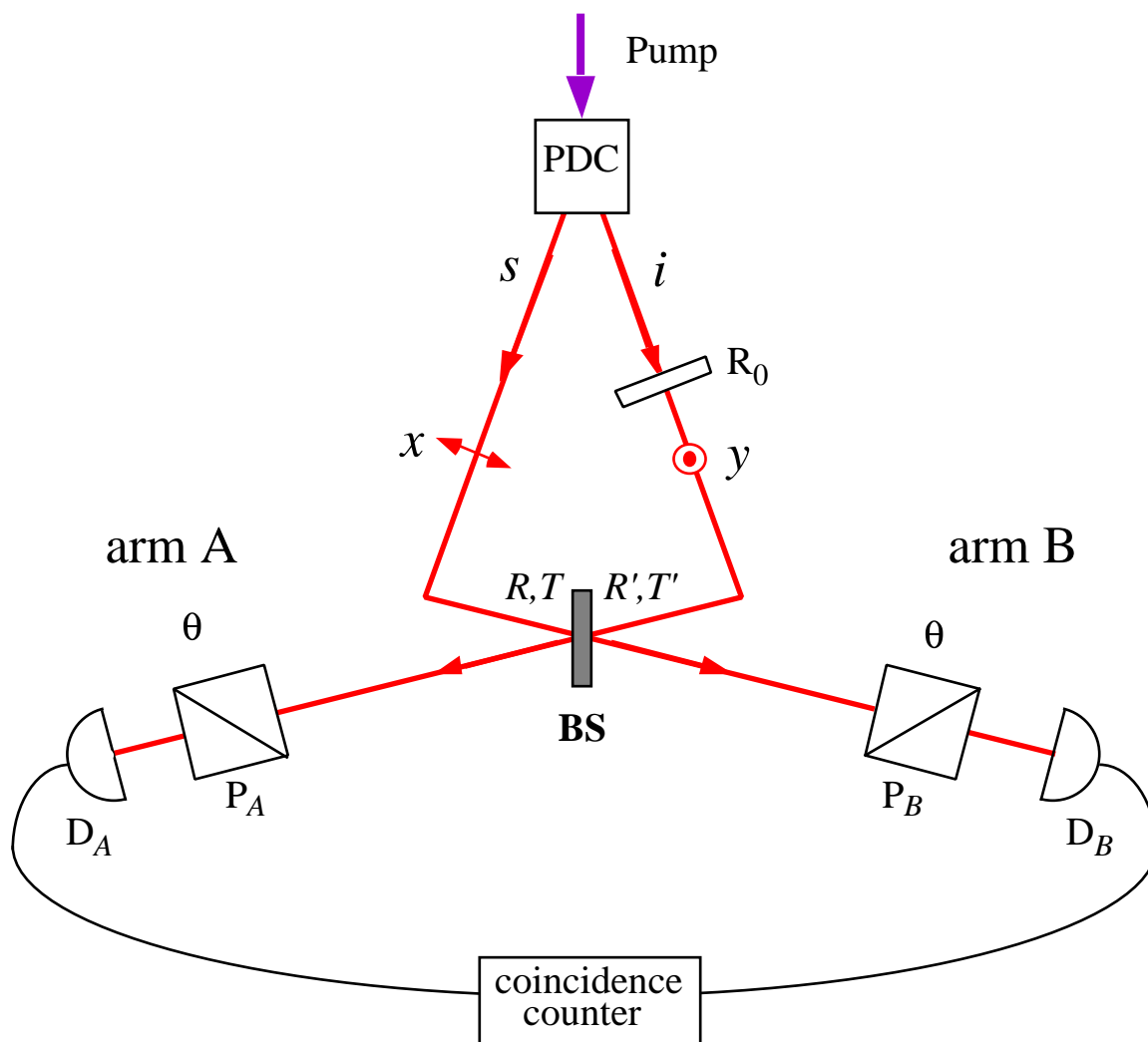


Figure 6.4 Schematic of an experiment to test local realism by verifying the Hardy-Jordan propositions. As in Chapter 5, Figure 5.3, the idler polarization is made orthogonal to that of the signal with the help of the rotator R_0 . The photons impinge onto a beamsplitter, then emerge into arms A and B where they pass through a polarizer P before falling onto a detector D. In this experiment, an asymmetric beamsplitter -- ideally with reflectivities $|R|^2 = |R'|^2$ close to 32% and transmissivities $|T|^2 = |T'|^2$ close to 68% -- is used.

where the labels A and B refer to the modes for arms A and B , and the complex transmissivities T, T and reflectivities R, R characterize the beamsplitter BS. If we consider only coincidence counts, this non-entangled state may be projected and renormalized within the subspace where one photon is in each arm:

$$|\psi_S^{(1)}\rangle = \frac{1}{\sqrt{|RR|^2 + |TT|^2}} \left\{ RR |1\rangle_{Ax} |1\rangle_{By} + TT |1\rangle_{Bx} |1\rangle_{Ay} \right\}. \quad (6.18)$$

This is an asymmetric, non-maximally entangled state of the form (6.1), provided that $|RR|^2 \neq |TT|^2$. The coincidence counts observed in this subspace are indicative of the correlations of the entire ensemble of signal and idler photons if we make a third assumption: the beamsplitter transmits or reflects photons at random.

6.2.3 Predicted counting rates

As in Section 5.2.3, the probability of registering a pair of photons with perfectly efficient detectors after the polarizers, given that there is one photon in each arm, is calculated via the quantum mechanical expectation value

$$\begin{aligned} P_{AB}(\theta_A, \theta_B) &= \langle \psi_S^{(1)} | \hat{a}_A^\dagger(\theta_A) \hat{a}_B^\dagger(\theta_B) \hat{a}_B(\theta_B) \hat{a}_A(\theta_A) | \psi_S^{(1)} \rangle \\ &= \left| \hat{a}_B(\theta_B) \hat{a}_A(\theta_A) | \psi_S^{(0)} \rangle \right|^2. \end{aligned} \quad (6.19)$$

Here $\hat{a}_A(\theta_A)$ and $\hat{a}_B(\theta_B)$ are the annihilation operators for the field modes reaching the detectors, which may be written in terms of the output modes at BS as

$$\begin{aligned} \hat{a}_A(\theta_A) &= \cos(\theta_A) \hat{a}_{Ax} + \sin(\theta_A) \hat{a}_{Ay}, \\ \hat{a}_B(\theta_B) &= \cos(\theta_B) \hat{a}_{Bx} + \sin(\theta_B) \hat{a}_{By}. \end{aligned} \quad (6.20)$$

With the help of these relations, the joint probability in Eq. (6.19) may be evaluated [9] as

$$P_{AB}(\theta_A, \theta_B) = \frac{|TT \cos(\theta_A) \sin(\theta_B) - RR \sin(\theta_A) \cos(\theta_B)|^2}{|RR|^2 + |TT|^2} \quad (6.21)$$

after the annihilation operators act on the state in (6.18). Similarly,

$$P_{AB}(\theta_A, \bar{\theta}_B) = \frac{|TT \cos(\theta_A) \cos(\bar{\theta}_B) - RR \sin(\theta_A) \sin(\bar{\theta}_B)|^2}{|RR|^2 + |TT|^2} \quad (6.22)$$

$$P_{AB}(\bar{\theta}_A, \theta_B) = \frac{|TT \sin(\bar{\theta}_A) \sin(\theta_B) - RR \cos(\bar{\theta}_A) \cos(\theta_B)|^2}{|RR|^2 + |TT|^2} \quad (6.23)$$

and

$$P_{AB}(\theta_A, \theta_B) = \frac{|TT \cos(\theta_A) \sin(\theta_B) - RR \sin(\theta_A) \cos(\theta_B)|^2}{|RR|^2 + |TT|^2}. \quad (6.24)$$

The last three probabilities must be zero in order to satisfy the first, second, and fourth Hardy-Jordan conditions (6.13), (6.14), and (6.16), respectively. When these conditions are imposed, we have, with the help of the reciprocity relations $|T| = |T|$, $|R| = |R|$, and $TR^* = -T^*R$,

$$\begin{aligned} \frac{|R|^2}{|T|^2} &= -\cot(\theta_A) \cot(\theta_B) \\ &= -\tan(\theta_A) \tan(\theta_B) \\ &= \cot(\theta_A) \tan(\theta_B). \end{aligned} \quad (6.25)$$

These relations allow the joint probability in (6.21) to be written as

$$P(\theta_A, \theta_B) = \frac{|T|^4 (|T/R|^4 - 1)^2 \cos^2(\theta_A)}{(|T|^4 + |R|^4) (1 + |T/R|^{12} \cot^2(\theta_A))}, \quad (6.26)$$

which takes on its maximum value when

$$\tan(\theta_A) = |T/R|^3. \quad (6.27)$$

Eqs. (6.25) then give

$$\begin{aligned}\tan(\theta_B) &= |R/T|^3 \\ \tan(\theta_A) &= -|T/R| \\ \tan(\theta_B) &= -|R/T|\end{aligned}\tag{6.28}$$

while the maximum value of $P(\theta_A, \theta_B)$ for a given beamsplitter is

$$P_{\max}(\theta_A, \theta_B) = \frac{|T|^4 (|T/R|^4 - 1)^2}{(|T|^4 + |R|^4)(1 + |T/R|^6)}.\tag{6.29}$$

The largest possible value is $P_{\max}(\theta_A, \theta_B) = .09$ [3], which occurs when $|T|^2 = .32$, $|R|^2 = .68$ or vice versa.

6.3 Experimental procedure and results

6.3.1 Apparatus

The apparatus for our experiment [10] was nearly identical to the one described in Section 5.3.1, with the main difference being the absence of the quarter-wave plates (see Figure 6.5.) Once again, the pump source was a cw Ar⁺ laser beam with a wavelength of 351.1 nm. The pump power was 100 mW, and this beam was incident on a 2.5 cm LiIO₃ downconversion crystal (PDC) cut and oriented for frequency-degenerate type-I phase-matching. The signal and idler beams had a mean wavelength of $\lambda = 702.2$ nm and were selected by a combination of 1 mm apertures near the PDC and in front of the detectors. The idler polarization was rotated by the multi-order half-wave plate R₀.

The measured values of the beamsplitter transmissivity and reflectivity were $|R|^2 = .30$ and $|T|^2 = .70$; for these, Eqs. (6.27) and (6.28) yielded the following optimum polarization angles for the experiment:

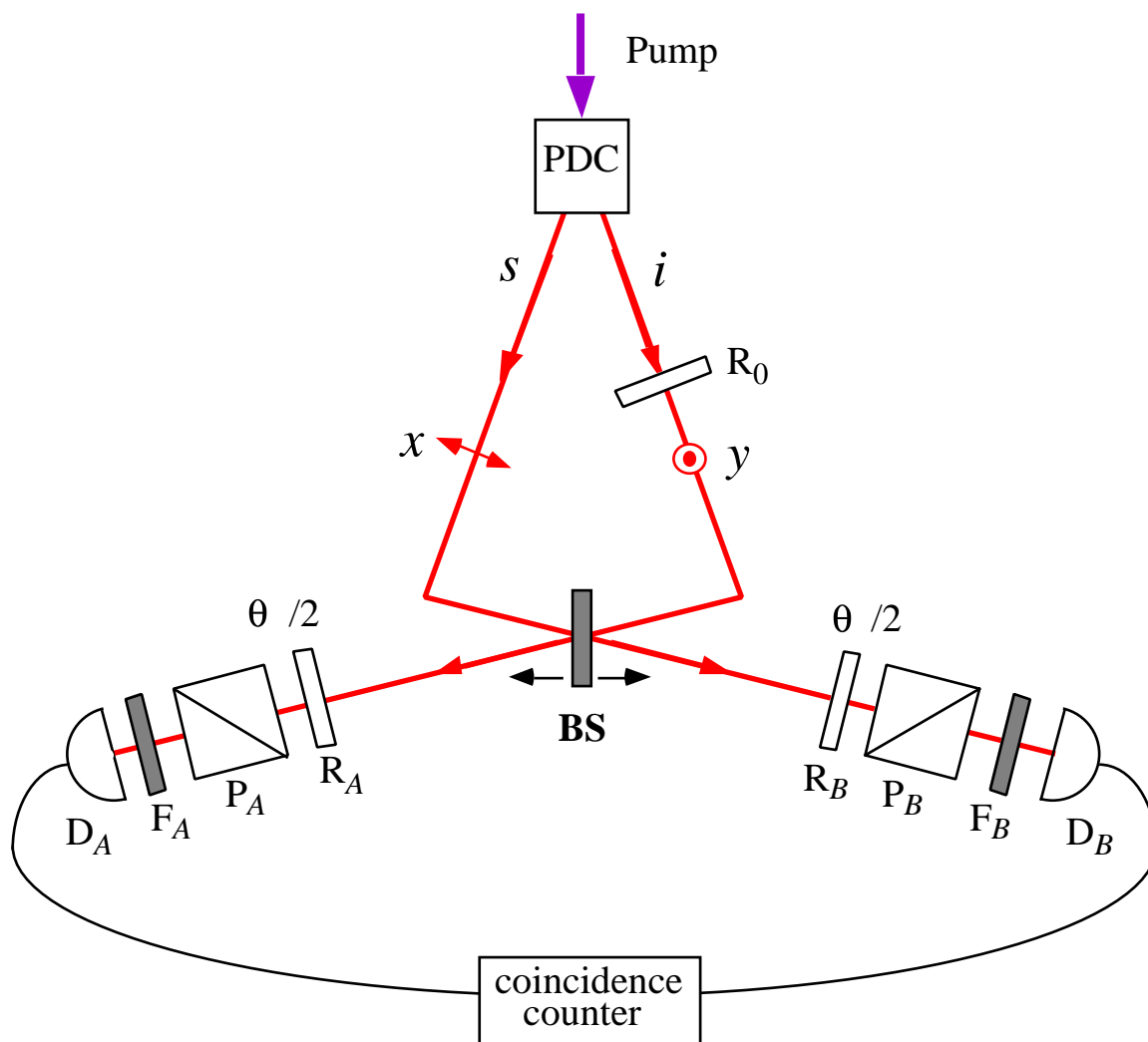


Figure 6.5 Diagram of the performed experiment, which differed slightly from the schematic presented in Figure 6.4. As in the experiment of Chapter 5, the beamsplitter was mounted on a motorized translation stage for the purpose of equalizing the signal and idler path lengths to BS. The rotators R_A and R_B were used to select the polarizations transmitted to the detectors by the fixed polarizers P_A and P_B , while interference filters F_A and F_B were used in conjunction with apertures (not shown) to select the frequency-degenerate downconversion.

$$\begin{aligned}
\theta_A &= 74.3^\circ \\
\theta_A &= -56.8^\circ \\
\theta_B &= 15.7^\circ \\
\theta_B &= -33.2^\circ
\end{aligned}
\tag{6.30}$$

As in the previous experiment, the detected polarizations were selected by rotating the multi-order half-wave plates (R_A, R_B) before the light impinged onto fixed Wollaston polarizing beamsplitters (P_A, P_B). All three half-wave plates were antireflection coated and produced retardation errors of $\phi < k\lambda/200$. The polarizers had transmission extinction ratios of $1:10^5$. The photodetectors, spectral filters, collection lenses, and counting electronics were all exactly as described in Section 5.3.1.

In order to verify the Hardy-Jordan conditions (6.13) - (6.16) with the joint probabilities given by (6.7), it was necessary to show that the coincidence counting rates $R(\theta_A, \bar{\theta}_B)$, $R(\bar{\theta}_A, \theta_B)$, and $R(\theta_A, \theta_B)$ were all zero, while $R(\bar{\theta}_A, \bar{\theta}_B)$ was non-zero. But reporting a null result in this experiment might have begged the question, “were the counting rates zero for the right reasons?” Fortunately, the Hong-Ou-Mandel two-photon interference dip [11] discussed in Chapter 3 provided a way to show that the zero probabilities were “true zeros” and not experimental artifacts, by translation of BS. As the pure state (6.17) is only valid when the four outcomes at the beamsplitter are indistinguishable, any imbalance in the signal and idler optical path lengths to BS results in timing information which reduces the entanglement of the state (6.18). In particular, if the path lengths differ by more than the $500 \mu\text{m}$ coherence length of the detected signal and idler wavepackets, this timing information results in complete distinguishability of the two-photon paths. The proper description of the system under these circumstances is not a pure state, but a mixed state represented by a diagonal density operator which is incapable of exhibiting the quantum interference effects necessary to satisfy the Hardy-Jordan conditions.

Therefore, after the polarizer angles were set by appropriate orientation of R_A and R_B , the beamsplitter was translated in 10 - 50 μm increments over a range of 1 mm, centered near the equilibrium position where the signal and idler path lengths to BS were equal. The Hong-Ou-Mandel coincidence dips were then recorded for the four critical pairs of angles in the Hardy-Jordan conditions.

6.3.2 Results

The interference dips in the two-photon coincidence rates for each of the four Hardy-Jordan polarization pairs are shown in Figure 6.6. Counts were recorded for 10 seconds at each position of the beamsplitter. The table shows the number of counts recorded at the minimum of each dip; counts were also recorded at these positions for the remaining pairs of angles required to compute $R(-, -)$ via the polarization completeness relation

$$R(-, -) = R(\theta_A, \theta_B) + R(\bar{\theta}_A, \theta_B) + R(\theta_A, \bar{\theta}_B) + R(\bar{\theta}_A, \bar{\theta}_B). \quad (6.31)$$

The probabilities in (6.13) - (6.16) were then computed according to (6.7), so as to yield the following experimental results for the Hardy-Jordan conditions:

$$P(\theta_A, \bar{\theta}_B) = 0.0034 \pm 0.0004 \quad (6.32)$$

$$P(\bar{\theta}_A, \theta_B) = 0.0040 \pm 0.0004 \quad (6.33)$$

$$P(\theta_A, \theta_B) = 0.0990 \pm 0.0020 \quad (6.34)$$

$$P(\bar{\theta}_A, \bar{\theta}_B) = 0.0070 \pm 0.0005. \quad (6.35)$$

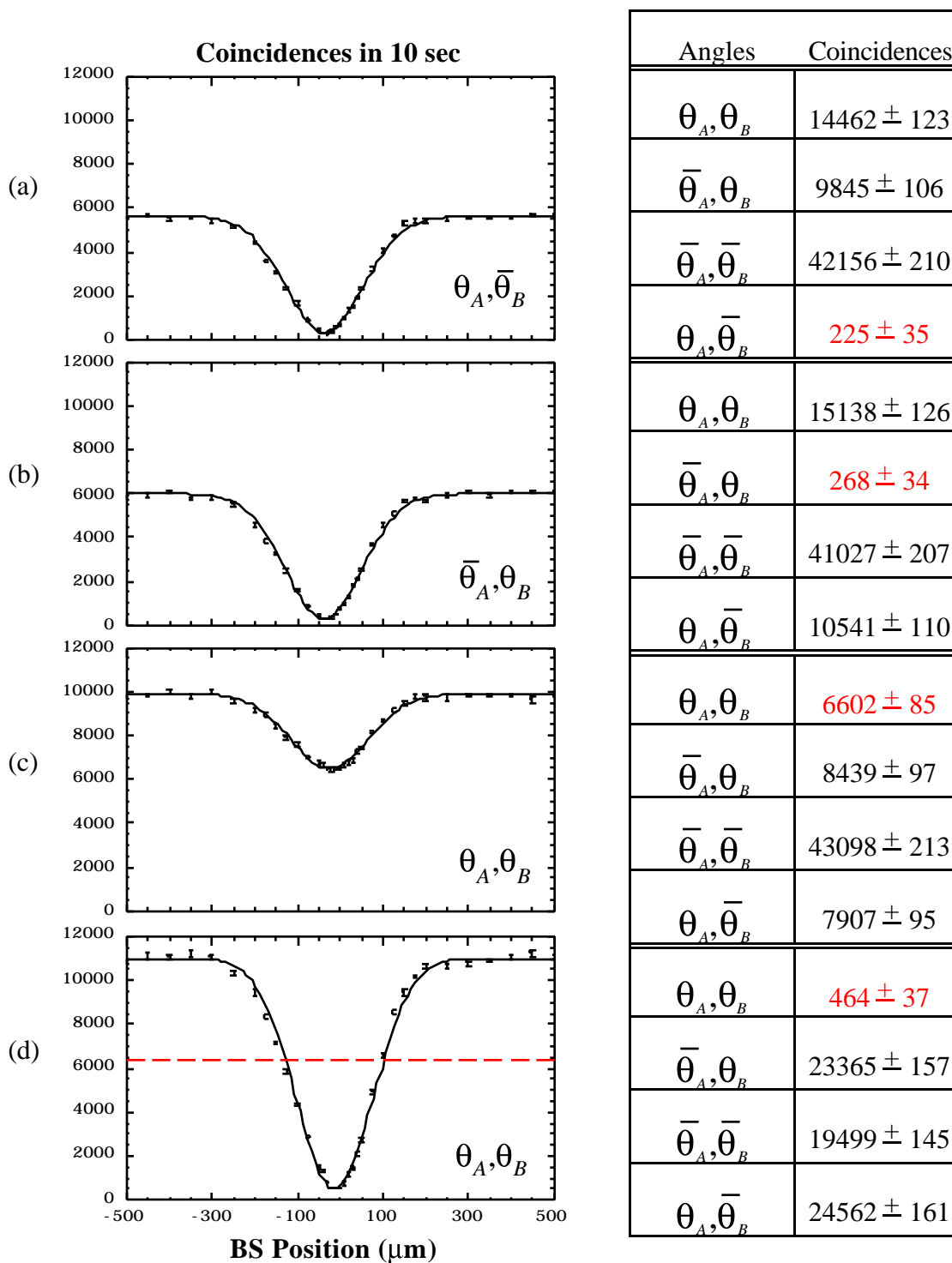


Figure 6.6 Hong-Ou-Mandel interference dips and minimum coincidence counts recorded during 10 second intervals for all of the angles relevant to the Hardy-Jordan conditions.

6.4 Discussion

6.4.1 Dutch doors with broken latches

The measured probabilities in (6.32) - (6.35) are meant to be compared to the theoretical predictions for the Hardy-Jordan probabilities (6.13) - (6.16). We did not observe true zeros for the first, second, and fourth probabilities, for reasons probably connected to the distinguishability of the coincidence paths after the beamsplitter. Imperfections in the crystal can cause mismatch of the signal and idler modes at BS, thereby making a certain portion of the outgoing beams spatially distinguishable so as to inhibit the interference of the two-photon amplitudes in (6.17) [12]. Even with undistorted wavefronts, mode-matching at the beamsplitter is a delicate operation which is degraded by slight misalignments or vibrations of the mirrors.

Nevertheless, the experimental results can be shown to conflict with locality and realism when interpreted as follows: the first two conditions show the operation of the “latches” in the Dutch doors of Figure 6.3. Ideally, when a bottom door is open, the top door is never found closed, as indicated by (6.13) and (6.14). In fact, though, these configurations were observed in a small fraction of the trials, indicating an occasional failure of the latching mechanism. For the left-hand door, the latch failed in .34 % of the trials. This implies that the first conditional probability (6.3) in the original formulation of the Hardy-Jordan conditions is not unity, but can be found via the following argument: starting from Eq. (6.10),

$$\begin{aligned}
 P(\theta_B | \theta_A) &= \frac{P(\theta_A, \theta_B)}{P(\theta_A, -)} \\
 &= \frac{[P(\theta_A, -) - P(\theta_A, \bar{\theta}_B)]}{P(\theta_A, -)} \\
 &= 1 - \frac{P(\theta_A, \bar{\theta}_B)}{P(\theta_A, -)}.
 \end{aligned} \tag{6.36}$$

With $P(\theta_A, \bar{\theta}_B)$ given by (6.32) and the data in Figure 6.6 used to determine $P(\theta_A, -) = 0.220 \pm 0.003$ according to (6.9), the conditional probability is

$$P(\theta_B | \theta_A) = 0.9845 \pm 0.0020. \quad (6.37)$$

That is, the latch worked correctly and forced the left top door to be open for 98% of the trials when the left bottom door was opened. Similarly, we may establish that the latch for the right-hand doors worked also with probability

$$P(\theta_A | \theta_B) = 0.9826 \pm 0.0019, \quad (6.38)$$

instead of the unit probability given by (6.4). Now because the combination θ_A, θ_B corresponding to the bottom doors was found to occur with probability .0990, we would expect the top two doors, θ_A, θ_B to be found in at least the fraction of the trials given by

$$\begin{aligned} P_{\min}(\theta_A, \theta_B) &= (0.0990 \pm 0.0020) \times (0.9845 \pm 0.0020) \times (0.9826 \pm 0.0019) \\ &= 0.0950 \pm 0.0034, \end{aligned} \quad (6.39)$$

corresponding to the dashed line in Figure 6.6 (d). However, this combination was only found to occur with the fourteen times smaller probability

$$P(\theta_A, \theta_B) = 0.0070 \pm 0.0005, \quad (6.40)$$

in contradiction with the local-realistic minimum by 26 standard deviations.

6.4.2 Supplementary assumptions revisited

Have we now verified the existence of the Hardy-Jordan “Dutch doors” in the laboratory, thereby proving that nature violates local realism? Just as with experiments based on Bell’s inequalities, the answer is “Yes, with certain provisions.”

We recall that the first two of Hardy's propositions were used to establish the action of the Dutch doors in the following way: whenever a bottom door is found open (θ_A or θ_B is detected), the corresponding top door must also be found open (θ_B or θ_A is also detected). We attempted to establish was something close to this in our experiment: if a bottom door is found open (θ_A or θ_B is detected), the corresponding top door *cannot be found closed* ($\bar{\theta}_B$ or $\bar{\theta}_A$ is not detected). If the top doors cannot be found closed in these cases, does that imply that they were necessarily open? Only if it is true that there are no alternative states for the doors besides "open" and "closed", which is to say, that if a polarization measurement is made along axis θ_B , it must either register as having polarization θ_B or the orthogonal polarization $\bar{\theta}_B$. As noted in the previous chapter, the description of polarization via a complete set of two orthonormal vectors is an established tenet of both the classical and the quantum mechanical descriptions of light, but it need not hold for every alternative, local realistic theory.

We also found it necessary to assume, as in Chapter 5, that the beamsplitter reflects or transmits photons completely at random, so that the subensemble of the trials in which one photon ends up in each arm of the apparatus is representative of the whole ensemble of photons emitted from the PDC. Again, quantum mechanics incorporates this assumption automatically, but it need not be true for LHV theories [13].

Finally, and most importantly, the detectors used in our experiment were not perfectly efficient. The fact is that in some of the trials, we did not obtain any information at all about the polarization state of one or the other photon. It is as if our Dutch doors were at the end of a crowded ballroom, and our line of sight was sometimes blocked, thereby indicating failure of one of the detectors. We have made the assumption that what we see of these doors when we get a clear view represents their behavior at all times. This is reasonable if one believes, for example, that the people walk

in front of the doors in a random fashion, completely independent of the state of the doors. This is the “random non-detection” type of fair-sampling assumption [14] mentioned earlier in the context of Bell’s inequalities (see Section 5.4.2.) On the other hand, perhaps the people in the ballroom are performing an elaborate dance which requires them to be in the way whenever the top two doors are open: this would explain why we never see this situation when we look for it. At least one such theory, based on non-random detector failure, has already been constructed to explain the results of our experiment in an entirely local realistic fashion [15,16].

Therefore, these experimental results do not provide conclusive evidence against locality and realism. Instead, like the one reported in Chapter 5, this experiment demonstrates a conflict between five seemingly reasonable statements: There exist in nature elements of physical reality as defined by *realism*; The settings of one analyzer do not affect measurements at the other, or at the source, as demanded by *Bell locality*; The *fair sampling* assumption is valid; Polarization is a two-dimensional linear vector; The beamsplitter is unbiased.

6.4.3 Comparison with the experiment of Boschi et al.

Quite recently, a similar experiment was reported by Boschi, De Martini, and Di Giuseppe [17]. Their experimental arrangement differed from the one we have presented in three respects: a polarization rotator was added to the signal beam emerging from the PDC, the beamsplitter BS was replaced with a polarizing beamsplitter, PBS, and another pair of detectors (\bar{D}_A, \bar{D}_B) was added to monitor the unused output ports of the polarizers P_A and P_B . By rotating the signal and idler polarizations independently, the parameters R and T for the PBS could be varied

continuously¹ to create arbitrary non-maximally entangled states of the form (6.18) -- provided that the random beamsplitter assumption is used to validate the projection of the state into the subensemble where one photon emerges from each side of the beamsplitter. By monitoring the previously unused output ports of the polarizers, the counting rates $R(\theta_A, \theta_B)$, $R(\theta_A, \bar{\theta}_B)$, etc. could be monitored simultaneously with the half-wave plates set to θ_A, θ_B .

Boschi et al. claim that by monitoring these additional output ports of the polarizers, they were able to create EPR elements of reality which were more “unambiguous” than the ones created in our experiment. Their concern is that, in the experiment just presented, when the polarizations θ_A, θ_B are monitored, nothing can be said about the photon pairs which were *not* detected -- that is, whether they went undetected as a result of detector failure, polarizer absorption, or polarizer rejection (indicating a polarization of $\bar{\theta}_A$ or $\bar{\theta}_B$). The authors claim that it is unsatisfactory to monitor the rates $R(\theta_A, \theta_B)$, $R(\theta_A, \bar{\theta}_B)$ separately, as we did, in order to establish the conditional probabilities (6.3) and (6.4). They state that only by monitoring all four of these rates together can one claim to have established an element of reality “unambiguously” according to the EPR criterion that “*every time* $D_B(\theta_B)$ registers a ‘click’ on mode-B... a ‘click’ is also registered by $D_A(\theta_A)$ on mode-1 and *never* by $\bar{D}_A(\bar{\theta}_A)$.”²

However, this claim is invalid for their experiment, just as it is for ours, because in both cases the detectors were not 100% efficient. If there is one photon in each mode, then when D_B registers a click, there is a less-than-100% chance that a “click” is also registered by D_A (or \bar{D}_A). In both experiments, the claim that the polarization of a

¹ However, the experiment must be performed with fixed values of these parameters.

² This is quoted directly from reference [17], with the angle notation adapted to be consistent with that of this chapter.

photon emerging from one side of PBS is an EPR “element of reality” rests on the ability to predict with certainty that photon’s polarization *whether or not it is measured*, when the other photon possesses some other polarization. In other words, one must be able to say that *every time* a photon in arm B is found to have polarization θ_B , the photon in arm A must be found to have polarization θ_A . But in practice, this can be established experimentally only for the detected photons; nothing can be said about photons which went undetected.

However, if we assume that the distributions of measured events are representative of what *would* have been measured with ideal (100% efficient) detectors, then something that happens with probability one within the subensemble can be used to establish a property for *every* photon whether or not we have actually measured it. In this manner, both experiments rely on the same fair sampling assumption to establish the existence of the EPR elements of reality.

Also, because both experiments assume, in the spirit of Einstein locality, that the properties of the emitted photon pairs are independent of the analyzer settings, it does not matter whether the rates $R(\theta_A, \theta_B)$, $R(\theta_A, \bar{\theta}_B)$, etc. are measured simultaneously or not. In both cases, the counterfactual reasoning needed to construct the Hardy-Jordan paradox is made possible by the combination of realism and locality. As in Chapter 5, the locality assumed for this experiment is the stronger *Bell locality*, which insists that the analyzers and source are all independent of one another even when they do not have spacelike separation.

The experiment of Boschi et al., like the one outlined in this chapter, demonstrated that the three probabilities in (6.13), (6.14), and (6.16) can be near zero, while the probability in (6.15) is nonzero. With the same supplementary assumptions, their data violated local realism by 14 standard deviations. Despite some superficial

differences, then, the results of Boschi et al. show no more and no less than the results reported here.

References for Chapter 6

- [1] A. Einstein, B. Podolsky, and N. Rosen, *Phys. Rev.* **47**, 777 (1935).
- [2] D. M. Greenberger, M. A. Horne, A. Shimony, and A. Zeilinger, *Am. J. Phys.* **58**, 1131 (1990).
- [3] L. Hardy, *Phys. Rev. Lett.* **71**, 1665 (1993).
- [4] T. F. Jordan, *Phys. Rev. A* **50**, 62 (1994).
- [5] D. Branning, *Am. Sci.* **85**, 160 (1997).
- [6] J. R. Torgerson, Ph.D. thesis, University of Rochester, 1997 (unpublished).
- [7] N. H. Bohr, *Phys. Rev.* **48**, 696 (1935).
- [8] N. D. Mermin, *Phys. Today* **47**, 9 (1994).
- [9] J. R. Torgerson, D. Branning, and L. Mandel, *App. Phys. B* **60**, 267 (1994).
- [10] J. R. Torgerson, D. Branning, C. H. Monken, and L. Mandel, *Phys. Lett. A* **204**, 323 (1995).
- [11] C. K. Hong, Z. Y. Ou, and L. Mandel, *Phys. Rev. Lett.* **59**, 2044 (1987).
- [12] T. P. Grayson and G. A. Barbosa, *Phys. Rev. A* **49**, 2948 (1994).
- [13] A. Garuccio, in *Fundamental Problems in Quantum Theory: A Conference Held in Honor of Professor John A. Wheeler*, edited by D. M. Greenberger and A. Zeilinger, *Annals of the New York Academy of Sciences* Vol. 755 (New York Academy of Sciences, New York, 1995), p. 632.
- [14] A. Garuccio, *Phys. Rev. A* **52**, 2535 (1995).
- [15] A. Cabello and E. Santos, *Phys. Lett. A* **214**, 316 (1996).
- [16] J. R. Torgerson, D. Branning, C. H. Monken, and L. Mandel, *Phys. Lett. A* **319**, 214 (1996).
- [17] D. Boschi, F. De Martini, and G. Di Giuseppe, *Phys. Lett. A* **228**, 208 (1997).

This page intentionally left blank.

Chapter 7

Summary

In the first part of this thesis, we examined a series of experiments that highlighted the central role for interference of distinguishing “which-path” information. In the quantum eraser experiment of Chapter 2, we encountered a subtle variation on this idea. Because the idler photons from the two downconverters are capable in principle of being used as “which path” markers for the signals, the counting rate at the signal photodetector does not display interference. However, when we recombined the idler beams and destroyed their function as “which path” markers, the interference returned, in that we could recover subensembles of the signal counts that exhibit fringes and “antifringes.” The determination of whether a given signal photon detection belonged in the “fringe” or “antifringe” set was made by correlating it with the outcome of the polarization measurement of the idler photons in the “eraser” basis. The total set of single-channel signal counts, being the sum of the “fringe” and “antifringe” subensembles, still did not display interference. This is a reflection of the fact that, as far as second-order measurements were concerned, it was still possible, in principle, to identify the path of the signal photons, because the idlers could have been used instead as which-path markers without disturbing the signal measurements in any way. Interference only returned in those fourth-order measurements where the “which path” information -- contained in the idler polarization -- was erased.

In Chapter 3, it was shown that spectral information can also serve to identify the paths of photon pairs in a Hong-Ou-Mandel interferometer. In particular, spectral distinguishability of the photon pairs is the (sometimes unwanted) result of pumping a

type-II downconversion process with an ultrafast pump. If ultrafast type-II processes are to be considered as sources for multi-particle quantum interferometry experiments, this spectral distinguishability will have to be reckoned with. A novel method of restoring spectral indistinguishability to these photon pairs -- by symmetrizing their joint emission spectrum -- was demonstrated in Chapter 4. Though the source of a peculiar phase shift in the fourth-order fringes was never identified, the method was shown to improve the visibility of the quantum interference of these photon pairs quite dramatically, without the loss in counting rates or timing resolution that would result from the use of spectral filters. The link between the symmetry of the joint emission spectrum and the indistinguishability of the photon pairs may be exploited by researchers to improve designs for quantum teleportation experiments, quantum computing schemes, or nonlocality demonstrations with multiple particles.

A truly vast literature on the completeness of quantum mechanics and related questions has arisen since the publication of the famous Einstein-Podolsky-Rosen paper in 1935. In the intervening years, Bell's theorem was used to show that quantum mechanics cannot be completed by a deeper theory of local-realistic hidden variables, and this pointed the way to experiments that might determine whether this "nonlocality" is just a strange flaw in an otherwise sound quantum theory, or a strange fact of nature that is correctly described by quantum theory. While the experiments to date have not been able to answer this question conclusively, they do make one thing abundantly clear: the local hidden variable theories which remain as contenders must be at least as counterintuitive as quantum theory, in that they can preserve locality and realism only at the expense of the fair-sampling assumption. The nonlocality experiments of Chapters 5 and 6 are similar but weaker demonstrations of this fact, because they require the use of an additional "random beamsplitter" assumption due to

the way the entangled state was generated. Nevertheless, it is the hope of this author that the experiment reported in Chapter 6, in particular, might have some value as a simple demonstration of how counterfactual reasoning about the outcomes of quantum mechanical experiments can lead to unavoidable logical contradictions.

A major goal of the research in this field is a conclusive, loophole-free test to determine whether or not nature is bound by locality and realism. Such an experiment could be based on Bell's inequalities, Hardy's propositions, the Greenberger-Horne-Zeilinger measurements, or on some other scheme which has yet to be discovered. Whatever form the experiment ultimately takes, it will certainly rely on quantum interference effects of entangled particles like the ones reported throughout this thesis.

The author has participated in several research efforts not described in this thesis. These include an experimental demonstration of time-dependent interference, a theoretical investigation of downconversion in the presence of phase-conjugate mirrors, an experimental test of a local-hidden-variable model for photodetection, and a theoretical analysis of multiphoton interference effects at a beamsplitter. Accounts of these are included in the list of publications.

This page intentionally left blank.

Appendix A

Quantum state for type-I downconversion with a cw pump

A.1 The interaction picture and the weak-field approximation

All of the analysis in this thesis has been carried out in the interaction picture, in which the Hamiltonian describing the system is written as the sum of a free Hamiltonian and an interaction Hamiltonian:

$$\hat{H} = \hat{H}_f + \hat{H}_I. \quad (\text{A.1})$$

The time evolution of any operator is then governed by the Heisenberg equation of motion using only the free Hamiltonian,

$$\frac{d}{dt} \hat{O}(t) = [\hat{O}(t), \hat{H}_f], \quad (\text{A.2})$$

while the state of the system at an arbitrary time, $|\psi(t)\rangle$, evolves from the initial state $|\psi(0)\rangle$ via the Schrödinger equation with only the interaction Hamiltonian:

$$|\psi(t)\rangle = \exp \frac{1}{i\hbar} \int_0^t \hat{H}_I(t) dt |\psi(0)\rangle. \quad (\text{A.3})$$

If the interaction described by \hat{H}_I is weak, and if the interaction time T is short, we may approximate this unitary transformation using the first two terms of the Taylor series expansion for the exponential in (A.3). This results in the (non-unitary) evolution

$$|\psi(T)\rangle \approx \left(1 + \frac{1}{i\hbar} \int_0^T \hat{H}_I(t) dt \right) |\psi(0)\rangle. \quad (\text{A.4})$$

We will take the initial state of the system to be

$$|\psi(0)\rangle = |0\rangle_s |0\rangle_i |vac\rangle. \quad (\text{A.5})$$

That is, there are initially no photons in either the signal or idler modes.

A.2 Hamiltonian for the parametric downconversion interaction

To carry out the procedure above for the downconversion system shown in Figure A.1, we must find expressions for the quantized free and interaction Hamiltonians for the fields within the downconversion crystal. We begin with the classical expression for the total energy of an electromagnetic field in a dielectric medium within a volume V :

$$\begin{aligned} H &= \frac{1}{2} \int_V d^3r \frac{1}{\mu_0} \mathbf{B}^2(\mathbf{r}, t) + \mathbf{E}(\mathbf{r}, t) \cdot \mathbf{D}(\mathbf{r}, t) \\ &= \frac{1}{2} \int_V d^3r \frac{1}{\mu_0} \mathbf{B}^2(\mathbf{r}, t) + \epsilon_0 \mathbf{E}^2(\mathbf{r}, t) + \mathbf{E}(\mathbf{r}, t) \cdot \mathbf{P}(\mathbf{r}, t). \end{aligned} \quad (\text{A.6})$$

The first two terms are the energy of the free electromagnetic field, while the last represents the contribution from the induced polarization within the medium. The induced polarization may be written as an expansion in powers of the incident electric field, with the leading terms

$$\mathbf{P}(\mathbf{r}, t) = \chi^{(1)} \mathbf{E}(\mathbf{r}, t) + \chi^{(2)} \mathbf{E}(\mathbf{r}, t) \mathbf{E}(\mathbf{r}, t), \quad (\text{A.7})$$

where $\chi^{(1)}$ and $\chi^{(2)}$ are the first and second-order electric susceptibility tensors which characterize the linear and lowest-order nonlinear responses of the medium, respectively.¹ As we are considering the interaction to be due to the nonlinear response

¹ This relation describes an instantaneous response to the incident electric field, implying that the susceptibilities are independent of frequency. This is not strictly true, of course: the nonlinear media do exhibit dispersion, and in fact the dispersive properties can become important in the ultrafast domain, where large pump bandwidths are involved. For the moment, we shall restrict our attention to frequencies far from any resonances in the material, so that these dispersive effects are small.

of the medium, we will include the linear response as part of the free Hamiltonian, so that

$$H_f = \frac{1}{2} \int_V d^3r \frac{1}{\mu_0} \mathbf{B}^2(\mathbf{r}, t) + \varepsilon \mathbf{E}^2(\mathbf{r}, t) \quad (\text{A.8})$$

where $\varepsilon = \varepsilon_0 + \chi^{(1)}$ is the linear dielectric constant of the medium. This leaves us with the interaction Hamiltonian

$$H_I = \frac{1}{2} \int_V d^3r \mathbf{E}(\mathbf{r}, t) \cdot \chi^{(2)} \mathbf{E}(\mathbf{r}, t) \mathbf{E}(\mathbf{r}, t). \quad (\text{A.9})$$

To make the transition from the classical to the quantum mechanical description of this system, we must quantize the fields in the above expressions. Some care has to be taken in doing so, but as long as we remain in the perturbative regime where the nonlinear interaction is weak, we can follow the usual prescription of replacing the classical electric fields with their corresponding free-field Hilbert-space operators. These operators are constructed by decomposing the fields into sums over a discrete set of modes that are planewave solutions of Maxwell's equations within a quantization volume L^3 , and then replacing the time-dependent parts of the mode functions with the photon annihilation and creation operators $\hat{a}(\mathbf{k}, t)$ and $\hat{a}^\dagger(\mathbf{k}, t)$. The results are

$$\hat{\mathbf{E}}(\mathbf{r}, t) = \frac{1}{L^{3/2}} \sum_{\mathbf{k}, s} \ell(\omega) \left[\hat{a}_{\mathbf{k}, s}(t) \boldsymbol{\varepsilon}_{\mathbf{k}, s} e^{i\mathbf{k} \cdot \mathbf{r}} - \hat{a}_{\mathbf{k}, s}^\dagger(t) \boldsymbol{\varepsilon}_{\mathbf{k}, s} e^{-i\mathbf{k} \cdot \mathbf{r}} \right] \quad (\text{A.10})$$

and

$$\hat{\mathbf{B}}(\mathbf{r}, t) = \frac{1}{L^{3/2}} \sum_{\mathbf{k}, s} \ell(\omega) \frac{n(\omega)}{c} \left[\hat{a}_{\mathbf{k}, s}(t) (\boldsymbol{\kappa} \times \boldsymbol{\varepsilon}_{\mathbf{k}, s}) e^{i\mathbf{k} \cdot \mathbf{r}} - \hat{a}_{\mathbf{k}, s}^\dagger(t) (\boldsymbol{\kappa} \times \boldsymbol{\varepsilon}_{\mathbf{k}, s}) e^{-i\mathbf{k} \cdot \mathbf{r}} \right], \quad (\text{A.11})$$

where $\ell(\omega) = i\sqrt{\hbar\omega/2\varepsilon}$. The polarization label $s = 1, 2$ denotes the two orthogonal transverse polarizations that are allowed at each frequency, the $\boldsymbol{\varepsilon}_{\mathbf{k}, s}$ are complex unit vectors describing the two basis polarizations for each mode, and $\mathbf{k} = k\boldsymbol{\kappa}$ is the

propagation vector for each mode, with magnitude equal to the wavenumber $k = \omega n(\omega)/c$, and direction κ . Here $n(\omega)$ is the frequency-dependent index of refraction in the dielectric. The annihilation and creation operators satisfy the commutation relations

$$\begin{aligned} [\hat{a}_{\mathbf{k},s}(t), \hat{a}_{\mathbf{k},s}^\dagger(t)] &= \delta_{\mathbf{k},\mathbf{k}} \delta_{s,s} \\ [\hat{a}_{\mathbf{k},s}(t), \hat{a}_{\mathbf{k},s}(t)] &= 0 \\ [\hat{a}_{\mathbf{k},s}^\dagger(t), \hat{a}_{\mathbf{k},s}^\dagger(t)] &= 0 \end{aligned} \quad (\text{A.12})$$

and are “ladder” operators in the sense that they change the number of photons, n , in the mode \mathbf{k}, s according to

$$\begin{aligned} \hat{a}_{\mathbf{k},s}(t)|n\rangle_{\mathbf{k},s} &= \sqrt{n}|n-1\rangle_{\mathbf{k},s} \\ \hat{a}_{\mathbf{k},s}^\dagger(t)|n\rangle_{\mathbf{k},s} &= \sqrt{n+1}|n+1\rangle_{\mathbf{k},s}. \end{aligned} \quad (\text{A.13})$$

A.3 Dynamics of the field operators

It is helpful to compute the time evolution of the field operators. Using (A.10) and (A.11), the quantized Hamiltonian for the free fields may be written as

$$\hat{H}_f = \sum_{\mathbf{k},s} \hbar\omega \left(\hat{a}_{\mathbf{k},s}^\dagger(t) \hat{a}_{\mathbf{k},s}(t) + \frac{1}{2} \right). \quad (\text{A.14})$$

This Hamiltonian can be inserted into (A.2) along with the commutation relations (A.12) to show that in a free field, the annihilation and creation operators evolve in time according to

$$\begin{aligned} \frac{d}{dt} \hat{a}_{\mathbf{k},s}(t) &= \frac{1}{i\hbar} [\hat{a}_{\mathbf{k},s}(t), \hat{H}] = -i\omega \hat{a}_{\mathbf{k},s}(t) \\ \frac{d}{dt} \hat{a}_{\mathbf{k},s}^\dagger(t) &= \frac{1}{i\hbar} [\hat{a}_{\mathbf{k},s}^\dagger(t), \hat{H}] = i\omega \hat{a}_{\mathbf{k},s}^\dagger(t) \end{aligned} \quad (\text{A.15})$$

with solutions

$$\begin{aligned}\hat{a}_{\mathbf{k},s}(t) &= \hat{a}_{\mathbf{k},s}(0)e^{-i\omega t} \\ \hat{a}_{\mathbf{k},s}^\dagger(t) &= \hat{a}_{\mathbf{k},s}^\dagger(0)e^{i\omega t}.\end{aligned}\tag{A.16}$$

The free electric field operator may therefore be rewritten as

$$\begin{aligned}\hat{\mathbf{E}}(\mathbf{r}, t) &= \frac{1}{L^{3/2}} \sum_{\mathbf{k},s} \ell(\omega) \hat{a}_{\mathbf{k},s} \boldsymbol{\varepsilon}_{\mathbf{k},s} e^{i(\mathbf{k} \cdot \mathbf{r} - \omega t)} + \text{h.c.} \\ &= \hat{\mathbf{E}}^{(+)}(\mathbf{r}, t) + \hat{\mathbf{E}}^{(-)}(\mathbf{r}, t)\end{aligned}\tag{A.17}$$

where the notation for the time argument of $\hat{a}_{\mathbf{k},s}(0)$ has been suppressed. The letters “h.c.” stand for the Hermitian conjugate of the term immediately to the left. $\hat{\mathbf{E}}^{(+)}(\mathbf{r}, t)$ is often referred to as the positive-frequency part of the electric field operator, and is also known as the complex analytic signal. For one-dimensional problems, a simpler, scalar version of this operator, for which $\ell(\omega) = 1$, is often used:

$$\hat{E}^{(+)}(\mathbf{r}, t) = \sqrt{\frac{\delta\omega}{2\pi}} \sum_{\mathbf{k},s} \hat{a}_{\mathbf{k},s} e^{i(\mathbf{k} \cdot \mathbf{r} - \omega t)}.\tag{A.18}$$

This represents a single field component, dimensionally renormalized so that the product $\hat{E}^{(-)}\hat{E}^{(+)}$ has units of photons per second. The quantity $\delta\omega = 2\pi c/L$ is the mode-spacing within a one-dimensional “quantization length” of dimension L .

A.4 The multimode state

We are now in a position to compute $|\psi(T)\rangle$ in Eq. (A.4). We intend to substitute the field operator (A.17) into (A.9) to produce an explicit expression for \hat{H}_I , which can then be inserted into (A.4). We note that the electric field within the interaction region is the sum of the pump, signal, and idler fields,

$$\begin{aligned}
\hat{\mathbf{E}}(\mathbf{r}, t) &= \hat{\mathbf{E}}_p(\mathbf{r}, t) + \hat{\mathbf{E}}_s(\mathbf{r}, t) + \hat{\mathbf{E}}_i(\mathbf{r}, t) \\
&= \frac{1}{L^{3/2}} \sum_{\mathbf{k}_p} \ell(\omega) \hat{a}_{\mathbf{k}_p, e} \boldsymbol{\varepsilon}_e e^{i(\mathbf{k}_p \cdot \mathbf{r} - \omega_p t)} + \text{h.c.} \\
&\quad + \frac{1}{L^{3/2}} \sum_{\mathbf{k}_s} \ell(\omega) \hat{a}_{\mathbf{k}_s, o} \boldsymbol{\varepsilon}_o e^{i(\mathbf{k}_s \cdot \mathbf{r} - \omega_s t)} + \text{h.c.} \\
&\quad + \frac{1}{L^{3/2}} \sum_{\mathbf{k}_i} \ell(\omega) \hat{a}_{\mathbf{k}_i, o} \boldsymbol{\varepsilon}_o e^{i(\mathbf{k}_i \cdot \mathbf{r} - \omega_i t)} + \text{h.c.}
\end{aligned} \tag{A.19}$$

Here we have incorporated the fact that type-I phase-matching conditions require the pump to be e -polarized, while the signal and idlers are both o -polarized. Inserting this field operator directly into (A.9) yields a plethora of terms, most of which will not contribute anything when acting on the initial vacuum state. The most important terms for downconversion are

$$\hat{H}_I = \frac{1}{2} \frac{1}{L^{9/2}} \sum_{\mathbf{k}_p} \sum_{\mathbf{k}_s} \sum_{\mathbf{k}_i} \tilde{\chi}_{eoo}^{(2)} \boldsymbol{\varepsilon}_e \boldsymbol{\varepsilon}_o \boldsymbol{\varepsilon}_o e^{i(\omega_p - \omega_s - \omega_i)t} \int_V d^3r e^{i(\mathbf{k}_p - \mathbf{k}_s - \mathbf{k}_i) \cdot \mathbf{r}} \hat{a}_{\mathbf{k}_p, e} \hat{a}_{\mathbf{k}_s, o}^\dagger \hat{a}_{\mathbf{k}_i, o}^\dagger + \text{h.c.} \tag{A.20}$$

where $\chi_{eoo}^{(2)}$ is the element of the electric susceptibility tensor that couples the pump field with e -polarization to the signal and idler fields with o -polarizations². The first term above corresponds to the downconversion process, indicating the annihilation of a pump photon and the creation of a signal and an idler photon. The Hermitian conjugate of this term corresponds to up-conversion, in which the signal and idler photons are annihilated to produce a pump photon; this term gives a zero contribution when the initial signal and idler state is the vacuum, but is included here to ensure that \hat{H}_I is Hermitian.

For the case of cw pumping, the pump field is usually taken to be a monochromatic plane-wave, consisting of only a single mode with propagation vector \mathbf{k}_p and frequency ω_p . Furthermore, it is considered to be intense enough that it is not

² The notation that indicates the frequency dependence of the susceptibility has been suppressed. By our earlier arguments, this term is not allowed to depend on frequency, but we will see shortly that we can include a frequency dependence for the susceptibility quite easily.

significantly affected by the occasional annihilation of one photon. Because the pump field is usually produced by a laser, it is taken to be in a coherent state $|V\rangle_{\mathbf{k}_p,e}$, which is a right eigenstate of the annihilation operator $\hat{a}_{\mathbf{k}_p,e}$. With these assumptions, we may treat the pump as a classical monochromatic field with a constant amplitude V_0 :

$$\mathbf{E}_p(\mathbf{r}, t) = V_0 \boldsymbol{\varepsilon}_e e^{i(\mathbf{k}_p \cdot \mathbf{r} - \omega_p t)}. \quad (\text{A.21})$$

Using this instead of the mode expansion for the pump in (A.20) yields a simpler interaction Hamiltonian:

$$\hat{H}_I = \frac{1}{2} \frac{1}{L^3} \sum_{\mathbf{k}_s, \mathbf{k}_i} V_0 \tilde{\chi}_{eoo}^{(2)} \boldsymbol{\varepsilon}_e \boldsymbol{\varepsilon}_o \boldsymbol{\varepsilon}_o e^{-i(\omega_p - \omega_s - \omega_i)t} \int_V d^3r e^{i(\mathbf{k}_p - \mathbf{k}_s - \mathbf{k}_i) \cdot \mathbf{r}} a_{\mathbf{k}_s,o}^\dagger a_{\mathbf{k}_i,o}^\dagger + \text{h.c.} \quad (\text{A.22})$$

We may simplify it further by noting that the important signal and idler fields are sums over the range of detected modes, as determined by the apertures depicted in Figure A.1. For small apertures, the range of allowed propagation directions is sufficiently restricted that we may consider the pump, signal, and idler fields all to have fixed propagation directions κ_p , κ_s , and κ_i . Then we may replace the sum over propagation vectors with a sum over frequencies:

$$\hat{H}_I = \frac{1}{2} \frac{\delta\omega}{2\pi} \sum_{\omega_s, \omega_i} \ell_x \ell_y \ell_z V_0 \tilde{\chi}_{eoo}^{(2)} \boldsymbol{\varepsilon}_e \boldsymbol{\varepsilon}_o \boldsymbol{\varepsilon}_o e^{-i(\omega_p - \omega_s - \omega_i)t} (\omega_p; \omega_s, \omega_i) a_{\mathbf{k}_s,o}^\dagger a_{\mathbf{k}_i,o}^\dagger + \text{h.c.} \quad (\text{A.23})$$

Here $\delta\omega$ is the mode spacing, which is usually taken to the limit $\delta\omega \rightarrow 0$ as the sums are replaced by integrals at the end of any calculations. The function

$$\begin{aligned} (\omega_p; \omega_s, \omega_i) &= \frac{1}{\ell_x \ell_y \ell_z} \int_V d^3r e^{i(\mathbf{k}_p - \mathbf{k}_s - \mathbf{k}_i) \cdot \mathbf{r}} \\ &= e^{i(\mathbf{k}_p(\omega_p) - \mathbf{k}_s(\omega_s) - \mathbf{k}_i(\omega_i)) \cdot \mathbf{r}_0} \int_{m=1}^3 \text{sinc} \left[\frac{1}{2} \left(\mathbf{k}_p(\omega_p) - \mathbf{k}_s(\omega_s) - \mathbf{k}_i(\omega_i) \right)_m \ell_m \right]. \end{aligned} \quad (\text{A.24})$$

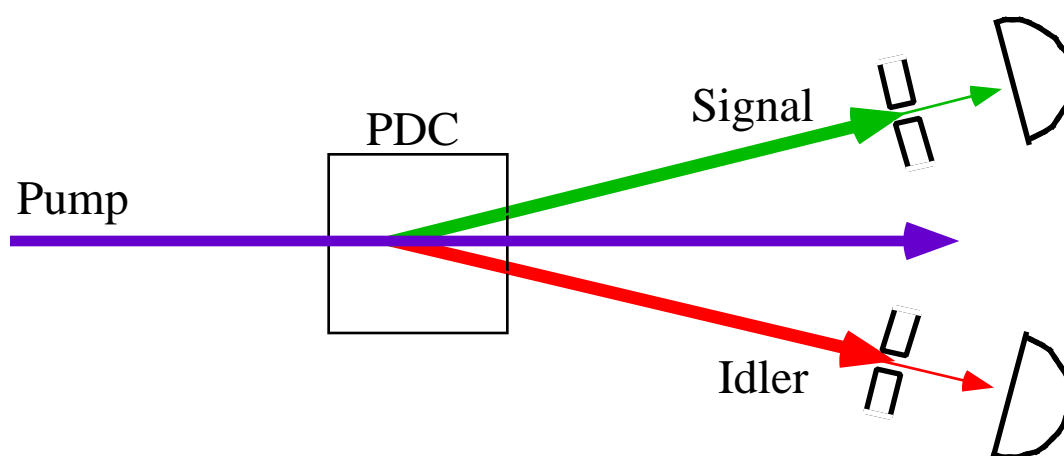


Figure A.1 A cw pump beam produces signal and idler beams in the process of spontaneous parametric downconversion. The signal and idler beams are produced over a range of propagation directions, but this range is narrowed by placing pinhole apertures in front of the detectors, so that we may treat the signal and idler beams each as having a single propagation direction.

is the phase-matching function for the pump, signal, and idler modes. The various ℓ_m refer to the x , y , and z dimensions of the interaction region (see Figure A.2), and \mathbf{r}_0 is the position at the center of the interaction region.

Inserting the interaction Hamiltonian in (A.23) into (A.4), and letting the creation operators act on the initial vacuum state, we have

$$|\psi(T)\rangle = |vac\rangle + \frac{gV_0\ell_x\ell_y\ell_z}{i\hbar} \int_0^T dt \frac{\delta\omega}{2\pi} e^{-i(\omega_p - \omega_s - \omega_i)t} \left(\omega_p; \omega_s, \omega_i \right) |1\rangle_{\mathbf{k}_s, o} |1\rangle_{\mathbf{k}_i, o} \quad (\text{A.25})$$

where the parameter

$$g = \tilde{\chi}_{eoo}^{(2)} \epsilon_e \epsilon_o \epsilon_o \quad (\text{A.26})$$

reflects the strength of the coupling between the modes. Carrying out the time integration gives

$$|\psi(T)\rangle = |vac\rangle + \eta \frac{\delta\omega}{2\pi} e^{-i(\omega_p - \omega_s - \omega_i)T/2} T \text{sinc}\left[\frac{1}{2}(\omega_p - \omega_s - \omega_i)T\right] \times \left(\omega_p; \omega_s, \omega_i \right) |1\rangle_{\omega_s, o} |1\rangle_{\omega_i, o} \quad (\text{A.27})$$

where we have dropped the directional mode labels \mathbf{k}_s , \mathbf{k}_i in favor of frequency labels ω_s, ω_i , and the dimensionless parameter

$$\eta = \frac{gV_0\ell_x\ell_y\ell_z}{i\hbar} \quad (\text{A.28})$$

is the magnitude of the perturbation on the initial vacuum state.

The state in (A.27) represents a superposition of amplitudes for emission of a signal and idler pair at various discrete frequencies. It is often referred to as the “multimode” state for parametric downconversion. We see that although the pump was taken to be monochromatic, the signal and idler photons each have a range of possible

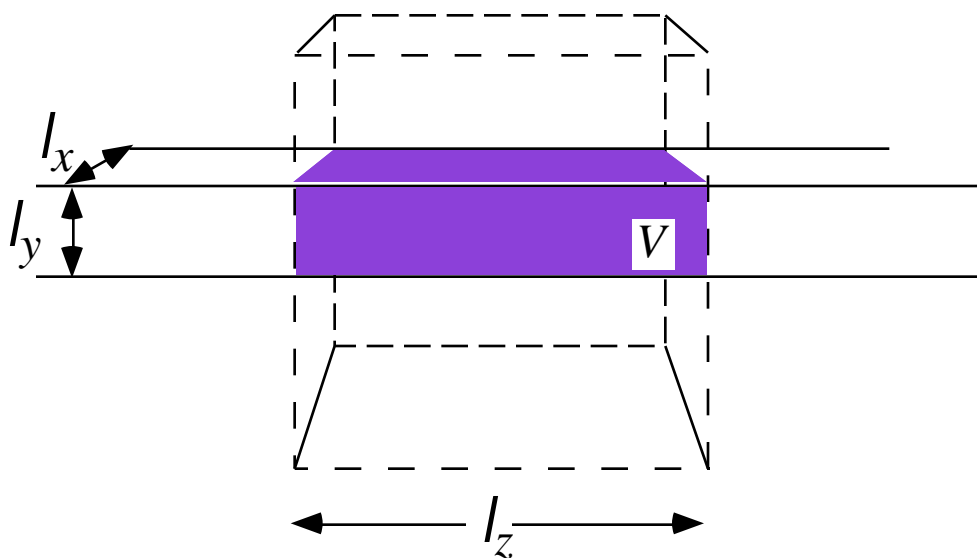


Figure A.2 The interaction volume is determined by the length of the crystal along the direction of propagation, z , and by the transverse dimensions of the pump beam, which is taken to have a rectangular cross-section for simplicity.

frequencies, weighted by the product of $\text{sinc}\left[\frac{1}{2}(\omega_p - \omega_s - \omega_i)T\right]$ and $(\omega_p; \omega_s, \omega_i)$.

The first of these terms is peaked at the value

$$\omega_p - \omega_s - \omega_i = 0, \quad (\text{A.29})$$

and for interaction times that are long compared with the coherence time of the downconverted light, it behaves somewhat like a delta function that ensures the fields satisfy the energy conservation phase-matching requirement. Since the pump frequency is fixed, this term really only places a constraint on the sum of the signal and idler frequencies. For this long-time limit, it is possible to rewrite the multimode state as³

$$|\psi\rangle = |vac\rangle + \eta \int_{\omega_s} \delta\omega \left(\omega_s, \omega_p - \omega_s\right) |1\rangle_{\omega_s, o} |1\rangle_{\omega_p - \omega_s, o} \quad (\text{A.30})$$

where we have suppressed the notation for the time dependence of $|\psi\rangle$, which is understood to describe the light at a time after the downconversion interaction is completed. In the limit $\delta\omega \rightarrow 0$ we have the continuous multimode superposition state

$$|\psi\rangle = |vac\rangle + \eta \int_0 d\omega_s \left(\omega_s, \omega_p - \omega_s\right) |1\rangle_{\omega_s, o} |1\rangle_{\omega_p - \omega_s, o}. \quad (\text{A.31})$$

The states in the preceding two equations are examples of frequency-entangled states, because they are pure states for the signal and idler photon pair which cannot be factored into products of separate states for each photon. When the photons are emitted, the frequency of each one is undefined until it is measured -- but because of the anticorrelation guaranteed by the phase-matching function, a measurement of either the signal or the idler frequency alone is enough to determine the frequency of both photons.

³ In the following two equations, the phase-matching function $(\omega_p; \omega_s, \omega_i)$ has been redefined, and has the dimensions of inverse frequency

A.5 The two-mode state

In the expressions above for the multimode state, the phase-matching function determines the relative weights in the sum for the various allowed combinations to be emitted. Inspection of (A.24) reveals that this function is peaked at the value

$$\mathbf{k}_p(\omega_p) - \mathbf{k}_s(\omega_s) - \mathbf{k}_i(\omega_i) = 0, \quad (\text{A.32})$$

becoming more sharply peaked as the interaction region dimensions ℓ_m are increased. In the limit of infinite interaction volume, $\delta(\mathbf{k}_p - \mathbf{k}_s - \mathbf{k}_i)$ becomes a delta function which ensures that the momentum conservation phase-matching requirement is satisfied.

Of course, in practice the downconversion crystals are not of infinite length, and the pump mode is not an infinitely wide planewave, so that $\delta(\mathbf{k}_p - \mathbf{k}_s - \mathbf{k}_i)$ may be nonzero over quite a broad range of values for ω_s and ω_i . This broad bandwidth indicates that the signal and idler photons are actually excitations of “wavepacket” modes which may be quite short in duration. In the lab, with typical crystal lengths of several cm and beam spot sizes of a few mm, these wavepackets may only be a few ps in duration, corresponding to bandwidths on the order of 10^{12} Hz.

Nevertheless, it is often convenient to treat the signal and idler modes as if they were monochromatic, rather than broadband. The motivation for doing so is that it simplifies the analysis of almost any experiment, while still demonstrating the nonclassical features that we have discussed in the previous sections. This assumption can be made quite easily by restricting the integral in (A.31) to just those frequencies that exactly satisfy the momentum phase-matching condition. In this monochromatic approximation, we have

$$|\psi(T)\rangle = |vac\rangle + \eta |1\rangle_{\omega_s, o} |1\rangle_{\omega_i, o} \quad (\text{A.33})$$

where the factor η now includes the product $\delta\omega(\omega_s, \omega_i)$. This state is a reasonable approximation so long as the weak interaction condition

$$|\eta|^2 \ll 1 \quad (\text{A.34})$$

is satisfied: the state is then normalized according to

$$\begin{aligned} \langle \psi(T) | \psi(T) \rangle &= \langle vac | vac \rangle + |\eta|^2_{\omega_s, o} \langle 1|1 \rangle_{\omega_s, o} \times_{\omega_i, o} \langle 1|1 \rangle_{\omega_i, o} \\ &= 1 + |\eta|^2 \\ &1. \end{aligned} \quad (\text{A.35})$$

This page intentionally left blank.

Appendix B

The quantum state for type-II downconversion with a broadband pump

B.1 Derivation

In Appendix A we derived an expression for the two-photon state produced in a cw-pumped type-I downconversion process. We will follow the same perturbative procedure here, but with the added complications that come from type-II phase-matching conditions and the broad range of frequencies available for downconversion within the ultrafast pump pulse.

The collinear type-II downconversion process is depicted in Figure B.1, in which a collimated pump beam is incident on a birefringent nonlinear crystal. We will consider the downconversion produced by a single pump pulse, with an electric field given by

$$\mathbf{E}_p^{(+)}(t) = V_0 v(z - ct) \boldsymbol{\varepsilon}_e e^{i(\mathbf{k}_p(\omega_p) \cdot \mathbf{r} - \omega_p t)}. \quad (\text{B.1})$$

Here V_0 represents the maximum amplitude of the pump field, while $v(z - ct)$ is a dimensionless “envelope” function which propagates in the z direction. Once again we are treating the pump field classically and assuming that the non-depleted pump and coherent-state pump approximations hold (see Appendix A). The pump beam is assumed to have a linear polarization $\boldsymbol{\varepsilon}_e$ along the extraordinary axis of the crystal, while the signal and idler fields are assumed to have polarizations along the ordinary and extraordinary axes, respectively, as demanded by the type-II phase-matching considerations in Section 1.3.3. Furthermore, the pump, signal and idler propagation directions, κ_p , κ_s , and κ_i are all fixed for collinear propagation along z , so that sums

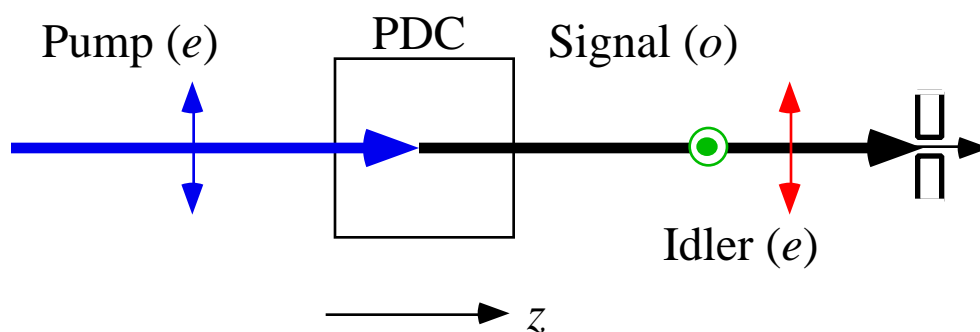


Figure B.1. Type-II collinear parametric downconversion. For negative uniaxial crystals such as BBO, the pump wave must have extraordinary polarization, while the signal and idler beams have ordinary and extraordinary polarizations, respectively.

over the propagation vectors may be replaced by sums over frequencies. Experimentally, this condition is ensured with the help of the pinhole apertures shown in Figure B.1.

With these considerations in mind, we may take the interaction Hamiltonian in the interaction picture to have the form

$$\hat{H}_I = \frac{1}{2} \frac{\delta\omega}{2\pi} \frac{V_0 \tilde{\chi}_{eoe}^{(2)} \epsilon_e \epsilon_o \epsilon_e \ell_x \ell_y}{\omega_o \omega_e} \int_z dz e^{-i(\omega_p + \omega_o - \omega_e)t} e^{i(k_p + k_o - k_e)z} v(z - ct) \times \hat{a}_{\mathbf{k}(\omega_o),o}^\dagger \hat{a}_{\mathbf{k}(\omega_e),e}^\dagger + \text{h.c.} \quad (\text{B.2})$$

by analogy with equation (A.22).

In the weak-interaction limit, the state after a time T is then

$$\begin{aligned} |\psi(T)\rangle &= 1 + \frac{1}{i\hbar} \int_0^T \hat{H}_I(t) dt |vac\rangle \\ &= 1 + \frac{g V_0 \ell_x \ell_y}{i\hbar} \int_0^T dt \frac{\delta\omega}{2\pi} \int_z dz e^{-i(\omega_p - \omega_o - \omega_e)t} e^{i(k_p - k_o - k_e)z} v(z - ct) \\ &\quad \times \hat{a}_o^\dagger(\omega_o) \hat{a}_e^\dagger(\omega_e) + \text{h.c.} \Big] |vac\rangle \end{aligned} \quad (\text{B.3})$$

where $g = \tilde{\chi}_{eoe}^{(2)} \epsilon_e \epsilon_o \epsilon_e$ in analogy with (1.26), and the notation

$$\hat{a}_\eta^\dagger(\omega_\mu) = \hat{a}_{\mathbf{k}(\omega_\mu),\eta}^\dagger \quad (\text{B.4})$$

has been introduced to represent the creation operators for the signal and idler modes with frequencies ω_o and ω_e , and polarizations $\eta = o, e$. Next we let

$$ct = z - ct \quad (\text{B.5})$$

so that

$$\begin{aligned} |\psi(T)\rangle &= 1 + \frac{g V_0 \ell_x \ell_y}{i\hbar} \frac{\delta\omega}{2\pi} \int_{\omega_o} \int_{\omega_e} dz e^{i[(k_p(\omega_p) - k_o(\omega_o) - k_e(\omega_e)) - (\omega_p - \omega_o - \omega_e)]z/c} \\ &\quad \times \int_{-T}^{T/c} dt w(ct) e^{i(\omega_o + \omega_e)t} \hat{a}_o^\dagger(\omega_o) \hat{a}_e^\dagger(\omega_e) + \text{h.c.} |vac\rangle \end{aligned} \quad (\text{B.6})$$

with the full time dependence of the pump field represented by

$$w(t) = v(ct)e^{i\omega_p t}. \quad (\text{B.7})$$

Because $w(t)$ is nonzero only for a small range of times, the limits of the time integral may be extended to $\pm \infty$, so that the state is then given by

$$|\psi(T)\rangle = \left[1 + \frac{gV_0\ell_x\ell_y}{i\hbar} \int_{\omega_o}^{\omega_e} \delta\omega \int_{-z}^z dz e^{i[(k_p(\omega_p) - k_s(\omega_o) - k_i(\omega_e)) - (\omega_p - \omega_o - \omega_e)]/c} z \right. \\ \left. \times \alpha(\omega_o + \omega_e) \hat{a}_o^\dagger(\omega_o) \hat{a}_e^\dagger(\omega_e) + \text{h.c.} \right] |vac\rangle \quad (\text{B.8})$$

where

$$\alpha(\omega) = \frac{1}{2\pi} \int_{-\infty}^{\infty} dt w(t) e^{i\omega t} \quad (\text{B.9})$$

is the Fourier transform of the temporal profile of the pump pulse. The z -integral yields ℓ_z multiplied by the phase-matching function

$$\left(\omega_p; \omega_o, \omega_e \right) = \text{sinc} \left[\frac{1}{2} \left\{ \left(k_p(\omega_p) - k_s(\omega_o) - k_i(\omega_e) \right) - \left(\omega_p - \omega_o - \omega_e \right) / c \right\} L \right] \\ \times e^{i(k_p(\omega_p) - k_s(\omega_o) - k_i(\omega_e))z_o} \quad (\text{B.10})$$

where $L = \ell_z$ is the length of the crystal along the direction of propagation. If the crystal is cut and aligned for type-II phase matching, the second term in brackets reduces to zero, so that this function takes on the familiar form

$$\left(\omega_o, \omega_e \right) = e^{i(k_p(\omega_o + \omega_e) - k_s(\omega_o) - k_i(\omega_e))z_o} \text{sinc} \left[\frac{1}{2} \left(k_p(\omega_o + \omega_e) - k_s(\omega_o) - k_i(\omega_e) \right) L \right] \quad (\text{B.11})$$

The state is now given by

$$|\psi\rangle = \left[1 + \eta \int_{\omega_o}^{\omega_e} \delta\omega \alpha(\omega_o + \omega_e) \left(\omega_o, \omega_e \right) \hat{a}_o^\dagger(\omega_o) \hat{a}_e^\dagger(\omega_e) + \text{h.c.} \right] |vac\rangle \quad (\text{B.12})$$

with the dimensionless parameter

$$\eta = \frac{g\ell_x\ell_y\ell_z V_0}{i\hbar} \quad (\text{B.13})$$

defined in much the same way as in (A.28). We have dropped the dependence on T in the notation for $|\psi\rangle$, with the understanding that the state is valid (up to a phase) for all times after the interaction is completed. Letting the creation and annihilation operators in (B.12) act on the vacuum state yields the final expression

$$\begin{aligned} |\psi\rangle &= |vac\rangle + \eta \delta\omega \int_{\omega_o, \omega_e} \alpha(\omega_o + \omega_e) |\omega_o, \omega_e\rangle_{\omega_o} |\omega_e\rangle_{\omega_e} \\ &= |vac\rangle + \eta |\psi^{(1)}\rangle, \end{aligned} \quad (\text{B.14})$$

where we have introduced the following notation for a fock state with a single photon in the signal or idler modes:

$$|\omega_\mu\rangle_{\eta} = \hat{a}_\eta^\dagger(\omega_\mu) |vac\rangle. \quad (\text{B.15})$$

B.2 Normalization

The norm of this state is

$$\langle\psi|\psi\rangle = 1 + |\eta|^2 B \quad (\text{B.16})$$

where

$$B = \int_{\omega_o, \omega_e} (\delta\omega)^2 |\alpha(\omega_o + \omega_e)|^2 |\omega_o, \omega_e|^2 \quad (\text{B.17})$$

is the dimensionless norm of the state $|\psi^{(1)}\rangle$. Taking the limit as the mode spacing $\delta\omega$ tends to zero we have

$$B = \int_0^0 d\omega_o d\omega_e |\alpha(\omega_o + \omega_e)|^2 |\omega_o, \omega_e|^2. \quad (\text{B.18})$$

For the particular choice of a normalized gaussian pump spectrum centered at twice the mean frequency of the degenerate signal and idler beams, we have

$$\alpha(\omega_o + \omega_e) = \frac{2}{\sigma\sqrt{\pi}} e^{-\frac{\omega_o + \omega_e - 2\bar{\omega}}{\sigma}}^2, \quad (\text{B.19})$$

so that B becomes

$$B = \frac{4\sqrt{2\pi}}{\sigma\tau_-}, \quad (\text{B.20})$$

with

$$\tau_- = L \left. \frac{\partial k_o}{\partial \omega} - \frac{\partial k_e}{\partial \omega} \right|_{\bar{\omega}}. \quad (\text{B.21})$$

The state in (B.14) is a valid approximation so long as the magnitude of the perturbation on the initial state is small. This condition is satisfied when

$$|\eta|^2 \langle \psi^{(1)} | \psi^{(1)} \rangle = |\eta|^2 B \ll 1. \quad (\text{B.22})$$

In this case, the norm of the state in (B.16) is approximately equal to one, even though $|\psi^{(1)}\rangle$ is not normalized to one.

Appendix C

Quantum state for the “Engineering Indistinguishability” experiment

C.1 Derivation

In Chapter 3 and Appendix B, the labels o and e were used for the polarizations of the signal and idler beams created in a collinear type-II downconversion process. However, because each photon from the new source in Chapter 4 is a superposition of an e and an o -polarized photon from the two creation processes, we can avoid some confusion by choosing new polarization labels for the signal and idler modes. We will identify the polarization direction parallel to the optical table and to the extraordinary axis of the PDC, as x , and the polarization direction orthogonal to this as y (see Figure 5.1b).

The electric field of the e -polarized ultrafast pump pulse will be treated classically, as in Appendix B. The form is identical to that given in (B.1)

$$\mathbf{E}_p^{(+)}(t) = V_0 v(z - ct) \mathbf{e}_e e^{i(\mathbf{k}_p(\omega_p) \cdot \mathbf{r} - \omega_p t)}. \quad (\text{C.1})$$

Initially, the signal and idler modes are unoccupied, in the vacuum state. After the first pass through the downconversion crystal, the state of the light is given by

$$|\Psi_1\rangle = \left(1 + \frac{1}{i\hbar} \int_0^T \hat{H}_{II}(t) dt \right) |vac\rangle \quad (\text{C.2})$$

where T is the interaction time (equal to the pump duration), and the interaction Hamiltonian in the interaction picture has the form analogous to that in (B.2):

$$\hat{H}_{II} = \frac{1}{2} \frac{\delta\omega}{2\pi} \int_{\omega_o} \int_{\omega_e} V_0 \tilde{\chi}_{eoe}^{(2)} \boldsymbol{\epsilon}_e \boldsymbol{\epsilon}_o \boldsymbol{\ell}_x \boldsymbol{\ell}_y \int_z dz e^{-i(\omega_p + \omega_o - \omega_e)z} e^{i(k_p + k_o - k_e)z} \nu(z - ct) \times a_{\mathbf{k}(\omega_o)y}^\dagger a_{\mathbf{k}(\omega_e)x}^\dagger + \text{h.c.} \quad (\text{C.3})$$

Following the procedure in Appendix B, equations (B.3) - (B.14), we have for the quantum state of the light after the first pump pulse:

$$\begin{aligned} |\psi_1\rangle &= 1 + \eta \delta\omega \int_{\omega_o} \int_{\omega_e} \alpha(\omega_o + \omega_e) (\omega_o, \omega_e) \hat{a}_{y1}^\dagger(\omega_o) \hat{a}_{x1}^\dagger(\omega_e) + \text{h.c.} |vac\rangle \\ &= |vac\rangle + \eta \delta\omega \int_{\omega_o} \int_{\omega_e} \alpha(\omega_o + \omega_e) (\omega_o, \omega_e) |\omega_o\rangle_{y1} |\omega_e\rangle_{x1} \end{aligned} \quad (\text{C.4})$$

with η defined in (B.13) and (ω_o, ω_e) defined in (B.11). The terms $\hat{a}_\eta^\dagger(\omega_\mu)$ and $|\omega_\mu\rangle_\eta$ have the meanings given in (B.4) and (B.15), with the polarization labels $x1$ and $y1$ denoting the signal and idler modes for the first downconversion process.

After passing through the $\lambda/4$ plate twice and being reflected back into the downconversion crystal, the signal and idler photons have their polarizations exchanged, while their frequencies are preserved. The field operators for the modes returning to the crystal are therefore related to the “process one” signal and idler modes by

$$\begin{aligned} \hat{a}_x(\omega_o) &= -\hat{a}_{y1}(\omega_o) \\ \hat{a}_y(\omega_e) &= \hat{a}_{x1}(\omega_e). \end{aligned} \quad (\text{C.5})$$

Thus, the state before the second pass of the pump pulse may be rewritten in terms of the final field modes as

$$|\psi_1\rangle = |vac\rangle - \eta \delta\omega \int_{\omega_o} \int_{\omega_e} \alpha(\omega_o + \omega_e) (\omega_o, \omega_e) |\omega_o\rangle_x |\omega_e\rangle_y. \quad (\text{C.6})$$

The signal and idler modes for the second downconversion process are related to those for the first process by the phases $\theta_s = k_s(\omega_s)\ell_{signal}$ and $\theta_i = k_i(\omega_i)\ell_{idler}$. Meanwhile, the

pump pulse has acquired a phase $\theta_p = k_p (\omega_p) \ell_{pump}$ during its propagation to M1 and back, so that the interaction Hamiltonian for the second downconversion process is given by

$$\hat{H}_{I2} = e^{i\theta} \frac{1}{2} \frac{\delta\omega}{2\pi} \int_{\omega_o} \int_{\omega_e} V_0 \tilde{\chi}_{eoe}^{(2)} \epsilon_e \epsilon_o \epsilon_e \ell_x \ell_y \ell_z dz e^{-i(\omega_p + \omega_o - \omega_e)t} e^{i(k_p + k_o - k_e)z} \nu(z - ct) \times a_{\mathbf{k}(\omega_o),y}^\dagger a_{\mathbf{k}(\omega_e),x}^\dagger + \text{h.c.} \quad (\text{C.7})$$

where $\theta = \theta_s + \theta_i - \theta_p$. Treating $|\psi_1\rangle$ as the initial state for the second process, the state of the light after the second interaction is

$$|\psi\rangle = 1 + e^{i\theta} \eta \delta\omega \int_{\omega_o} \int_{\omega_e} \alpha(\omega_o + \omega_e) (\omega_o, \omega_e) \hat{a}_y^\dagger(\omega_o) \hat{a}_x^\dagger(\omega_e) + \text{h.c.} |\psi_1\rangle. \quad (\text{C.8})$$

Letting the creation and annihilation operators act on $|\psi_1\rangle$ and keeping only the terms of lowest order in η gives

$$|\psi\rangle = |vac\rangle - \eta \delta\omega \int_{\omega_o} \int_{\omega_e} \alpha(\omega_o + \omega_e) (\omega_o, \omega_e) |\omega_o\rangle_x |\omega_e\rangle_y + e^{i\theta} \eta \delta\omega \int_{\omega_o} \int_{\omega_e} \alpha(\omega_o + \omega_e) (\omega_o, \omega_e) |\omega_o\rangle_y |\omega_e\rangle_x \quad (\text{C.9})$$

which may be written more compactly as

$$|\psi\rangle = |vac\rangle + \eta \delta\omega \int_{\omega_o} \int_{\omega_e} \alpha(\omega_o + \omega_e) (\omega_o, \omega_e) \left[|\omega_o\rangle_x |\omega_e\rangle_y - e^{i\theta} |\omega_o\rangle_y |\omega_e\rangle_x \right] = |vac\rangle + \eta |\psi^{(1)}\rangle. \quad (\text{C.10})$$

C.2 Normalization

The norm of this state is

$$\langle\psi|\psi\rangle = 1 + 2|\eta|^2 (B - K \cos(\theta)) \quad (\text{C.11})$$

where

$$B = (\delta\omega)^2 \int_{\omega_o}^{\omega_e} |\alpha(\omega_o + \omega_e)|^2 (\omega_o, \omega_e) d\omega \quad (\text{C.12})$$

as in (B.17), and

$$K = (\delta\omega)^2 \int_{\omega_o}^{\omega_e} |\alpha(\omega_o + \omega_e)|^2 (\omega_e, \omega_o) (\omega_o, \omega_e) d\omega. \quad (\text{C.13})$$

As in Appendix B, we may evaluate these terms in the limit $\delta\omega \rightarrow 0$ using the normalized gaussian pump spectrum

$$\alpha(\omega_o + \omega_e) = \frac{2}{\sigma\sqrt{\pi}} e^{-\frac{(\omega_o + \omega_e - 2\bar{\omega})^2}{\sigma^2}}, \quad (\text{C.14})$$

giving

$$B = \frac{4\sqrt{2\pi}}{\sigma\tau_-} \quad (\text{C.15})$$

and

$$K = 2B \frac{\sqrt{2\pi}}{\sigma(\tau_o + \tau_e)} \operatorname{erf} \frac{\sigma(\tau_o + \tau_e)}{4\sqrt{2}}. \quad (\text{C.16})$$

The state in (C.10) is a valid approximation so long as the magnitude of the perturbation on the initial state is small. Noting from the integral definitions of B and K that $K \ll B$, we see that

$$\frac{\langle \psi^{(1)} | \psi^{(1)} \rangle}{4B} = 2(B - K \cos(\theta)) \quad (\text{C.17})$$

Evidently the condition for the “weak interaction” approximation is

$$|\eta|^2 \langle \psi^{(1)} | \psi^{(1)} \rangle = |\eta|^2 4B \ll 1. \quad (\text{C.18})$$

Once again, the norm of $|\psi\rangle$ is approximately equal to one even though $|\psi^{(1)}\rangle$ is not normalized to one.

Appendix D

Locking system for an interferometer

D.1 Conceptual arrangement

In the experiment described in Chapter 4, two downconversion processes were generated within a Michelson interferometer as depicted in Figure 5.3. As in any interference experiment, it was important to keep the difference in path lengths as constant as possible during each counting interval. For short counting times, this can usually be accomplished with passive stabilizing techniques such as minimizing air currents, maintaining constant temperature, and eliminating sources of vibration or decoupling from these sources. However, with our apertures (Figure 5.6) closed down for better interference visibility, the low coincidence counting rate of 15/sec implied that long counting times were necessary to acquire good statistics at each point. Under these circumstances passive techniques were no longer sufficient.

To achieve better control over the fluctuations, we constructed the active locking system shown in Figure D.1. The beam from a frequency-stabilized 5 mW HeNe laser beam was expanded with a 10 cm focal length lens and injected into the unused port of the Michelson interferometer at a small angle relative to the arms. Although the dichroic mirror MD2 is coated for transmission in the red, a small fraction of the HeNe beam was still diverted to mirror M2, from which it was reflected back through MD2. Most of the incident HeNe light was transmitted through MD2 to M1, where it was reflected back to MD2. Once again, most of this light passed through MD2, but a small fraction was reflected. For a proper choice of the input beam's incident angle, the two beams displayed a set of vertical "tilt" fringes at the collection mirror M3. This mirror was

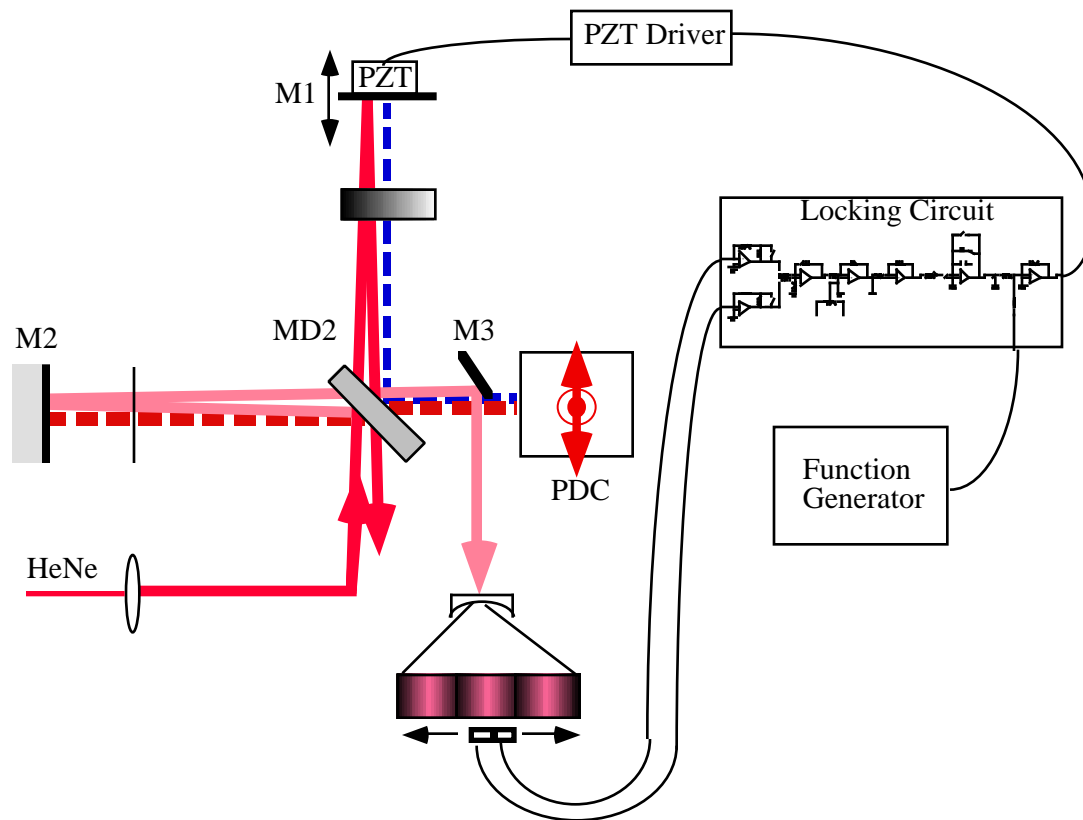


Figure D.1 Locking system for the 2-color Michelson interferometer. The HeNe beam incident from the left forms a set of interference fringes which are imaged onto a pair of photodiodes. The difference signal is integrated and used as a control input to the piezoelectric driver. A change in the fringe position at the diodes results in a correcting voltage at the piezoelectric transducer (PZT).

placed just outside the path of the downconverted light, and reflected the HeNe fringes onto a cylindrical lens (that extended their widths to about 3 mm each. A typical fringe pattern contained 8-10 fringes, for a total pattern width of around 3 cm. The spot size incident on the cylindrical lens was about 1 cm. As the path lengths in the interferometer changed, so too did the lateral positions of these fringes; the precise position of the fringe pattern was used to create a position control signal which could be sent back to the PZT to correct for the fluctuations.

The fringe pattern fell onto a pair of adjacent photodiodes, and the difference between the outputs of these two photodiodes was amplified, integrated, and sent to the PZT driver with the help of the locking circuit shown in Figure D.2. A difference signal of “zero” occurred when a fringe was centered exactly between the two diodes. If a fluctuation caused the fringe to move, the difference signal would become more negative or positive, which either added to or subtracted from the integrated position signal being sent to the PZT driver. The PZT-mounted mirror M1 would move in response to this increased signal, until it arrived at some new position which returned the HeNe fringe to its centered position across the diodes, generating a difference signal of zero and causing no further change to the position signal. In this way, the PZT was continually fed a control voltage of exactly the right amount so that the path length difference remained “locked” to this stable point. For the experiment, the scans in θ were achieved by mounting the pair of photodiodes on a translation stage under computer control. As the diodes were translated to different positions across the fringe pattern, the locking point was forced to move with them, so that the same fringe stayed centered on the diodes at all times. This shift in the fringe position corresponded to a change in the relative path lengths of the two interferometer arms. A diode translation of one fringe width (about 3 mm) corresponded to a change of path length difference by

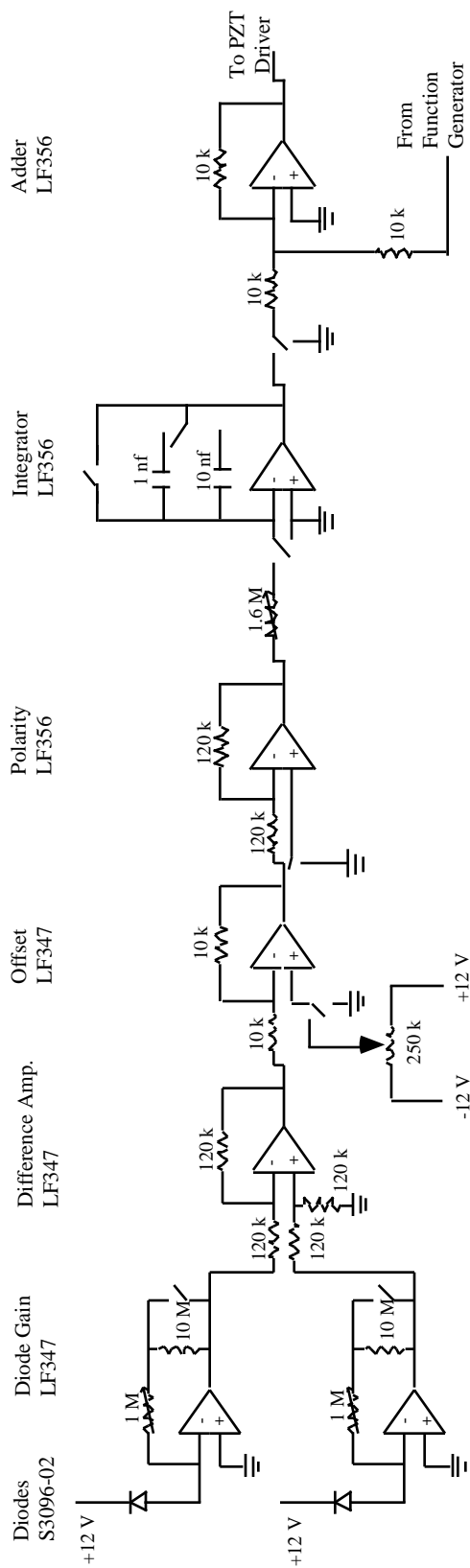


Figure D.2. Locking circuit schematic. All resistor values are in ohms.

$\lambda_{\text{HeNe}} = 633 \text{ nm}$; in practice, about 2 mm of translation were needed to scan through the 405 nm period for θ .

D.2 Operational details

The photodiodes were provided with a +12 V bias supply from the locking circuit, and each returned a current which was converted to a voltage using operational amplifiers in a “trans-impedance” configuration. The gain for each diode could be adjusted by varying the resistance of the negative feedback across the op-amps. The signals were then subtracted, and a variable offset was added so that the difference signal could be zeroed at the correct point, with a fringe centered exactly on the diodes.

A difference signal of zero can be generated either by centering a dark or a bright fringe across the diodes. However, only one of these configurations returns an error signal of the correct sign for negative feedback: the other generates a “correction” of the wrong sign, which further displaces the fringes away from the zero point. To facilitate locking either to the bright or dark fringes, a polarity inverter was included in the locking circuit.

The next element in the circuit is the integrator. With the switch set so that the difference signal V_{in} arrives at the inverting input of the op-amp, the output signal is given by

$$V_{out}(t) = \frac{-1}{RC} \int^t dt V_{in}(t) \quad (\text{D.1})$$

with the gain determined by the choices of R and C. The Fourier transform of this relation,:

$$\tilde{V}_{out}(\omega) = \frac{-1}{i\omega RC} \tilde{V}_{in}(\omega) = e^{i\frac{\pi}{2}} \frac{1}{\omega RC} \tilde{V}_{in}(\omega), \quad (\text{D.2})$$

shows that the gain is infinite at DC, and falls off inversely with frequency as ω .

The gain is unity at the “cutoff frequency”

$$\omega_c = \frac{1}{RC} \quad (\text{D.3})$$

The lower the values of R and C, the higher the gain will be at all frequencies, and the faster the response of the integrator will be to changes in the input signal (higher cutoff frequency) -- all desirable characteristics. However, in practice, we are forced to limit the cutoff frequency to the value

$$\omega_{180} = \frac{2\pi}{2T_{R.T.}} \quad (\text{D.4})$$

where $T_{R.T.}$ is the time required for a signal to make one round trip through the electronic and optical system. Signals with this frequency will arrive back at the input 180 degrees out of phase from the output, a sign change which results in positive feedback instead of negative feedback. If the net gain of the system is above unity for this frequency, oscillations will result. In practice, the value of R was changed by adjusting a potentiometer while monitoring the integrated error signal. R was set to the lowest value that did not cause oscillations. Typically the value of R was around 1 M Ω , when C was 10 nf.

The final element in the locking circuit is an adder, which allowed control of the PZT driver from an external source such as a function generator. This was used from time to time during the alignment, to send a “ramp” voltage to the PZT. The integrator was turned off so that the circuit did not try to lock the position of the mirror while it was under external control.